



LUND UNIVERSITY

Scaling and Gating Attosecond Pulse Generation

Heyl, Christoph

2014

[Link to publication](#)

Citation for published version (APA):

Heyl, C. (2014). *Scaling and Gating Attosecond Pulse Generation*. [Doctoral Thesis (compilation), Atomic Physics]. Atomic Physics, Department of Physics, Lund University.

Total number of authors:

1

General rights

Unless other specific re-use rights are stated the following general rights apply:

Copyright and moral rights for the publications made accessible in the public portal are retained by the authors and/or other copyright owners and it is a condition of accessing publications that users recognise and abide by the legal requirements associated with these rights.

- Users may download and print one copy of any publication from the public portal for the purpose of private study or research.
- You may not further distribute the material or use it for any profit-making activity or commercial gain
- You may freely distribute the URL identifying the publication in the public portal

Read more about Creative commons licenses: <https://creativecommons.org/licenses/>

Take down policy

If you believe that this document breaches copyright please contact us providing details, and we will remove access to the work immediately and investigate your claim.

LUND UNIVERSITY

PO Box 117
221 00 Lund
+46 46-222 00 00

SCALING AND GATING ATTOSECOND PULSE GENERATION

Christoph M. Heyl

Doctoral Thesis
2014



LUND UNIVERSITY

Philipps



Universität
Marburg

SCALING AND GATING ATTOSECOND PULSE GENERATION

© 2014 Christoph M. Heyl

All rights reserved

Printed in Sweden by Media-Tryck, Lund, 2014

Division of Atomic Physics
Department of Physics
Faculty of Engineering, LTH
Lund University
P.O. Box 118
221 00 Lund
Sweden

Department of Physics
Phillips-Universität Marburg
Renthof 5
35037 Marburg
Germany

www.atomic.physics.lu.se

www.uni-marburg.de/fb13

ISSN 0281-2762

Lund Reports on Atomic Physics, LRAP 496 (2014)

ISBN 978-91-7623-157-9 (PRINT)

ISBN 978-91-7623-158-6 (PDF)

ABSTRACT

High-order harmonic generation (HHG) provides the basis for attosecond light sources delivering coherent pulses in the extreme ultraviolet spectral region. Such light sources are employed for a variety of applications within imaging, attosecond spectroscopy, and high-precision frequency metrology. However, the rather low efficiency of the HHG process, which implies a limited pulse energy and repetition rate, places restrictions on many applications.

In this thesis, the scaling of different parameters controlling the generation conditions for HHG in gases is analyzed. A general scaling model is developed, which allows scaling of the pulse energy and repetition rate of attosecond sources over many orders of magnitude, while maintaining temporal and spatial pulse characteristics. The scaling model is applied to different attosecond beam lines, which were developed and built as part of this thesis work. This includes a high-repetition rate (200 kHz) beam line used for photoelectron emission microscopy applications, and an intense harmonic beam line delivering pulses with up to $3 \mu\text{J}$ in the extreme ultraviolet, which was used for coherent imaging as well as for nonlinear spectroscopy applications.

In addition, microscopic sub-cycle control mechanisms based on multi-color field synthesis are studied, as well as noncollinear generation geometries. It is shown that a noncollinear geometry can be used to angularly streak attosecond pulse trains, allowing access to single pulses within the train. This technique is of interest for attosecond pump-probe measurements as well as for isolated attosecond pulse generation inside an optical cavity, a scheme that promises attosecond pulses at unprecedented power levels and repetition rates.

POPULAR SCIENCE SUMMARY

This thesis is concerned with the efficient generation of ultra-short light pulses, far beyond the visible spectral range. Such light pulses can reach durations below 100 attoseconds, where one attosecond is one billionth of a billionth of a second. Why do we want to generate such extreme light pulses?

Our knowledge of basic processes in physics and chemistry is to a large extent based on our understanding of the microscopic world of atoms and molecules. In the macroscopic world, objects move on timescales which are easily accessible to our senses, but in the microscopic world, objects move much more rapidly. The lighter the object, the smaller the energy needed to make the object move and the shorter the time scale on which the movement happens. The movement of electrons within atoms or molecules, a fundamental process essential, for example, for chemical reactions, happens on timescales of a few femtoseconds or less (1 femtosecond = 1000 attoseconds, equal to one millionth of a billionth of a second). Measuring electron dynamics in molecules, is a first step towards the realization of a so-called *molecular movie*, a movie that would allow us to see electronic and structural processes as they take place in chemical reactions. What kind of tools do we need to monitor such processes?

Since the early days of photography, a short flash of light or a short exposure time in a photographic camera has allowed us to freeze the motion of an object in time. The first time-resolved “measurements” allowed to monitor the motion of a galloping horse. Ultrashort laser pulses provide similar access to dynamics which happen on time scales, which are approximately twelve orders of magnitude shorter. The time resolution is thereby determined by the temporal length of the laser pulse. Nowadays such pulses can reach a duration of a few femtoseconds. Approaching the attosecond regime is possible via a process called *high-order harmonic generation*. This process allows us to convert a fraction of the energy of a short laser pulse from the visible spectral range (or close to it) into wavelengths approaching the X-ray regime. During this light-conversion process, a train of attosecond pulses is formed. Today, twenty-seven years after the discovery of high-order harmonic generation, extreme light sources based on this technique are used in many laboratories. Their usability is, however, still quite limited, mainly due to the fact that the generated attosecond light pulses are very weak. Also, an ideal attosecond experiment demands single attosecond pulses instead of trains of many pulses. Both of these issues are addressed in this thesis.

While the first high-order harmonics generated contained only a very small fraction of the energy of the generating laser pulse, modern attosecond sources reach approximately one million times higher values but still only a hundred thousandth part of the laser pulse energy. Such efficiencies are usually achieved with high-power

laser systems. In this thesis, a general scaling model is developed and applied for several attosecond beam lines: at the Lund Laser Center (Sweden), at the University of Marburg (Germany), and for the development of an attosecond beam line for the European Extreme Light Infrastructure facility ELI-ALPS in Hungary. The model explains how the pulse energy of attosecond pulses can be scaled over many orders of magnitude while maintaining identical pulse characteristics. In particular, it is shown that efficient attosecond pulse generation is possible even with weak laser pulses, which enables the generation of many pulses per second, an essential requirement for many spectroscopy applications.

In addition, a new technique is developed in this thesis, allowing the efficient isolation of a single attosecond pulse from the generated pulse train. The technique promises to be applicable to attosecond pulse generation directly inside a so-called optical cavity, a resonator in which laser pulses can be trapped. Such an approach should allow the generation of isolated attosecond pulses at unprecedented power levels and repetition rates. When generated this way, attosecond pulses have another remarkable property: they form a frequency comb in the extreme ultraviolet, which can be used as a high-precision frequency ruler, promising new possibilities for extremely precise definitions of frequency and time.

POPULÄRVETENSKAPLIG SAMMANFATTNING

Denna avhandling behandlar den effektiva genereringen av korta ljuspulser som har mycket kortare våglängder än synligt ljus. Dessa ljuspulser kan vara kortare än 100 attosekunder. En attosekund är en miljarddels miljarddel av en sekund. Men varför vill vi generera så korta ljuspulser?

Kunskapen om fundamentala processer inom fysik och kemi baserar sig i stor utsträckning på förståelsen av den mikroskopiska världen av atomer och molekyler. I den makroskopiska världen rör sig föremålen på tidsskalor som är lätta att uppfatta för våra sinnen, medan i den mikroskopiska världen rör sig objekten mycket snabbare. Ju lättare objektet är, desto mindre är den energi som krävs för att sätta objektet i rörelse och desto kortare är rörelsens tidskala. Elektronernas rörelse inom atomer och molekyler är en fundamental process som är väsentlig till exempel för kemiska reaktioner och som sker på tidsskalor så korta som några femtosekunder (1 femtosekund = 1000 attosekunder, lika med en miljondels miljarddel av en sekund) eller ännu kortare. Att mäta elektronernas dynamik i molekyler är det första steget till en molekylfilm, en film som visar elektroniska och strukturella processer i kemiska reaktioner. Vilka verktyg behövs för att observera sådana processer?

Sedan fotografins barndom har en kort ljusblinx eller en kort exponeringstid möjliggjort att frysa ett objekts rörelse. Genom de första tidsupplösta mätningarna kunde man mäta en galopperande hästs rörelsemöster. På samma sätt tillåter korta laserpulser att mäta dynamiska processer som äger rum på tidsskalor som är 12 storleksordningar kortare. Tidsupplösningen begränsas av laserpulsens längd. Idag kan sådana laserpulser vara några femtosekunder korta. Att nå attosekundstidsskalan är möjligt genom en process som kallas för hög övertongenerering. Processen möjliggör konvertering av en liten del av laserpulsernas energi från det synliga (eller nära det synliga) området till våglängder som nå ända in i röntgenområdet. I denna ljuskonverteringsprocess skapas ett så kallat tåg av attosekundspulser. Idag, 27 år efter upptäckten av övertongenereringsprocessen, används extrema ljuskällor som är baserade på övertongenerering i många laboratorier. Tillämpbarheten är dock begränsad, framför allt för att attosekundspulser är mycket svaga. Dessutom kräver det perfekta attosekundsexperiment isolerade attosekundspulser istället för ett pulståg. Både frågorna behandlas i denna avhandling.

De första höga övertoner som producerades innehöll bara en väldigt liten del av laserpulsens energi. Däremot kan moderna attosekundspulskällor, baserad på högef-

fektslaser-system, nå miljoner gånger högre värden men ändå bara en hundratusendel av laserpulsens energi. I denna avhandling utvecklas en allmän skalningsmodell som tillämpas på olika attosekundspulskällor, vid såväl Lunds Laser Centrum, som vid Universitetet i Marburg (Tyskland) och för utvecklingen av en attosekundspulskälla vid den europeiska anläggningen ELI-ALPS i Ungern. Modellen förklarar hur attosekundspulsernas energi kan skalas över många storleksordningar utan att påverka pulsernas egenskaper. Således påvisas att en effektiv attosekundspulsgenerering är möjlig även med svaga laserpulser som möjliggör generering av många pulser per sekund. Detta är en viktig förutsättning för många spektroskopiapplikationer.

I denna avhandling utvecklas dessutom en ny teknik för att isolera en enskild puls från attosekundspulståget. Denna teknik utlovar tillämpbarhet av attosekundsgenereringen i en optisk kavitet, en resonator som håller laserpulser fångade. Att producera isolerade attosekundspulsar i en sådan resonator tillåter mycket högre genomsnittlig effekt och mycket högre repetitions-hastighet. Men attosekundspulser som genereras i en optisk kavitet har ytterligare en anmärkningsvärd egenskap: de ger upphov till en frekvenskam i det extremt ultravioletta området. En sådan frekvenskam kan användas som en mycket exakt linjal för frekvenser och utlovar nya möjligheter för definitionen av frekvens och tid.

POPULÄRWISSENSCHAFTLICHE ZUSAMMENFASSUNG

Diese Arbeit behandelt die effiziente Erzeugung von ultrakurzen Lichtpulsen, deren Wellenlängen viel kürzer sind als die des sichtbaren Lichts. Solche Lichtpulse können kürzer sein als 100 Attosekunden. Eine Attosekunde hat eine Dauer von einem Milliardstel eines Milliardstels einer Sekunde. Warum wollen wir solche Lichtpulse erzeugen?

Unser Wissen über fundamentale Prozesse in Physik und Chemie basiert weitgehend auf dem Verständnis der mikroskopischen Welt aus Atomen und Molekülen. In der makroskopischen Welt bewegen sich Objekte auf Zeitskalen, die für unsere Sinne leicht erfassbar sind. In der mikroskopischen Welt hingegen bewegen sich die Objekte sehr viel schneller. Je leichter ein Objekt, desto weniger Energie wird benötigt um das Objekt in Bewegung zu setzen und desto kürzer ist die Zeitskala auf der die Bewegung abläuft. Die Bewegung von Elektronen innerhalb von Atomen und Molekülen, zum Beispiel, ist ein fundamentaler Prozess, der entscheidend ist für chemische Reaktionen und der auf Zeitskalen von einigen Femtosekunden (1 Femtosekunde = 1000 Attosekunden, ein Millionstel eines Milliardstels einer Sekunde) oder schneller abläuft. Die Elektronendynamiken in Molekülen zu messen, ist ein erster Schritt zur Realisierung eines „Molekülfilms“ der elektronische Vorgänge und strukturelle Umwandlungsprozesse in chemischen Reaktionen zeitaufgelöst abbildet. Welche Werkzeuge werden benötigt, um solche Prozesse sichtbar zu machen?

Seit dem Anfang der Fotografie werden kurze Lichtblitze oder kurze Belichtungszeiten dazu eingesetzt, schnelle Bewegungsabläufe abzubilden. Die ersten solcher zeitaufgelösten Messungen machten es möglich, den Bewegungsablauf eines galoppierenden Pferdes zu studieren. Auf vergleichbare Weise erlauben kurze Laserpulse die Messung dynamischer Prozesse, die sich auf Zeitskalen abspielen, die 12 Größenordnungen kleiner sind. Die erreichbare Zeitauflösung wird dabei von der Länge des Laserpulses bestimmt. Heutzutage ist es möglich, Laserpulse mit einer Länge von wenigen Femtosekunden zu erzeugen. Attosekundenzeitskalen können durch die Erzeugung von sogenannten Höheren Harmonischen erreicht werden. Dieser Prozess erlaubt die Konvertierung eines geringen Teils der Laserpulsenergie aus dem sichtbaren (oder nahe dem sichtbaren) Spektralbereich zu kurzen Wellenlängen, die den Röntgenbereich erreichen können. In diesem Lichtumwandlungsprozess wird ein sogenannter Pulszug, das heißt mehrere aufeinanderfolgende Attosekundenpulse, erzeugt. Heutzutage, 27 Jahre nach der Entdeckung des Harmonischerzeugungprozesses, werden Lichtquel-

len, die auf diesem Prozess basieren, in vielen Laboren eingesetzt. Die Verwendbarkeit der erzeugten Pulse ist allerdings eingeschränkt, vor allem aufgrund der sehr niedrigen Pulsenergien. Außerdem werden für ein ideales Attosekundenexperiment einzelne Laserpulse an Stelle eines Pulszuges benötigt. Beide Aspekte werden in dieser Arbeit behandelt.

Die ersten höheren Harmonischen enthielten nur einen verschwindend kleinen Teil der aufgewendeten Laserpulsenergie. Moderne Attosekundenpulsequellen, meist auf Hochleistungslasern basierend, können dagegen millionenfach höhere Werte und damit etwa ein Hunderttausendstel der Laserpulsenergie erreichen. In dieser Arbeit wird ein allgemeines Skalierungsmodell entwickelt und auf verschiedene Attosekundenquellen am Laserzentrum in Lund (Schweden) sowie an der Universität Marburg als auch für die Entwicklung einer Attosekundenpulsequelle für die europäischen Forschungsanlage ELI-ALPS in Ungarn, angewendet. Das Modell erklärt, wie die Energie der Attosekundenpulse über viele Größenordnungen skaliert werden kann, ohne weitere Pulseigenschaften zu ändern. Dadurch wird insbesondere gezeigt, dass die effektive Erzeugung von Attosekundenpulsen auch mit relativ schwachen Laserpulsen möglich ist. Das bedeutet, dass viele Pulse per Sekunde erzeugt werden können, was eine Voraussetzung für viele Spektroskopieanwendungen ist.

In dieser Arbeit wird außerdem eine neue Methode zur Isolierung einzelner Pulse aus dem Pulszug entwickelt. Die Methode sollte sich zur Erzeugung einzelner Attosekundenpulse in einem optischem Resonator eignen. Einzelne Attosekundenpulse in einem Resonator zu erzeugen, ermöglicht viel höhere mittlere Leistungen und Repetitionsraten. Außerdem haben Attosekundenpulse, die in einem Resonator erzeugt werden, eine weitere einzigartige Eigenschaft: Sie bilden einen Frequenzkamm im extremen ultravioletten Spektralbereich. Ein solcher Frequenzkamm kann als sehr exaktes „Lineal“ zur Frequenzmessung verwendet werden und verspricht neue Möglichkeiten für die Definition von Frequenz und Zeit.

LIST OF PUBLICATIONS

This thesis is based on the following papers, which will be referred to by their Roman numerals in the text:

I Spectrally Resolved Maker Fringes in High-Order Harmonic Generation

C. M. Heyl, J. Gdde, U. Hfer and A. L’Huillier.
Physical Review Letters **107**, 033903 (2011).

II High-Order Harmonic Generation with μJ Laser Pulses at High Repetition Rates

C.M. Heyl, J. Gdde, A. L’Huillier and U. Hfer.
Journal of Physics B **45**, 074020 (2012).

This paper was selected by the journal editors as a “*Highlight article 2012*”.

III Carrier–Envelope Phase Dependent High-Order Harmonic Generation with a High-Repetition Rate OPCPA-System

P. Rudawski, A. Harth, C. Guo, E. Lorek, M. Miranda, C. M. Heyl, E. W. Larsen, J. Ahrens, O. Prochnow, T. Binhammer, U. Morgner, J. Mauritsson, A. L’Huillier and C. L. Arnold.
Submitted for publication.

IV High-Order Harmonic Generation Using a High-Repetition Rate Turnkey Laser

E. Lorek, E. W. Larsen, C. M. Heyl, S. Carlstrm, D. Paleek, D. Zigmantas, and J. Mauritsson.
Submitted for publication.

V Attosecond Pulse Walk-Off in High-Order Harmonic Generation

D. Kroon, D. Gunot, M. Kotur, E. Balogh, E. W. Larsen, C. M. Heyl, M. Miranda, M. Gisselbrecht, J. Mauritsson, P. Johnsson, K. Varj, A. L’Huillier and C. L. Arnold.
Optics Letters **39**, 2218 (2014).

VI A High-Flux High-Order Harmonic Source

P. Rudawski, C. M. Heyl, F. Brizuela, J. Schwenke, A. Persson, E. Mansten, R. Rakowski, L. Rading, F. Campi, B. Kim, P. Johnsson and A. L'Huillier.
Review of Scientific Instruments **84**, 073103 (2013).

VII Conceptual Design Report for a Gas HHG Beam Line at ELI-ALPS

C. M. Heyl, P. Rudawski, F. Brizuela, P. Johnsson, C. L. Arnold and A. L'Huillier.
Report ELI-ALPS, (2012).

VIII Compression of TW-class Laser Pulses in a Planar Hollow Waveguide for Applications in Strong-Field Physics

A. Jarnac, F. Brizuela, C. M. Heyl, P. Rudawski, F. Campi, B. Kim, L. Rading, P. Johnsson, A. Mysyrowicz, A. L'Huillier, A. Houard and C. L. Arnold.
Accepted for publication in European Physics Journal D.

IX Efficient High-Order Harmonic Generation Boosted by Below-Threshold Harmonics

F. Brizuela*, C. M. Heyl*, P. Rudawski*, D. Kroon, L. Rading, J. M. Dahlström, J. Mauritsson, P. Johnsson, C. L. Arnold and A. L'Huillier;
(* authors contributed equally).
Scientific Reports **3**, 1410 (2013).

X Interference Effects in Two-Color High-Order Harmonic Generation

X. He, M. Dahlström, R. Rakowski, C. M. Heyl, A. Persson, J. Mauritsson, and A. L'Huillier.
Physical Review A **82**, 033410 (2010).

XI Digital In-Line Holography on Amplitude and Phase Objects Prepared with Electron Beam Lithography

J. Schwenke, E. Lorek, R. Rakowski, X. He, A. Kvennefors, A. Mikkelsen, P. Rudawski, C. M. Heyl, I. Maximov, S. G. Pettersson, A. Persson, and A. L'Huillier.
Journal of Microscopy **247**, 196201 (2012).

XII Macroscopic Phase Effects in Noncollinear High-Order Harmonic Generation

C. M. Heyl, P. Rudawski, F. Brizuela, J. Mauritsson and A. L'Huillier.
Physical Review Letters **112**, 143902 (2014).

XIII Noncollinear Optical Gating

C. M. Heyl, S. Bengtsson, S. Carlström, J. Mauritsson, C. L. Arnold and A. L'Huillier.

New Journal of Physics, Fast Track Communications **16**, 052001 (2014).

In the version of this paper included in this thesis, Figure 4 was replaced by an updated version, published in a Corrigendum as: *New Journal of Physics* **16**, 109501 (2014).

XIV Gating Attosecond Pulses in a Noncollinear Geometry

C. M. Heyl*, M. Louisy*, M. Miranda, D. Kroon, M. Kotur, E. W. Larsen, S. N. Bengtsson, D. Guénot, L. Rading, F. Brizuela, P. Rudawski, F. Campi, B. Kim, J. Mauritsson, P. Johnsson, A. L'Huillier and C. L. Arnold;
(* authors contributed equally).

In preparation.

Related publication by the author, which is not included in this thesis:

Spatial and Spectral Properties of the High-Order Harmonic Emission in Argon for Seeding Applications

X. He, M. Miranda, J. Schwenke, O. Guilbaud, T. Ruchon, C. Heyl, E. Georgadiou, R. Rakowski, A. Persson, M. B. Gaarde, and A. L'Huillier.
Physical Review A **79**, 063829 (2009).

ABBREVIATIONS

ALH	Attosecond Light House
APT	Attosecond Pulse Train
BS	Beam Splitter
CEP	Carrier–Envelope Phase
CVBG	Chirped Volume Bragg Grating
CV	Continuous Wave
DBS	Dichroic Beam Splitter
DBS	Double Chirped Mirror
DFG	Difference Frequency Generation
DPA	Down-Chirped Pulse Amplification
ELI–ALPS	Extreme Light Infrastructure – Attosecond Light Pulse Source
FEL	Free-Electron Laser
FM	Frequency Modulation
FROG–CRAB	Frequency Resolved Optical Gating for Complete Reconstruction of Attosecond Bursts
FWHM	Full-Width at Half-Maximum
GVD	Group Velocity Dispersion
HHG	High-Order Harmonic Generation
IAP	Isolated Attosecond Pulse
IR	Infrared
NCHHG	Noncollinear High-Order Harmonic Generation
NOG	Noncollinear Optical Gating
NOPA	Noncollinear Optical Parametric Amplifier/Amplification
OPA	Optical Parametric Amplifier/Amplification
OPCPA	Optical Parametric Chirped Pulse Amplifier/Amplification
RABITT	Reconstruction of Attosecond Beating by Interfering Two-photon Transitions
SFA	Strong Field Approximation
SFG	Sum–Frequency Generation

SHG	Second-Harmonic Generation
SVEA	Slowly Varying Envelope Approximation
TDSE	Time-Dependent Schrödinger Equation
WFR	Wavefront Rotation
XUV	Extreme Ultraviolet (approx. $10 < \hbar\omega < 124$ eV)

CONTENTS

1	Introduction	1
1.1	Introduction to Nonlinear Optics and High-Order Harmonic Generation	1
1.2	Characteristics and Applications of High-Order Harmonic and Attosecond Sources	3
1.2.1	High-Order Harmonics – Attosecond Pulse Trains	4
1.2.2	Broadband XUV Sources – Isolated Attosecond Pulses	5
1.2.3	Harmonic Combs – Coherent fs XUV Pulses	6
1.2.4	XUV Frequency Combs – Narrow Band XUV-CW “Lasers”	7
1.3	Limitations in Attosecond Science	8
1.4	Scope and Outline of this Thesis	9
2	High Order Harmonic and Attosecond Pulse Generation	11
2.1	An Ultrashort Introduction to Electromagnetic Waves and Short Pulses	11
2.1.1	Linear Properties	12
2.1.2	Nonlinear Properties	15
2.2	Introduction to High-Order Harmonic Generation	15
2.2.1	The Three-Step Model	16
2.2.2	The Quantum Mechanical Model	19
2.2.3	Dipole Amplitude and Phase	20
2.2.4	Isolated Attosecond Pulses	25
2.2.5	Temporal Characterization of Attosecond Pulses	26
2.3	Macroscopic Effects in High-Harmonic Generation	28
2.3.1	Basic Principles of Phase Matching	29
2.3.2	Phase Matching Characteristics in HHG	32
2.4	Macroscopically Induced Spatial and Spectral Structures	38
2.4.1	Spectral Maker Fringes	39
2.4.2	Multi-Source Interferences	41
2.5	Quasi-classical Modeling	41
3	Repetition Rate vs Intensity – Two Complementary Scaling Directions	43
3.1	Introduction: Scaling Repetition Rate and Intensity	43
3.1.1	A Generalized Scaling Model	45
3.1.2	A Generalized Macroscopic Model	49
3.2	Downscaling and High-Repetition Rate HHG	50
3.2.1	The 200 kHz OPCPA System in Lund	51
3.2.2	The 100 kHz System in Marburg	53
3.3	Upscaling and Intense XUV Pulses	54
3.3.1	The Intense Harmonic Beam Line in Lund	55
3.3.2	A Novel Attosecond Beam Line for ELI-ALPS	56
3.4	Average Power Scaling	57
3.4.1	Enhancing the Single Atom Response using Multi-Color Field Synthesis	58
4	Noncollinear High-Order Harmonic Generation	63
4.1	Introduction to High-Order Noncollinear Wave-Mixing	64
4.1.1	Different Regimes of NCHHG	64

4.1.2	Controlling NCHHG with Driving Field Intensities	70
4.2	Macroscopic Phase Effects in NCHHG	72
4.2.1	Transverse Macroscopic Effects	72
4.2.2	Propagation Effects	75
4.3	Noncollinear Optical Gating	77
4.3.1	Introduction to a New Gating Concept	77
4.3.2	Comparison with Other Gating Methods	79
4.3.3	Applying NOG to the Extremes of the Two Scaling Directions	81
4.4	Experimental Implementation of NCHHG	83
5	Summary and Outlook	85
	Comments on the papers	89
	Acknowledgements	93
	Curriculum Vitae	95
	Bibliography	97

Papers

I	Spectrally Resolved Maker Fringes in High-Order Harmonic Generation	117
II	High-Order Harmonic Generation with μJ Laser Pulses at High Repetition Rates	123
III	Carrier–Envelope Phase Dependent High-Order Harmonic Generation with a High-Repetition Rate OPCPA-System	134
IV	High-Order Harmonic Generation Using a High-Repetition Rate Turnkey Laser	144
V	Attosecond Pulse Walk-Off in High-Order Harmonic Generation	153
VI	A High-Flux High-Order Harmonic Source	159
VII	Conceptual Design Report for a Gas HHG Beam Line at ELI-ALPS	168
VIII	Compression of TW-class Laser Pulses in a Planar Hollow Waveguide for Applications in Strong-Field Physics	183
IX	Efficient High-Order Harmonic Generation Boosted by Below-Threshold Harmonics	190
X	Interference Effects in Two-Color High-Order Harmonic Generation	198
XI	Digital In-Line Holography on Amplitude and Phase Objects Prepared with Electron Beam Lithography	205
XII	Macroscopic Phase Effects in Noncollinear High-Order Harmonic Generation	213
XIII	Noncollinear Optical Gating	222
XIV	Gating Attosecond Pulses in a Noncollinear Geometry	236

INTRODUCTION

Today, extreme ultraviolet (XUV) sources based on high-order harmonic generation (HHG) are used in many laboratories. This is due to the interesting and partly unique properties of the light pulses generated via HHG. Besides their short time duration, these include a high spatial coherence [1], good beam quality, and a wide photon energy range reaching into the X-ray spectral region [2–4]. Furthermore, if generated via a frequency-locked laser, HHG radiation can provide high precision frequency combs in the XUV spectral region [5].

This chapter provides a short introduction to high-order harmonic and attosecond sources, including an overview of their characteristic properties in the time and frequency domains. Important applications which make use of these properties are introduced. In the second part of this chapter, general limitations in attosecond science are briefly discussed, followed by a description of the scope and outline of this thesis.

1.1 Introduction to Nonlinear Optics and High-Order Harmonic Generation

Soon after the invention of the laser in 1960 [6], the first nonlinear response of an optical medium was observed, namely the second harmonic signal of the laser frequency [7], generated in a quartz crystal. The nonlinearity manifests itself in the induced polarization, which exhibits a nonlinear behavior with increasing field strength when sufficiently high field intensities are reached. This behavior has far-reaching consequences, and contradicts assumptions which had been fundamental throughout the long history of optics. Basic properties of light such as its speed or frequency could depend on the light intensity.

Since the first observation of a nonlinear optical process, an extensive range of techniques using nonlinear effects has been developed. Maybe most importantly, nonlinear optical processes provide a means to up-convert coherent laser radiation to multiples of the original frequency. Conventional laser operation is limited to a spectral range not far beyond the visible spectral region. This is because of the limited availability of suitable energy transitions, as well as disadvantageous scaling of the pumping power with laser frequency. There are, however, many applications in various fundamental and applied research fields which demand coherent light sources far beyond the vis-

ible, including the XUV or even the X-ray spectral regions. To reach these spectral regions is possible via HHG, a process discovered in 1987 [8, 9]. Nowadays, attosecond sources based on HHG, can reach photon energies in the the keV range [10, 11]. While the field strength of harmonics of a driving frequency typically decrease rapidly with increasing harmonic order, high-order harmonics exhibit a plateau-like behavior, allowing the generation of weak, but equally intense frequencies over a broad spectral range.

A fundamental requirement for nonlinear optical processes is a high field intensity, typically reached by confining the laser power to a small spatial region and a very short time interval – a laser pulse. Such coherent light pulses can be generated by mode locking a laser resonator [12], that is, by inserting an optical element which preferentially transmits fields with high intensities, leading to a coherent superposition of all the frequencies supported by the laser resonator, and thus to the formation of short pulses. The pulse duration τ is thereby limited by the spectral bandwidth $\Delta\nu$ via the time-bandwidth product, also known in frequency analysis as the Gabor limit [13]:

$$\tau \cdot \Delta\nu \geq 0.44 \tag{1.1}$$

Here, Gaussian profiles and FWHM values are assumed. The time-bandwidth product sets a general limit: the broader the spectrum supported, the shorter the pulse duration that can be reached. The spectral bandwidth is typically limited by the supporting gain medium, as well as by the resonator itself, which has to allow a phase-locked round-trip for the entire bandwidth [12]. Nowadays, octave-spanning laser systems can be realized in the visible/near infrared [14], thus supporting pulse durations down to a few femtoseconds ($1 \text{ fs} = 10^{-15} \text{ s}$). Such pulses consist of only a few cycles of the carrier frequency.

Short laser pulses do not only enable high field intensities. They also allow the measurement of processes which evolve on very short time scales, typically by using pump–probe schemes, where a first laser pulse is used to initiate a process, and a second pulse, which arrives after an adjustable time delay, probes its dynamics. The temporal resolution is typically determined by the pulse duration. While ground-breaking experiments have been performed on femtosecond time scales, for example in femtochemistry [15], there are dynamical electronic processes in systems such as atoms [16], molecules [17] or solids [18] that require even shorter time scales. One fundamental limitation on the duration of a laser pulse results from its central frequency, because that determines the duration of a single cycle of the carrier wave. For broadband Titanium Sapphire lasers, the single cycle limit is 2.7 fs. In order to reach even shorter time scales, it is necessary to leave the visible spectral range. This can be done by using nonlinear optical processes such as harmonic generation. The spectral composition of high-order harmonics allows the formation of ultra short pulses in the XUV spectral region, with durations in the attosecond regime. A key requirement for attosecond pulses to form is a locked phase between all the generated harmonic orders, i.e. the coherence of the driving laser pulse needs to be transferred to the generated harmonics. Despite different assumptions, directly after the first observation of high-order harmonics, it was found that the HHG process is extremely coherent [5] and leads to short attosecond pulses. Nevertheless, it took more than ten years to measure [19] and isolate [20] the first attosecond pulses, mainly due to the lack of appropriate characterization techniques.

1.2 Characteristics and Applications of High-Order Harmonic and Attosecond Sources

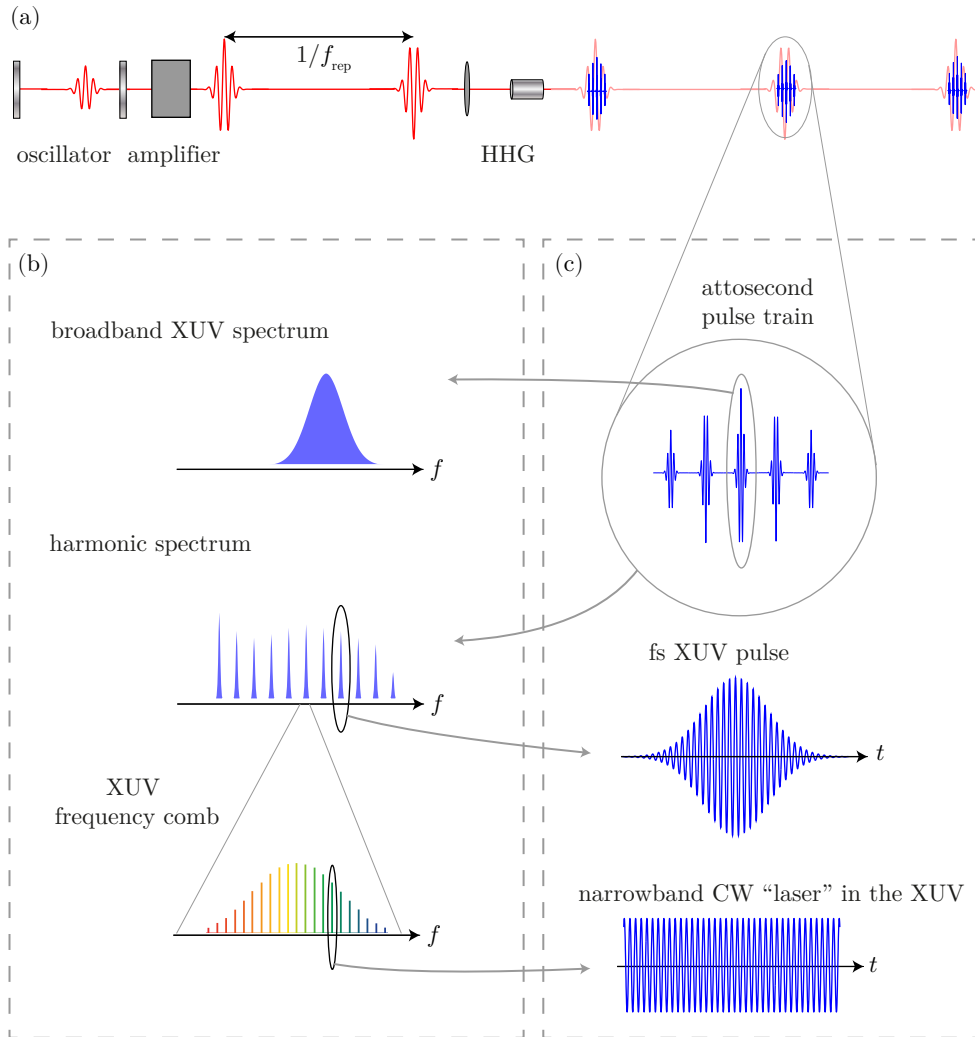


Figure 1.1: Schematic of a high-order harmonic source (a) and its spectral (b) and temporal (c) characteristics.

A typical harmonic source providing coherent pulses in the XUV is depicted schematically in Fig. 1.1 (a). The laser pulses are generated inside a laser oscillator, as indicated in the figure. Each time the pulse passes the out-coupling mirror (in modern laser systems other optical elements are typically used for out-coupling), a small fraction of its energy is transmitted, leading to a train of pulses, separated temporally by $1/f_{\text{rep}}$, where the repetition rate $f_{\text{rep}} = c/L_o$ is defined by the optical path length of the oscil-

lator L_o (the length of one optical round trip), and c is the speed of light in vacuum. In modern high-power laser systems, these pulses are then typically sent through an amplification system to increase their energy by several orders of magnitude while preserving their short duration. The amplified pulses are then focused into a nonlinear medium (typically a rare gas target) where high-order harmonics are generated. Driving the HHG process with a multi-cycle pulse leads to the generation of a train of attosecond pulses, the temporal representation of a high-order harmonic spectrum.

The schematic XUV source depicted in Fig. 1.1 provides a number of precise tools that can be used for many different applications, making use of their unique properties in the temporal [Fig. 1.1 (c)] as well as in the spectral [Fig. 1.1 (b)] domain. In the temporal domain, HHG leads to a train of attosecond pulses. Different techniques can be applied to temporally isolate a single attosecond pulse of this train, usually by manipulating the generation process itself. In the spectral domain, a harmonic frequency comb is formed, made up of harmonics of the driving laser frequency ω , typically separated spectrally by 2ω . A spectral selection of one of those harmonics provides coherent XUV pulses which are slightly shorter than the driving laser pulse. Addressing the spectral composition of the generated XUV radiation with much higher resolution allows access to another, very precise frequency comb [21, 22]. Each harmonic order q consists of thousands of narrow frequency comb lines. This XUV frequency comb can be understood as the harmonic up-conversion of the driving laser frequency comb. The frequencies of the laser comb can be written as¹ $f_m = f_{\text{CE}} + mf_{\text{rep}}$, defined by the repetition rate as well as by the carrier-envelope offset frequency $f_{\text{CE}} = \Delta\phi_{\text{CE}}f_{\text{rep}}/2\pi$, where $\Delta\phi_{\text{CE}}$ is the difference in *carrier-envelope phase* between consecutive laser pulses in the time domain [23]. The carrier-envelope phase denotes the relative phase between the carrier wave and the pulse envelope, which is defined more precisely in section 2.1.1. The corresponding XUV comb frequencies are thus given by $f_n = qf_{\text{CE}} + nf_{\text{rep}}$. n and m are large integers.

Although the harmonic source development performed within this thesis work was mainly motivated by the temporal aspects of the XUV radiation produced via HHG, i.e. their ultra-short time duration, the corresponding properties in the frequency domain can be very useful for other applications. Historically, laser development was driven by two distinct research communities with largely divergent goals, who regarded short pulse duration or precisely defined frequencies as the main useful property [24]. However, a convergence of the fields of ultrafast optics and precision laser spectroscopy has taken place, mainly during the last decade. The various temporal and spectral properties that HHG sources can provide are listed in the following sections, and a few important applications are introduced.

1.2.1 High-Order Harmonics – Attosecond Pulse Trains

Due to the coherence of the HHG process, the generated high-order harmonics form a train of phase locked XUV pulses with a duration of around one hundred attoseconds. Such pulse trains can be used, for example, to probe the attosecond-scale time evolution of periodic processes driven by the fundamental laser field [25, 26].

A prominent example is the electron stroboscope, an experiment performed a few years ago in Lund. Here, a train of attosecond XUV pulses is used to ionize atoms

¹ f_{CE} and f_{rep} need to be stabilized for a precise definition of f_n .

periodically in a strong laser field, their momentum distribution being controlled by the underlying laser field [27]. As in a stroboscope, this scheme allows to “freeze” the electron momentum distribution and to image coherent electron scattering processes.

In a related experimental scheme, attosecond XUV pulses are used for excitation into the continuum while the driving laser field acts as a probe, leading to energy sidebands in the detected photoelectron spectra through interferences between the created electron wave packets. This way, by cross-correlating the attosecond pulse train with the fundamental laser field in a detection gas, while monitoring the generated photoelectron spectrum, the phase difference between consecutive harmonic orders can be extracted [28]. This scheme is usually applied to temporal characterization of the attosecond pulse train via reconstruction of attosecond beating by interfering two-photon transitions (the so called “RABITT” scheme) [19], discussed in more detail in section 2.2.5.

Recently, the measurement of ionization time delays in atoms has attracted a great deal of interest, motivated by the fundamental question: how long does it take to ionize an atom? The phase imprinted by the time delay between electrons ionized from different sub-shells can be accessed via electron wave packet interferometry, using a RABITT-like measurement scheme. In Lund, both single [29] and double ionization [30] time delays have been measured using interferometric schemes employing attosecond pulse trains together with the driving laser field. Other groups have used isolated attosecond pulses to address ionization time delays in tungsten crystals [18] and in neon atoms [31].

1.2.2 Broadband XUV Sources – Isolated Attosecond Pulses

Broadband isolated attosecond pulses can be seen as the ultimate tool for attosecond science experiments. Employing such pulses instead of pulse trains allows us to avoid the periodicity restriction inherently present when attosecond pulse trains are used. Isolated attosecond pulses (IAPs) are typically used in pump–probe schemes in combination with the fundamental laser pulse. The interpretation of experiments in such a scheme can, however, be challenging as they are typically performed in the regime of temporal overlap between a short XUV pulse and a long but intense laser pulse, which can induce strong-field processes. An ideal experiment would combine two isolated attosecond pulses: one for pump excitation and one as a time-delayed probe [32]. Due to the experimental difficulties of generating two IAPs with controllable delay and sufficient intensity, this scheme has only been applied in a few experiments [33–35] but promises new possibilities for time-resolved studies of ultrafast electron dynamics.

The broad spectral bandwidth of isolated attosecond pulses is ideally suited to so-called *transient absorption* measurements [16]. Combining a single attosecond pulse with an intense fundamental laser pulse can provide time-resolved spectral information from gases, liquids and solids. This information is imprinted onto the attosecond pulse after the interaction with the sample and is thus accessible via its spectrum [32]. The laser pulse can thereby act as pump pulse, initializing a process which is then probed with the attosecond pulse; or it can be used as probe, perturbing the free decay of a transition in the XUV. Transient absorption spectroscopy can provide information on dynamics occurring below the ionization threshold, typically inaccessible to other

common techniques in attosecond science, which are often based on ionization and subsequent charged particle detection [36].

A prominent example of an experiment where isolated attosecond pulses are used to probe dynamics induced with a laser pulse, is the so called attosecond nanoplasmonic-field microscope. Nanoplasmonics describes the collective electron dynamics on the surface of metal nanostructures, promising applications in nanoscale computing and in the development of optoelectronic devices [37]. Due to their broad spectral bandwidth, surface plasmons can evolve on attosecond timescales. Stockman and co-workers proposed combining the temporal resolution of attosecond pulses with the spatial resolution provided by photoelectron emission microscopy to study these plasmon dynamics. The concept has so far been demonstrated on femtosecond time scales [38]. Recently, a few initial experimental attempts towards the realization of this experiment have been performed [39, 40], including, amongst others, in Lund.

Although they are typically weak, because of their extremely short duration, attosecond pulses allow us for the first time to reach XUV intensities sufficient to probe nonlinear processes in the XUV spectral region [35, 41, 42], thus opening a new regime of extreme nonlinear optics. At the intense harmonics beam line in Lund, initial proof-of-principle studies allowed the observation of multi-photon ionization of neon induced by a tightly-focused attosecond pulse train. The attosecond pulse train was first propagated a distance of 6 m in order to increase the beam diameter before being tightly refocused with two toroidal mirrors (in a Wolter configuration) into a gas jet. The given experimental parameters allowed to reach XUV intensities around 10^{13} W/cm² [43].

1.2.3 Harmonic Combs – Coherent fs XUV Pulses

A single harmonic order can be isolated from the generated harmonic spectrum by spectral selection. This is typically done by a monochromator assembly based on diffraction gratings or multilayer mirrors. As an XUV pulse consisting of a single harmonic order has a slightly shorter duration than the generating laser pulse, it can be applied to probe dynamics in the femtosecond regime.

An important example is photoemission studies of ultrafast dynamics in solids and at solid surfaces [44], pioneered by Richard Haight [45], and currently being pursued by several research groups [46–54]. This topic formed the main motivation for the HHG source development within the framework of this thesis in Marburg, which is discussed in detail in Paper II (see also Paper I). In the last two decades, pump–probe schemes employing femtosecond pulses in the visible and near-ultraviolet regime have enabled a number of novel experiments probing electron dynamics on surfaces [55–64], as well as phase transitions in solids [65]. Employing high-order harmonics as the pump or probe pulses in such experiments allows an extension of the available photon energy range far beyond the visible region. This is particularly interesting since it enables access to the entire two-dimensional electronic band structure in many solid surfaces. In this case, the range of detectable electron momenta can cover the complete surface Brillouin zone [66].

Another application where coherent XUV sources are required is coherent imaging [67]. Because the achievable resolution when imaging microscopic objects is limited by the wavelength of the light source, nanoscale imaging requires wavelengths in the few-nm regime. At these wavelengths, the use of imaging optics is very limited, a prob-

lem which can be circumvented by lensless imaging methods. Here, a high-resolution image of an object is reconstructed from one or more measured diffraction patterns. Such coherent imaging methods are promising for applications such as biological cell imaging [68], especially if used in combination with XUV sources in the spectral range of the water window. In Lund, a lensless imaging system has been developed, based on digital in-line holography [69]. At the onset of this thesis work, the 21st harmonic, generated at the intense harmonic beam line in Lund (see section 3.3.1), was used to image nanostructures on SiN membranes. This experiment is described in detail in Paper XI. The generated harmonic radiation was spectrally filtered and tightly refocused using a multilayer-coated Schwarzschild objective. Placing a partially transmitting object a short distance behind the XUV focus allowed the creation of XUV diffraction patterns in the far-field, coherently superimposed by part of the illuminating radiation, which thus acted as a reference for holographic reconstruction. Via an iterative algorithm, amplitude and phase information about the object could be reconstructed numerically. The method delivered images with a resolution down to 1.5 μm and was mainly limited by the numerical aperture used, but also by shot-to-shot beam pointing and power fluctuations, which restricted the accumulation of multiple holographic images over several laser shots. Single-shot imaging was possible [69], but did not lead to high-quality images. This was a strong motivation for subsequent beam-line upgrades to produce a higher photon flux and allow a tighter refocusing of the generated XUV radiation. A further limitation arises because of the relatively broad spectral bandwidth, which results in a blurring of the diffraction pattern. A very recent approach circumvents the bandwidth limitation arising in conventional coherent-imaging schemes by using two temporally delayed laser pulses. Scanning the pulse-to-pulse time delay allows the reconstruction of diffraction-limited images for all spectral components in the pulse [70].

1.2.4 XUV Frequency Combs – Narrow Band XUV-CW “Lasers”

The temporal periodicities imposed by the repetition rate of the laser system and the repetition rate of the attosecond pulse trains or isolated attosecond pulses, define a corresponding periodic structure in the frequency domain, a frequency comb. Such combs provide extremely coherent [5] continuous wave (CW) references in the XUV which can be used to measure frequencies with extremely high precision. The spacing between the spectral lines, defined by the repetition rate, is typically very narrow, thus making their use for spectroscopy challenging. In order to achieve a sufficiently large spacing, a high repetition rate is needed. This can be realized by driving the HHG process inside a so-called *enhancement cavity*, an optical cavity in which many laser pulses are coherently superimposed, thus enhancing the pulse energy while retaining the high repetition rate. Nowadays, frequency combs in the visible spectral range are frequently applied to characterize the light emitted by lasers, atoms, molecules, stars, or other objects. In 2005, John L. Hall and Theodor W. Hänsch received the Nobel price in physics for the development of optical frequency combs. In the same year, researchers in Boulder and Garching succeeded in producing the first XUV frequency combs [21, 22].

As in the visible spectral range, XUV frequency combs can directly be applied for ultra-high precision spectroscopy [71]. Two-photon transitions are especially good candidates to be measured with such a comb, since the comb modes can add up

pair-wise to the same transition energy. In this case, the linewidth is determined by the linewidth of a single comb line while the transition probability depends on the power of the entire comb [72]. Another interesting approach, dual comb spectroscopy, includes two frequency combs with slightly detuned repetition rates [73]. Mixing the frequencies of those two combs can lead to the appearance of heterodyne beat notes in the radio frequency range. Amplitude and phase information from a sample, measured across the entire spectral range of the XUV comb is thus directly mapped into radio frequency signals. Applications for XUV frequency combs include spectroscopy of hydrogen and highly charged ions [74], fundamental tests of quantum electrodynamics [75], and the measurement of possible drifts in physical constants. Another promising application is the precise measurement of nuclear transitions for new optical clocks [76].

1.3 Limitations in Attosecond Science

Although temporal information is essential for understanding fundamental processes in matter, such as charge migration, chemical reactions, or just the process of ionization, time is not a quantum mechanical observable [77]. Instead, it can be addressed, for example, by using a pump–probe delay or by measuring phase shifts which can be related to time evolution. Not every phase shift, however, provides time information. Extracting time information can therefore be a rather complicated procedure and complex theoretical models are often needed [32].

When measuring ultrafast processes, another limitation comes into play: the Fourier limit defined in equation (1.1), which is closely related to the uncertainty principle of quantum mechanics and which sets a limit on the simultaneously achievable temporal and spectral resolution. In practice, if attosecond pulses are, for example, used to probe ultrafast processes, their large spectral bandwidth might address a large number of electronic transitions, thus limiting spectral precision. The relevant time scale of interest can thereby be defined by the spectral bandwidth of the process to be measured and vice versa.

A rather technological limitation in attosecond science arises from the fact that the average power of attosecond pulses is rather small. Although other approaches are in development [78, 79], the common mechanism employed for attosecond pulse generation is high-order harmonic generation which is, a very inefficient process. Therefore, a high photon flux in the XUV places strong requirements on the employed laser systems. Modern laser systems based on optical parametric amplification (OPA) allow a significant increase in the average power of femtosecond lasers. Nevertheless, it is the average power that restricts repetition rate and pulse energy. Interestingly, many attosecond experiments set requirements mainly for one of these two parameters.

High XUV pulse energies are, for example, required for experiments involving non-linear processes in the XUV since high intensities are needed in this case. Also in single-shot coherent imaging schemes [69], high XUV pulse energies are required for achieving a good signal-to-noise ratio. To day, high-order harmonic pulses containing several μJ could be generated [80], see also Paper VI. High repetition rates, on the other hand, are important for measurements where electrons or ions are detected. Such experiments typically require a rather low pulse energy in order to avoid space charge effects but high repetition rates are desirable in order to improve statistics.

Other examples where high repetition rates but low pulse energies are required are experiments involving coincidence detection and, unambiguous identification of particles originating from a single ionization event. Historically, high-order harmonics have mostly been generated using high-power, low-repetition rate (≤ 1 kHz) laser systems since such systems make it easier to reach the high intensities needed for HHG. Today, the repetition rate of HHG sources has been scaled up into the multi-MHz regime, both employing single pass generation schemes [81] as well as the generation inside enhancement cavities [82].

The limitations set by the low power of attosecond pulses can partly be avoided by other XUV or even X-ray sources such as synchrotrons or free electron lasers (FELs). While synchrotrons can easily generate short-wavelength light, the emitted radiation is normally not coherent, and the pulse duration is limited by the size of the electron bunches in the synchrotron ring. FELs instead can provide coherent and intense short-pulse XUV radiation, although their temporal and spatial beam quality cannot compete with tabletop HHG sources. Besides their limited pulse duration, which currently does not reach the attosecond regime, FELs and synchrotrons are large-scale facilities while XUV sources based on HHG can nowadays fit on a small optical table (see, for example, Paper IV).

1.4 Scope and Outline of this Thesis

A major part of the work resulting in this thesis was performed in Lund, Sweden in the group of Prof. Anne L'Hullier which has extensive experience in HHG and attosecond spectroscopy. This thesis also includes a project carried out in the surface science group of Prof. Ulrich Höfer in Marburg, Germany, which was focused on the development of a high-repetition rate attosecond source for photoemission spectroscopy studies on surfaces. The work at the two Universities was carried out aiming for a doctoral double degree. During the first three years of the PhD project, the author was supported by the Marie Curie Initial Training Network ATTOFEL.

Within this thesis, the scalability of attosecond XUV sources in two complementary directions has been investigated: towards higher repetition rates (Papers II, I, III and IV), and towards higher XUV pulse energies (Papers VI and VII). The focus thereby lies on the HHG process, and on the experimentally control parameters available for optimizing HHG in those directions. In particular, the scaling of macroscopic generation parameters is analyzed when the laser pulse energy used for HHG is scaled towards very low (a few μJ) or high (several 100 mJ) values. Dedicated XUV beam lines have been designed and built for both regimes. The intense harmonics beam line in Lund has been used for coherent diffraction imaging studies (Paper XI). Characteristic effects as well as novel characterization and control methods useful at high and/or low pulse energy generation schemes, are investigated. This includes identification and analysis of Maker fringes in the spectral domain (Paper I), sub-cycle control of the HHG process (Papers X and IX), as well as noncollinear generation geometries (Paper XII). Based on noncollinearly driven HHG, a new method for isolated attosecond pulse gating has been developed (Papers XIII and XIV), promising advances for the generation of IAPs in both scaling directions: intense IAPs at low repetition rates, and IAPs at high repetition rates and average power levels.

The thesis is organized as follows: chapter 2 introduces ultra-short laser pulses and

high-order harmonic generation, and discusses important microscopic and macroscopic effects arising during HHG in gases. Chapter 3 discusses macroscopic scaling as well as microscopic sub-cycle control of attosecond pulse generation, and introduces the harmonic and attosecond beam lines developed and built as part of this thesis work. The last chapter, chapter 4, discusses noncollinear HHG, focusing on macroscopic aspects of high-order noncollinear wave mixing processes, and introducing a new gating method for IAPs. It is followed by a summary and a brief outlook.

HIGH ORDER HARMONIC AND ATTOSECOND PULSE GENERATION

The XUV emission arising from HHG in gases typically contains a fingerprint of three different contributions: (i) the microscopic single atom response occurring periodically in several consecutive halfcycles of the driving laser field, but on a subcycle level; (ii), the femtosecond response, that is, variations of the subcycle response over the duration of the laser pulse and (iii), the macroscopic response: variations of the femtosecond response across the generation medium.

This chapter introduces the basic principles underlying HHG and attosecond pulse generation, and covers all three contributions. The first part of this chapter is a short introduction to the basic principles of electromagnetic waves and laser pulses. The second part introduces HHG, including both subcycle and multicycle aspects. In the third part, macroscopic effects are discussed and basic phase matching characteristics typical for HHG in gases are introduced. The last part of this chapter briefly introduces the model used for HHG simulations within the work of this thesis.

2.1 An Ultrashort Introduction to Electromagnetic Waves and Short Pulses

This section introduces the basic properties of ultrashort laser pulses¹, including linear and nonlinear propagation effects, assuming non-resonant conditions. A detailed overview of short laser pulse phenomena can be found for example in Ref. [83].

¹A laser pulse in this case denotes coherent electromagnetic radiation confined to a short time interval and explicitly includes pulses in spectral regions where laser-like processes are difficult to achieve, as for example in the XUV regime.

2.1.1 Linear Properties

Propagation in Vacuum

The propagation of electromagnetic fields is generally described by Maxwell's equations. For propagation in vacuum, Maxwell's equations lead to an homogeneous wave equation for the electrical field $E(\mathbf{r}, t)$ (for simplicity reasons, the magnetic field is not explicitly included here:

$$\nabla^2 E(\mathbf{r}, t) - \frac{1}{c^2} \frac{\partial^2 E(\mathbf{r}, t)}{\partial t^2} = 0, \quad (2.1)$$

Here and in what follows, a linear polarization is considered. Assuming that $E(\mathbf{r}, t)$ can be separated into a temporal and a spatial component, i.e. $E(\mathbf{r}, t) = E_s(\mathbf{r}) \cdot E_t(t)$, which is the case if the slowly varying envelope approximation (SVEA) can be applied [83] and in the absence of spatio-temporal couplings [84], equation (2.1) can be written as:

$$(\nabla^2 + k^2)E_s(\mathbf{r}) = 0, \quad (2.2)$$

$$\text{and} \quad \left(\frac{\partial^2}{\partial t^2} + \omega^2 \right) E_t(t) = 0, \quad (2.3)$$

where $k = |\mathbf{k}|$ is the absolute value of the wavevector, and $\omega = kc$ the angular frequency. Equation (2.2) is usually referred to as the Helmholtz equation.

For small angles between \mathbf{k} and $\hat{\mathbf{z}}$, the unit vector along the optical axis, the wave equation can be simplified to a paraxial form. Defining $\nabla_{\perp} = \partial/\partial x + \partial/\partial y$ as the transverse component of the Laplace operator, the paraxial form of the Helmholtz equation reads as²:

$$\left(\nabla_{\perp}^2 - i2k \frac{\partial}{\partial z} \right) E_r(\mathbf{r}) = 0. \quad (2.4)$$

Important solutions to this equation are Gaussian beams, with the lowest order solution, also known as fundamental mode:

$$E_r(\rho, z) = A_0 \frac{W_0}{W(z)} \exp \left[-\frac{\rho^2}{W(z)^2} \right] \exp \left[-ikz - ik \frac{\rho^2}{2R(z)} + i\zeta(z) \right], \quad (2.5)$$

where ρ denotes the radial coordinate and A_0 the amplitude. $W(z) = W_0 \sqrt{1 + (z/z_0)^2}$ ($\approx \Theta_0 z$ for $z \gg z_0$) is the $1/e^2$ -beam radius of the intensity profile at position z with Θ_0 defining the beam divergence angle. $2W_0 = 2W(0) = 4\lambda f_{\#}/\pi$ denotes the beam waist diameter, with $f_{\#} = f/(2W_f)$ defining the f-number of the focused beam with focal length f , wavelength λ and $1/e^2$ -beam radius before focusing $W_f = W(f)$. $R(z) = z[1 + (z_0/z)^2]$ denotes the wavefront radius of curvature and $\zeta = \tan^{-1}(z/z_0)$ the Gouy phase, with $z_0 = \pi W_0^2/\lambda$ being the Rayleigh length.

In the simplest case, the time dependent part of the wave equation yields a monochromatic wave which can be described in the time domain by: $E_t(t) = \mathcal{E}(t) \exp(i\omega t)$, where $\mathcal{E} = \sqrt{2I/\epsilon_0 c}$ is the real field envelope and I the intensity. ϵ_0

²The spatial component E_s is written as E_r in the paraxial equation.

denotes the vacuum permittivity. A laser pulse can be seen as a sum of monochromatic waves and thus, due to the superposition principle, it is likewise a solution to equation (2.3). The temporal representation of a laser pulse is:

$$E(t) = \mathcal{E}(t) \exp [i(\omega_0 t - \phi(t))] \quad (2.6)$$

where ω_0 denotes the carrier frequency and $\phi(t)$ is a time dependent phase. The real field envelope $\mathcal{E}(t)$ is often described by a Gaussian function and can be written as: $\mathcal{E}(t) = E_0 \exp(-2 \ln(2)(t - t_0)^2/\tau^2)$, where τ is the pulse duration (FWHM of the intensity profile) and t_0 defines the temporal pulse center. If the spectral bandwidth is small compared to ω_0 , the variation of $\mathcal{E}(t)$ and $\phi(t)$ within one optical cycle is also small, and the SVEA can be applied.

The frequency representation of a laser pulse is obtained via Fourier transformation:

$$\tilde{E}(\omega) = \mathcal{F}(E_t(t)) = \int dt E(t) \exp(-i\omega t) = \tilde{\mathcal{E}}(\omega) \exp[-i\Phi(\omega)]. \quad (2.7)$$

Here, $\tilde{\mathcal{E}}(\omega)$ is the spectral amplitude and $\Phi(\omega)$ the spectral phase.

Both temporal and spectral phase are often described by a Taylor expansion around the pulse center t_0 and the central frequency ω_0 , respectively. In both domains, the zero order phase denotes the carrier-envelope phase (CEP), while the first order describes a linear variation in time (frequency), corresponding to an offset in frequency (time). Any higher order phase term is most easily understood in the time domain, defining a variation of the instantaneous frequency $\omega_i = \omega_0 - \partial\phi/\partial t$ with time, called *chirp*³.

Propagation in a Dielectric Medium

The properties of laser pulses containing many optical cycles, and consequently a small spectral bandwidth [see equation (1.1)], do not change upon propagation⁴ as long as the wavevector does not depend on the frequency, as e.g. for propagation in vacuum. For propagation in a dielectric medium, the wavevector becomes a function of frequency, because the induced polarization, P , affects the propagation, a phenomenon called *dispersion*. In order to include this effect, equation (2.1) has to be modified, leading to the inhomogeneous wave equation:

$$\nabla^2 E(\mathbf{r}, t) - \frac{1}{c^2} \frac{\partial^2 E(\mathbf{r}, t)}{\partial t^2} = \frac{1}{\epsilon_0 c^2} \frac{\partial^2 P(\mathbf{r}, t)}{\partial t^2}. \quad (2.8)$$

In linear optics, P is given by $P = \epsilon_0 \chi E$, where χ is the electric susceptibility, which is related to the refractive index by $n^2 = 1 + \chi = \epsilon/\epsilon_0$, ϵ denoting the relative permittivity of the medium. Now, the wavevector k is a complex function of frequency:

$$k(\omega) = [n(\omega) + in'(\omega)] \frac{\omega}{c}. \quad (2.9)$$

³In the literature, different definitions for chirp exist. Here, a chirp denotes a linear or nonlinear frequency variation in time.

⁴Strictly speaking, this statement is valid only for monochromatic waves, but it can be seen as a good approximation for many-cycle pulses. Also, changes in the spatial distribution due to an angular spread do of course occur.

Here, the real part of the refractive index n describes dispersion, while the imaginary part, n' , describes amplification or absorption in the medium. Generally, the propagation of a laser pulse through a dielectric medium will change its phase as well as its amplitude. A pulse with an initial phase Φ_i and electrical field amplitude E_i can be described after propagating a distance z by:

$$E_f(\omega) = E_i(\omega) \exp[-\kappa(\omega)z] \cdot \exp[-i\Phi_i(\omega) + k(\omega)z], \quad (2.10)$$

where the absorption coefficient κ is related to the imaginary part of the refractive index⁵, defined in equation (2.9), by $\kappa = 2\pi n'/\lambda$. In order to describe timing effects arising from the change in phase upon propagation, $k(\omega)$ can be expanded around the central frequency:

$$k(\omega) = k_0 + k_1(\omega - \omega_0) + \frac{1}{2!}k_2(\omega - \omega_0)^2 + \dots, \quad (2.11)$$

where k_0 defines the phase velocity $v_\phi(\omega_0) = \omega_0/k_0 = c/n$, the speed at which the carrier wave of the pulse travels. The second term defines the group velocity $v_g = 1/k_1 = [(\partial k/\partial \omega)|_{\omega_0}]^{-1}$, i.e. the velocity of the pulse envelope. For $v_\phi \neq v_g$ the group velocity causes a *group delay* of the pulse envelope with respect to a pulse propagating in a non-dispersive⁶ medium. The third order component $k_2 = (\partial^2 k/\partial \omega^2)|_{\omega_0}$ defines the group velocity dispersion (GVD), describing a linear change of the group velocity with frequency, and corresponds to a linear chirp in the time domain, i.e. a linear frequency variation with time. Due to *normal dispersion* ($k_2 > 0$) most materials introduce a positive chirp (the frequency increases with time) in the visible and near infrared (NIR) spectral region.

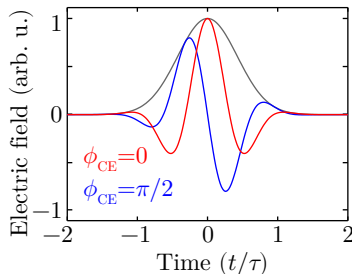


Figure 2.1: Electrical field of a few-cycle laser pulse, plotted for two different CEPs. The gray line indicates the field envelope, which is identical for both pulses.

In conditions where only the first term of equation (2.11) contributes, ultrashort laser pulses travel without changing their temporal and spectral properties. In a dispersive medium, i.e. if the first two terms in equation (2.11) have non-negligible contributions, the difference between the phase and group velocities leads to a variation of the CEP,

⁵The imaginary part of the refractive index is sometimes labeled κ in the literature. Also, the absorption coefficient, partly denoted α in the literature, differs by a factor of two from the κ used in this thesis, because it is defined by the decay of intensity and not field strength, as here.

⁶Non-dispersive in this case means that the refractive index is constant for frequencies $\omega \approx \omega_0$.

which can be expressed as a function of propagation distance z :

$$\phi_{\text{CE}}(z) = \phi_{\text{CE}}(0) + \left(\frac{z}{v_g} - \frac{z}{v_\phi} \right) = \phi_{\text{CE}}(0) + \left. \frac{\partial n}{\partial \omega} \right|_{\omega_0} \frac{\omega_0^2}{c} z. \quad (2.12)$$

The change of the CEP upon propagation was used in Paper [III](#) for CEP-dependent measurements of high harmonic spectra. Here, the CEP was controlled by moving a glass wedge in the beam path.

Higher order contributions in equation (2.11) redistribute the frequency content of the pulse in the time domain and lead to a temporal broadening of the pulse envelope.

2.1.2 Nonlinear Properties

At high intensities, when the electrical field is no longer negligible compared to the local fields inside the material, the wavevector depends on the intensity, and so the temporal, spectral, and spatial properties of the laser pulse can change upon propagation. In this case, the polarization becomes a nonlinear function of E :

$$P = \underbrace{\epsilon_0 \chi^{(1)} E}_{\text{linear}} + \underbrace{\epsilon_0 \chi^{(2)} E^2 + \epsilon_0 \chi^{(3)} E^3 + \dots}_{\text{nonlinear term}} \quad (2.13)$$

As $E(t)^m \propto [\exp(i\omega_0 t)]^m \propto \exp(im\omega_0 t)$, a nonlinear component of order m implies a polarization oscillating with frequency $m\omega_0$. This basic principle is the reason for the emission of harmonics of the fundamental frequency ω_0 . The amplitude of these so-called perturbative harmonics decreases rapidly with harmonic order, an effect which is in strong contrast to HHG, which will be introduced in section 2.2.

Besides the generation of harmonics, other nonlinear processes that influence the amplitude, phase, and frequency of the driving field can be observed. The first nonlinear term ($\chi^{(2)}$) leads to effects such as second harmonic generation or parametric amplification. In isotropic media, $\chi^{(2)} = 0$ and $\chi^{(3)}$ becomes the dominant nonlinear term, leading, for example, to an intensity-dependent refractive index $\tilde{n} = n + n_2(I)$. The third order component can cause intensity-dependent phase modulations (*self-phase modulation*), resulting in spectral broadening, as is used for pulse compression (see Paper [VIII](#)) and beam focusing (*Kerr-lensing* [[85](#)]), applied for mode-locking of fs-laser oscillators.

2.2 Introduction to High-Order Harmonic Generation

HHG and attosecond pulse generation, seen at the level of a single atom, include two main aspects: the generation of femtosecond XUV pulses, i.e. high-order harmonics of the driving field frequency, and the generation of attosecond pulses (pulse trains and isolated pulses). Both aspects are characteristics of the same process, seen from two different points of view. While high-order harmonics are typically described with a time-dependent amplitude and phase at a central frequency $q\omega_0$, evolving on a femtosecond time scale, attosecond pulses correspond to a spectrally broad XUV emission, which typically occurs every half cycle of the driving laser frequency, and is most easily represented in the spectral domain.

In this section, fundamental phenomena occurring on a subcycle level will be outlined, followed by a description of femtosecond aspects. Both quasi-classical and quantum mechanical models are introduced. Within this thesis, the quasi-classical model is mainly used. Quantum mechanical aspects are taken into account where the quasi-classical description is not sufficient.

2.2.1 The Three-Step Model

After the discovery of HHG in 1987 by two different research groups [8, 9], a three step model describing HHG quasi-classically, was introduced [86–88]. Despite the fact that HHG is a complex process, which demands a quantum mechanical treatment for a full description, the three step model provides a very intuitive description, and quite accurately describes basic characteristics of HHG such as the cut-off energy, the occurrence of different branches of electron trajectories, and the presence of the so-called *attochirp* (introduced in section 2.2.3).

In the three-step model, an electron leaves the atom via tunnel ionization (Step I). It then moves along a classical trajectory, being accelerated by the strong laser field (Step II), before finally recombining with the ion (Step III). The three steps are briefly described below.

The first step, tunnel-ionization, marks the border between the regime of extreme nonlinear optics where high-order harmonic generation occurs, and perturbative nonlinear optics. At field intensities around 10^{14} W/cm², large enough to subsequently accelerate the electrons, tunnel ionization⁷ is typically the dominant ionization process. The oscillating laser field periodically perturbs the ionization potential of the atom, allowing the electron to escape from the atomic potential twice per cycle.

The trajectory taken by the electron after it has left the atom is determined by the time of ionization t_i and the strength and frequency of the driving laser field. For a laser field $E(t) = E_0 \sin(\omega t)$, a simple classical derivation assuming that the electron leaves the atom at the origin with zero velocity [$x(t=0) = 0$ and $\dot{x}(t=0) = 0$], leads to:

$$x(t) = \frac{eE_0}{m\omega^2} [\sin(\omega t) - \sin(\omega t_i) - \omega(t - t_i) \cos(\omega t_i)]. \quad (2.14)$$

Here e and m are the electron charge and mass, respectively. During its excursion in the external laser field, the electron is accelerated to a maximum value of $8U_p$, where U_p denotes the *ponderomotive energy*, given by:

$$U_p = \frac{e^2 E_0^2}{4m\omega^2} = \frac{e^2 \lambda^2 I}{8\pi^2 m \epsilon_0 c^3}. \quad (2.15)$$

U_p is the average kinetic energy of an electron moving in a sinusoidal electric field. Here, λ denotes the laser wavelength and I the field intensity.

In the third step, the electron returns to the ion where it may recombine. In the classical picture, it is the return energy T_r with which the electron comes back to the ion that determines the photon energy emitted upon recombination. It is given by:

$$T_r = 2U_p [\cos(\omega t_r) - \cos(\omega t_i)]^2. \quad (2.16)$$

⁷Here, driving fields in the visible or near infrared (IR) spectral regions are considered. For even higher intensities, the electron can leave the atom above the suppressed Coulomb barrier. A detailed discussion of ionization processes in strong laser fields and their dependencies on wavelength and intensity can be found, for example, in Ref. [89].

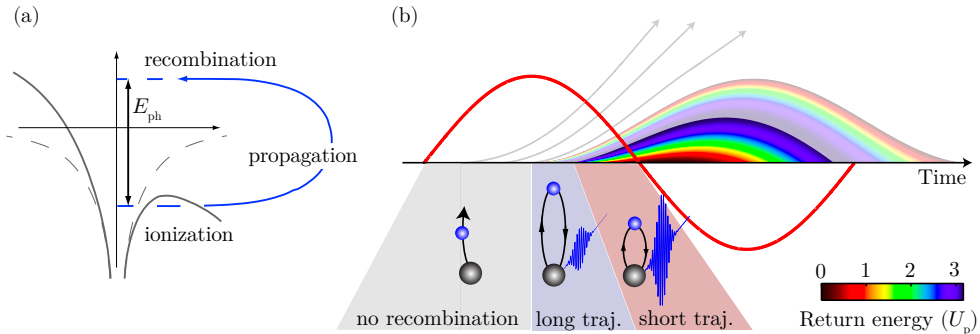


Figure 2.2: Illustration of the three-step process. (a) The distortion of the Coulomb potential leads to tunnel ionization, acceleration of the electron in the external laser field and possibly recombination. (b) Classical trajectories, which depend on the time of ionization. The red line indicates the sinusoidal laser field, gray and colored trajectories indicate non-returning and returning electrons, respectively. The color scale visualizes the return energy in units of U_p with saturated colors for short trajectories and transparent colors for long trajectories. Adapted from Paper IX.

T_r can reach values up to $3.17U_p$, thus determining the maximum photon energy for the HHG process, the so-called cut-off energy [90]:

$$E_{ph} \leq I_p + 3.17 U_p. \quad (2.17)$$

Because of its dependence on U_p , the harmonic cut-off energy increases linearly with intensity and quadratically with wavelength. Both parameters are therefore important if high photon energies are needed. At high intensities, saturation effects typically restrict the maximum photon energy to values below the cut-off energy defined in equation (2.17). Especially for long laser pulses, the medium can be fully ionized before the peak of the pulse. Ionization typically causes depletion of the generation medium, prevents phase-matched generation, and can defocus the driving laser beam.

The three-step model is illustrated in Figure 2.2. In (a), the distorted Coulomb potential is shown and the three steps of HHG are indicated. The trajectories that an electron can take in a sinusoidal laser field are displayed in (b), the colors indicating the return energy. Three different branches of electron trajectories can be identified, determined by the time the electron leaves the atom. For a sinusoidal laser field with field cycle period T , the trajectories can be classified as follows:

Trajectory	Tunneling time (T)	Recombination time (T)
Electrons that do not recombine	$0 < t_i < 1/4$	-
Long trajectory	$1/4 < t_i < 1/3$	$0.95 < t_r < 5/4$
Short trajectory	$1/3 < t_i < 1/2$	$1/2 < t_r < 0.95$

T_r increases with t_r for the short trajectories and decreases for the long trajectories. The maximum return energy can be expected where both trajectories merge, i.e. for $t_i \approx T/3$.

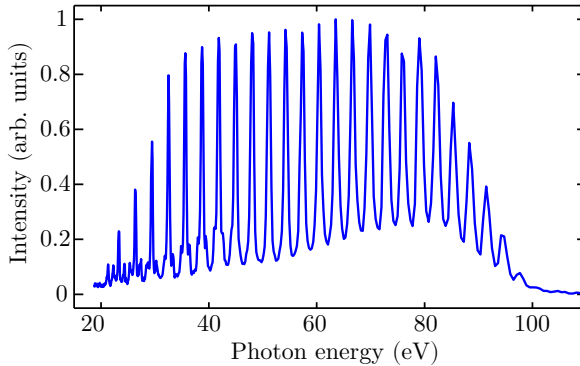


Figure 2.3: Single shot HHG spectrum generated in neon with a 40 fs fundamental pulse. The spectrum was measured at the intense harmonic beam line introduced in section 3.3.1 and presented in detail in Paper VI.

Both short and long electron trajectories can contribute to XUV emission. Even longer trajectories, occurring when the electron returns a second time after being scattered by the ion, may contribute. Quantum diffusion, however, leads to a very low recombination probability for such very long trajectories and thus the XUV emission resulting from rescattered electrons is typically very weak. XUV radiation arising from different electron trajectories can typically be distinguished using properties such as spectral and spatial characteristics, which depend on the so-called *dipole phase*, the phase accumulated by the electron while traversing its trajectory, defined in section 2.2.3.

For a sinusoidal laser field, the three-step process is repeated every half cycle of the fundamental field. The periodicity in time leads to a periodicity in frequency, and odd order harmonics of the laser field frequency are emitted. Figure 2.3 shows a typical harmonic spectrum generated in neon with many spectrally confined odd harmonic orders. The spectrum shows a characteristic plateau, which ends at the cut-off energy where the intensity drops. The decreasing intensity for low photon energies can be explained by a reduced detector efficiency for this spectral range.

Figure 2.3 shows another characteristic feature. The spectral width of the harmonic order increases with photon energy, an effect caused by two different mechanisms. One of these is the intensity dependence of the cut-off law, defined in equation (2.17). During the laser pulse, the intensity changes with time, and so does the harmonic cut-off. Since lower harmonic orders require lower intensities, they can be generated over a larger temporal window compared to the higher orders. A measured harmonic spectrum shows the time-integrated XUV emission, and temporal confinement (as is typical for higher harmonic orders, only generated close to the peak of the pulse) results in spectral broadening. This effect is used for the generation of isolated attosecond pulses, as is discussed in section 2.2.4. The other mechanism involves phase modulation effects arising due to the intensity dependence of the dipole phase, which is explained in more detail in section 2.2.3. With increasing harmonic order, the dipole phase changes more and more rapidly with intensity, and consequently with time, leading to an increased spectral width.

2.2.2 The Quantum Mechanical Model

A quantum mechanical model for HHG was derived shortly after the quasi-classical model was proposed [91, 92]. It is based on an approximate solution of the time-dependent Schrödinger equation (TDSE) and is referred to as the *Strong field approximation* (SFA) or *Lewenstein model*. The TDSE of an atom in a strong laser field can be written as:

$$[\hat{T} + \hat{V} + eyE(t)]|\psi(t)\rangle = i\hbar\frac{\partial}{\partial t}|\psi(t)\rangle, \quad (2.18)$$

where \hat{T} and \hat{V} denote the kinetic energy operator and the atomic potential, and the last term on the left side is the dipole operator for the specified laser field $E(t)$, polarized along y . In order to solve equation (2.18), a few approximations are made within the SFA formalism [93], described qualitatively below:

- i The electron is propagating freely in the continuum, and the continuum states are not influenced by \hat{V} . This approximation is valid if the laser field is strong compared to the atomic binding field, as expressed in the name *Strong field approximation*.
- ii The ground state is not depleted⁸. In practice, this implies that the intensity is not too high, especially for long driving laser pulses.
- iii Only one bound state, i.e. the ground state, is considered. This approximation is justified if no resonances perturb the process.

In contrast to perturbation theory, where a single basis set is typically used, together with a Hamiltonian describing the interaction, the SFA formalism uses two basis sets in order to define a time-dependent wave function $\psi(t)$. In agreement with approximation (i), $\psi(t)$ can be written as the sum of a bound and a continuum part [91]:

$$|\psi(t)\rangle = |\psi_B(t)\rangle + |\psi_C(t)\rangle = e^{i\frac{I_p t}{\hbar}} \left[|0\rangle + \int dk^3 c(t) |k\rangle \right]. \quad (2.19)$$

Here, the amplitude of the ground state $|0\rangle$ was set to one, in agreement with approximation (ii). The amplitude of the continuum state, $c(t)$ can be calculated by solving the TDSE, neglecting \hat{V} , i.e. using so-called Volkov states. In the quantum mechanical description, it is the nonlinear behavior of the time-dependent dipole moment $d(t)$ that causes the emission of high-order harmonics. $d(t)$ is proportional to the position expectation value of the electron and can thus be written as:

$$d(t) = \langle \psi(t) | ey | \psi(t) \rangle = \frac{e}{i\hbar} \int_{-\infty}^t dt' \int dk^3 d_k^*(t) \exp[-iS(k, t, t')/\hbar] d_k(t'), \quad (2.20)$$

where $d_k(t) = d_k(k + eA(t)/\hbar)$ is the transition matrix element, which depends on the vector potential of the electrical field, A . $S(k, t, t')$ is the action, which defines the phase the electron acquires during propagation in the continuum:

$$S(k, t, t') = \frac{\hbar^2}{2m} \int_{t'}^t dt'' \left\{ [k + eA(t'')/\hbar]^2 + I_p \right\}. \quad (2.21)$$

⁸This approximation was made in the initial SFA formalism. Depletion effects are typically taken into account in SFA calculations used today.

Equation (2.20) has a tidy physical interpretation, as it represents the quantum mechanical description of the three-step model. The electron tunnels into the continuum at time t' , acquires a phase upon propagation, and returns to the bound state, where it interferes with the bound state wave function, leading to emission of high-order harmonics. In contrast to the classical picture, the quantum mechanical electron can tunnel out at any time $t' < t$ and, may recombine with any momentum at a later time: i.e. all paths are possible and can, in principle, contribute to HHG. In the spirit of Feynman's path integral formalism [94], each path the electron takes can be associated with a quasi-classical action. The most likely paths are those which minimize the action, i.e. the classical ones. Equation (2.20) can be solved with the help of saddle-point approximations [91], yielding complex quantities for t_i and t_r . The imaginary part of $t_{i,r}$ can be seen as a trace of the tunneling process [95].

For HHG in gases, the polarization induced by the laser field is proportional to the single atom dipole moment defined through equation (2.20), multiplied by the medium's density. The polarization serves as an input to the inhomogeneous wave equation [equation (2.8)] describing propagation through the nonlinear medium. The high-order harmonic spectrum radiated from a single atom is given by the Fourier transform of the dipole expectation value (see. e.g. Ref. [96]). The spectral emission intensity thus reads as:

$$I(\omega) \propto \left| \omega^2 \int_{-\infty}^{\infty} dt d(t) \exp(-i\omega t) \right|^2. \quad (2.22)$$

Note that the ω^2 -term comes from classical electrodynamics, yielding a spectral intensity proportional to ω^2 multiplied by the square of the absolute value of the Fourier transform of the dipole.

A simulation code based on the SFA was used within the framework of this thesis in order to verify the experimental findings (Papers IX and XII) and the theoretical predictions (Paper XIII).

2.2.3 Dipole Amplitude and Phase

If we consider only the classical quantum paths, equation (2.20) can be rewritten as a sum over all contributing paths. The corresponding spectral amplitude for harmonic order q then reads as [95, 97]:

$$D_q = \sum_j A_j(q, I) \exp[i\Phi_j(q, I)], \quad (2.23)$$

where the sum over j denotes the sum over short and long electron trajectories. Within the high harmonic plateau, the dipole amplitude $A_j(q, I)$ is only weakly dependent on the harmonic order. However, the dipole phase $\Phi_j(q, I)$, changes significantly within the plateau. It also depends strongly on the trajectory considered, as well as on the driving field intensity. It therefore has a large impact on the spectral and spatial properties of the attosecond pulses, both on a subcycle level and over the duration of the driving laser pulse. $\Phi_j(q, I)$ can be written as:

$$\Phi_j(q, I) = q\omega_0 t_r - \frac{1}{\hbar} \int_{t_i}^{t_r} dt \left[\frac{p^2}{2m} + I_p \right], \quad (2.24)$$

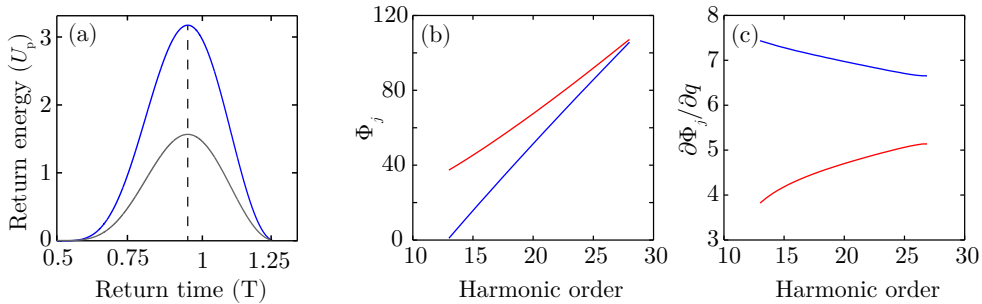


Figure 2.4: (a) Return energy as a function of return time for two different intensities $I_{1,2}$ with $I_1 = 2I_2$, displayed in units of $U_p(I_1)$. The plot shows two characteristic features. First, for a given harmonic order, the return time depends on the intensity. Second, the slope, which is related to the variation of the dipole phase with frequency, changes with I . The dashed vertical line indicates the position of the cutoff, separating short ($t_r < 0.95T$) and long ($t_r > 0.95T$) electron trajectories. (b,c) Φ_j and $\partial\Phi_j/\partial q$ in argon as a function of harmonic order, calculated for an intensity of $1.5 \cdot 10^{14}$ W/cm². Red: short, blue: long trajectory.

where $p = p(q, I)$ denotes the electron momentum. As in the three-step model, the classical ionization and recombination times ($t_{i,r}$) are considered here. Strictly speaking, using classical trajectory simulations to calculate $\Phi_j(q, I)$ is an approximation [95], but it can be useful to help with understanding the underlying physical processes as well as for minimizing computation time. The first term in equation (2.24) is a phase term, which depends on the intensity and the harmonic order and which arises from the timing of when the electron recombines. This term is present in the three-step model, as illustrated in Figure 2.4 (a). The second term describes the phase acquired by the electron upon propagation.

In what follows, the characteristic dependence of $\Phi_j(q, I)$ on intensity and frequency is illustrated, together with basic implications for the temporal and spectral characteristics of the emitted attosecond pulses, both on a subcycle level as well as over the duration of the laser pulse.

Subcycle Phase Modulations

For short and long trajectories, t_r clearly depends on energy, increasing (decreasing) with frequency for the short (long) trajectories. The corresponding variation of $\Phi_j(q, I)$ with ω over the spectral bandwidth under consideration, defines a delay in the time domain, a so-called *group delay*:

$$t_d = \frac{\partial\Phi_j(q, I)}{\partial\omega} \quad (2.25)$$

Both Φ_j and its first spectral derivative are displayed in Figure 2.4 (b,c), calculated using quasi-classical trajectory simulations. The group delay itself changes as a function of frequency, varying approximately linearly with ω . This has a significant impact on the temporal characteristics of the attosecond pulses, seen on a subcycle level. The

second order spectral phase defines a group delay dispersion, the so-called *attochirp*, which is positive for the short trajectory and negative for the long trajectory:

$$G_{\text{dd}}^j = \frac{\partial^2 \Phi_j(q, I)}{\partial^2 \omega} \quad (2.26)$$

Due to the attochirp, attosecond pulses are usually chirped, and complicated pulse structures can be expected if both short and long trajectories interfere. For the short trajectory, the attochirp can be compensated by a dispersive metallic filter [98] and nearly transform-limited attosecond pulses can be generated [99].

Multicycle Phase Modulations

For a given photon energy, and so a given return energy, $\Phi_j(q, I)$ changes slightly for the short trajectory, and significantly for the long trajectory, as the generation intensity is changed. For both trajectories, $\Phi_j(q, I)$ decreases approximately linearly with increasing intensity. The dipole phase can be approximated as:

$$\Phi_j(q, I) \approx \alpha_0 + \alpha I, \quad (2.27)$$

where both $\alpha_0 = \alpha_0^j(q)$ and $\alpha = \alpha^j(q)$ depend on the trajectory and harmonic order. α_0 is often neglected, but needs to be taken into account when the spectral dependence of $\Phi_j(q, I)$ is considered. In the notation used in equation (2.27), α is negative. As the intensity of a laser pulse used for HHG usually changes rapidly in time, the phase of the emitted XUV radiation is modulated on a femtosecond time scale. This phase modulation causes a variation of the instantaneous frequency and leads to spectral broadening of the emitted harmonics. For a Gaussian laser pulse, the instantaneous (central) frequency of harmonic order q can be written as:

$$\omega_q(t) = q\omega_0 + \frac{\partial \Phi_j}{\partial t} = q\omega_0 + \alpha(q) \frac{\partial I}{\partial t} \approx q\omega_0 - \alpha(q) \frac{8 \ln(2) I_0}{\tau^2} t, \quad (2.28)$$

where I_0 is the peak intensity and ω_0 denotes the carrier frequency of the driving laser field. The resulting chirp is negative, leading to a blue-shifted leading edge and a red-shifted trailing edge of the harmonic pulse, as illustrated in Figure 2.5 (b). While $|\alpha|$ and thus the harmonic chirp, is small for the short trajectory, a large frequency modulation can be expected for the long trajectory and for short laser pulses. This way, spectrally broad XUV radiation can be generated even with many-cycle laser pulses. Note that in this case, a broad spectral bandwidth does not imply a short attosecond pulse train.

The temporal variation of the instantaneous frequency is used in Paper I in order to map temporal amplitude modulations, caused by phase matching effects, into the spectral domain, as is discussed in more detail in section 2.4.1.

Another important phase modulation occurring on a multi-cycle level comes from the fact that the group delay defined in equation (2.25) depends on the laser field intensity [97], that is:

$$\frac{\partial t_{\text{d}}}{\partial I} = \frac{\partial^2 \Phi_j}{\partial \omega \partial I} \quad \begin{cases} < 0 & \text{for the short trajectory} \\ > 0 & \text{for the long trajectory} \end{cases}. \quad (2.29)$$

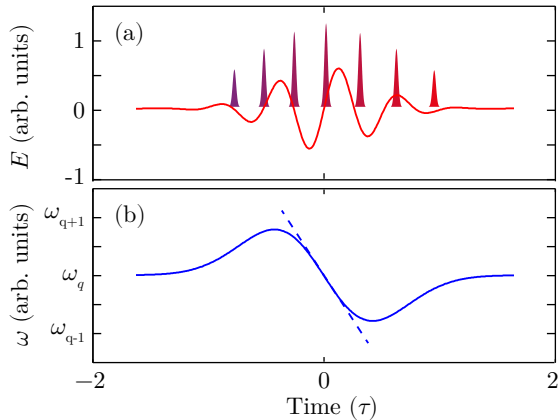


Figure 2.5: Multi-cycle phase modulation effects. (a) For the short trajectory, the spacing between consecutive attosecond pulses increases with time. The red line indicates the driving field. (b) Modulation of the instantaneous central frequency of individual harmonic orders (blue solid line) together with the linear approximation (blue dashed line) used in equation (2.28).

For a short laser pulse, the rapid intensity variation leads to a changing t_d with time. For short (long) trajectory harmonics t_d decreases (increases) at the leading edge of the laser pulse and increases (decreases) at the trailing edge. Due to the nonlinear variation of the intensity with time, also $\partial t_d / \partial t$ changes in time, leading to a variation of the temporal spacing between consecutive attosecond pulses in the pulse train. The spacing increases (decreases) for the short (long) trajectory emission throughout the pulse train, as depicted in Figure 2.5 (a).

The harmonic chirp can be compensated by a positive fundamental chirp, leading to asymmetric spectral broadening effects when the harmonic emission is measured as a function of the fundamental chirp [100]. This way, both dipole phase induced spectral broadening effects as well as the group delay variation through the attosecond pulse train can be compensated.

CEP-Dependent Dipole Phase Modulations

When the duration of a laser pulse reaches the few-cycle regime, the CEP becomes an important parameter, controlling the interaction of the pulse with the sample of interest on a sub-cycle level. Harmonic spectra generated with a few-cycle pulse typically show CEP dependencies such as spectral shifts or changes from continuous to modulated spectra. However, many-cycle pulses can also generate harmonic spectra with clear CEP-dependent features. If the spectral width of individual harmonics exceeds the separation between adjacent harmonics, CEP-dependent spectral interference fringes can be observed [101, 102]. This effect is well known and commonly used for CEP measurements, in this case employing so-called f - $2f$ -interferometry [103]. The interferences between adjacent harmonics accordingly define a higher order qf - $(q+2)f$ -interferometry scheme.

For few-cycle laser pulses, the phase modulation across the temporal pulse profile can reach values large enough to increase the phase shifts between consecutive half cycles by π and beyond. Approaching this regime, the exact location of the driving laser field with respect to the pulse envelope becomes a critical parameter, and significant effect on the harmonic spectrum can be observed when the CEP is changed [101, 102, 104–108]. For two consecutive attosecond pulses, generated at time t and $t + T/2$, the phase difference between the two pulses is a function of frequency, ω , and can be written as:

$$\Delta\Phi(\omega, t) = \pi + \frac{\omega\pi}{\omega_0} + \alpha(\omega) [I(t + T/2) - I(t)]. \quad (2.30)$$

The first two terms in this equation account for the emission symmetry and the temporal offset between consecutive half cycles, the third term describes the intensity-dependent dipole phase. Although, strictly speaking, this simple model is only correct for long driving pulses (α is usually derived for continuous driving fields), it can be used for a qualitative description of effects which arise when few-cycle pulses are used.

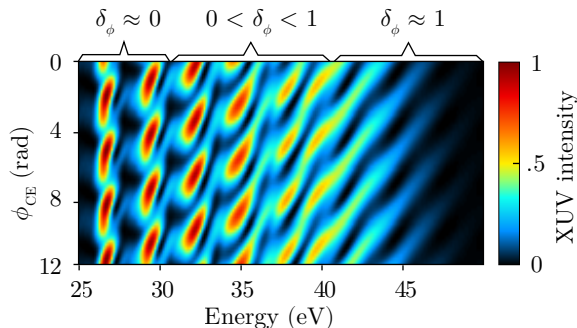


Figure 2.6: Simulated CEP-dependent harmonic spectra generated in argon. Three characteristic features can be observed: spectral fringes continuously shifting with CEP ($\delta_\phi \approx 1$), odd harmonic orders exhibiting intensity modulations ($\delta_\phi \approx 0$), and a transition region ($0 < \delta_\phi < 1$). The spectra were calculated using SFA simulations for a pulse length of 5 fs.

Figure 2.6 displays simulated HHG spectra in argon which mimic the experimental observations presented in Paper III. The simulation considers the single atom response, calculated using the SFA formalism. In the cut-off region, the harmonic orders shift continuously in the spectral domain as the CEP is changed. Towards lower photon energies, CEP-dependent, non-continuous spectral shifts can be observed, while modulated odd harmonic orders appear around 25–30 eV. Most of the observed effects can be explained by dipole phase induced phase modulations, and are more prominent at higher photon energies where α reaches larger values.

For small α -values⁹, and considering frequencies corresponding to an odd harmonic orders, $I(t + T/2) \approx I(t)$ and thus $\Delta\Phi(\omega, t) \approx 0$ (modulo 2π). In this case, the XUV emission from consecutive half cycles adds constructively for odd harmonic orders, q with $\omega = q\omega_0$. For large α -values, $\Delta\Phi(\omega, t)$ can reach values of π (and beyond),

⁹The absolute value of α is considered here. For the dipole phase approximation used within this thesis, α is negative for most harmonic orders.

leading to the emission of even harmonic orders. As $I(t)$ is strongly time, and thus CEP, dependent, $\Delta\Phi(\omega, t)$ changes with CEP. This variation can be written as: $\delta_\phi = \partial\Delta\Phi/\partial\phi_{\text{CE}}$, where ϕ_{CE} denotes the CEP. For a Gaussian laser pulse and following equation (2.30), δ_ϕ can be approximated as:

$$\delta_\phi \approx \frac{2 \ln 2}{\pi} \frac{T^2}{\tau^2} I_0 \alpha \propto \frac{T^2}{\tau^2} I_0 \alpha. \quad (2.31)$$

While $\Delta\Phi$ determines the appearance of even or odd harmonic orders, the spectral shift of individual harmonic lines, i.e. the transition from even to odd orders, can simply be seen as an intensity- and thus CEP-dependent variation of the central harmonic frequency, defined in equation (2.28). For $\delta_\phi = n_\phi$, where n_ϕ is an integer, the slope of the spectral shift of individual harmonic orders matches the π -periodicity imposed by the CEP and a continuous spectral shift can be observed (as is visible for $\delta_\phi \approx 1$ in Figure 2.6). In contrast, for $\delta_\phi \neq n_\phi$, e.g. for $0 < \delta_\phi < 1$, non-continuous spectral shifts appear. For $\delta_\phi \approx 0$, the harmonic lines do not shift anymore but are still affected by small phase changes.

The phase changes discussed here are immediately connected to changes in the timing between consecutive attosecond pulses, as $\Delta\Phi$ is not only a function of the CEP but also changes with frequency, see, for example, Ref. [107]. The spectral phase shifts discussed above are directly connected to changes of the CEP of the generated attosecond pulses, most easily represented in the time domain and discussed in section 3.4.1, using the example of subcycle phase control with multi-color driving fields. Experimental results showing the characteristic spectral features discussed above, measured at the high-repetition rate beam line in Lund, can be found in Paper III. A related phenomenon, namely spatial phase effects arising in noncollinear HHG is discussed in section 4.2.1, as well as in Paper XII, and the analogy to the CEP-effects discussed here is outlined.

2.2.4 Isolated Attosecond Pulses

The temporal representation of a high-order harmonic spectrum is an attosecond pulse train (APT), but a broad XUV spectrum can support isolated attosecond pulses (IAPs) with durations around 100 as [109]. In order to generate an isolated attosecond pulse or alternatively, to isolate a single pulse from the pulse train, different methods can be applied, based on manipulating the generation process via temporal shaping of the driving field [79, 110–112], via spectral selection [113–115], or via spatial-temporal couplings used for angular streaking of the attosecond pulse emission [116]. The different methods can be classified into three gating schemes, as illustrated in Figure 2.7, and briefly outlined below. A more detailed review of the available techniques can be found in Ref. [117].

Temporal Gating: In all temporal gating schemes, such as polarization [110, 111] or ionization [112] gating, the HHG process is modified temporally, such that the generation of all pulses but one is suppressed. This can be done by driving HHG with an electrical field with temporally varying ellipticity, such that XUV emission is only efficient at the pulse center where the field is linearly polarized. In the ionization gating scheme, laser field intensities exceeding the saturation level for ionization are used, leading to generation of an attosecond pulse at

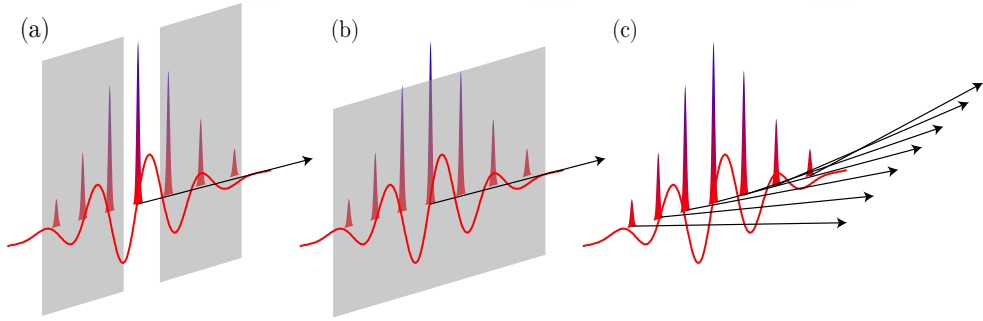


Figure 2.7: Gating schemes for IAP generation: (a), temporal gating, (b) spectral gating, and (c), angular streaking.

the leading edge of the pulse, while all subsequent pulses are suppressed as the medium is ionized directly at the beginning.

Spectral gating: For spectral gating, also known as amplitude gating [113, 114], the temporal gate is defined in the Fourier domain by a simple spectral amplitude selection. For few-cycle laser pulses, the spectral composition of consecutive attosecond pulses changes dramatically, an effect simply determined by the cut-off law. Selecting the cut-off region spectrally can therefore allow the selection of the IAP generated at the peak of the laser pulse.

Angular streaking: With the help of spatio-temporal couplings [116], the emission direction of all the attosecond pulses in the train can be changed over time, leading to direct spatial separation of the individual IAPs in the far-field. This method is discussed in more detail in section 4.3 as well as in Paper XIII.

All of the above techniques require few-cycle laser pulses in order to allow a sufficiently short gate. The pulse duration requirement can be relaxed significantly when different gating techniques are combined. A typical example is the combination of polarization gating and multi-color field synthesis, which allows the generation of only one pulse per cycle [118], usually referred to as *double optical gating* (DOG) [119, 120].

2.2.5 Temporal Characterization of Attosecond Pulses

Standard diagnostic tools such as autocorrelation methods cannot easily be applied to the temporal characterization of attosecond pulses. The reason is the lack of accessible nonlinear frequency conversion processes in the XUV, as well as the high intensity required to drive such processes. Instead, cross-correlation techniques are typically employed. The standard technique for the temporal characterization of attosecond pulse trains is the so-called *reconstruction of attosecond beating by interfering two-photon transitions* (RABBITT) [121]. For isolated attosecond pulses, streaking methods can be applied, forming the basis of frequency resolved optical gating for complete reconstruction of attosecond bursts (FROG-CRAB) [122].

Both methods, RABITT and FROG-CRAB are based on ionizing atoms in the presence of the XUV field superimposed with the generating laser field, as is illustrated

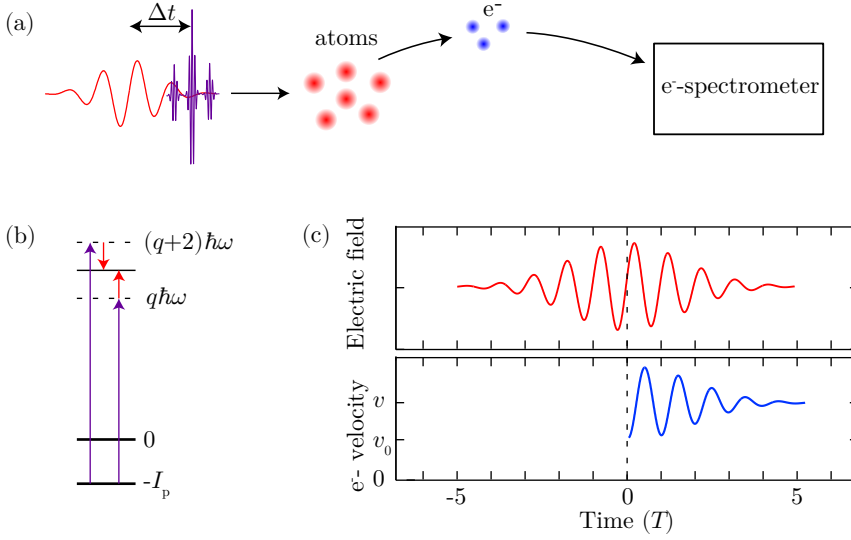


Figure 2.8: (a) Illustration of the experimental schemes used for attosecond pulse characterization: RABITT and streaking. (b) Two-photon processes involved in RABITT measurements, in which two pathways can lead to the same final electron energy. (c) Attosecond streaking: temporal evolution of the electron momentum of an electron released into the continuum with an initial velocity v_0 via single photon ionization by an IAP when a laser field is present.

in Figure 2.8(a). The kinetic energy distribution of the emitted photoelectrons is detected as a function of the delay Δt between the XUV and laser pulses. While the RABITT method employs two-photon processes and a weak probing laser field, FROG-CRAB is based on single photon ionization by the XUV pulse while a strong dressing laser field is used as an ultrafast phase modulator, streaking the electron wave packet.

The RABITT method is based on a measurement of the phase difference between consecutive harmonics which can be written as a group delay (see equation (2.25)):

$$t_d = \frac{\partial \Phi_j(q, I)}{\partial \omega} \approx \frac{\Phi_j(q+2, I) - \Phi_j(q, I)}{2\omega} \quad (2.32)$$

As illustrated in Figure 2.8(b), when ionizing atoms with an XUV pulse train, the presence of a weak fundamental laser field leads to the appearance of sidebands in the photoelectron spectrum. These sidebands are located between the electron energies corresponding to adjacent harmonic orders, i.e. at the energies of even harmonics. Each sideband energy can be produced by two pathways, involving the absorption or emission of one laser photon. Due to interferences between the two pathways, the sideband photoelectron signal oscillates as a function of the delay Δt . The modulation signal at energy $\hbar(q+1)\omega$ can be written as:

$$S_{q+1} \propto \cos[2\omega_0 \Delta t - \Delta \Phi(q+2, q) - \Delta \phi_{\text{at}}]. \quad (2.33)$$

Here, $\Delta\Phi(q+2, q)$ denotes the phase difference between harmonic order $q+2$ and q , $\Delta\phi_{\text{at}}$ is a small intrinsic phase difference arising due to the ionization process itself, which is often neglected. The sideband modulations can directly be used to extract phase differences between adjacent harmonics and therefore the phase across the entire spectrum. In combination with a measurement of the spectrum, this allows for reconstruction of the APT.

The RABITT technique allows only temporally averaged and relative phase measurements. Therefore, pulse to pulse variation and the absolute phase with respect to the driving laser field are not detectable. Further higher order processes can perturb the two-photon interference signal. A low laser intensity may be used to minimize these perturbations.

The RABITT scheme cannot only be used for pulse characterization, but gives access to $\Delta\phi_{\text{at}}$, a phase term, which can be related to ionization time delays [29, 30]. Within the framework of this thesis, the RABITT scheme was used to measure the influence of changes in the macroscopic generation conditions on the group delay of the generated attosecond pulses, see Paper V.

The streaking scheme is illustrated in Figure 2.8 (b), where the temporal evolution of the electron momentum is shown, together with the streaking laser field. Via single photon ionization by the XUV pulse, an attosecond electron wave packet is generated in the continuum. The present laser field modifies, i.e. streaks this wave packet [123], acting as a phase gate for a frequency-resolved-optical-gate-like measurement [122]. Phase and amplitude information from the XUV field are transferred to this wave packet and the temporal structure of the XUV pulse can be reconstructed from a characterization of the wave packet as a function of the delay between XUV and laser field. A detailed description of the FROG-CRAB technique can be found for example in Ref. [124].

Another limitation, present in both measurement schemes, results from spatial averaging effects. Very recently developed methods approach this problem by employing a noncollinear geometry for in situ characterization of the generated XUV pulse [125].

2.3 Macroscopic Effects in High-Harmonic Generation

The spatio-temporal characteristics of XUV pulses produced via HHG, depend not only on the single atom response, but are affected by amplitude and phase variations across the three dimensional nonlinear medium, as discussed in a number of articles, for example, in Refs. [126–131]. Macroscopic aspects of HHG, often referred to as phase matching effects, commonly denote effects arising from the propagation of the XUV field and the generating laser field along the optical axis \hat{z} through the nonlinear medium. More generally, one can define two different types of macroscopic effect: (i) effects that arise in a nonlinear medium with nonzero transverse dimension, i.e. those due to amplitude and phase variations along the radial coordinate¹⁰, x , and which can be described using a medium of zero length in the propagation direction¹¹, and (ii), effects that are caused by propagation, i.e. phase matching effects.

¹⁰We assume rotational symmetry about \hat{z} in the following.

¹¹A *zero length medium* denotes a medium of infinitesimal length δz , for example, a medium consisting of a single layer of atoms.

Transverse macroscopic effects are essential for the directional emission of coherent radiation and need to be considered when strong phase or amplitude modulations are introduced along x , as, for example, in the case of spatio-temporal couplings [84], strong radial dipole phase gradients [126] or noncollinear generation geometries. Transverse macroscopic effects will be discussed in more detail for the special case of noncollinear HHG in section 4.2.1. Phase matching effects are sometimes seen as a necessary evil which needs to be incorporated for a complete description of HHG and attosecond pulse generation. Their understanding and optimization is especially important for efficient frequency conversion. In what follows, the fundamentals of phase matching in HHG will be introduced.

2.3.1 Basic Principles of Phase Matching

General Introduction

Propagation effects in HHG can most easily be illustrated using a k-vector model. In order to ensure phase-matched generation, the wavevector of the generated field has to match the sum of the generating field vectors. The following discussion considers the wavevectors defined by the carrier wave of the fundamental field and the discrete harmonic orders, i.e. a phase velocity mismatch $\Delta\mathbf{k}(q)$. The model can, however, be generalized for continuous XUV emission, as in isolated attosecond pulse generation, by using a continuous representation of $\Delta\mathbf{k}(\omega)$. In conditions where the wavevector of the fundamental or the harmonic frequencies varies significantly with frequency, as is typically the case for HHG driven by fundamental fields with wavelengths much shorter than 800 nm as well as for many low-order frequency mixing processes, group velocity mismatches, which are neglected here, have to be taken into account as well.

The wavevector mismatch between the generated harmonic field and the induced polarization at frequency $q\omega_0$ can be written as¹²:

$$\Delta\mathbf{k}(q) = q\mathbf{k} - \mathbf{k}_q. \quad (2.34)$$

The influence of a phase mismatch present in harmonic generation can most easily be illustrated using a one dimensional model. The generated signal is the coherent sum over all single atom emitters in the nonlinear medium of length L and can be written as:

$$S_q \propto \left| \int_0^L dz d_q \exp[i(\Delta k + i\kappa_q)(L - z)] \right|^2, \quad (2.35)$$

where d_q denotes the dipole amplitude for harmonic order q and κ_q is the absorption coefficient, denoted as κ in equation (2.10). If d_q and κ_q are constant across the nonlinear medium, equation (2.35) simplifies to:

$$S_q \propto |d_q|^2 e^{-\kappa_q L} \cdot \frac{\cosh(\kappa_q L) - \cos(\Delta k L)}{\Delta k^2 + \kappa_q^2} \quad (2.36)$$

$$\xrightarrow{\kappa_q \rightarrow 0} |d_q|^2 L^2 \text{sinc}^2\left(\frac{\Delta k L}{2\pi}\right), \quad (2.37)$$

¹²The wavevector mismatch is sometimes defined with opposite sign in the literature.

with $\text{sinc}(x) = \sin(\pi x)/(\pi x)$. Equation (2.36) is formally identical to equation (1) in Ref. [127] where Δk and κ_q are replaced by the coherence and the absorption lengths. For $\kappa_q = 0$, the well known sinc function describing phase matching in the absence of reabsorption effects is obtained. Figure 2.9 illustrates phase-matched and

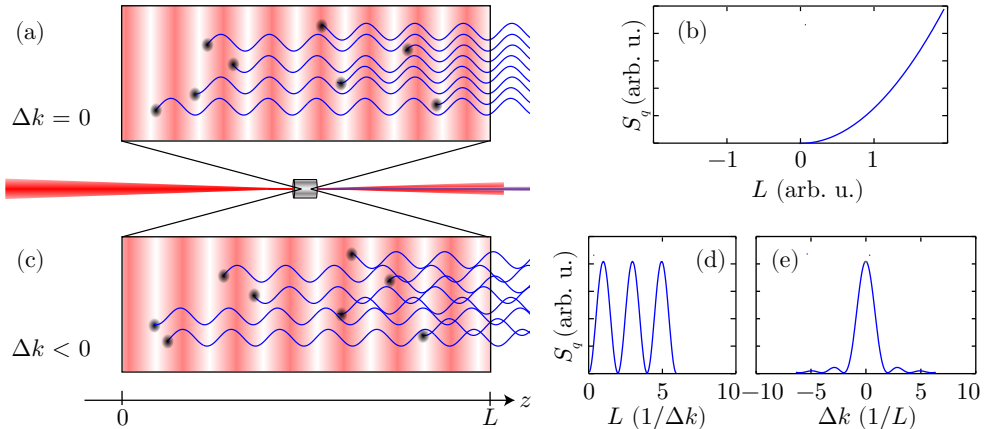


Figure 2.9: Phase-matched (first row) and non phase-matched (second row) harmonic generation, illustrated using the example of second harmonic generation. The red shading indicates the fundamental field $[\Re(E)^2]$. In (b) and (d), the corresponding harmonic signal in the absence of reabsorption is plotted as a function of the medium length. (e) shows the harmonic signal as a function of Δk for a constant medium length.

non phase-matched harmonic generation. If $\Delta k = 0$, all atoms within the generation medium emit the generated harmonics in phase, and the overall signal (the generated harmonic power) grows quadratically with medium length, L . For non phase-matched generation, the signal grows almost quadratically for small L , but starts to oscillates for larger L . For a constant medium length, the signal decreases with increasing Δk with the typical sinc function-like behavior.

The wavevector mismatch Δk can also be expressed as a phase mismatch $\Delta\phi_z$ if a particular propagation direction, e.g. the optical axis, is considered. With $\Delta k_z = \partial\Delta\phi_z/\partial z$, we can define an effective phase mismatch due to dispersion by integrating Δk along the propagation path through the nonlinear medium of length L :

$$\Delta\phi_z(q) = \int_z^L dz' \Delta k_z(q), \quad (2.38)$$

where Δk_z denotes the component of $\Delta \mathbf{k}$ along the optical axis. Similarly, reabsorption of the generated XUV radiation can be taken into account by integrating $e^{-\kappa_q z}$ along the propagation path. Displaying $\Delta\phi_z$ modulo 2π in the generation volume as a function of z and x (in the case of rotational symmetry) allows an intuitive visualization of phase matching effects (see Figure 2.10). This method is applied in this thesis as well as in Paper II, while in earlier work, the coherence length $L_{\text{coh}} = \pi/\Delta k_z$ is often used [126, 130] to illustrate phase matching graphically.

Phase Mismatch Components in HHG

For HHG in gases, $\Delta\mathbf{k}$ can be written as a sum over four components:

$$\Delta\mathbf{k} = \Delta\mathbf{k}_g + \Delta\mathbf{k}_d + \Delta\mathbf{k}_n + \Delta\mathbf{k}_p, \quad (2.39)$$

where $\Delta\mathbf{k}_g$ denotes the wavevector mismatch due to the Gouy phase, $\Delta\mathbf{k}_d$ is the wavevector mismatch induced by the dipole phase, and $\Delta\mathbf{k}_n$ and $\Delta\mathbf{k}_p$ are caused by dispersion in the partially ionized medium. All four components are described below. For the sake of convenience, only propagation along the optical axis is considered, and the index z is omitted.

Δk_g For HHG in a free focus geometry, as used within this thesis work, the focusing process itself leads to a geometrical phase offset between the phase fronts of the focused beam and a plane wave. This is due to an advanced propagation of the wavefronts across the focus, which increases linearly with wavelength. Neglecting the small Gouy phase of the harmonic beam, the total Gouy phase mismatch between the fundamental and the generated harmonic beam can be expressed as:

$$\Delta k_g(x, z) = -q \frac{\partial}{\partial z} \left[\zeta(z) - \frac{kx^2}{2R(z)} \right] \xrightarrow{x, z \rightarrow 0} -\frac{q}{z_0} \quad (2.40)$$

Where $\zeta(z)$ denotes the phase offset along the optical axis, while the second term in the center bracket accounts for the off-axis components of the Gouy phase shift. At the focus, Δk_g has a maximum, being approximately constant for small z .

For HHG in a guided geometry, Δk_g has to be replaced by a wavevector mismatch arising from propagation in the wave guide [129, 132]. This has the same sign as Δk_g but in contrast to the wavevector mismatch introduced by the Gouy phase, it is constant over the generation medium.

Δk_d The dipole phase defined by equation (2.24) leads to another phase mismatch component, as the phase depends on the intensity within the medium, and so varies with spatial position. Using the approximation defined in equation 2.27, the wavevector mismatch introduced by the dipole phase can be written as [133]:

$$\Delta k_d(x, z) = \alpha \frac{\partial I(x, z)}{\partial z} \quad (2.41)$$

In a free focus geometry, the intensity varies with x and z , leading to dramatic variations of $\Delta\phi_d = \alpha I$ within the nonlinear medium, especially for the long trajectory contribution.

Δk_n The wavevector mismatch due to dispersion in the neutral gas can be written as:

$$\Delta k_n = q \frac{\omega}{c} (n_1 - n_q). \quad (2.42)$$

The refractive index for the fundamental laser beam n_1 can be estimated via the static polarizability α_{dip} of the interaction gas (tabulated, for example, in Ref. [134]):

$$n_1 = 1 + N_0 \frac{\alpha_{\text{dip}}}{2\epsilon_0}, \quad (2.43)$$

where N_0 is the gas density¹³. The above expression follows from a Taylor expansion of the refractive index $n_0 = \sqrt{1 + \chi}$ with $\chi = N_0 \alpha_{\text{dip}} / \epsilon_0$. Note that n_0 denotes the usual refractive index, the intensity dependent part n_2 can often be neglected for HHG in gases, as its contribution is small compared to the other four mismatch components. Values for n_q can be found for example in Refs. [135, 136].

Δk_p The wave vector mismatch due to dispersion in the plasma can be calculated similarly as Δk_d , when n_1, n_q are replaced by the plasma refractive index values n_1^e, n_q^e :

$$\Delta k_p = q \frac{\omega}{c} (n_1^e - n_q^e), \quad (2.44)$$

with

$$n_q^e = \sqrt{1 - \frac{N_e}{N_c}}, \quad (2.45)$$

where N_e denotes the free electron density and $N_c = \epsilon_0 m \omega^2 / e^2$ is the so-called *critical density* at which the plasma frequency $\omega_p = \sqrt{N_e e^2 / m \epsilon_0}$ equals the laser frequency. N_e can be calculated with the ADK model [137]. During the ionization process, the refractive index drops from unity (no plasma) to zero as N_e reaches N_c [138]. As N_c scales quadratically with frequency, the plasma mostly affects the propagation of the fundamental field, leading to a phase velocity above the vacuum speed of light.

The signs of the different wavevector components introduced above are listed below, together with a comparison of the resulting phase velocities of the fundamental (c_1) and harmonic (c_q) waves:

	Sign	Refractive indices	Phase velocities
Δk_g , Focusing	negative		$c_1 > c_q > c$
Δk_d , Dipole	$\left\{ \begin{array}{l} \text{negative, for } z < 0 \\ \text{positive, for } z > 0 \end{array} \right.$		
Δk_n , Neutral		positive	$n_1 > 1 > n_q$
Δk_p , Plasma	negative	$n_1^e < n_q^e < 1$	$c_1 > c_q > c$

2.3.2 Phase Matching Characteristics in HHG

Generating high-order harmonics fully phase-matched implies that $\Delta \mathbf{k} = 0$ for all x, z and t , a condition which is strictly speaking not possible to achieve. While Δk_n can be approximated as spatially and temporally constant, all other components vary spatially and temporally, thus making phase matching a spatially localized transient process which depends on a number of parameters, in particular on the gas pressure, the intensity, the nonlinear medium, and the focusing condition. *Phase-matched*

¹³As N_0 denotes the gas density, n_1 can be seen as an approximate refractive index for the neutral gas, valid for a low degree of ionization, or when approximating the refractive index of the ions as n_1 .

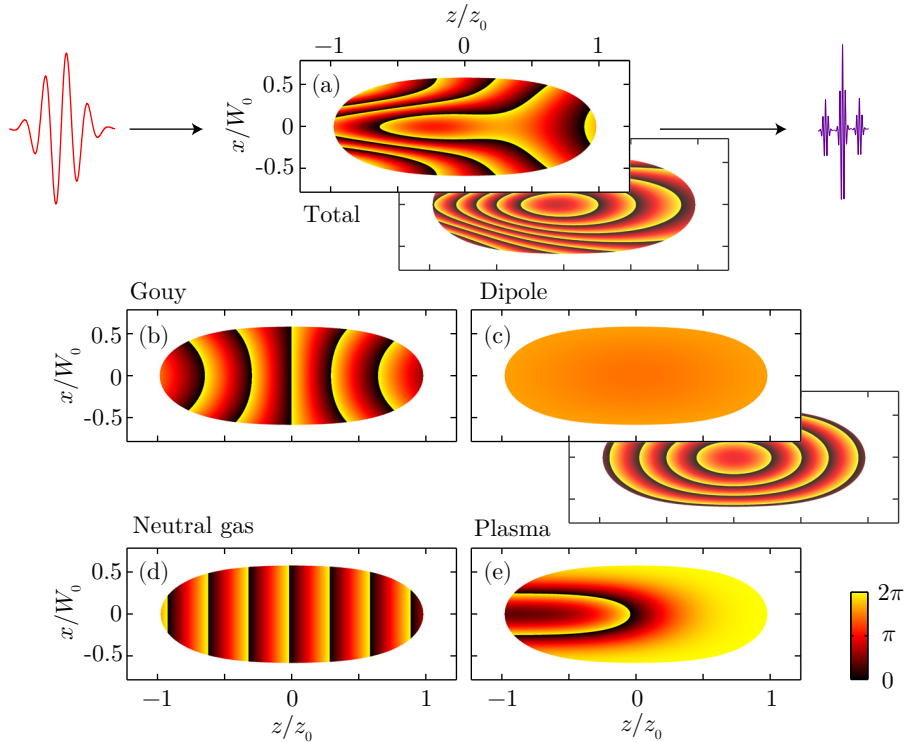


Figure 2.10: Phase matching maps for the short (a)–(e) and long [recessed figure panels (a) and (c)] trajectories. The total phase mismatch $\Delta\phi_z$ is shown in (a). (b)–(e) display phase matching maps for the separate contributions: Gouy phase (b), dipole phase (c), neutral gas (d) and plasma (e) dispersion. The white area indicates the positions within the focal volume for which the intensity drops below the threshold intensity defined by the three step model, which is needed to generate the harmonic order under consideration, here $q = 23$.

generation therefore denotes the case when high-order harmonics are generated phase-matched within a significant volume of the nonlinear medium, and during a time interval which is possibly much shorter than the duration of the laser pulse. Using this definition, it follows that phase-matched generation does not necessarily correspond to a globally maximized photon flux, and can be achieved for a rather large range of generation parameters. This is different to what is known from low-order frequency conversion processes in crystals, where temporal and spatial variations of the phase matching conditions can typically be neglected, leading to a narrow parameter range for which phase matching can be achieved. In what follows, the characteristic features of the different phase mismatch components present for HHG in gases are outlined, followed by a discussion of dynamical phase matching effects.

Figure 2.10 displays typical phase matching maps for HHG in argon, considering a peak intensity of $2 \cdot 10^{14} \text{ W/cm}^2$. The phase mismatch $\Delta\phi_z$ modulo 2π , is plotted as a function of the longitudinal and radial coordinates, centered at the focus of the driving laser beam. Phase-matched XUV emission in the forward ($+z$) direction requires a constant value for $\Delta\phi_z$, i.e. $\Delta k_z = 0$. The phase matching maps are calculated for the

23rd harmonic of a 800 nm driving laser pulse, and for a pulse duration of $\tau = 45$ fs. The displayed maps visualize phase matching at the temporal peak ($t = 0$) of the pulse.

In (a), the total phase mismatch is displayed for the short trajectory contribution, where phase-matched generation is possible within a significant part of the generation volume around $z = \pm z_0/2$. The corresponding phase matching maps displaying all the individual components described above are shown in (b)–(e). In (a) and (c), a second, recessed, map displays the corresponding phase mismatches for the long trajectory contribution. Short and long trajectory only differ by a different dipole phase, all other components are identical for both trajectories. While the dipole phase, displayed in (c), changes weakly with intensity and thus with x and z for the short trajectory, strong variations are typical for the long trajectory, leading to a rapid variation of $\Delta\phi_z$ with x and z . At low ionization levels (the displayed maps correspond to 3.8% ionization at the focus and at the peak of the pulse), the dipole phase causes a dominant contribution to the total phase mismatch for the long trajectory. Phase-matched generation is therefore only possible in a small volume around the focus and at off-axis positions. The phase mismatch due to the dipole phase is the only contribution with different signs in front of and behind the focus, caused by the increasing or decreasing laser field intensity along the optical axis. Although weak, this behavior typically leads to phase matching conditions for the short trajectory that are slightly better behind the focus than in front of it.

Both phase mismatches induced by the dipole phase and by plasma dispersion (e) contribute to a significant variation of $\Delta\phi_z$ along x , leading to an increased divergence of the emitted XUV radiation. In contrast, Gouy phase (b) and neutral gas dispersion (d) contribute terms with only weak or negligible radial variation.

Strategies allowing the optimization of the macroscopic generation conditions are discussed below. The discussion includes phase matching and reabsorption effects. Major reshaping effects of the fundamental pulse, for example, due to plasma defocusing [139], which typically occurs at very high intensities and gas pressures, are mentioned when relevant but are not discussed in detail. Some of the principles introduced below are also discussed in the literature, see, for example, Ref. [131].

Pressure Induced Phase Matching

In order to optimize phase matching, the gas pressure p is a very important tuning parameter [127, 131]. The gas pressure determines the magnitude of $\Delta k_{n,p}$, which are proportional to p . The gas pressure can thus be used to adjust those components so as to compensate the wavevector mismatch due to the Gouy phase and the dipole phase.

If one of the two pressure independent components $\Delta k_g \neq 0$ or $\Delta k_d \neq 0$, phase matching is obtained at a particular pressure, denoted as the *phase matching pressure*, or p_{match} below. For reasons of simplicity, taking $\Delta k_g \neq 0$ but $\Delta k_d = 0$, as the case for generation at the focus point, we obtain:

$$p_{\text{match}} \left[\frac{\partial \Delta k_n}{\partial p} + \frac{\partial \Delta k_p}{\partial p} \right] + \Delta k_g = 0 \quad (2.46)$$

Here, the wave vector mismatch due to dispersion is rewritten as $\Delta k_{n,p} = p \cdot \partial \Delta k_{n,p} / \partial p$, the partial derivatives being independent of pressure.

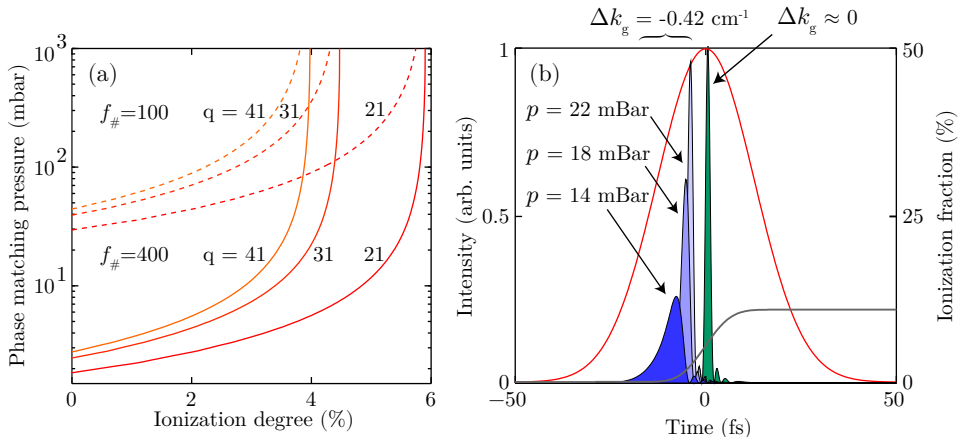


Figure 2.11: The influence of the gas pressure on HHG: (a) phase matching pressure as a function of the degree of ionization for different harmonic orders (for an 800 nm driving field) and focusing geometries, adapted from Paper VI. (b) Illustration of pressure induced, transient phase matching. $S_{23}(t)$ is shown for three different gas pressures, and values of $\Delta k_g = -0.42 \text{ cm}^{-1}$ (blue peaks) and $\Delta k_g = 0$ (green peak, here $p = 20 \text{ mbar}$). The red line indicates the fundamental field intensity for a 30 fs pulse, the gray line shows the degree of ionization calculated for argon at a peak intensity of $2.3 \cdot 10^{14} \text{ W/cm}^2$.

For a given harmonic order and focal length, equation (2.46) defines a relation between p_{match} and the degree of ionization, r_{ion} , which determines Δk_p . Since Δk_p is always negative, equation (2.46) can only be fulfilled if $|\Delta k_n| \geq |\Delta k_p|$, i.e. if the fraction of ionization is kept below a critical value $r_{\text{ion}}^{\text{max}}$ which depends on the gas used for generation, and is typically a few per cent.

Figure 2.11 (a) shows the variation of p_{match} as a function of r_{ion} for different harmonic orders and focusing geometries. At low degrees of ionization, p_{match} varies only weakly with ionization level and harmonic order. For higher degrees of ionization, p_{match} has an asymptotic behavior, and phase matching is achieved only for a small ionization, and thus intensity, interval. In contrast, at low degrees of ionization, a much larger intensity interval supports phase-matched generation. In addition, the phase matching bandwidth, the harmonic order range over which phase-matched generation is possible, decreases with increasing ionization level.

Figure 2.11 illustrates clearly that phase-matched generation is possible for a large range of pressures and degrees of ionization. Considering that the dipole response increases nonlinearly with increasing intensity, and that an increased generation pressure should allow more atoms to contribute, one could assume that the overall generation efficiency increases with increasing intensity and pressure. However, generation at higher intensities does not necessarily result in an increased efficiency, as in this case, phase-matched generation is limited to small volumes and short time intervals. This effect can be illustrated using a simple 1D-model for HHG, assuming a constant dipole response along a nonlinear medium with length L . Taking into account the quadratic dependence of the generated signal with the density of the nonlinear medium, as is characteristic for coherent wave-mixing processes, the generated harmonic signal can

be expressed as [see equation (2.36)]:

$$S_q(t) \propto d_q(t)^2 p^2 \cdot S_\phi(L, \Delta k(t), \kappa_q), \quad (2.47)$$

where $S_\phi(L, \Delta k, \kappa_q)$ denotes a *phase matching function*. Following equation (2.37), this function can be written as $S_\phi(L, \Delta k) = L^2 \text{sinc}^2[\Delta k(t)L/(2\pi)]$, if $\kappa_q \approx 0$. As described in section 2.5, a simple nonlinear power scaling is assumed in order to approximate how the harmonic dipole amplitude $d_q(t)$ varies with the laser field intensity.

Figure 2.11 (b) displays S_{23} for three different gas pressures. With increasing pressure, phase matching is achieved at higher intensities, and thus later in time. Further, higher pressures confine phase-matched emission to shorter time intervals. However, the time-integrated signal, and thus the generated XUV pulse energy, is only weakly dependent on the pressure. The case presented is for gas pressures at which $|\Delta k_n| \geq |\Delta k_g|$. In this case, equation (2.46) can be fulfilled for sufficiently large r_{ion} . The larger p , the higher r_{ion} for which $p = p_{\text{match}}$. The intensity and focusing conditions determine whether phase-matched generation happens earlier or later in the pulse.

If the length of the generation volume is short compared to the Rayleigh length, the wave vector mismatch arising from the Gouy phase can be neglected. In this case, equation (2.46) is pressure-independent and can be fulfilled if $|\Delta k_n| = |\Delta k_p|$. This situation is shown by the green peak in Figure 2.11 (b). Now, phase-matched generation is confined to a small interval in space and time for which $r_{\text{ion}} = r_{\text{ion}}^{\text{max}}$, and a change of the gas pressure no longer shifts the emission peak. A pressure-independent phase mismatch component such as the Gouy phase typically shifts phase-matched generation to lower ionization levels, but also leads to a less transient behavior and to a broader spectral bandwidth.

Figure 2.11 (b) shows rather short temporal phase matching windows. Considering the three-dimensional generation volume rather than using a one-dimensional model leads to a less transient behavior, since the intensity changes spatially across the nonlinear medium. However, even in the three dimensional case, phase-matched generation is confined to smaller temporal and spatial windows at high generation intensities and pressures. Similar effects can be observed following depletion of the neutral medium, i.e. if all atoms are ionized within a short temporal window [112], as is used for gating purposes in Paper VII. A temporal confinement of the harmonic emission implies spectrally broader harmonics, but can lead to a spectrally more narrow phase matching window, restricting the bandwidth of the attosecond pulses. The spatio-temporal dependency of phase matching and depletion effects, typically leads to spatial temporal couplings, as is discussed in detail in Ref. [140].

The above discussion clearly shows that phase matching in HHG is a rather complex process. In practice, the optimization of macroscopic generation parameters is most easily done by an iterative tuning of multiple control parameters, particularly pressure, intensity, and gas cell position. Such a procedure was used in Paper VI. In particular, a simple measurement of the total harmonic signal – the time integrated S_q as a function of gas pressure – can reveal important information about the macroscopic generation conditions, as is discussed below. An alternative method for the characterization of macroscopic generation conditions is discussed in detail in Paper XII [see also section 4.2]. Here, a noncollinear probe is used to extract a global phase mismatch parameter.

Quadratic and Superquadratic Signal Growth

In the literature, a quadratic growth of the harmonic signal with gas pressure is sometimes misleadingly associated with phase-matched harmonic generation. Quadratic growth is a consequence of coherent, but not necessarily phase-matched, addition of the generated harmonic signal from all the contributing single-atom emitters. The coherent addition of the generated electrical field, E_q , implies a linear growth of the amplitude of this field with the number of contributing emitters, N , if the overall phase matching condition does not change with N . Consequently, the generated photon flux, the harmonic signal, scales as $S_q \propto N^2$.

This basic behavior is well described by equation (2.47). The total harmonic signal, S_q , is proportional to p^2 if $S_\phi = \text{constant}$. For HHG in gases, this is typically the case at low generation pressures where dispersion and reabsorption in the gas is negligible. A quadratic signal growth with pressure is thus a clear indication that the phase matching conditions are not changing significantly with gas pressure. However, as discussed above, phase-matched generation requires atomic dispersion as long as a pressure independent phase mismatch component is present, as is typically the case for HHG in gases. This implies that the phase matching conditions change with gas pressure, i.e. S_ϕ is no longer constant for gas pressures around $p \approx p_{\text{match}}$ and S_q does not grow quadratically with p . For $\partial S_\phi / \partial p > 0$, the phase matching conditions improve with p , leading to a super-quadratic growth of the total harmonic signal with gas pressure [141]. The signal can increase with pressure until S_ϕ reaches its global maximum. As the pressure increases, phase matching is first achieved at low ionization fractions, i.e. at the leading edge of the pulse. As discussed above, increasing p further, shifts phase-matched generation to higher ionization levels. The time-integrated signal, however, does not increase significantly with p in this regime. If the intensity is high enough, such that the critical ionization level can be reached, phase-matched generation is possible even at very high gas pressures. The limit in this case is set by plasma defocussing of the fundamental field and/or reabsorption. For lower intensities, Δk_n dominates when the pressure is increased beyond the point where phase-matched generation occurs at the maximum ionization level. Now, $\partial S_\phi / \partial p < 0$ and the harmonic signal decreases with increasing pressure. Note that S_ϕ can show an oscillatory behavior with pressure, known as Maker fringes [142]. In HHG in gases, Maker fringes induced by gas pressure variations are often smeared out due to temporal and spatial integration. Nevertheless, pressure-induced Maker fringes have been observed [143] and can cause high-contrast interference fringes in the spectral domain, as introduced in section 2.4.1 as well as in Paper I.

Absorption Limited Generation

The generation of high-order harmonics in gases is usually accompanied by reabsorption of the generated XUV photons in the nonlinear medium (denoted simply as *absorption* here). Absorption effects are briefly discussed below, mainly following the derivation in Ref. [127]. While absorption can be minimized at low gas densities, for pressures around p_{match} , high enough to cause significant dispersion effects, absorption effects can usually not be neglected. In practice, absorption simply limits the effective length of the nonlinear medium.

The maximum harmonic signal can be generated for a sufficiently long medium if

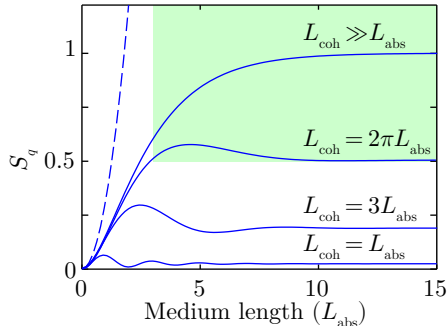


Figure 2.12: Absorption limited generation: harmonic signal S_q as a function of the length of the nonlinear medium, normalized to the maximum absorption limited signal obtained for phase-matched generation. The solid lines represent the harmonic signal for four different values of L_{coh} including the optimum case of absorption-limited generation with $\Delta k \approx 0$ ($L_{\text{coh}} \gg L_{\text{abs}}$). The dashed line displays a quadratic signal growth with medium length, corresponding to absorption-free generation and $\Delta k \approx 0$. The green area indicates $L_{\text{med}} > 3L_{\text{abs}}$ and $L_{\text{coh}} > 2\pi L_{\text{abs}}$. The illustration was inspired by Fig. 1 in Ref. [127].

$\Delta k \approx 0$, i.e. if the coherence length $L_{\text{coh}} = \pi/\Delta k$ is much larger than the absorption length $L_{\text{abs}} = 1/2\kappa_q$. For even longer media, the harmonic signal does not increase further, but the risk that the driving laser pulse gets distorted prior to generation increases because of nonlinear propagation in the first part of the long medium. As a rule of thumb, and in order to ensure that the harmonic signal reaches at least half of its maximum value, the conditions

$$L_{\text{med}} > 3L_{\text{abs}} \quad \text{and} \quad L_{\text{coh}} > 2\pi L_{\text{abs}} \quad (2.48)$$

should be fulfilled, as is illustrated in Figure 2.12.

Care must be taken to ensure that the nonlinear medium does not reach beyond the length of the maximum generation volume, defined by the threshold intensity necessary to generate the harmonic radiation under consideration. Following this restriction ensures that the generated XUV radiation is not absorbed outside the effective generation volume. Confining the gas to a sufficiently small volume is especially challenging at very tight focussing geometries, where the effective medium length can reach values well below 1 mm.

2.4 Macroscopically Induced Spatial and Spectral Structures

Interference phenomena are intimately connected to HHG, as they determine the HHG process both on the single atom level as well as macroscopically. Microscopic interference effects, that is, interference structures appearing in the spectral domain caused by the dipole response of a single atom emitter, include interferences between consecutive attosecond pulses in the pulse train, as discussed in section 2.2.3, as well as interferences between different quantum paths, for example, between the short and the long trajectories. Such *quantum path interferences* have been subject of several studies [144–151] where interference fringes in the spatio-spectral far-field profile of

individual harmonic orders have been interpreted as interferences between different quantum paths.

Below, two different macroscopic effects that can cause similar far-field interferences are discussed. The first effect, the appearance of temporal Maker fringes in the spectral domain and its spatial analog was identified during this thesis work and is presented in Paper I. The second effect, spectral and spatial interference fringes caused by spatio-temporal couplings, as recently discussed in Ref. [140], is described briefly.

2.4.1 Spectral Maker Fringes

As explained above, Δk is a highly time-dependent quantity. For sufficiently large variations, such that the product $\Delta k L$ changes by several π , the harmonic signal can exhibit high contrast temporal amplitude modulations, or temporal Maker fringes. However, such modulations are typically averaged out if the time-integrated harmonic signal is detected.

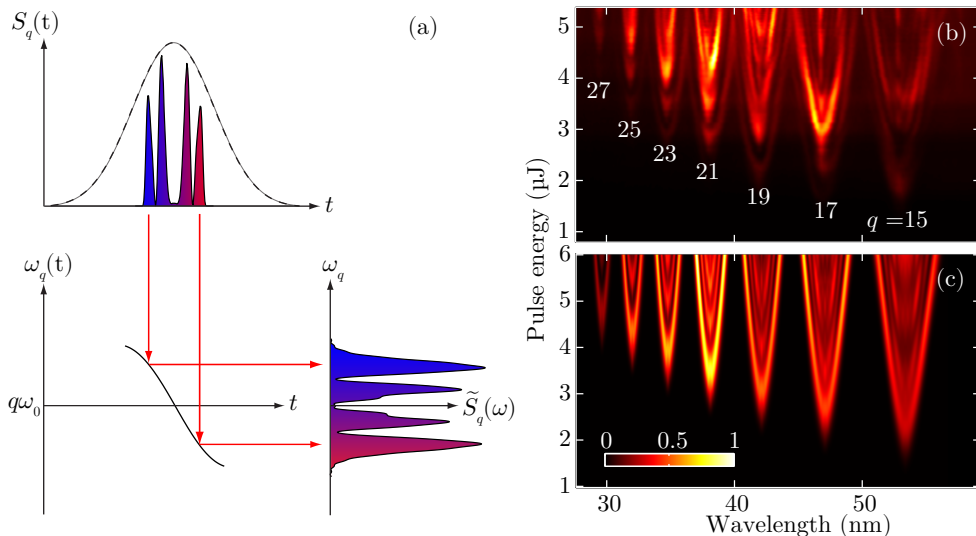


Figure 2.13: Spectrally resolved Maker fringes: (a) Temporal amplitude modulations induced by the dipole phase are mapped directly into the spectral domain, because of a modulation of the instantaneous central frequency ω_q . Intensity-dependent measured (b) and simulated (c) harmonic spectra show a clear modulation of the harmonic signal with laser field intensity. The experimental spectra were measured with the 100-kHz system presented in section 3.2.2. Adapted from Paper I.

Temporal amplitude modulations can be directly accessed if a streaking technique is used, mapping time onto an experimentally accessible quantity. If a chirp is imposed onto the generated harmonic signal, temporal Maker fringes can be mapped out into the spectral domain. According to equation (2.28), the instantaneous central frequency ω_q is modulated by temporal dipole phase variations. Large dipole phase variations can be expected, especially for the long electron trajectory. As a conse-

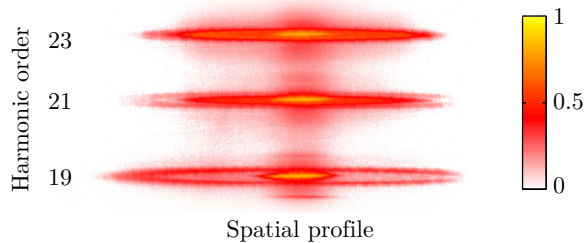


Figure 2.14: Spatio-spectrally resolved Maker fringes: a measured harmonic spectrum showing ring-shaped fringes which can be attributed to Maker fringes of the long electron trajectory. The spectrum was recorded using the high-repetition rate system operating at 1030 nm, described in section 3.2.1.

quence, Δk_d and ω_q vary with time, leading to amplitude modulated and strongly chirped XUV emission.

The process is illustrated in Figure 2.13 (a), where a simulated harmonic signal corresponding to emission from the long trajectory is displayed, together with the instantaneous central frequency and the corresponding spectral intensity. High-contrast amplitude modulations are visible in both the temporal and spectral domain. While the harmonic emission at the leading edge of the pulse is blue-shifted, a red shift is observed at the trailing edge. The variation of ω_q maps the temporal amplitude modulations directly into the spectral domain. Note that the results presented in Figure 2.13 correspond to experimental conditions where the long trajectory dominates but is not generated phase-matched, as is typically the case at very tight focusing geometries and when low gas pressures are used [152].

Both dipole phase induced harmonic signal modulations as well as the corresponding frequency variations are intensity dependent. Higher intensities lead to more rapid amplitude and frequency modulations. Consequently, more Maker fringes are visible at higher intensities, and they are spread over a larger spectral bandwidth. This effect can clearly be seen in Figure 2.13 (b), where measured and simulated harmonic spectra are displayed as a function of the laser pulse energy. An analytical description of the intensity dependent mapping process can be found in Paper I.

Analogous to the temporal-spectral mapping, a spatial near-field to far-field mapping causes very similar intensity modulations in the spatial domain, leading to ring-shaped fringes if the emitted harmonics are detected spatio-spectrally resolved. An example of such ring-shaped structures can be seen in the HHG spectrum shown in Figure 2.14. The analogy between temporal-spectral mapping and spatial near-field to far-field mapping is discussed in more detail in section 4.2.1. Spatial Maker fringes are discussed in Paper I and can also be seen in the harmonic spectra shown in Paper IV. Analogous to the temporal-spectral mapping, a spatial near-field to far-field mapping causes very similar intensity modulations in the spatial domain, leading to ring-shaped fringes if the emitted harmonics are detected spatio-spectrally resolved. An example of such ring-shaped structures can be seen in the HHG spectrum shown in Figure 2.14. The analogy between temporal-spectral mapping and spatial near-field to far-field mapping is discussed in more detail in section 4.2.1. Spatial Maker fringes are discussed in Paper I and can also be seen in the harmonic spectra shown in Paper IV.

2.4.2 Multi-Source Interferences

Another type of macroscopic effect, recently discussed in Ref. [140] can cause interference fringes in the spatial and spectral domains. At very high driving field intensities, nonlinear propagation dynamics can cause the formation of multiple harmonic sources: maxima of the harmonic dipole amplitude occur along the transversal spatial coordinate x as well as in time. While the formation of a multi-source structure in the spatial domain causes spatial interferences in the far-field angular profile, a temporal amplitude modulation leads to spectral interferences. Again, ring-shaped fringes and two-dimensional interference patterns can be observed in the spatio-spectral domain if the emitted harmonics are detected spatio-spectrally resolved.

While Maker fringe-like structures typically appear at rather low gas pressures and intensities where the long trajectory can dominate, interference effects arising due to the formation of multiple harmonic sources are typical for high intensities and rapid ionization.

Although they are discussed separately in Paper I and Ref. [140], there is no fundamental restriction preventing both effects from being observed simultaneously. In particular, rapid ionization effects can lead to dynamical blue shifts, and thus once more to a shift of the central frequency with time. Similar to phase modulations caused by the dipole phase, plasma-induced phase modulations can modulate the harmonic amplitude and map these modulations into the spectral domain.

In conclusion, the above effects clearly illustrate the complex dynamical processes that can determine the harmonic emission characteristics. The disentanglement of such processes from effects caused by the single atom response remains a complex challenge for most experiments, where harmonic generation is used as a probing method for the generation medium itself.

2.5 Quasi-classical Modeling

In this thesis, two different methods are used to simulate HHG and attosecond pulse generation. Both methods are based on approximations of the harmonic source field $\tilde{E}_{\text{xuv}}(\omega, z, x, y) = \mathcal{F}_t[E_{\text{xuv}}(t, z, x, y)]$, calculated as a function of the laser field $E(\omega, z, x, y)$ and the properties of generation gas. Here, \mathcal{F}_t denotes the temporal Fourier transformation. Starting with the simplest case, where propagation effects in the nonlinear medium are neglected and the medium length is approximated as $L \approx 0$, a simple Fourier diffraction integral (Fraunhofer approximation) along the transverse spatial coordinates x, y yields the XUV field $\tilde{E}_{\text{xuv}}(\omega, z, x', y')$ in the far-field:

$$\check{E}_{\text{xuv}}(\omega, \beta_x, \beta_y) \propto \mathcal{F}_{x,y}[\tilde{E}_{\text{xuv}}(\omega, x, y)] = \int_{-\infty}^{\infty} dx \int_{-\infty}^{\infty} dy \tilde{E}_{\text{xuv}}(\omega, x, y) e^{-i(K_x x + K_y y)}, \quad (2.49)$$

where $K_{x,y} = \frac{\omega}{c} \beta_{x,y}$ are functions of the far-field angles $\beta_x = x'/z$ and $\beta_y = y'/z$. For a rotational symmetry, the two-dimensional Fourier integral can be replaced by a one dimensional Hankel transformation, which itself can be numerically evaluated by means of a fast Fourier transformation [153]. In this case, the second transverse dimension can be omitted, as is done below.

In order to take propagation effects into account, the laser field is approximated as a Gaussian beam, and a Gaussian temporal profile was assumed, neglecting reshaping

effects on the pulse envelope and any influence of the generated fields on the generation process. Phase offsets between the fundamental and the harmonic carrier waves occurring due to dispersion are taken into account by integrating the wave vector mismatch along the optical axis according to equation (2.38). The total XUV field is given by the coherent sum over all contributing fields along the length of the nonlinear medium.

The single dipole response is calculated using the SFA approximation in order to solve the TDSE, as is briefly discussed in section 2.2.2. In a second, quasi-classical model, the harmonic polarization at frequency $q\omega$ was approximated using a simple, computationally fast method. For a single quantum path, the generated field at harmonic order q can be approximated as:

$$E_q(t, z, x) = \mathcal{E}_q(t, z, x) \exp [iq\phi_\omega + \Delta\phi_z(q)], \quad (2.50)$$

with $E_{\text{xuv}}(t, z, x) = \sum_{q\omega > I_p} E_q(t, z, x)$. ϕ_ω denotes the phase of the driving laser field. The phase mismatch between the generated XUV field and the induced polarization at the considered harmonic frequency, $\Delta\phi_z(q)$ contains both dispersion and dipole phase components introduced in section 2.3.1. The harmonic field envelope is approximated via a simple nonlinear power scaling of the fundamental field intensity as: $\mathcal{E}_q \propto I^3$. Similar approximations have been made in the literature in order to account for a reasonable nonlinear behavior, see, for example, Refs. [41, 131, 154]. A weak variation of the spectral envelope $\tilde{\mathcal{E}}_q(\omega)$ with harmonic order is taken into account by mimicking experimentally measured spectra. The dipole phase is approximated using the simple linear relation with the laser field intensity defined in equation (2.27). Even though this quasi-classical model is based on discrete harmonic orders, it is possible to simulate the basic characteristics of spectrally continuous XUV emission, and thus IAPs.

k

REPETITION RATE VS INTENSITY — TWO COMPLEMENTARY SCALING DIRECTIONS

High-order harmonics and attosecond pulses are commonly generated using high power, femtosecond laser systems delivering pulses at repetition rates up to a few kilohertz. Because of limitations on the average power of these systems, and the rather low conversion efficiency into the XUV, the average XUV power, which is given by the product of the repetition rate and the pulse energy, is currently limited to values well below 1 mW. In recent years, the technical limitations on XUV attosecond sources have been pushed in two different directions: towards μJ -XUV pulse energies but at low repetition rates, and towards multi-MHz repetition rates but at low pulse energies. These source development directions are mainly driven by experimental demands, which often place requirements predominantly on one of these two parameters.

In this chapter, the scaling of high-order harmonic and attosecond sources in those two directions is discussed. The first part of this chapter introduces a new scaling model, developed as part of this thesis work, which is able to predict the scaling of the necessary experimental parameters across and even beyond the entire energy and repetition rate range available with modern high-power laser systems. It is also shown how the scaling model can be applied to discuss macroscopic generation conditions independently of the focusing geometry used for the generation. The different laser systems and the corresponding high-harmonic and attosecond beam lines used for this thesis work are then described. While scaling of the repetition rate and the pulse energy can be discussed without having to consider a change in the average XUV power generated, methods for enhancing the average power are briefly discussed in the last part of this chapter.

3.1 Introduction: Scaling Repetition Rate and Intensity

High-order harmonic generation is a strong field process, demanding intensities around 10^{14} W/cm^2 . The intensity requirement determines the focusing geometry that has

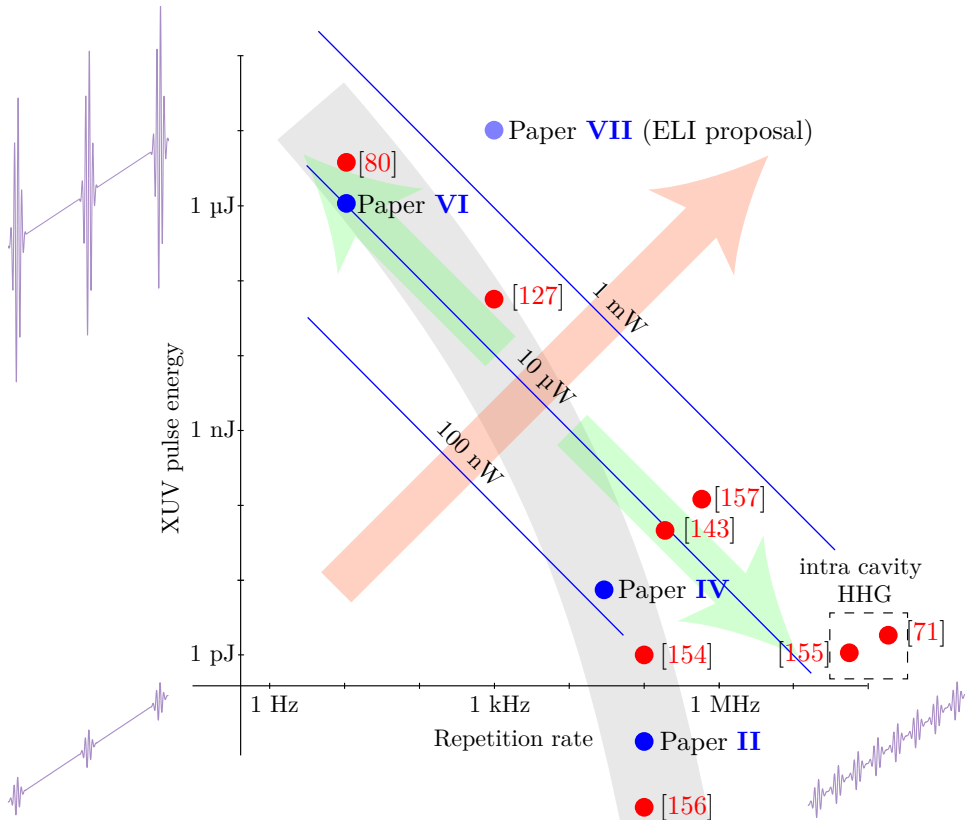


Figure 3.1: Scaling repetition rate, pulse energy and average power. The green arrows indicate repetition rate and pulse energy scaling at constant average power. The red arrow, indicates average power scaling. The different markers locate the parameters of the XUV sources used or designed in this thesis (blue dots) as well as other HHG sources with comparably high average power in the XUV which have been reported in the literature (red dots). Pulse energies of one harmonic order above 20 eV are considered, disregarding possible losses arising from a separation of the fundamental and harmonic fields. The gray area indicates the trend of lower XUV power towards higher repetition rates discernible in the literature, disregarding recent Refs. [71, 143, 155, 157]. The displayed value for Paper VII is an estimation based on the expected laser parameters, and assuming a conversion efficiency of 10^{-5} .

to be used in order to achieve the required intensity. For femtosecond laser pulses and pulse energies well above 100 mJ, down to a few μJ , such intensities can easily be reached. HHG is thus possible within a large range of pulse energies and repetition rates, provided that the required laser source is available.

With decreasing focal length¹, the size of the focal volume decreases, both in the

¹As in Paper II, the focal length is used in this context as a scaling parameter, assuming a constant beam diameter before focusing. More generally, the f-number, or the beam waist diameter

longitudinal, and the radial direction. In addition, the wavevector mismatch introduced by the Gouy phase changes with focal length. Both parameters have a direct impact on the macroscopic generation conditions. The Gouy phase and focal volume have been seen as critical parameters limiting the available photon flux, especially for tight-focus geometries [81, 82, 156]. In very early work, the conversion efficiency was predicted to scale as b^3 , where b is the confocal parameter of the focused laser beam [158]. More recent work presents somewhat different efficiency scaling models for the loose focus regime [41, 159, 160]. Midorikawa and co-workers mention the possibility of scaling at fixed conversion efficiency [41] and apply basic principles, which are also used in the scaling model described in this thesis, to the loose focus regime [161]. Most experimental results described in the literature seem to confirm a significantly reduced conversion efficiency for tight-focus generation schemes. An overview of different HHG sources providing comparably high average power in the XUV, is presented in Figure 3.1, including examples at both extremes of the scaling directions. Although very different laser systems are used, and disregarding for the moment Refs. [71, 143, 155], the average XUV power decreases with decreasing pulse energy and increasing repetition rate, as indicated by the gray shaded zone. While the average laser power available does not vary much within the scaling range presented, the reported conversion efficiencies² vary from above 10^{-5} at 10 Hz to 10^{-8} at 100 kHz.

As part of this thesis, a theoretical model was developed which predicts a conversion efficiency which is independent of focal length. More generally, the model shows the scalability of any macroscopic generation condition, i.e. phase-matched or non phase-matched HHG. It is based on the scaling of all relevant parameters determining the macroscopic generation conditions, with focal length. Most importantly, it predicts a high *phase matching pressure* and a short nonlinear medium (see section 2.3.2) when using short focal lengths. Confining a high-density gas target to a few tens of μm is technically challenging and high conversion efficiencies at tight focus geometries have been reached only recently [143]. Rothhardt and co-workers [143] follow the scaling model described below and introduced in Paper II, leading to high average XUV powers generated at a repetition rate of 200 kHz. The values reported are close to the highest values obtained with low repetition rate (< 1 kHz) systems. Other high-repetition rate schemes that achieve similar or even higher XUV average power are based on intra-cavity HHG [71, 155] or high power fiber laser systems [157].

The scaling model developed here has also been applied to the loose-focus regime (Paper VI). Furthermore, a conceptual design has been developed for a gas-HHG beam line that should deliver XUV pulses with high peak and average power, well above the reported values of currently operating HHG-beam lines (Paper VII).

3.1.1 A Generalized Scaling Model

The generated XUV photon flux can be expressed as a function of the gas pressure and the dimensions of the nonlinear medium. For the sake of convenience, one can start by considering a rectangular generation medium exposed to a spatially constant intensity, and assume that the generation is fully phase-matched. The following derivation is, however, not restricted to these simple conditions but can be generalized to any

can serve as a scaling parameter.

²If not specified otherwise, the conversion efficiency denotes the ratio of the generated power in the XUV, spectrally integrated over one harmonic order and the laser power used for generation.

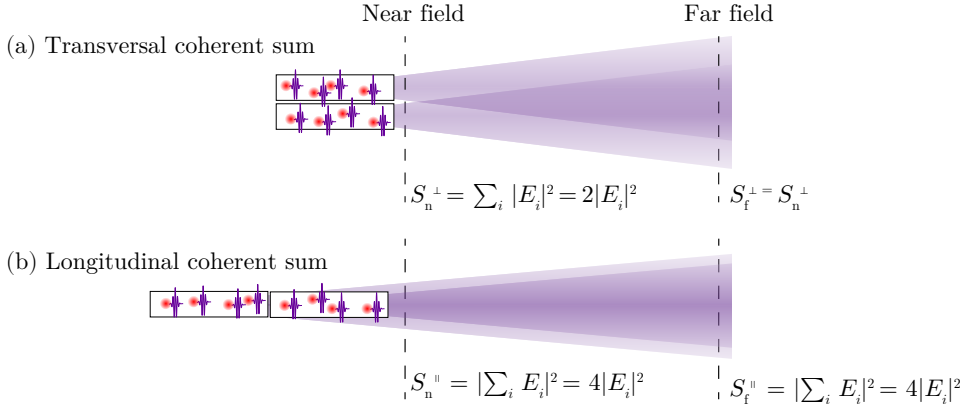


Figure 3.2: Principle of coherent field addition: Placing two sources emitting coherent radiation next to each other as in (a) leads to a total generated power which is only half the value generated from two sources placed behind each other in the beam emission direction, as in (b). In the notation used in the figure, spatial integrals over the beam profile are omitted.

medium geometry and phase matching condition, as discussed below. The generated XUV pulse energy is proportional to:

$$E_q \propto p^2 L^2 D^2, \quad (3.1)$$

where L and D denote the medium's length and transverse dimension, respectively. This equation, also used in earlier work [41], can be motivated by considering a fundamental principle of coherent field addition, illustrated in Figure 3.2. Consider a small volume filled with single atom emitters radiating a coherent signal $S_i = |E_i|^2$. Placing two of these volumes next to each other, results in a coherent addition of the emitted signals. Depending on the relative position of the two volumes, different total signal strengths can be expected. If the two volumes are placed next to each other with a transverse offset with respect to the emission direction, the signal addition is most easily understood in the near-field, while placing them longitudinally allows constructive signal addition to be easily described in both the near and the far-field. In both cases, energy conservation yields the same total signal in the near and far-field. For transverse coherent addition, the total signal emitted in the near-field can be calculated as the sum over the intensity from each source, i.e. by incoherent addition, yielding $S_n^+ = 2S_i$ and thus $S_f^+ = 2S_i$. If the two sources are placed next to each other with a longitudinal offset in the beam propagation direction, the near (and far) field signal is simply the coherent sum of both sources, yielding $S_f^+ = 4S_i$. This simple illustration explains in an intuitive way why the total harmonic signal generated from an ensemble of atoms scales quadratically with the length of the medium and linearly with the transverse dimensions D_x and D_y . For $D = D_x = D_y$, and taking into account the density of the medium, this yields equation (3.1).

In order to estimate how the total harmonic signal scales with focal length, the scaling of each of the parameters entering equation (3.1) has to be evaluated, and the possible influence of macroscopic propagation effects has to be taken into account,

i.e. most importantly, the influence of phase matching and absorption. If generation happens at the focus of a laser beam, a more complicated medium geometry has to be accommodated. For now, we shall still consider phase-matched generation, but will allow a spatially varying laser field intensity distribution, as well as a non-cubic medium geometry. Equation (3.1) is still valid so long as the intensity distribution is scaled spatially with D and L .

In order to keep the intensity constant while scaling f , the laser pulse energy E_f has to scale as $E_f \propto f^2$, following simple Gaussian optics. Considering further that the Rayleigh length of a focused laser beam scales as $z_0 \propto f^2$, equation (2.40) yields: $\Delta k_g \propto 1/f^2$. In order to keep the balance between Δk_g and $\Delta k_{n,p}$ while changing f and thus Δk_g , equation (2.46) demands that the generation pressure scales as $p \propto 1/f^2$. The overall phase shift between the XUV field and the generating laser field induced due to dispersion on propagation through the nonlinear medium can be kept constant for a constant pressure-length product, pL , and so the medium length has to scale as $L \propto f^2$. If we also take into account the fact that both the longitudinal intensity distribution of a focused Gaussian beam and the corresponding Gouy phase distribution scale linearly with the Rayleigh length, the phase shift accumulated in passing through the generation medium because of the Gouy phase and the dipole phase can also be kept constant when scaling f if $L \propto f^2$. It follows that the overall phase matching conditions can be kept constant while scaling f if the above scaling relations are taken into account. As with phase matching, absorption is also determined by the optical density integrated along the beam propagation axis, and thus by pL , absorption effects are likewise focal length-scaling invariant, if these scaling relations are maintained. The same principle applies for nonlinear propagation effects, for example, from plasma dispersion, which can lead to defocussing of the generating beam, as is discussed in Ref. [143].

While the length of the focal volume of a Gaussian beam scales as $L_{\max} \propto f^2$, its diameter scales linearly with f , $D_{\max} \propto f$. Here L_{\max} and D_{\max} define the volume within which a certain threshold intensity is reached, such as the threshold intensity needed to generate a given harmonic order.

The scaling relations are summarized in the following table:

Scaling parameter	f	E_f	p	L	L_{\max}	D_{\max}	N	E_q	η_q
f	–	f^2	$1/f^2$	f^2	f^2	f	f^2	f^2	constant
W_0	–	W_0^2	$1/W_0^2$	W_0^2	W_0^2	W_0	W_0^2	W_0^2	constant
E_f	$\sqrt{E_f}$	–	$1/E_f$	E_f	E_f	$\sqrt{E_f}$	E_f	E_f	constant

Here, the beam waist radius $W_0 \propto f$ and the laser pulse energy E_f are listed as alternative scaling parameters. Inserting the above scaling relations into equation (3.1) yields:

$$E_q \propto f^2. \quad (3.2)$$

The number of contributing single atom emitters, N , scales as:

$$N \propto pLD^2 \propto f^2. \quad (3.3)$$

Taking into account the scaling relation for the laser pulse energy, equation (3.2) yields a conversion efficiency $\eta_q = E_q/E_f$ which is focal length-scaling invariant. Equa-

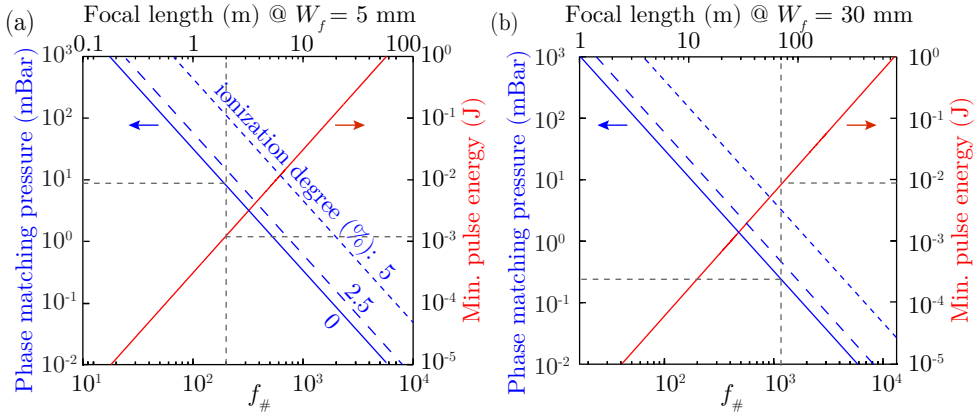


Figure 3.3: Phase matching pressure and minimum required laser pulse energy for HHG in argon as a function of focal length and f-number of the focused Gaussian laser beam. In (a), typical parameters employed at the intense harmonic beam line in Lund (section 3.3.1) are indicated (gray dashed lines). In (b), the parameter considered for the ELI proposal, phase 1 (section 3.3.2) are shown. The pulse energy was calculated assuming a peak intensity of $1.5 \cdot 10^{14} \text{ W/cm}^2$ and a pulse length of 45 fs in (a) and 10 fs in (b). Adapted from Paper VI.

tion (3.2) still predicts a quadratically increasing XUV power with focal length, as a larger number of single atom emitters can be used to convert more energy into the XUV.

Figure 3.3 displays the phase matching pressure p_{match} defined in equation (2.46) as a function of the focusing geometry, i.e. as a function of f and f-number $f_{\#} = f/(2W_f)$, with W_f denoting the beam radius before focusing. As discussed above, p_{match} scales as $p_{\text{match}} \propto 1/f^2$. The figure also shows the minimum pulse energy required to reach an intensity sufficiently high for efficient HHG. Note that the pulse energy indicated was calculated for an ideal Gaussian beam. In practice, due to imperfect beams with $M^2 > 1$, higher values have to be considered. At pulse energies around a few mJ and for $\tau \approx 45$ fs (a), a focal geometry with f-numbers around 200 is required, corresponding to a 2 m focal length at $W_f = 5$ mm. In such generation conditions, a generation gas pressure around 10 mbar is required which can easily be achieved in both continuous or pulsed gas cells. For much larger pulse energy values around 100 mJ, and accordingly very weak focusing, the necessary generation pressure can drop to values well below 10^{-1} mbar. At the same time, the required gas cell length increases dramatically. Loose-focus HHG schemes are discussed in section 3.3. Beam lines based on such high power loose focusing schemes are discussed in detail in Papers VI and VII. In the other direction, towards μJ -level pulse energies, as are typically reached at repetition rates approaching the MHz regime, gas pressures exceeding 1 bar are necessary. At the same time, L_{max} reaches values well below 1 mm, setting high technical demands on the design of the gas medium. Section 3.2 as well as Papers I, II, III and IV discuss tight-focus HHG schemes.

3.1.2 A Generalized Macroscopic Model

Although derived for phase-matched HHG, the scaling relations introduced in section 3.1 are not restricted to such simple conditions. As discussed below, they explicitly include non phase-matched HHG and generation using laser beams with complicated spatio-temporal characteristics.

Considering rotational symmetry, the two-dimensional intensity and phase distribution of a focused laser beam can be plotted as a function of the spatial coordinates x and z , normalized to the Rayleigh length and the beam waist radius. If Gaussian optics are applied, the normalized distribution is independent of focal length. As harmonic dipole amplitude and phase can be expressed as a function of the laser field amplitude and phase, we can accordingly define a harmonic dipole distribution, normalized to z_0 and W_0 which is thus also focal length-scaling invariant. Furthermore, scaling the gas density as $p \propto 1/f^2$, ensures that any dispersion phase term is kept constant during propagation through the medium, as f is varied. This explicitly includes phase terms that might lead to a phase mismatch between the phase of the induced dipole at a given position z_1 within the medium and the harmonic field generated at $z < z_1$. Describing the harmonic source distribution in space and time as independent of f implies that even the far-field XUV emission can be regarded as being independent of focal length if a correct normalization of the emission angle is carried out. Again, the fundamental field distribution, for example, the divergence angle Θ_0 , can be used as a normalization parameter.

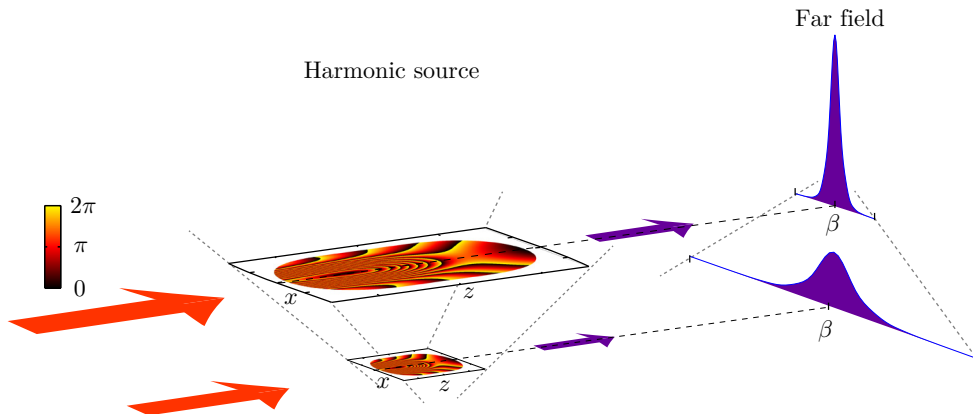


Figure 3.4: Scaling HHG sources with focal length: phase matching maps $[\Delta\phi_z(x, z) \bmod 2\pi]$ and corresponding harmonic spatial far-field profiles for two different focal lengths, calculated using the scaling relations introduced in section 3.1. When normalized to the beam parameter of the fundamental beam (W_0 , z_0 and Θ_0), the harmonic source and far-field spatial profiles are invariant with scaling of the focal length.

Figure 3.4 illustrates harmonic source scaling for rather complicated generation conditions and two different focal lengths. Two-dimensional phase matching maps (introduced in Figure 2.10) are plotted together with the calculated harmonic far-field intensity profile of the 21st harmonic order. Although the focusing conditions are quite different, the normalized phase matchings maps and far-field spatial profiles

are identical, as is to be expected if all relevant macroscopic parameters are scaled correctly.

Following the above argumentation, macroscopic effects in HHG can be fully normalized to characteristic spatial properties of the driving laser beam and consequently, they can be discussed independently of the focal length. In other words, characteristic effects observed in HHG using a certain focusing geometry can be transferred to other focusing geometries if the correct scaling relations for all parameters determining macroscopic effects are used. This has far-reaching consequences for current and future high-order harmonic source design. Given a particular harmonic source operating with specific parameters, other harmonic sources can be constructed by simple up or downscaling of the experimental conditions in order to match the parameters of a different laser source. This has been done within the framework of this thesis in a conceptual design for an attosecond beam line at ELI-ALPS, as is presented in Paper VII.

The discussion of macroscopic aspects in HHG presented in section 2.3.2 can be generalized using normalized macroscopic parameters: a normalized generation volume and far-field propagation angle, as well as a normalized gas density. As mentioned above, the dimensions of the generation volume and the far-field propagation angle can easily be normalized to the parameters of the driving laser beam. Besides these geometrical factors, the gas pressure is an important parameter that needs to be normalized in order to allow a discussion of propagation effects which is independent of the focal length. A pressure p_0 , which scales as $p_0 \propto 1/f^2$, can be used as a normalization parameter. p_0 can, for example, be defined via the dispersion properties of a certain harmonic order with respect to the wavevector mismatch introduced by the Gouy phase. The normalized gas pressure can thus be written as $n_p = p/p_0$ with $p_0 = p_0(\text{gas}, \lambda, q) = -\Delta k_g [\partial \Delta k_n / \partial p]^{-1} \approx (q/z_0) [\partial \Delta k_n / \partial p]^{-1}$. Control parameters which effect the macroscopic generation conditions are listed below, together with possible normalization parameters:

	Control parameter	Normalization parameter
Length of generation volume	L	z_0
Diameter of generation volume	D	W_0
Far-field propagation angle	β	Θ_0
Gas pressure	p	$p_0 = p_0(\text{gas}, \lambda, q)$

3.2 Downscaling and High-Repetition Rate HHG

In order to increase the repetition rate of high-order harmonic and attosecond sources despite the low laser pulse energy available, mainly three different schemes have been applied:

Single pass HHG As in usual gas HHG schemes, the laser pulse is focused into a gas target. The required intensities are reached by employing a tight focus geometry. This approach has been pioneered by Lindner and co-workers [156] and was employed in Papers I, II, III and IV.

Field-enhanced HHG Here, the local field enhancement close to metal nanostructures placed in the focus of a laser beam is used to reach the necessary intensities [162]. Such a scheme has been tested directly with an oscillator. However, since the effective generation volume is very small, a coherent buildup, leading to efficient HHG, cannot be expected [163, 164].

Intra-cavity HHG In this approach, HHG is driven either directly inside an oscillator [165] or an external cavity is used to enhance the intensity reached by a single laser pulse by superimposing consecutive pulses from a pump laser [21, 22]. Such enhancement cavities have been pumped either directly by an oscillator or by an amplified laser system. The scheme is technically challenging but promising for efficient HHG. To date, the highest average power HHG sources are based on this scheme. A novel concept employing intra-cavity HHG in connection with the gating technique introduced in section 4.3 is presented in section 4.3.3.

In this thesis the single pass tight-focus approach has been investigated, and implemented in several setups. As predicted by the scaling relations introduced in section 3.1, phase matched HHG driven with μJ -laser pulses in a tight-focus geometry usually requires gas pressures above 1 bar and very short generation media. Because of this technical challenges, the macroscopic generation conditions in the high-repetition rate HHG sources presented below are not yet fully optimized.

3.2.1 The 200 kHz OPCPA System in Lund

The high-repetition rate attosecond beam line in Lund is driven by an optical parametric chirped pulse amplification (OPCPA) laser system, which was developed by

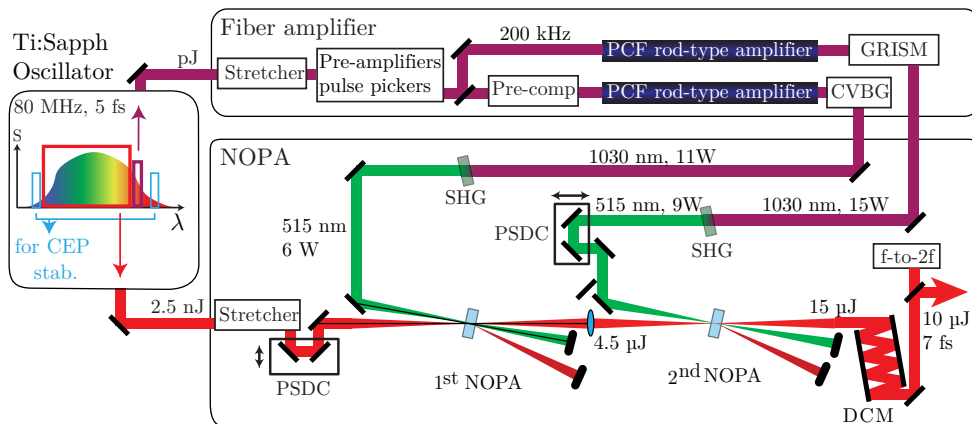


Figure 3.5: The Lund OPCPA-system consisting of a broadband Ti:Sapphire Oscillator, a fiber amplifier, and two NOPA-stages. The abbreviations used in the Figure are: PCF – photonic crystal fiber, CVBG – chirped volume Bragg grating, SHG – second-harmonic generation, PSDC - pump-signal delay control, DCM – double-chirped mirrors. Adapted from Paper III

the company VENTEON in Hannover [166]. An overview of this system is presented in Figure 3.5.

The system is based on three main components: an octave-spanning, CEP stabilized Ti:Sapphire oscillator, a fiber amplifier, and a two-stage noncollinear optical parametric amplifier (NOPA). A small fraction of the long wavelength-part (around 1030 nm) of the broadband spectrum generated in the oscillator is used as a seed for the fiber amplifier. The amplifier includes a three stage preamplifier, followed by two ytterbium-doped rod type photonic crystal fiber amplifiers, operating at a 200 kHz repetition rate. After frequency doubling, the amplifier output serves as the pump for the two NOPA stages. The main output of the oscillator (5 fs, 2.5 nJ) is amplified through noncollinear parametric amplification to 4.5 μ J in the first stage, and about 15 μ J in the second stage. The amplified pulses are finally compressed to below 7 fs with 10 μ J energy using double-chirped mirrors.

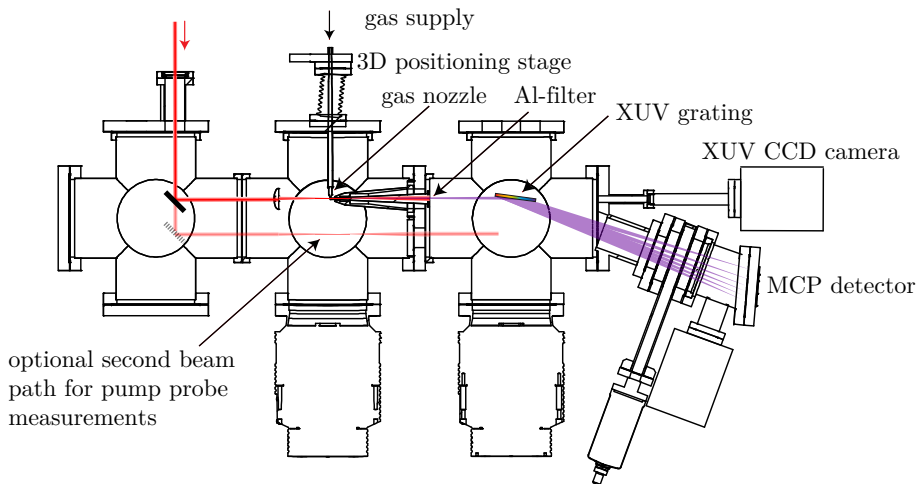


Figure 3.6: Setup for high-repetition rate HHG in Lund, containing a generation and a characterization chamber, which are connected by a pinhole through which the XUV beam passes. The laser pulses are focused with an achromatic lens into a continuous gas jet emerging from an end-fire nozzle. Focal lengths of $f = 50 - 150$ mm are employed.

The HHG setup for high-repetition rate HHG in Lund, designed as part of this thesis work, is shown schematically in Figure 3.6. The incoming laser pulses are focused with an achromatic lens into the continuous gas jet, emerging from an *end-fire nozzle*³ which can be adjusted by a 3D translation stage. The vacuum chamber consists of two parts, separated by a 1 mm pinhole, which ensures a pressure below 10^{-6} mbar in the detection chamber while 10^{-2} mbar can be reached in the generation chamber. The system is pumped by three 5001/s turbo-molecular pumps. The generated harmonics are recorded spectrally and spatially resolved using a home-built XUV-spectrometer based on a varied line space XUV grating (Hitachi, Grating 001-0639, 600 lines/mm).

³An *end-fire nozzle* denotes a gas nozzle consisting of an open-ended tube [82], as sketched in Figure 3.8 (b).

A more detailed description of this system, including an investigation of CEP-effects in harmonic spectra (which are also discussed in section 2.2.3), can be found in Paper III.

The high-harmonic setup described above has also been tested using a commercially available Yb:KGW laser system, which delivers 170 fs pulses at 1030 nm at a repetition rate tunable between 1 kHz and 600 kHz. The corresponding pulse energy varies between 0.5 mJ and 10 μ J. The main advantage of such a system compared to high-power Ti:Sapphire or OPCPA systems is its compactness and user friendliness. Results obtained with this system are presented in Paper IV.

3.2.2 The 100 kHz System in Marburg

The high repetition rate HHG setup in Marburg is driven by a commercial laser system from Coherent Inc., consisting of a Ti:Sapphire oscillator (Mira) and a regenerative amplifier (Rega). The amplifier is continuously pumped by a 10 W neodymium:yttrium-vanadium laser (VERDI-10). For the HHG experiments, the system was operated at a 100 kHz repetition rate, delivering 7 μ J pulses of 45 fs duration. By replacing the

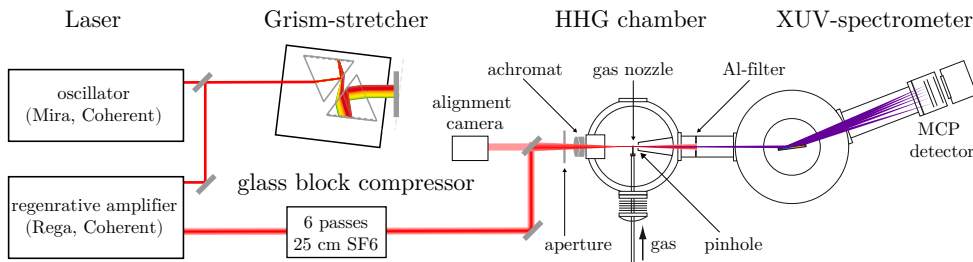


Figure 3.7: High-repetition rate HHG setup in Marburg consisting of: Ti:Sapphire oscillator, Grism-stretcher, regenerative amplifier operating at 100 kHz, glass block compressor and a vacuum apparatus containing a gas nozzle. The laser beam is tightly focused into a continuous gas jet using an achromatic lens ($f = 60$ mm). The generated harmonic radiation is imaged spectrally and spatially using a home-built spectrometer assembly. Adapted from Paper II.

standard stretcher-compressor unit offered by Coherent, the system was changed to down-chirped pulse amplification (DPA) operation, where simple material dispersion can be used for pulse compression (see Figure 3.7).

The laser pulses are focused into a continuous gas jet using an achromatic lens with $f = 60$ mm. The generated harmonics pass a 200 nm aluminum filter and are then recorded spectrally and spatially resolved using an XUV spectrometer assembly similar to the one described in section 3.2.1.

Two different gas target geometries have been tested with the setup, as shown in Figure 3.8. In configuration (a), the laser beam was focused through the gas nozzle, whereas in (b), the focus was placed in front of an open end-fire nozzle. Following the scaling relation introduced in section 3.1, a generation gas pressure in the range of 1 bar is required for efficient, phase-matched generation. The length of the generation volume has to be well below 1 mm in order to avoid reabsorption outside the generation volume. Such conditions can only be realized with an end-fire nozzle. The pressure

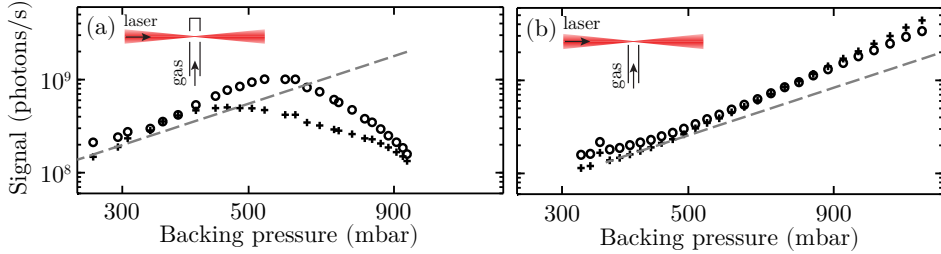


Figure 3.8: Spatially and spectrally integrated intensity of harmonics 15 (+) and 17 (o), generated in xenon using two different gas nozzle geometries. In (a), the laser beam is focused through a 50 μm pinhole in the nozzle, in (b), the focus is located directly in front of the open nozzle with an inner diameter of 90 μm . The gray dashed line indicates a quadratic signal growth with pressure. Adapted from Paper II.

scans in Figure 3.8 clearly indicate the onset of absorption effects at high pressures in (a) while the harmonic signal increases slightly more than quadratically with backing pressure over the entire pressure range tested in (b). While the signal is limited by reabsorption outside the generation volume in (a), the results shown in (b) indicate that the optimum pressure conditions are not reached. The maximum pressure was limited by the pumping system. Note that the generation pressure is significantly lower than the backing pressure.

The 100 kHz HHG system in Marburg is described in further detail in Paper II and was used for the experiments presented in Paper I.

3.3 Upscaling and Intense XUV Pulses

Scaling high-harmonic and attosecond sources to high pulse energies requires loose focusing geometries and high laser pulse energies. Following the scaling relation introduced in section 3.1, the quadratic scaling of the longitudinal dimension of a focused laser beam with focal length implies very long generation media with low gas density. HHG at loose focusing geometries allows another approach, which is briefly introduced in the following but due to its limitations it is not used for the beam lines presented in this thesis.

Instead of generating in a long but low density gas medium, a short medium with high gas pressure can be used. Keeping the pressure-length product $p \cdot L$ constant while changing from one to the other scheme, ensures the same dispersion and absorption properties along the medium. The main differences between these two schemes are phase matching effects due to Gouy phase and dipole phase. In principle, a long medium can be “squeezed” to values over which these two phase mismatch terms do not play a role anymore. One might conclude that this should simplify phase-matched generation. As explained in detail in section 2.3.2, the contrary is the case: this approach, makes phase matching more transient and spatially more localized, which can reduce the harmonic flux. Also, it limits the phase matching bandwidth, i.e. the bandwidth of the harmonic comb (not the bandwidth of individual harmonics). The loose-focus HHG beam lines presented in the following, are therefore based on the low-density, long-medium concept.

3.3.1 The Intense Harmonic Beam Line in Lund

The high power 10 Hz Ti:Sapphire laser system has been the main system used for strong-field physics at the Lund Laser Center since 1992. The system is under constant development and was upgraded several times during the author's PhD project. The laser system is shown in Figure 3.9. It is based on a passively mode locked

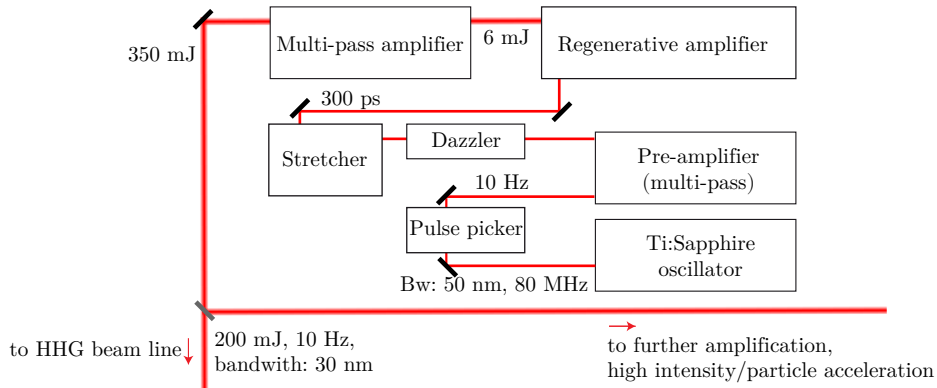


Figure 3.9: Overview of the high power 10 Hz laser system in Lund. The low energy arm of this system (200 mJ, 45 fs) is used to drive the intense harmonic beam line.

Ti:Sapphire oscillator, which delivers pulses with a bandwidth of 50 nm at 80 MHz repetition rate. After passing a pulse picker, where the repetition rate is reduced to 10 Hz, the pulses are sent through a multipass preamplifier, which is mainly used to increase the temporal pulse contrast. Subsequently, the pulses pass a Dazzler, which is used for pre-compensation of gain-narrowing effects in the main amplifiers, and are then stretched to approximately 300 ps. The two main components in the amplification chain are two amplifiers, a regenerative and a multipass amplifier, which increase the pulse energy up to 350 mJ. The pulses are then split into two parts, one part (up to 200 mJ) is used for the intense harmonic beam line, the other part is subsequently amplified in a further multipass amplifier, reaching pulse energies of 1 J. For a 40 fs, pulse duration, this corresponds to peak powers of 40 TW. This high-power output is used mainly for electron and proton acceleration experiments, which are not subject of this thesis.

Today, the intense harmonic beam line is located in a fifteen meter-long corridor, next door to the high power laser system. It consists of a large optical table assembly on which pulse filtering, compression and focusing take place, and on which the harmonic generation chamber is mounted. The generated harmonic radiation propagates through a vacuum tube mounted on a rail system, and into a diagnostic chamber, where it is analyzed both spectrally and spatially. From the diagnostic chamber, the XUV pulses can be sent further into an application chamber. A 6 m propagation path length between the generation cell and the application chamber allows for beam expansion and subsequent tight focusing in order to reach high XUV intensities in the application chamber.

The beam line was rebuilt twice during the author's PhD project, with the aim of

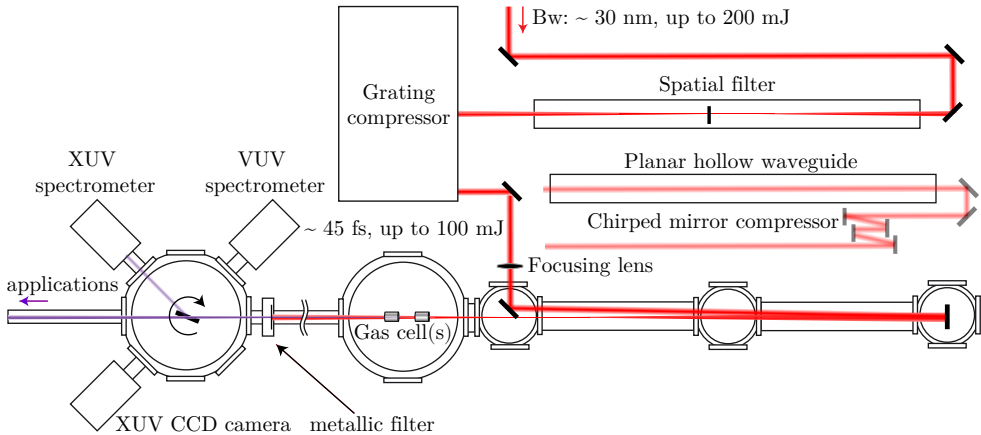


Figure 3.10: Overview of the intense harmonic beam line in Lund. The laser pulses enter the beam line uncompressed and pass a spatial filter before compression. Optionally, pulse post-compression down to approximately 15 fs is possible in a planar hollow waveguide setup (Paper VIII). A modular vacuum chamber system allows different focusing geometries with up to $f = 9$ m. The displayed setup shows the dual-cell configuration used in Paper IX.

increasing the focal length and the harmonic pulse energy. The experimental results presented in Papers VI, IX and XII were obtained with the previous beam line version, mostly with focal lengths of 2 m.

The laser pulses enter the beam line uncompressed and are then focused into a conical pinhole with a waist diameter of $500\ \mu\text{m}$. The pinhole acts as a spatial filter, cleaning the spatial pulse profile. After compression in a grating compressor, the laser pulses can optionally be sent through a post-compression setup. Instead of employing a hollow capillary [167], as in usual post-compression schemes, a planar hollow waveguide [168], filled with 400 mbar of argon, is used for spectral broadening. This scheme is used in order to allow compression of pulses with high pulse energy while keeping the waveguide dimensions within technically practicable limits and ensuring high transmission, as is discussed in detail in Paper VIII. The laser pulses are focused using very loose focusing geometries with focal lengths of up to 9 m. A modular vacuum chamber system permits easy switching between different focusing geometries. Various gas target geometries have been used. The results presented in Papers VI, IX, XII and VIII were obtained using a pulsed gas cell of 1 cm or 2 cm length. In more recent experiments a 6 cm long continuous gas cell was used in combination with the 9 m focal length. This configuration allowed an increase in the energy of the XUV pulse, generated in argon, up to $3\ \mu\text{J}$, measured between 16 and 45 eV.

3.3.2 A Novel Attosecond Beam Line for ELI-ALPS

Based on the theoretical scaling model introduced in section 3.1 and based on the experimental experience with the intense harmonic beam line in Lund, a conceptual design for a new attosecond beam line at the European facility ELI-ALPS has been developed as part of this thesis work. A detailed description of the conceptual design

can be found in the report, listed as Paper [VII](#) in this thesis. A brief overview of the beam line is given below.

The expected extreme laser parameters for this beam line demand an upscaling of the generation parameters in order to optimize the energy conversion into the XUV. The main laser parameters, provided in two phases, are listed below:

	Pulse energy	Pulse duration	Repetition rate	Average laser power
Phase 1	30 mJ	< 10 fs	1 kHz	30 W
Phase 2	100 mJ	< 5 fs	1 kHz	100 W

In Phase 2, focal lengths of up to 90 m can be considered in combination with a gas medium length of up to 9 m. The estimated gas pressure for such a long gas target lies around $3 \cdot 10^{-2}$ mbar. These values are simply the result of a consistent up-scaling of parameters tested at the intense harmonic beam line in Lund. Even though the loose-focusing beam path can be folded multiple times, a total necessary beam line length exceeding 40 m was estimated. Harmonic and/or attosecond pulse generation happens in a long low-pressure gas medium. The generated harmonics co-propagate with the fundamental beam, being separated and recombined in an interferometric setup based on holey mirrors and anti-reflection coated fused silica plates, which reflect the XUV under grazing incidence but transmit a large part of the incident laser beam. A versatile characterization chamber allows different spectrometers and beam profile cameras to be connected, as well as transmission or redirection of the XUV and/or laser beam to user end-stations. Different beam line sections, such as the focusing unit, generation unit, interferometer, and the characterization/application unit are assembled in a modular way in order to allow for easy switching between different operation modes and for flexible adaption to other laser parameters.

3.4 Average Power Scaling

Scaling repetition rate and pulse energy does not require a scaling of the average XUV power as long as high values are required for only one of the two parameters. However, most experiments where attosecond pulses are used, would benefit from an increased average power. For example for experiments that involve nonlinear effects in the XUV, not only a high pulse energy is needed in order to reach the required intensities but also a higher repetition rate would be beneficial to improve statistics.

Increasing the average power in the XUV is possible by either increasing the driving laser power, in combination with an up-scaling of all relevant macroscopic generation parameters, or, alternatively, by increasing the conversion efficiency into the XUV. Modern short-pulse laser systems have already surpassed the average power of femtosecond Ti:Sapphire systems [169], and in particular, systems based on OPCPA technology promise further scalability [170, 171]. In this thesis, the second option, increasing the HHG conversion efficiency, has been investigated. This option includes two strategies: optimizing the macroscopic generation conditions and enhancing the single atom response. Macroscopic optimization is discussed in detail in section 2.3 while the enhancement of the single atom response through sub-cycle field control is discussed below.

3.4.1 Enhancing the Single Atom Response using Multi-Color Field Synthesis

High-order harmonic generation in gases is usually driven by sinusoidal laser fields. A number of studies investigate the possibility of driving the HHG process with other field shapes, achieved via multi-color field synthesis, in order to enhance the single atom response [172] or to extend the harmonic cut-off [173, 174]. Another approach employs a combination of a laser field and an attosecond pulse train to drive the HHG process [175–177]. Both approaches might be inherently present even in conventional single-field driven HHG schemes, in that secondary fields generated at the beginning of the nonlinear medium might influence the HHG process further downstream [178].

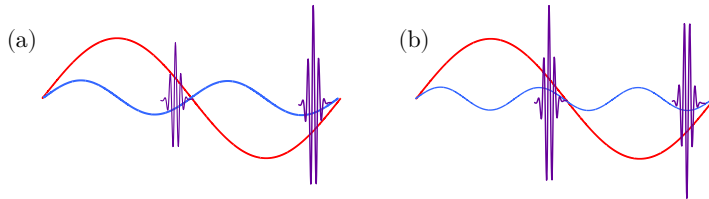


Figure 3.11: Sub-cycle control of the HHG process with a weak harmonic field. The red line indicates the sinusoidal driving laser field. The addition of a second harmonic field (a) leads to changes of relative amplitude and phase of the generated attosecond pulse in both half-cycles, a third harmonic field (b), alters both quantities identically in both half-cycles.

When a harmonic field is added to the sinusoidal laser field, different characteristic effects on the HHG process can be distinguished. This is most easily understood as an interference phenomenon [179]. Both half-cycles of the driving laser field can be seen as separate interferometer “arms” in which the XUV emission process is altered when a harmonic field is added. Figure 3.11 illustrates this concept using the example of the second (a) and the third (b) harmonic field. Generally, a weak harmonic field will change both the amplitude and phase of the generated XUV radiation, leading to spectral signatures, which depend on the relative phase between the fundamental and the harmonic field.

The addition of an odd harmonic field will alter the generation process in both half cycles identically. Consequently, there is no change in the relative phase between the two interferometer arms $\Delta\phi_{\text{CE}}$, i.e. the difference in CEP between consecutive attosecond pulses in the pulse train [118]. Also the amplitude of the generated XUV field changes, for example, because of a modified ionization probability, but does so identically in the two interferometer arms. In contrast, the addition of an even harmonic field leads to changes of $\Delta\phi_{\text{CE}}$. Since the symmetry is broken, even harmonic orders can appear in the generated harmonic spectrum. A change of $\Delta\phi_{\text{CE}}$ from π to 0, can lead to the suppression of odd harmonic orders and the emission of even ones. In addition, amplitude changes are different in the two interferometer arms, and enhancing the dipole amplitude in one arm leads to a reduced emission in the other. Interestingly, the control mechanisms provided by adding an harmonic field to the driving laser field, have many similarities with the subcycle control brought about through CEP tuning, discussed in section 2.2.3.

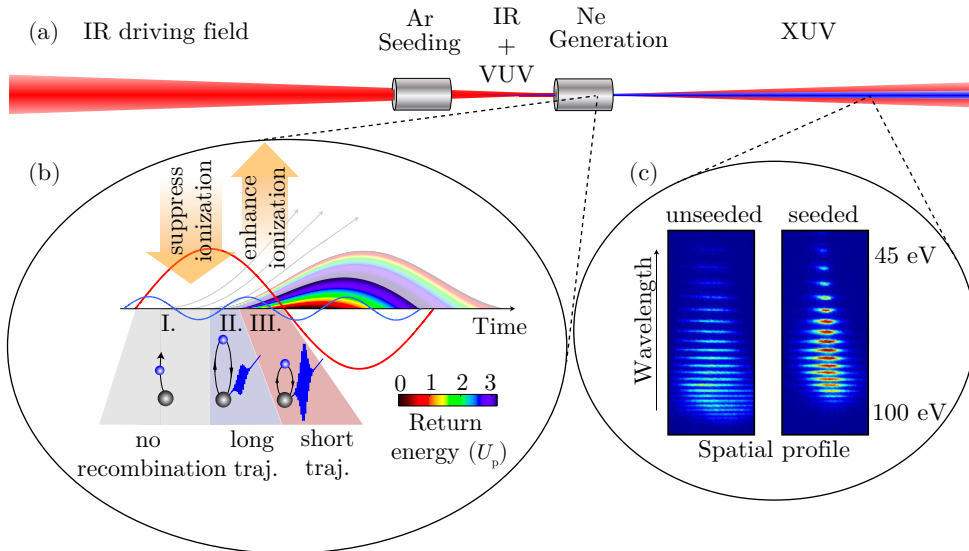


Figure 3.12: Enhanced HHG in a dual gas cell geometry: (a) experimental scheme, (b) quasi-classical picture for HHG in a multi-color field (fundamental and third harmonic) and (c), spatially resolved harmonic spectrum generated in neon without (unseeded) and with (seeded) argon gas present in the seeding cell. Adapted from Paper IX.

A detailed analysis of the phase effects induced by adding a second harmonic field can be found in Paper X. In Paper IX, amplitude effects induced by the addition of odd harmonic orders, which can lead to enhanced XUV emission, are investigated.

In this thesis, the addition of odd harmonics has been analyzed, both using an interferometric setup, and with a dual gas cell generation geometry. An in-line generation geometry based on two separate generation cells has the advantage of ensuring an automatic alignment and phase stability between the different driving fields. The method is illustrated in Figure 3.12. In (a), the experimental scheme is illustrated. The laser beam is focused ($f = 2$ m) into a pulsed neon gas cell (the *generation cell*), placed close to the focus of the driving laser beam. A second gas cell (the *seeding cell*), filled with argon, is placed a few centimeter before it. Under certain conditions, the high harmonic signal generated in the neon cell was enhanced up to an order of magnitude when high-pressure argon gas was supplied to the seeding cell. Detailed studies of the emitted harmonic signal as a function of the generation pressure, gas cell position and field intensity allowed us to identify the relevant mechanism explaining the observed phenomenon, as discussed in detail in Paper IX.

An illustration of the underlying mechanism is shown in Figure 3.12 (b). The electron trajectories obtained in a sinusoidal field are shown, the color scale indicates the return energy. As discussed in section 2.2.1, three different trajectory classes can be identified, as indicated by the different tunnel ionization intervals I, II and III. For efficient HHG, the short trajectory (interval III) is the most important candidate because its phase is only weakly intensity-dependent. Short trajectory electrons are, however, released into the continuum via tunnel-ionization close to the zero-crossing

of the driving laser field while electrons born close to the field maximum contribute to long trajectory emission or do not recombine at all. This leads to a reduced ionization probability for short trajectory electrons compared to electrons ionized around $t \approx T/4$. By adding a third harmonic field, or more generally, by adding an odd harmonic to the fundamental driving field, the field can be enhanced for ionization times leading to short trajectory emission while the ionization probability around $t \approx T/4$ is reduced. Due to the nonlinearity of the tunnel-ionization process, this effect can be observed even at low field strengths where the electron trajectories are only weakly altered by the added harmonic field. Controlling the HHG process with odd harmonic fields ensures the suppression of destructive interference effects between consecutive half-cycles and allows for amplitude enhancement in all contributing half-cycles. A requirement for this effect is the right phase $\Delta\varphi$ between the fundamental and the added third harmonic field. The third harmonic field is mentioned here since its amplitude dominates all higher order harmonic fields generated in the seeding cell. In the experiment, $\Delta\varphi$ can simply be controlled via the the gas pressure in the seeding cell, leading to reduced ($\Delta\varphi \approx 1 \pm \pi$) or enhanced ($\Delta\varphi \approx 1$) HHG emission from the generation cell. In conditions, where an efficient enhancement could be observed, the gas pressure in the seeding cell exceeded the optimum pressure for HHG significantly, i.e. no high-order harmonic signal from the seeding cell was detectable and the influence of high-harmonics to the enhancement process could thus be excluded. This result also shines new light on previous experiments [175–177] where enhanced high-harmonic emission was attributed to a modified HHG process in which tunnel ionization is replaced by single photon ionization by high-order harmonics.

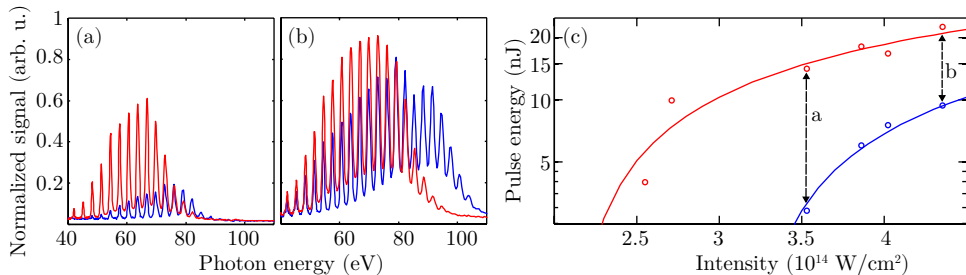


Figure 3.13: Seeded (red) and unseeded (blue) HHG spectra generated at a peak intensity of $3.5 \cdot 10^{14} \text{ W/cm}^2$ (a) and $5 \cdot 10^{14} \text{ W/cm}^2$ (b), respectively. In (c), the pulse energy of the 41st harmonic (circles) is plotted as a function of the intensity for both cases, together with fitted regression lines. Adapted from Paper IX.

The mechanism described above explains how the single atom emission can be enhanced by driving field shaping. As in other enhancement schemes, a key question is, whether the enhancement method is advantageous over “single color” HHG schemes, considering in both cases optimized generation conditions. For such a comparison, optimized seeded HHG should be compared to optimized unseeded HHG using the same laser pulse energy. Due to the experimental difficulties arising for such a direct comparison, seeded HHG was compared to optimized unseeded HHG for a number of different driving field intensities. Figure 3.13(a) and (b) show typical seeded and unseeded HHG spectra generated at peak intensities of $3.5 \cdot 10^{14} \text{ W/cm}^2$ and

$5 \cdot 10^{14} \text{ W/cm}^2$ respectively. The enhancement factor is clearly intensity dependent, as also shown in (c), where the pulse energy of the 41st harmonic is plotted as a function of intensity for both seeded and unseeded generation. While larger enhancement factors can be observed at low intensities, only a factor of two remains at $5 \cdot 10^{14} \text{ W/cm}^2$. Considering, however, that efficient seeded HHG is possible already at much lower intensities, we can expect that a larger total enhancement is possible if seeded HHG is optimized, e.g. by generating at even more loose focusing conditions.

NONCOLLINEAR HIGH-ORDER HARMONIC GENERATION

High-order harmonics are commonly generated using a single, broadband laser field, focused into a gas [180] or onto a solid target [181] such that the emitted XUV radiation copropagates with the driving field in a collinear manner. Unlike in many low-order frequency mixing processes, where noncollinear generation geometries are typically used to compensate for group delay mismatches [182], noncollinear schemes have not often been applied for HHG. Only in recent years, have noncollinear geometries started to find applications in extreme nonlinear optics. After an initial theoretical investigation by Birulin and co-workers [183], a few studies involving noncollinear generation have been reported [125, 184–189], analyzing the basic aspects of high-order wave mixing processes [188], as well as discussing in detail its use for intra-cavity XUV out-coupling [185–187], for probing of plasma dynamics [189], and for in-situ diagnostics of the generated XUV [125] and the probing laser field [190].

This chapter describes high-order harmonic and attosecond pulse generation in a noncollinear geometry, and provides a common context for the work in this thesis, and previous work on noncollinear HHG (NCHHG). New control and diagnostic schemes are introduced, based on NCHHG, as discussed in detail in Papers [XII](#), [XIII](#), and [XIV](#). The work on NCHHG presented here includes the development of a new gating technique which has great potential for IAP generation at the extremes of the two scaling directions discussed in this thesis.

After a general introduction in which the principles of high order noncollinear wave-mixing processes are outlined, the macroscopic aspects of NCHHG are discussed. The use of NCHHG methods for measuring and controlling phase matching, and for extracting information about the nonlinear dipole response of the generation medium, is then described. The second part of this chapter outlines the new gating method for IAPs: noncollinear optical gating (NOG), which is described in detail in Papers [XIII](#) and [XIV](#). Besides a general introduction to NOG, the relation to other attosecond gating schemes is discussed and an outlook is given for the application of this new gating technique for the generation of IAPs at high repetition rates or high pulse energies. The chapter closes with a short overview of the experimental implementation of NCHHG schemes.

4.1 Introduction to High-Order Noncollinear Wave-Mixing

NCHHG can be seen as an extension of the conventional HHG scheme, where laser pulses are focused into a gas target and harmonics of the driving laser frequency are emitted collinearly with the generating laser pulse, as illustrated in Figure 4.1. For NCHHG, two laser pulses are focused and overlapped in the nonlinear medium. The noncollinear angle opens a new degree of freedom, the spatial domain, which allows new control and characterization schemes, especially in combination with spatial mapping (see Paper XII) or spatio-temporal coupling (see Ref. [116] and Paper XIII). As discussed in more detail below, a noncollinear geometry can allow XUV emission over a broad angular range, exceeding the angle sector defined by the two driving field propagation angles. This is especially interesting for background-free generation and measurement schemes, since the emitted XUV radiation can directly be separated from the driving field by simple spatial filtering. Further, it easily accommodates wave-mixing using different driving central frequencies. NCHHG schemes with both single and dual color driving laser fields are discussed below.

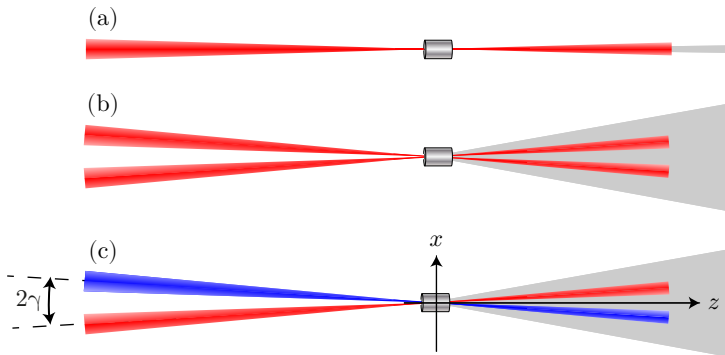


Figure 4.1: HHG schemes based on collinear (a) and noncollinear (b,c) generation, driven by single (a,b) or dual (b,c) color laser fields. In (a), the generated XUV radiation is emitted collinearly with the driving laser beam. In (b) and (c), the approximate angle sector where XUV emission can occur is indicated by the gray shaded background.

4.1.1 Different Regimes of NCHHG

NCHHG is a highly nonlinear process, which beautifully illustrates fundamental properties of light: its wave-like and particle-like characteristics. Both pictures can be used to explain the basic aspects of NCHHG, and can help to complement the understanding of the underlying physical processes. As in Paper XII, both pictures will be used in the following.

NCHHG seen as a wave-mixing process

In what follows, the geometry and coordinate system shown in Figure 4.1 (c) is used. In the wave picture, the two laser fields interfere where they intersect, leading to a

total field with modulated amplitude and phase across the laser beam profile. Figure 4.2 illustrates the intensity distribution $I(x)$ of two interfering beams of equal intensity and frequency, plotted across the beam profile for four different modulation periods. Below, the special case of mixing two fields with identical (central) frequencies is considered, followed by an extension to the more general case $\omega_1 \neq \omega_2$. For small noncollinear angles γ , with 2γ denoting the angle between the two driving field propagation directions (denoted, however, as γ in Paper XII), $I(x)$ can be written as:

$$I(x) \propto \cos^2 [kx \sin(\gamma) + \phi_x] \exp\left(-\frac{2x^2}{W_0^2}\right). \quad (4.1)$$

Here W_0 is the beam radius and ϕ_x denotes the relative phase of the two incident laser fields $E_{1,2}$ at the point of intersection. For $\phi_x = 0$ we obtain a symmetric intensity distribution with a central intensity maximum at the point of intersection ($x = 0$).

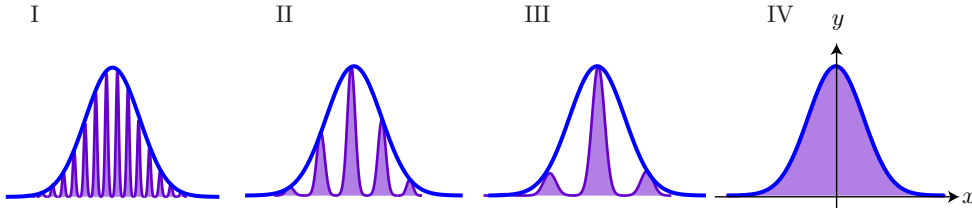


Figure 4.2: Schematic intensity distribution of two interfering driving fields. Different noncollinear angles mark different regimes for high-order noncollinear wave-mixing: (I) Many interference fringes such that there is only little intensity difference between adjacent fringes, (II) a few fringes only, significant intensity variation from fringe to fringe, (III) only a single dominating fringe is present and (IV), no spatial modulation (collinear generation).

The two interfering driving fields causes the formation of multiple harmonic sources along x , and the amplitude and phase of the dipole oscillating at a given harmonic frequency will be modulated. The resulting far-field XUV emission will therefore be a multi-source interference pattern and multiple harmonic beams can typically be expected, emitted at different angles. Depending on the number of contributing sources, different wave-mixing regimes may be identified. The number of driving field interference maxima, that is, the number of harmonic sources, depends on the transversal k-vector, $k_x = k \sin(\gamma)$, and thus increases with increasing noncollinear angle.

In order to understand the characteristics of the different wave-mixing regimes, we have to consider both amplitude and phase modulations of the generated XUV radiation along x . As introduced in section 2.2.3, the harmonic dipole phase depends on the driving field intensity and so different harmonic sources will emit XUV radiation with different phases. In particular, a variation of ϕ_x results in a movement of the harmonic source grating along x and thus produces a variation in the corresponding emission phases. Regime I is characterized by many sources, such that the intensity difference and consequently, the dipole phase difference between adjacent sources is small. Changing ϕ_x by π will simply move the driving field interference pattern by π/k_x , i.e. by one fringe. The phase of the emitted XUV radiation does not change significantly, thus the far-field XUV emission pattern does not change (disregarding

a constant phase offset across the far-field profile). In Regime II, only a few sources are present and so a change of ϕ_x results in a changing intensity difference between adjacent sources. In consequence, the harmonic dipole phase exerts a strong influence, and the far-field XUV pattern changes with ϕ_x . As introduced in Section 4.2 and described in detail in Paper XII, the ϕ_x -dependency of the XUV emission maps the dipole phase variations of the harmonic source into the far-field, thus allowing direct access to the dipole phase. Regime III is a special case of Regime II. Now, for $\phi_x = 0$, only a single contributing XUV source remains, k_x being sufficiently large to limit the intensity of the spatial satellite sources (the first intensity maxima at $x \neq 0$) so that they do not make any significant contribution to the XUV emission. As discussed in more detail below, Regime III is particularly interesting since it allows noncollinear harmonic emission without interference effects caused by multiple sources. Note that for $\phi_x = \pi/2$, two sources are formed even in Regime III, although the XUV flux is strongly reduced compared to when $\phi_x = 0$. Regime IV is the common collinear generation regime, with two laser fields superimposed and collinearly focused into the generation medium. It is thus strictly speaking not a NCHHG scheme, but is included here as a limiting case for the sake of completeness.

Generally-applicable boundaries for the regimes introduced above are not defined here, since they depend on a number of parameters, such as the laser intensity, the harmonic order, and the electron trajectory under consideration. Experimentally, the different regimes can easily be identified by measuring the far-field emission as a function of ϕ_x with spectral and spatial resolution. For determining the relevant regime, it is not only essential to consider the noncollinear angle, but more generally, the number of periods across the beam profile, which depends on both γ as well as on the focal spot radius W_0 . For example, reducing the noncollinear angle by a given factor while increasing the f-number of the focused beams in proportion, results in an identical source field, and consequently in identical far-field characteristics. Only the overall angular distribution changes: reducing γ and increasing W_0 decreases the angular divergence of the emitted radiation, but not its angularly normalized

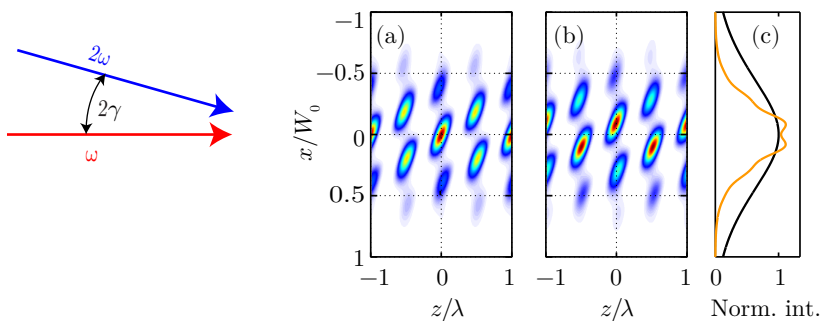


Figure 4.3: $\omega/2\omega$ source field interference. $\Re(E)^6$ of two noncollinearly interfering laser beams for a relative phase 0 (a) and π (b) at the point of intersection. The relative intensity of the two fields is $I_{2\omega}/I_\omega = 0.3$. In (c), the time integrated signal of (b) is plotted. The integrated intensity $I(x) = \sum_z \Re[E(x)]^2$ (black) does not show any spatial modulations while higher nonlinear signal modulations, e.g. $\sum_z \Re[E(x)]^6$ (orange), do persist after time integration.

distribution. For a definition of the different regimes, it is therefore convenient not to use the noncollinear angle as the relevant parameter, but instead to use the beam separation before focusing, δ , defined in units of the beam diameter (at $1/e^2$ of the intensity profile).

The wave picture introduced above is most intuitive for two driving fields with identical frequencies, but it can also be applied to fields with different frequencies, for example, for $\omega/2\omega$ -driven HHG. In this case, the interference pattern of the driving fields depends on time, and the time-integrated intensity distribution along x does not show any modulations. A high order nonlinear response, however, persists after time integration, as illustrated in Figure 4.3. Thus the time integrated high-harmonic dipole response also exhibits an amplitude modulation, and consequently, the multisource interference picture can still be applied. The harmonic source modulations in the ω/ω and the $\omega/2\omega$ -case have different modulation periods and as a result, different far-field interference patterns can be observed. The latter phenomenon can be understood more easily using the photon picture of NCHHG, introduced below.

The photon picture of NCHHG

High-order wave-mixing can also be described in terms of the photon nature of light – by adding frequencies and k-vectors. The up-conversion of two laser driving frequencies ω_1 and ω_2 leads to the emission of harmonic frequencies

$$\omega_1, \omega_2 \quad \rightarrow \quad \omega_q = m_1\omega_1 + m_2\omega_2, \quad (4.2)$$

where m_1 and m_2 are integers and with $q = m_1 + m_2$ for $\omega_1 = \omega_2$. The emission angles of the emitted harmonics can be deduced through k-vector addition:

$$\mathbf{k}_1, \mathbf{k}_2 \quad \rightarrow \quad \mathbf{k}_q = m_1\mathbf{k}_1 + m_2\mathbf{k}_2, \quad (4.3)$$

For sufficiently large γ , each harmonic order is spatially separated into several beamlets [188]. Note that, strictly speaking, equation (4.3) describes the ideal case of phase-matched generation. Phase matching effects in NCHHG and the more general case of non phase-matched NCHHG are discussed in detail in section 4.2.2.

Depending on the number of involved photons from the two different driving fields, different emission directions are defined, as is illustrated in Figure 4.4 for the case of an $\omega/2\omega$ -driving field. In general, m_1 and m_2 can be positive or negative, accounting for sum- and difference-frequency generation (SFG and DFG). Harmonics generated via SFG are emitted inside the sector defined by the two driving field propagation directions (shaded area in Figure 4.4). Generation processes involving DFG lead to the emission outside this sector.

Due to parity conservation, only an odd number of driving photons can be up-converted into a high-order harmonic photon: $m = m_1 + m_2$ has to be odd [188]. This restricts the possible driving photon combinations, especially in the case of $\omega/2\omega$ -driving fields, and leads to a four times larger angular separation of the emitted adjacent harmonic beamlets for $\omega_2 = 2\omega_1$ compared to the case when $\omega_1 = \omega_2$.

The different noncollinear angle regimes introduced using the wave picture, can also be described in the photon picture. In Regime I, all beamlets of a given harmonic order, q , are spatially separated in the far-field and do not interfere. Consequently, a variation of ϕ_x does not change the beamlet pattern in the far-field. In contrast, in Regime IV

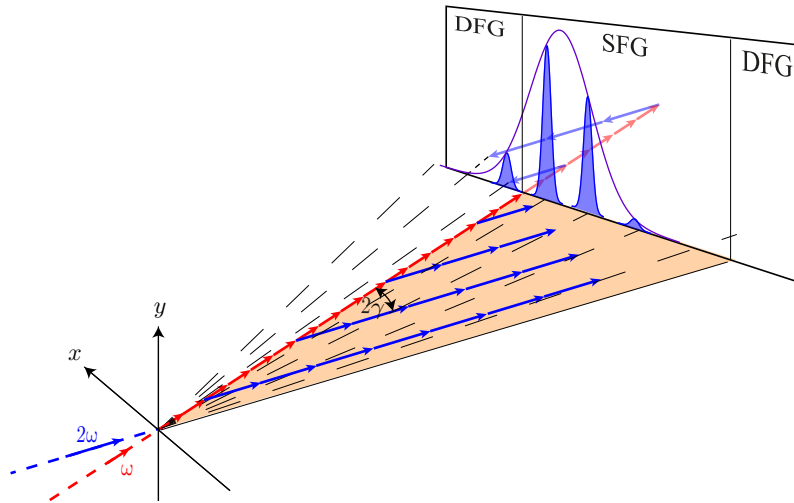


Figure 4.4: The photon picture of NCHHG: adding k-vectors of the fundamental driving fields leads to a number of different emission directions, here illustrated for the case of an $\omega/2\omega$ driving field and Regime I. The shaded area marks the angle sector where SFG emission can occur.

all beamlets overlap completely and interfere, as is typically the case in collinear $\omega/2\omega$ -HHG. Interference effects in this regime are discussed in detail in Paper X. Regimes II and III mark the transition from full angular separation to full spatial overlap. In Regime II, adjacent beamlets are partly overlapping and interference effects occur. In Regime III, more than just the adjacent beamlets can interfere, leading to the generation of a single XUV beam on the bisector angle for $\phi_x = 0$ and to complicated interferences and multiple XUV beams for $\phi_x = \pi$.

All three NCHHG regimes allow the direct noncollinear separation of generated XUV radiation from the fundamental driving fields. In Regime III the fundamental fields begin to be spatially separated in the far-field but the multisource interferences present in regimes I and II are suppressed (for $\pi = 0$), as is discussed in more detail in Paper XIII. Figure 4.5 illustrates NCHHG for regimes I and III. According to equation (4.3), and in agreement with the multisource interference model introduced above, the XUV beamlet distribution in regimes I and II is dependent on the harmonic order, and in general, XUV beams with different energies are not emitted at the same angle. This is clearly visible in Figure 4.5(c), which shows a simulated harmonic NCHHG spectrum for Regime I. For low harmonic orders in particular, the variation of angle with energy can allow for energy selection simply by spatial filtering. However, for a broader spectral range covering several harmonic orders, the energy-dependent angular distribution leads to spatially distorted APTs. In contrast, in Regime III, all harmonics are emitted collinearly at the bisector angle (for $\phi_x = 0$), as illustrated in Figure 4.5(d)–(f). Regime III is therefore particularly interesting for attosecond pulse generation, as is discussed in section 4.3 as well as in Papers XIII and XIV.

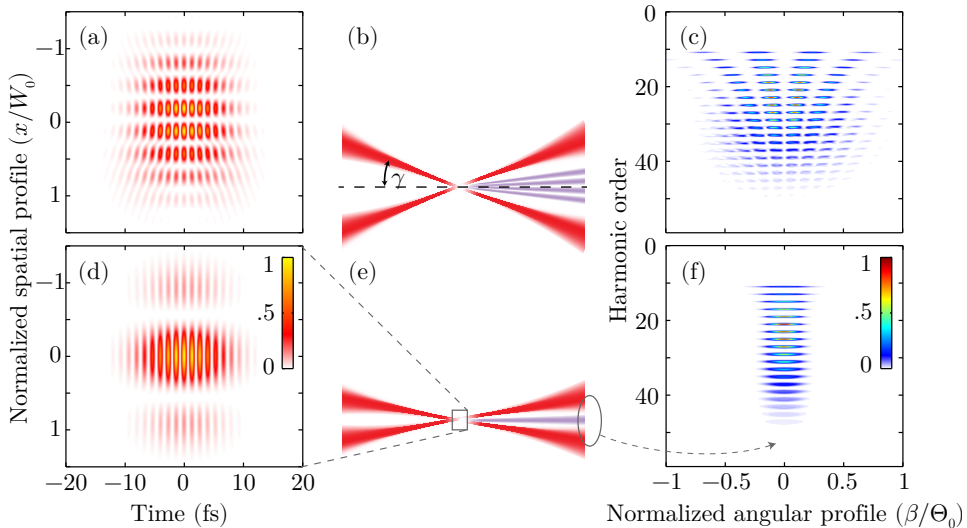


Figure 4.5: NCHHG illustrated for Regime I (first row) and Regime III (second row). The spatio-temporal fundamental field distribution at the focus, $[\Re(E)^2]$, is plotted in (a) and (d), while (c) and (f) show the corresponding spatially-resolved HHG spectrum, taking only short trajectories into account, and with a photon energy range having $q \geq 11$. The simulation was performed using the quasi-classical model introduced in section 2.5. The chosen parameters are: $\tau = 10$ fs, $\lambda = 800$ nm, with $\phi_x = \pi$, $\delta = 5$ for the first row and $\phi_x = 0$, $\delta = 1.4$ for the second row.

Applications of the different NCHHG angle regimes

NCHHG has been used or proposed for some applications, both within this thesis work (Papers XII and XIII), as well as in a few studies reported earlier [125, 184–189]. While the classification of the different angle regimes was developed as part of this thesis, previous implementations had already exploited different aspects of the regimes and their corresponding characteristics. A short overview of the applications is given below.

Both the pioneering work of Birulin *et. al.* [183] and more recent investigations by Bertrand and co-workers [188] focusing on the nonlinearities of high-order wave-mixing, consider rather large noncollinear angles, and are therefore concerned with Regime I. As pointed out in Ref. [188], NCHHG can provide the functionality of an all-optical beam splitter, delivering multiple, perfectly synchronized XUV pulses. In Regime I, the XUV beamlets are fully separated in angle, as is typically required for beam splitting purposes. The same angle regime is used by Ozawa and co-workers [187] in their experimental tests of NCHHG as an out-coupling method for intra-cavity HHG. For the same application, Wu and co-workers [186] consider regimes I and III, and in their numerical analysis they identify angularly distorted spatial profiles caused by multisource interferences in Regime III, as well as energy-independent emission at the bisector angle in Regime I.

Regime II is analyzed in detail in Paper XII. Here, the characteristic property

of Regime II, namely the dependency of the far-field emission on ϕ_x , is used in two different ways: (i) in order to access the dipole phase and to trace its variation with intensity and harmonic order; and (ii), as a probe for phase matching effects, as discussed in Paper [XII](#).

Regime III combines the unique property of NCHHG – the possibility for off-axis XUV generation – with the spatio-temporal characteristics of collinear generation schemes [[186](#)]. Recently, Kim and co-workers introduced a novel in-situ characterization method for both IAPs [[125](#)] and a probing laser field which employs Regime III [[190](#)]. Their method is based on SAP generation with a fundamental field and a non-collinearly superimposed, weak second harmonic probing field. The second harmonic field slightly modifies the phase of the generated XUV radiation across the beam profile in the source volume, resulting in a spatial shift of the emitted XUV beam. The analysis of this spatial deviation as a function of the delay between the generating and the probing field, allows the reconstruction of both the IAP and the probing field. The effect of a weak second and, more generally, the influence of the relative intensity of the two driving fields on the NCHHG process, is discussed Section [4.1.2](#). A second important application of Regime III, developed within this thesis work and discussed in section [4.3.1](#) as well as in Papers [XIII](#) and [XIV](#), is the gating of IAPs.

Finally, Regime IV simply constitutes collinear HHG with multiple driving fields, as is discussed in detail, for example, in Refs. [[118](#), [172](#), [174](#), [191](#)] as well as in Papers [X](#) and [IX](#). The addition of a second or multiple driving fields, usually at harmonic frequencies, leads to a cycle or halfcycle periodic modification of both the XUV amplitude and phase, as is discussed in Section [3.4.1](#).

4.1.2 Controlling NCHHG with Driving Field Intensities

Besides the noncollinear angle, the relative amplitude of the two driving laser fields is a very important control parameter for NCHHG. Its influence can be well described in both the particle (photon) and the wave picture. In the photon picture, the relative field amplitude determines the probability of involving photons from each of the two driving fields in the frequency conversion process. For equal driving field strengths and, again, for $\omega_1 = \omega_2$, the process with $m_1 = m_2 \pm 1$ is the most likely (note that $m_1 = m_2$ is forbidden due to parity conservation). Thus, noncollinear emission close to the bisector angle dominates, and the XUV flux decreases towards emission angles corresponding to beamlet indices with $m_1 \gg m_2$ (or vice versa), as is clearly visible in Figure [4.5](#) (c). Changing the relative field amplitude, changes the probability for involving photons from one or the other driving fields and so the center of mass of the far-field beamlet distributions, but does not change the beamlet position.

The process can be described more quantitatively within the wave picture. The important parameter controlled by the relative field amplitude is the orientation of the wavefronts of the combined field.

Considering two fields with envelopes $\mathcal{E}_{1,2}$ and wavevectors $\mathbf{k}_{1,2}$, the wavefront orientation can be defined through the composite wavevector at the point of intersection:

$$\mathbf{k}_{\text{tot}} = \frac{(\mathcal{E}_1 \mathbf{k}_1 + \mathcal{E}_2 \mathbf{k}_2)}{\sqrt{\mathcal{E}_1^2 + \mathcal{E}_2^2}}. \quad (4.4)$$

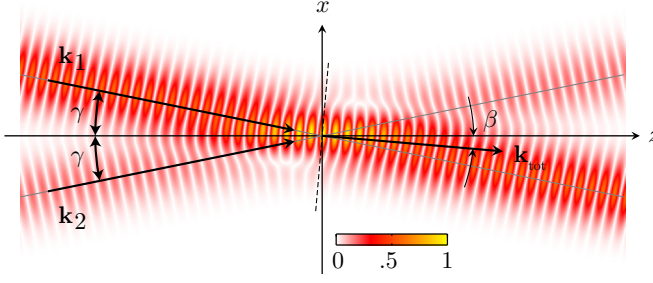


Figure 4.6: Noncollinear field superposition $[\Re(E)^2]$. The orientation of the wavefronts at the point of intersection of two noncollinearly overlapping fields depends on the relative field strength.

With the arrangement as in Fig. 4.6, equation (4.4) can be written as

$$\mathbf{k}_{\text{tot}} = \frac{(-\mathcal{E}_1 + \mathcal{E}_2) \sin(\gamma) \hat{\mathbf{x}} + (\mathcal{E}_1 + \mathcal{E}_2) \cos(\gamma) \hat{\mathbf{z}}}{\sqrt{\mathcal{E}_1^2 + \mathcal{E}_2^2}}. \quad (4.5)$$

By taking the scalar product between the unit vector in the transverse direction $\hat{\mathbf{x}}$ (see Figure 4.6) and \mathbf{k}_{tot} , we can define the angle β as the direction of \mathbf{k}_{tot} relative to the z -axis:

$$\sin(\beta) = -\hat{\mathbf{x}} \cdot \frac{\mathbf{k}_{\text{tot}}}{|\mathbf{k}_{\text{tot}}|} = \frac{(\mathcal{E}_1 - \mathcal{E}_2) \sin(\gamma)}{\sqrt{\mathcal{E}_1^2 - 4\mathcal{E}_1\mathcal{E}_2 \sin^2(\gamma) + 2\mathcal{E}_1\mathcal{E}_2 + \mathcal{E}_2^2}}. \quad (4.6)$$

For small γ , we obtain:

$$\beta = \gamma \frac{1 - \xi}{1 + \xi}. \quad (4.7)$$

Changing the amplitude ratio of the laser fields, $\xi = \mathcal{E}_2/\mathcal{E}_1$, causes a macroscopic tilt of the wavefronts and a change in the corresponding emission direction, β , thus shifting the center of mass of the beamlet distribution. Note that this applies for all three noncollinear angle regimes. The influence of the wavefront orientation on the beamlet distribution is directly analogous to the influence of the blazing angle of a diffraction grating. While the diffraction efficiency is defined by the blazing or wavefront orientation angle, the diffraction pattern is defined by the grating periodicity.

In order to obtain XUV emission via DFG outside the angle sector defined by the fundamental beams, an intense driving field has to be employed, in combination with a weak noncollinear field. In this case, the wavefront orientation of the intense field dominates and XUV emission can be expected mostly around the propagation direction of the intense driving field. In this case, both SFG and DFG may be observed. Due to the nonlinear scaling of the wave-mixing process [188], higher-order DFG processes become increasingly unlikely as the number of involved driving photons increases. Nevertheless it is possible that DFG processes dominate over SFG processes, as outlined below, and presented in more detail in Paper XII.

4.2 Macroscopic Phase Effects in NCHHG

Noncollinear wave-mixing requires a nonlinear medium with a macroscopic size in the transverse (x) direction. In fact, all of the wave-mixing concepts introduced above, including generation and control of XUV emission at certain angles, can be described by considering the collective dipole response of single atom emitters along x , driven by two noncollinear overlapping fields, i.e. by transverse macroscopic effects, as introduced in section 4.2.1 The efficiency of the process, on the other hand, is determined to a large extent by propagation effects, and therefore by the angles between the wavevectors of the driving fields $\mathbf{k}_{1,2}$ and the generated XUV field \mathbf{k}_q . Both kinds of macroscopic effects, introduced in section 2.3 are discussed below, for the special case of NCHHG.

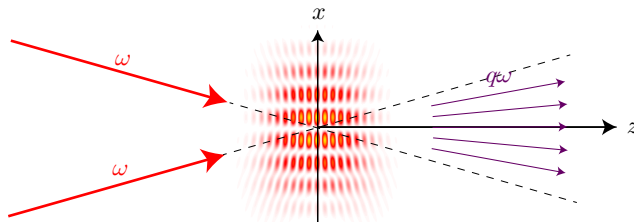


Figure 4.7: Transverse (along x) and longitudinal (along z) phase effects. Noncollinear wave-mixing can be described by the collective response of all single atom emitters along x while propagation effects along z determine the efficiency of the conversion process.

4.2.1 Transverse Macroscopic Effects

Transverse macroscopic effects include phase and amplitude effects in NCHHG, taking into account the spatio-temporal harmonic dipole response for a zero length medium, i.e. harmonic generation driven by a total driving field $E(x, t) = E_1(x, t) + E_2(x, t)$. Propagation effects are explicitly not included. Transverse macroscopic effects and their influence on the spatial far-field distribution can be understood with the help of an analogy in the time-domain, and its corresponding effects in the spectral domain. While the temporal response in a HHG medium defines the spectral phase and amplitude, the spatial response along x defines the spatial distribution in the far-field. This fundamental principle of wave propagation illustrates a fascinating analogy between CEP effects in attosecond pulse generation and spatial phase effects in NCHHG.

In Figure 4.8 (a), the total driving field $\Re(E)^2$ is plotted for a 1.5-cycle pulse and a beam separation before focusing of $\delta = 3$, defined in units of the beam diameter. In (b), the corresponding spatially resolved XUV spectrum is shown, calculated using the quasi-classical approach described in section 2.5. For both figure panels, corresponding side panels show temporal and spectral line-outs of driving field distribution and XUV spectra, respectively. The temporal line-outs represent the electrical driving field $\Re[E(t, x = 0)]^2$ corresponding to the generated XUV field $E_{\text{xuv}}(t, x = 0)$ along the

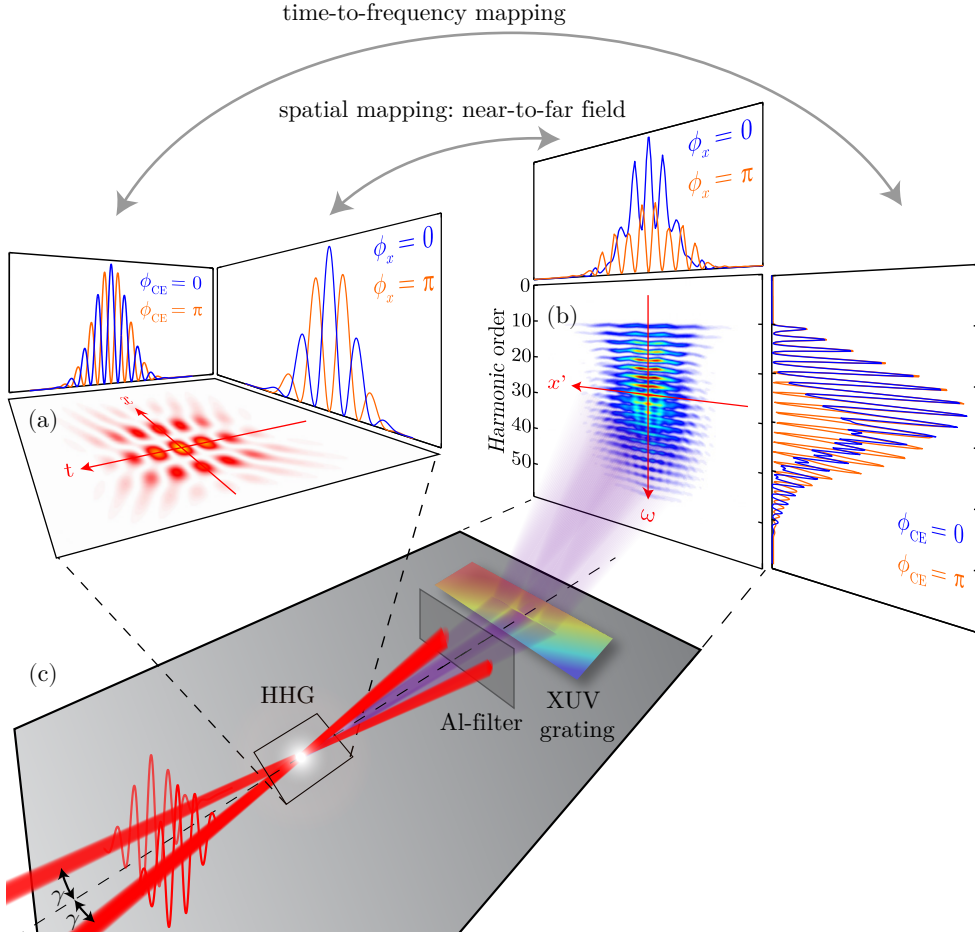


Figure 4.8: Illustration of NCHHG and the analogy between spatial and temporal phase effects. In (a), $\Re(E)^2$ is shown as a function of x and t ; (b) displays the corresponding XUV spectrum. (a) and (b) contain side panels with corresponding temporal, spectral and spatial lineouts for three cases: (i), blue solid lines, $\phi_x = 0$ and $\phi_{CE} = 0$ (these parameters are also used for the 2D-plots); (ii), orange solid line in temporal and spectral plots, $\phi_x = 0$ and $\phi_{CE} = \pi$ and (iii), orange solid line in the spatial plots, $\phi_x = \pi$ and $\phi_{CE} = 0$. The lineout location is marked with red lines in the corresponding 2D-plot. (c) A schematic of the experimental scheme.

bisector angle and the corresponding XUV spectrum $|\tilde{E}_{\text{xuv}}(\omega, \beta = 0)|^2$ in the far-field. The spatial line-outs show the transversal electrical driving field $\Re[E(t = 0, x)]^2$ at $t = 0$ and a corresponding Fraunhofer diffraction pattern for the 27th harmonic $|\tilde{E}_{\text{xuv}}(\omega = 27\omega_0, \beta)|^2$ in the far-field. These quantities are directly related via Fourier transformations. For simplicity reasons, the second spatial dimension is omitted below.

The spectral representation of the source field is given by the Fourier transformation:

$$\tilde{E}_{\text{xuv}}(\omega, x) = \mathcal{F}_t[E_{\text{xuv}}(t, x)] = \int_{-\infty}^{\infty} E_{\text{xuv}}(t, x)e^{-i\omega t} dt, \quad (4.8)$$

while the spatial distribution in the far-field can be calculated via the Fraunhofer diffraction integral:

$$\check{E}_{\text{xuv}}(\omega, \beta) \propto \mathcal{F}_x[\tilde{E}_{\text{xuv}}(\omega, x)] = \int_{-\infty}^{\infty} \tilde{E}_{\text{xuv}}(\omega, x)e^{-iKx} dx, \quad (4.9)$$

where $K = \frac{\omega}{c}\beta$ is a function of the far-field angle $\beta = x'/z$.

Equation (4.8) and (4.9) illustrate the analogy between time-to-frequency and spatial near-to-far-field mapping. In both cases, a complex driving field with carrier frequency ω and spatial carrier frequency K as well as a corresponding envelopes, \mathcal{E}_t and \mathcal{E}_x , respectively, causes a dipole response at a given harmonic frequency. For few cycle pulses, the temporal dipole response is strongly dependent on ϕ_{CE} while the spatial dipole response is determined by ϕ_x . The spatial analog to the pulse duration is the width of \mathcal{E}_x , which is determined by the focusing conditions. The generation of an attosecond pulse train has its spatial analogue in the formation of multiple XUV sources along x . In general, all the quantities present in the time-to-frequency mapping scheme defined via equation (4.8) can be related to corresponding quantities in the spatial mapping scheme. Note that in this analogy, a fixed frequency, i.e. a given harmonic order, is assumed. The corresponding quantities of both mapping schemes are listed below, considering proportionalities only – constant factors are not listed:

Time-to-frequency mapping	t	ω	ϕ_{CE}	τ	λ
Spatial mapping	x	β	ϕ_x	W_0	λ/γ

Particularly important for both temporal and spatial mapping are intensity-dependent phase terms such as the harmonic dipole phase, as they exhibit similar variations in both the temporal and spatial domains. Analogously to temporal phase variations, any phase variations along x , define spatial frequencies that are mapped out into the far-field angle. A constant phase along x , for example, leads to a collimated beam around $\beta = 0$, corresponding to a zero spatial frequency. A strong spatial phase variation across the harmonic source causes an increased divergence, and higher spatial frequencies appear. Also, multisource formations in the spatial and temporal domains cause interferences effects in the spatial and spectral far-field distribution [140], as discussed in more detail in section 2.4.1, as well as in Paper I.

Using the above analogy, spatial interferences occurring in NCHHG can be seen as being analogous to temporal interference effects. In the temporal domain, dipole phase effects are well known from HHG with few-cycle pulses where spectral shifts in the harmonic spectrum are observed as a function of ϕ_{CE} . These effects are discussed in section 2.2.3 and analyzed in Paper III. Spatial shifts of the far-field XUV beamlets as a function of ϕ_x follow the same principles as spectral shift with ϕ_{CE} , as discussed in Paper XII. In both cases, a variation of the phase of the XUV radiation emitted from

adjacent sources (temporally or spatially) causes a shift of the corresponding XUV distribution (spectrally or spatially). In the spectral domain, CEP-dependent spectral shifts can be observed for few-cycle driving laser pulses. In the spatial domain, spatial shifts that depend on ϕ_x can be observed in conditions where only a few harmonic sources are formed along x (Regime II). Figure 4.8 illustrates the case of a few cycle pulse in the temporal and spatial domains. Spectral (spatial) shifts are clearly visible when ϕ_{CE} (ϕ_x) is changed from 0 to π .

4.2.2 Propagation Effects

While the emission angles in NCHHG are determined by transverse macroscopic effects, phase matching effects determine the coherent buildup of the generated field at these angles. As in conventional collinear HHG schemes, phase matching has to be taken into account as soon as the nonlinear medium has a non-zero length in the direction of emission. As introduced in section 2.3.1, phase matching can be described by k-vector addition. For an efficient signal buildup, the sum of all contributing fundamental k-vectors has to be equal to the generated harmonic k-vector. Non phase-matched generation is characterized by the presence of a wavevector mismatch $\Delta\mathbf{k}$. As in collinear generation schemes, $\Delta\mathbf{k}$ typically includes four components, some of which are of different signs. For NCHHG, a geometrical offset due to the different propagation direction of the driving and generating fields has to be included:

$$\Delta\mathbf{k} = \Delta\mathbf{k}_{\parallel} + \Delta\mathbf{k}_{<}. \quad (4.10)$$

Here, $\Delta\mathbf{k}_{\parallel}$ denotes the wavevector mismatch present for collinear generation, defined in equation (2.39), while $\Delta\mathbf{k}_{<}$ is added by the noncollinear geometry.

In order to include phase matching effects in NCHHG, equation (4.3) can be modified, so as to no longer define the absolute value of \mathbf{k}_q , but instead, only its orientation¹:

$$\mathbf{k}_1, \mathbf{k}_2 \rightarrow \hat{\mathbf{k}}_q = \frac{(m_1\mathbf{k}_1 + m_2\mathbf{k}_2)}{\|m_1\mathbf{k}_1 + m_2\mathbf{k}_2\|}. \quad (4.11)$$

Figure 4.9 illustrates wavevector addition for collinear and noncollinear harmonic generation, for the case of an $\omega/2\omega$ -driving field. For phase-matched generation in the collinear case (a), a phase mismatch occurs for the corresponding noncollinear case, with positive (DFG) or negative (SFG) $\Delta\mathbf{k}_{<}$. Note that the length of the k-vectors does not change with the noncollinear angle since neither dispersion, nor focusing effects depend on γ . The wavevector mismatch added by the noncollinear geometry is thus a purely geometrical mismatch. With a non-zero phase mismatch in collinear generation (b), a corresponding noncollinear scheme can typically be found, allowing for phase-matched generation. In this case, the two terms in equation (4.10) compensate each other.

¹Equation (4.11) is strictly speaking still an approximation, neglecting a possible modification of the emission direction due to radial field gradient vectors [126] such as may be caused by a strongly intensity-dependent dipole phase.

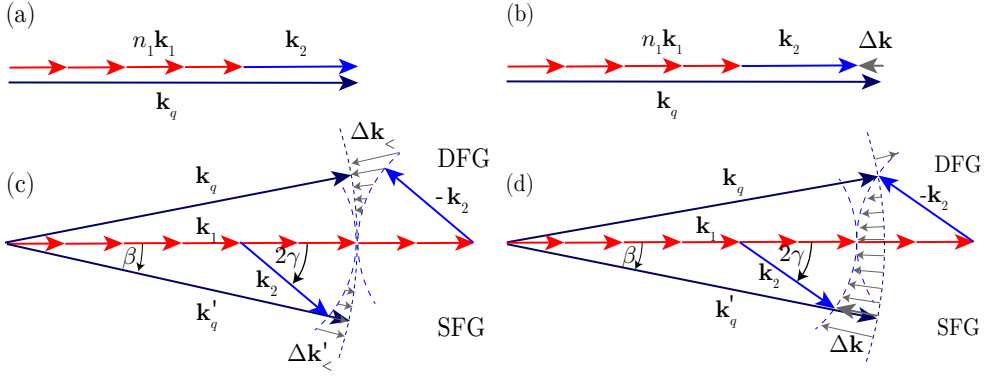


Figure 4.9: Schematic phase matching illustration for NCHHG driven by a $\omega/2\omega$ -laser field. In (a) and (b), collinear generation schemes are shown, considering phase-matched (a) and non phase-matched (b) generation. (c) and (d) depict the corresponding noncollinear schemes for both SFG and DFG processes. Adapted from Paper [XII](#).

$\Delta\mathbf{k}_{<}$ can be expressed as a function of γ and the involved photon numbers. For $\omega/2\omega$ -HHG, a simple geometrical wavevector addition leads to²:

$$\Delta\mathbf{k}_{<}^{\omega 2\omega} = 4m_2\gamma^2 \underbrace{\left(\frac{2m_2}{q} - 1\right)}_{<0} \frac{\omega}{c} \hat{\mathbf{k}}_q, \quad (4.12)$$

with $q = m_1 + 2m_2$. A limiting factor for HHG in gases is typically ionization and the resulting plasma dispersion. Both plasma dispersion and the phase offset arising from the Gouy phase of a focused laser beam lead to a negative $\Delta\mathbf{k}_{\parallel}$ which can, in principle, be compensated by a positive $\Delta\mathbf{k}_{<}$ if DFG processes are involved. Thus, DFG emission can dominate over SFG emission, as discussed in Paper [XII](#). Since such DFG processes involve more photons than SFG, this processes are otherwise less likely. Therefore an overall increased conversion efficiency has not been demonstrated, despite the improved phase matching.

Equation (4.12) can be generalized for other driving field combinations. Particularly interesting is the case of two identical driving fields and XUV emission around the bisector angle, as discussed in section 4.3. In this case, the wavevector mismatch reads as:

$$\Delta\mathbf{k}_{<}^{\omega\omega} = -\gamma^2 \frac{q}{2} \frac{\omega}{c}. \quad (4.13)$$

Equation (4.13) can be derived by geometrical wavevector addition and neglects a minor phase mismatch arising from off-axis contributions of a focused laser beam.

For noncollinear SFG, $\Delta\mathbf{k}_{<}^{\omega\omega}$ is negative and thus does not favor HHG at high fundamental field intensities or in tight-focusing geometries. However, because $\Delta\mathbf{k}_{<}^{\omega\omega}$ has a similar impact on HHG as a steep Gouy phase gradient, phase-matched generation is still possible, and high conversion efficiencies can be expected if the target pressure and dimensions are scaled correctly (see Paper [II](#) and section 4.3).

²Note that equation (4.12) differs by a factor of four from equation 2 in Paper [XII](#) due to a different definition of γ .

The dependence of $\Delta\mathbf{k}_{<}^{\omega\omega}$ on m_2 and thus on the emission angle can be used to obtain information about the phase matching conditions. By analyzing the spatial far-field distribution an effective $\Delta\mathbf{k}_{\parallel}$ can be extracted. This method is presented in Paper [XII](#).

4.3 Noncollinear Optical Gating

This section introduces a new gating method based on NCHHG, which allows the generation of isolated attosecond pulses. Using the basic mechanisms introduced above, NCHHG enables transient control of the XUV emission direction, which leads to a spatio-temporal streaking of APTs. A detailed description of the method can be found in Paper [XIII](#). First experimental results are presented in Paper [XIV](#).

4.3.1 Introduction to a New Gating Concept

Historically, the generation of IAPs has been based on driving the generation process with few cycle pulses in combination with temporal or spectral filtering, suppressing the XUV emission from all but one halfcycle, as illustrated in Figure [4.10](#) (a), (see also section [2.2.4](#)). As explained above, NCHHG offers another control dimension, the spatial domain. Combining transient control with spatial emission control, allows us to streak the APT spatially, as illustrated in Figure [4.10](#) (b). A similar technique has recently been introduced by Vincenti and co-workers [[116](#)].

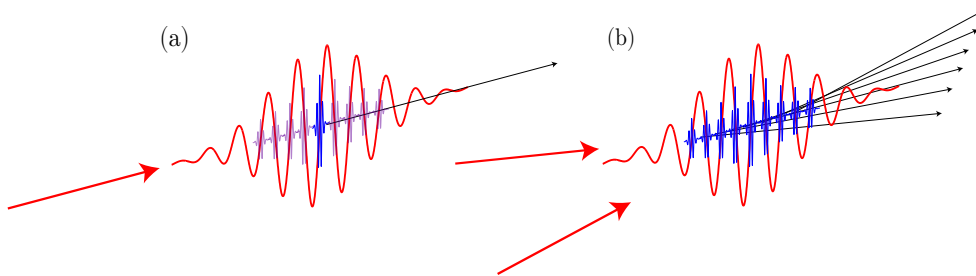


Figure 4.10: Two different gating concepts for IAP generation: (a) temporal selection of one of the pulses in the pulse train by suppressing all other pulses and (b), angular separation of all pulses in the train.

The basic principle of Noncollinear Optical Gating (NOG) can be easily understood with the help of equation (4.7). As the wavefront orientation, and so the XUV emission direction, can be directly controlled via the amplitude ratio of the two driving fields, ξ , transient control is possible via an ultrafast amplitude modulation, resulting in spatio-temporal wavefront rotation (WFR). This can easily be achieved by introducing a time delay between the two driving laser pulses. For two Gaussian laser pulses with $\mathcal{E}_{1,2} = \exp[-2\log(2)(t \pm \Delta t/2)^2/\tau^2]$ and pulse duration τ (FWHM), the resulting

WFR per unit time $v_r = \partial\beta/\partial t$ reads as:

$$v_r|_{t=0} = \gamma 2 \log(2) \frac{\Delta t}{\tau^2}. \quad (4.14)$$

Here we assume the WFR speed to be at its maximum value, occurring at $t = 0$ and leading to XUV emission at the bisector angle ($\beta = 0$). The angular separation between consecutive attosecond pulses increases with pulse delay. In order to avoid a local field minimum at the pulse center ($t = 0$) while maximizing the angular separation, the delay should be chosen as $\Delta t \approx \tau$. In this case, the corresponding wavefront rotation per halfcycle, equivalent to the angle “streaked” between consecutive attosecond pulses, can be written as:

$$\Delta\beta = \gamma \log(2) \frac{\lambda}{c\tau}. \quad (4.15)$$

In order to illustrate the timescales of the angular streaking process, we consider the example of $\lambda = 800$ nm, $\tau = 5$ fs and $\gamma = 7.5$ mrad. This corresponds to a wavefront rotation velocity of $3.3 \cdot 10^{11}$ rotations per second. During the duration of the total driving laser pulse, a rotation from $-\gamma$ to γ can be observed

In order to separate the individual attosecond pulses angularly, $\Delta\beta$ has to be larger than the divergence angle of a single pulse. The divergence angle depends on the spatial dimension of the harmonic source and thus on the focusing geometry and the noncollinear angle. Likewise, $\Delta\beta$ depends on the noncollinear angle. In order to ensure generation within Regime III, and thus to avoid spatial beam distortions due to the formation of multiple sources, the noncollinear angle and the focusing condition have to be chosen correctly. As derived in detail in Paper [XIII](#), multiple source effects can be suppressed while maximizing the angular separation, if the spatial beam separation before focusing (in units of the beam diameter) is chosen to be $\delta \approx \pi/2$.

Figure 4.11 shows simulation results for NOG, considering a two-cycle laser pulse and generation in neon. The spatio-temporal distribution of the electrical driving field is shown for $\Delta t = 0$ (a) and $\Delta t = 1.25\tau$ (d). In (b,e) and (c,f) temporal and spectral far-field intensity distributions of the generated attosecond pulses are shown. For the pulse duration considered, approximately four attosecond pulses are emitted on axis ($\beta = 0$) if $\Delta t = 0$. With increasing temporal delay, the duration of the total driving field increases, leading to the emission of a longer pulse train. The delay also leads to a rapid temporal variation of $\xi(t)$ and thus $\beta(t)$. The APT appears angularly streaked and the angularly resolved XUV spectrum turns into an XUV spectrogram, where each IAP is resolved spatially. The streaking process maps time onto far-field angle. The spatial axis in the far-field can thus be interpreted directly as a time axis with a temporal resolution of at least one half cycle, indicated with a red arrow in Figure 4.11 (f).

As each individual attosecond pulse can be accessed separately, the streaking process can be used to provide temporal information on dynamical processes in HHG, such as ionization effects which can lead to depletion of the generation medium. In addition, CEP effects are directly mapped into the spatial domain. As ϕ_{CE} is changed, the total field moves temporally under its envelope, and so does the XUV field under its spatial far-field envelope. CEP variations are thus directly encoded in the spatial positions of the spectral XUV continua.

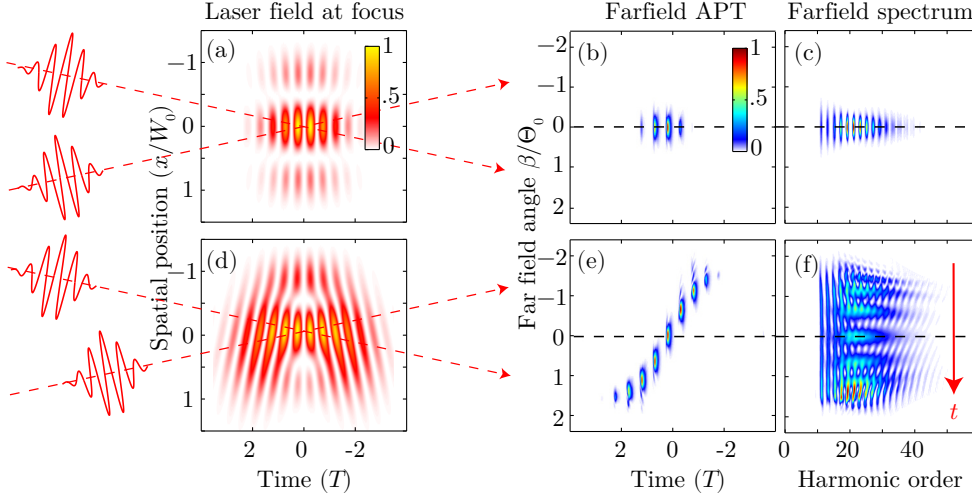


Figure 4.11: Spatio-temporal characteristics of the NOG process. (a) and (d) depict the normalized spatio-temporal distribution of $\Re(E)^2$, (b,e) and (c,f) show the angularly resolved far-field intensity distribution of the emitted XUV radiation in the temporal (b,e) and spectral (c,f) domains. The XUV emission was simulated using two-dimensional SFA calculations. In the first row, both driving pulses are temporally overlapped ($\Delta t = 0$). In the second row, the delay was set to $\Delta t = 1.25\tau$. Adapted from Paper [XIII](#).

For IAP gating, a simple spatial aperture can be used to isolate an attosecond pulse from the streaked pulse train. Likewise, more than one pulse can be selected spatially and possibly recombined for attosecond-pump-attosecond-probe measurements [192].

The XUV spectrogram obtained with NOG provides another interesting possibility: as both temporal and spectral information are displayed simultaneously, access to harmonic and attochirp (see section 2.2.3) can be provided in a single measurement. If adjacent streaked attosecond pulses are not fully angularly separated, they will interfere, leading to a modulated fringe pattern between the spectral continua. The spectral lineout (the harmonic spectrum measured in-between two adjacent spectral continua) of such a fringe pattern provides access to the temporal separation of two consecutive attosecond pulses, revealing the attochirp [193]. The orientation of the interference fringes across the spatial profile reflects the harmonic chirp.

4.3.2 Comparison with Other Gating Methods

NOG is closely related to the recently introduced Attosecond Lighthouse (ALH) technique. A direct comparison of the two techniques is presented in Figure 4.12. For both methods, optimal gating conditions are assumed, implying $\delta = \pi/2$ and $\Delta t = \tau$ for NOG and an angular chirp that maximizes the WFR for the ALH. In (a) and (d), the angular-temporal distribution of the fundamental field at the focusing element – directly after the focusing lens or mirror – is shown. For NOG, two laser pulses are used, which are separated spatially and temporally. The ALH employs an angularly chirped fundamental field, achieved, for example, by tilting a glass wedge in the beam

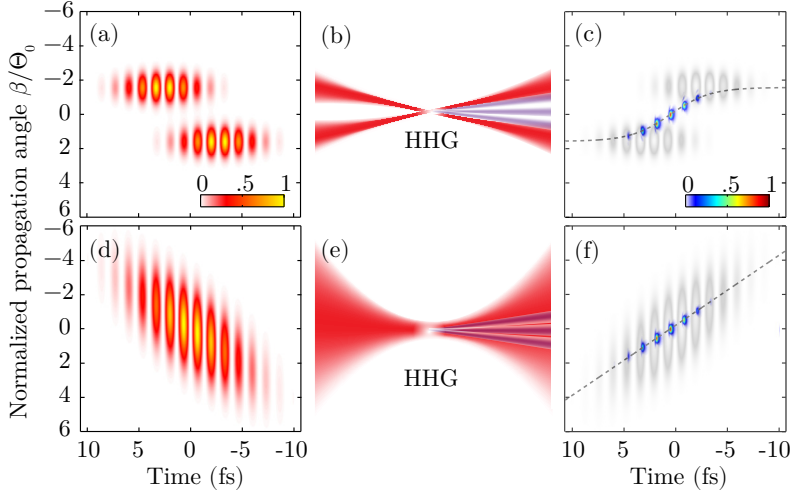


Figure 4.12: Comparison between NOG (a)–(c) and Attosecond Lighthouse (d)–(f). (a) and (d) show the laser field $[\Re(E)^2]$ at the focusing element, (b) and (d) illustrate the generation scheme, and (c) and (f) show both the fundamental field (gray) and the XUV intensity distribution in the far-field. The dashed lines in (c) and (f) indicate the spatio-temporal mapping, i.e. $\beta(t)$. The XUV emission was calculated using two-dimensional SFA simulations. Adapted from Paper [XIII](#).

path. A comparison of the two driving fields shows that the ALH technique can be seen as a continuous analogue of NOG. Both methods lead to a very similar field distribution in the focus, where the spatio-temporal WFR occurs.

In Figure 4.12 (c,f), the angular-temporal far-field characteristics of both the fundamental and XUV fields are shown. In both gating schemes, the APT appears angularly streaked. The spatio-temporal mapping obtained with the ALH is linear, while a nonlinear behavior can be observed for NOG. Interestingly, around $\beta = 0$, the streaking process is equally efficient: the same $\partial\beta/\partial t$ and the same angular divergence can be expected for both schemes. This is true for the temporal pulse separation of $\Delta t = \tau$. Even faster WFR, and thus a better separation of the generated IAPs, can be achieved in the NOG scheme for $\Delta t > \tau$, while the WFR speed is limited for the ALH [116].

A number of other techniques for the generation of IAPs have been demonstrated, see section 2.2.4. The method of choice should depend on the requirements set by the application as well as on the available laser source. In comparison with other common gating methods, such as amplitude gating [113, 114], ionization gating [112], polarization gating [110, 111], double optical gating [119, 120], and the ALH [116], NOG provides interesting options, especially concerning the following characteristics: (i) compatibility with generation of broadband XUV continua and thus short IAPs, (ii) the possibility to access more than one IAP, and (iii) the necessity for spectral filtering to eliminate the driving laser field.

As discussed in detail in Ref. [117], the schemes based on polarization gating or spatio-temporal gating allow for easy bandwidth scaling – as do ALH and also NOG –

because the gating efficiency increases with harmonic order. In contrast, if amplitude or ionization gating is employed, typically only the cutoff spectral region supports IAPs.

To date, ALH and NOG are the only schemes which can provide several synchronized IAPs, permitting new attosecond-pump–attosecond-probe schemes [192]. In all other gating schemes, only one IAP is selected and spatial splitting has to be employed to produce two or more attosecond pulses with controllable delay.

A unique advantage provided by NOG is the possibility for a noncollinear separation of the fundamental fields and the generated IAPs. As shown in Figure 4.12 (c,f), the noncollinear geometry allows direct separation of the generated XUV pulses emitted around $\beta = 0$ from the driving field. This implies that spectral filtering, which is costly in terms of the photon flux, can be simplified. In contrast, in all of the other gating schemes mentioned above, the fundamental field covers the angle sector into which the attosecond pulses are emitted.

Important aspects determining the viability of attosecond gating methods are the demands they make of the driving laser pulse. While the restrictions on spatio-temporal pulse distortions are rather low for ionization and amplitude gating, stringent requirements are set for ALH and NOG. As these gating processes employ spatio-temporal couplings, other temporal or spatial distortions can prevent efficient WFR and thus suppress the gate. It should also be noted that NOG seems to be technically more difficult to implement compared to other gating schemes, especially in comparison with the ALH, where the tilt of a glass wedge is sufficient to induce the needed angular chirp. NOG, on the other hand, requires an interferometric setup, as discussed in more detail in section 4.4, and the gating process requires precise spatial and temporal alignment.

4.3.3 Applying NOG to the Extremes of the Two Scaling Directions

In this section, the applicability of NOG to the extremes of the two scaling directions, namely for the generation of intense IAPs as well as for the generation of IAPs at very high repetition rates, is discussed. The presented experimental schemes should be seen as an outlook on potential directions in which NOG can be applied.

As introduced in section 4.3, NOG requires a spatial beam separation before focusing of $\delta \approx \pi/2$. This value is independent on the focal length, as a tighter focus implies both larger angular divergence and faster WFR. Thus, the effective angular separation and, in general, the far-field emission characteristics, are directly scalable with focal length. This implies that NOG can be used for both loose and tight-focusing schemes. The unique property of NOG, its provision of IAPs spatially separated from the driving field, has promising implications in both cases, as is discussed below.

Intense IAPs

An ideal attosecond-pump–attosecond-probe experiment would combine two isolated attosecond pulses with a controllable delay. Today, only a few groups have reported the successful implementation of such a scheme, based on spatially splitting an IAP

into a pump and a probe pulse [33–35]. Such schemes are mainly limited by the low flux on target [32], which has at least three main reasons, including:

- (i) the generally low conversion efficiency for attosecond pulse generation
- (ii) the requirement to split and recombine the IAP
- (iii) the necessity for spectral filtering

The conversion efficiency expected for NOG is similar to the conversion efficiencies reported for other gating schemes. For (ii) and (iii), NOG seems to offer a solution. Both filtering as well as spatial splitting can be avoided since more than one IAP can be spatially selected and recombined for pump–probe studies [192].

IAPs at Multi-MHz Repetition Rates

As discussed in Section 3.2, three different schemes have been employed for HHG at high repetition rates. Although technically challenging, intra-cavity HHG significantly exceeds the other schemes in terms of the average XUV power generated [71]. With current laser technology, the free focus scheme seems to allow the generation of IAPs at repetition rates approaching the MHz regime [108]. In contrast, intra-cavity IAP generation still remains to be realized. As the pulses employed for intra-cavity HHG reach 57 fs for Ytterbium based lasers [194] and 17 fs for Ti:Sapphire systems [165], the duration does not yet support IAP generation inside a cavity. The bandwidth supported by enhancement cavities is mainly limited by dispersion management, which becomes even more critical if further optical elements are inserted into the cavity, as is typically required to form a gate. As NOG does not require any manipulation of the driving laser field, no additional optical elements are needed in the cavity, and so it seems ideally suited for intra-cavity HHG. NOG should further allow the direct out-coupling of IAPs generated inside an enhancement cavity, thus complementing the noncollinear out-coupling schemes proposed earlier [185–187].

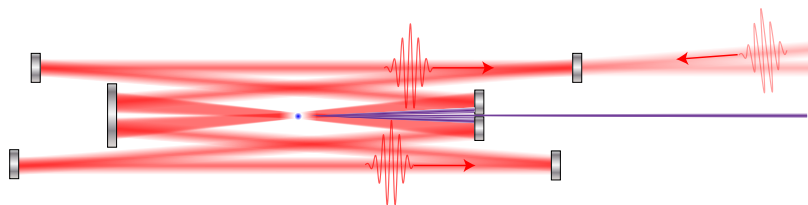


Figure 4.13: A novel scheme for intra-cavity IAP generation. An enhancement cavity containing two foci as well as two pulses should allow the generation of IAPs at unprecedented power levels and repetition rates.

A possible scheme for IAP generation inside an enhancement cavity is shown in Figure 4.13. The enhancement cavity used in this case should include two spatially matched foci and two laser pulses. The round-trip time for a laser pulse needs to be exactly two times T_{rep} . Further, a simple geometrical asymmetry in the cavity mirror arrangement should allow an effective temporal delay at the focus between the two

intra-cavity pulses. With sufficiently short intra-cavity pulses, such a scheme should allow intra-cavity IAP generation with repetition rates and average power levels potentially exceeding current IAP sources by orders of magnitude. In addition, IAPs generated inside a stabilized enhancement cavity would provide broadband frequency combs in the XUV, opening new possibilities for precision spectroscopy.

4.4 Experimental Implementation of NCHHG

This section describes the experimental implementation of NCHHG. Detailed experimental results for $\omega/2\omega$ -HHG are reported in Paper [XII](#), and the experimental validation of the NOG scheme is presented in Paper [XIV](#).

For this thesis work, NCHHG has been implemented with two different laser systems: at the intense harmonic beam line and at the kHz-beam line in Lund. These two systems are described in Chapter [3](#). Here, we focus on the implementation of the noncollinear generation geometry.

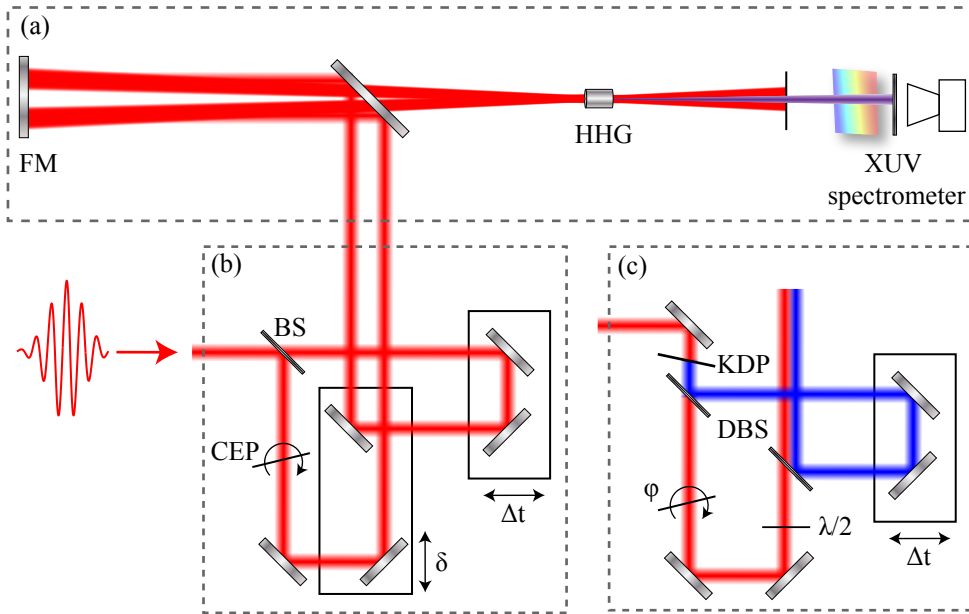


Figure 4.14: Schematic setup for NCHHG. (b) shows the the interferometer used for NOG and (c) displays the $\omega/2\omega$ -interferometer with the second harmonic being generated in a KDP crystal. In both cases, the two collinearly propagating beams leaving the interferometer, are sent with a spatial displacement onto a focusing mirror (FM) and subsequently focused noncollinearly into the HHG target. The focusing arrangement and detection scheme displayed in (a) is set up in a vacuum chamber. The control parameters are: pulse energy, polarization axis and beam size (controls not shown); temporal delay via a translation stage or a rotatable glass plate (Δt , φ), the spatial separation (δ) and the CEP/delay control (CEP). The interferometers use dispersion-compensated beam splitters (BS) and dichroic beam splitters (DBS).

In Figure 4.14, the interferometric setups used for NOG (b) and NCHHG with $\omega/2\omega$ -laser fields (c) are shown. In both cases, a Mach-Zehnder type interferometer is used. The incident laser pulse is split into two parts which propagate on different paths through the interferometer. A small spatial offset at the recombination beam splitter allows us to obtain two collinearly propagating laser pulses which are then focused with a spherical mirror into the HHG gas target. The spatial offset is thus transformed into a noncollinear angle. For larger noncollinear angles, the recombination beam splitter shown in (c) can be replaced by a mirror, as shown in (b).

For $\omega/2\omega$ -HHG, the incident laser pulse is sent through a KDP crystal, which generates the second harmonic. The beam splitters used in this case are dichroic beam splitters which transmit the wavelength range around 800 nm but reflect the second harmonic. Polarization and beam size can be controlled independently with the help of $\lambda/2$ -wave plates and irises in the two interferometer arms. The temporal delay is adjusted with a linear translation stage in one of the interferometer arms. Fine control is possible using a 200 μm glass (BK7) window which can be rotated in the beam.

For the gating experiments performed for this thesis, the spatial and spectral properties of the two laser pulses had to be as identical as possible. The interferometer in this case employs either a dispersion-compensated beam splitter, or uses simple spatial splitting with a D-shaped mirror. For temporal delay control, a piezo-driven translation stage is used. In addition, a rotatable glass plate provides fine control of group and phase-delay, and thus of the CEP of one of the pulses. The noncollinear angle can be continuously adjusted with a translation stage which controls the position of the last two mirrors in each arm and thus the beam separation.

The XUV emission is detected with a XUV spectrometer which allows us to obtain spatial and spectral information simultaneously. The focusing section, the HHG gas cell, and the spectrometer are kept under vacuum.

SUMMARY AND OUTLOOK

This thesis investigates the scalability of attosecond sources towards higher pulse energies and repetition rates. The focus lies on the scaling of experimental parameters which determine the macroscopic generation conditions, and includes the investigation of sub-cycle control mechanisms. In addition, the implementation of noncollinear geometries for high-order nonlinear wave mixing processes is investigated, and applied as a new method for isolated attosecond pulse gating.

A general scaling model for attosecond pulse generation has been developed (Paper **II**). The model predicts the focal length invariant scalability of macroscopic generation conditions, and shows that efficient generation is possible even with laser pulse energies in the few- μJ regime. The theoretical predictions were recently confirmed experimentally by Rothhardt and co-workers [143]. This result has direct consequences for high-repetition rate HHG (Papers **I**, **III** and **IV**), as well as for XUV frequency comb generation. In tight-focus conditions, the macroscopic origin of spectral and spatial interference features, which are often observed in HHG spectra, was identified (Paper **I**). Moreover, CEP-dependent harmonic spectra, indicating that the isolated attosecond pulse generation regime can be reached even at high repetition rates, were measured (Paper **III**) using the OPCPA laser based HHG setup in Lund, which was designed and built as part of this thesis work.

The scaling model was further applied to the loose focus generation regime, used at the intense harmonic beam line in Lund (Papers **VI** and **VIII**), which was developed and built within this thesis work. This beam line was used to investigate microscopic sub-cycle control mechanisms (Papers **IX** and **X**), and noncollinear generation geometries (Paper **XII**), and applied for coherent imaging experiments based on inline holography (Paper **XI**). Moreover, a conceptual design for a high-flux XUV beam line for the European facility ELI-ALPS was developed (Paper **VII**).

The work on noncollinear HHG (Paper **XII**) led to the invention of a new gating technique for isolated attosecond pulse generation. The technique was developed (Paper **XIII**) and experimentally tested (Paper **XIV**).

Both the intense harmonic beam line and the high-repetition rate beam line in Lund are under constant development. Recent progress at the intense harmonic beam line has led to the generation of XUV radiation with pulse energies of $3\ \mu\text{J}$ (measured above 16 eV), which places this beam line among the most intense attosecond XUV

beam lines worldwide. The high pulse energy in combination with a tight re-focusing arrangement has enabled the observation of the first XUV-induced double ionization signal in neon, promising further studies of nonlinear effects in the XUV. An interferometric setup, similar to the one developed in this thesis and presented in Paper VII, is being constructed and will allow XUV–XUV and XUV–IR pump–probe studies of molecules.

The high-repetition rate OPCPA-based beam line has recently allowed PEEM studies in which Ag nanowires were imaged. Compared to previous studies at the 1 kHz XUV beam line in Lund, the spatial resolution, which is mainly limited by space charge effects, could be improved significantly. An interferometric setup allowing for XUV-IR pump–probe studies is under construction, promising time-resolved studies of surface plasmons. Furthermore, a new gas target design and an improved pumping scheme are being constructed and will allow a significant increase in the XUV photon flux in order to reach the values predicted by the scaling model.

Based on the tight-focus HHG results obtained, a new HHG beam line was designed in Marburg, which will be used for photoelectron spectroscopy studies of surfaces.

The noncollinear gating scheme has been demonstrated experimentally at the 1 kHz XUV beam line in Lund. The first proof-of-principle studies have proven the feasibility of the new gating concept and have stimulated further investigations. The implementation of a noncollinear gate inside an optical cavity is planned, promising the generation of IAPs at unprecedented average power levels and repetition rates.

Looking into the future, the development of attosecond sources and coherent femtosecond sources based on HHG will most likely continue in the two directions discussed in this thesis. Towards higher XUV pulse energies, future development will rely predominantly on a further increase of the average power of femtosecond laser systems, in combination with a further upscaling of HHG schemes. This direction is, for example, being pursued at the European Facility ELI-ALPS. At the same time, alternative approaches which already allow high XUV pulse energies and pulse durations close to or beyond one femtosecond, are on the way. Such approaches include the generation of high-order harmonics from plasma mirrors where the generation of IAPs has recently been demonstrated [195] as well as free electron lasers (FELs). XUV pulses generated by FELs can be many times more intense than pulses from HHG sources, and they can reach shorter wavelength. In recent years, high-order harmonics generated in gases have been tested as a seed for FELs, improving the coherence and temporal properties of the generated pulses [196–198].

Two different routes promise further progress towards higher repetition rates and, possibly, higher average powers: the single pass tight-focus HHG scheme, and intra-cavity HHG. Again, further laser development will facilitate progress for both schemes. The possibility of scaling efficient HHG into the tight-focus regime, discussed in detail in this thesis, will enable efficient HHG sources driven by weak laser pulses. This is especially important for intra-cavity HHG. To date, cavity internal conversion efficiencies of around 10^{-8} – 10^{-7} have been reached. Due to a cavity-enhancement of around 100 to 1000, overall conversion efficiencies of 10^{-5} could be achieved, similar to the best values reported for single-pass HHG schemes. Increasing the cavity internal conversion efficiency using the scaling model presented in this thesis could enable a dramatic increase of the generated XUV power.

A number of different proof-of-principle experiments have demonstrated that attosecond pulses can be used, for example, for probing ionization dynamics [30, 31] and

electron motion in atoms [16] and condensed matter systems [18]. Moreover, high-order harmonic sources have allowed the development of new high-resolution imaging techniques [199]. Continued improvements to harmonic and attosecond sources will enable studies of more complex systems, and might allow the measurement and control of ultrafast electron dynamics in biomolecules, solid surfaces and nanostructures. Nanoscale imaging approaches, on the other hand, pursue the goal to image biological cells. In the future, such an approach may allow the rapid characterization and classification of cells, bacteria, or even viruses, especially if efficient XUV sources can be built which reach the water window spectral region.

Besides the future development of attosecond sources and the new experimental possibilities they allow, further progress can also be expected in experiments using the frequency comb aspects of frequency locked XUV sources. To date, XUV comb spectroscopy has been limited by the XUV power available in individual comb lines as well as by the maximum photon energy generated. Also, the harmonic comb structure on top of the XUV frequency comb restricts the available spectral range to rather narrow intervals defined by the harmonic comb. As mentioned above, the efficient tight-focus HHG approach presented in this thesis might be applicable for intra-cavity HHG schemes, potentially enabling an increase in the average power of XUV combs. Moreover, the implementation of attosecond pulse gating techniques such as NOG could allow the generation of broadband XUV combs. This is especially interesting for Fourier transform spectroscopy or dual comb spectroscopy studies in the XUV spectral region.

Last but not least, XUV frequency combs, locked to an atomic transition, promise to provide new frequency standards, reaching a precision far beyond the current limits of standard atomic clocks. Since 1967, the standard unit of time, one second, has been defined as 9 192 631 770 periods of a microwave transition of the caesium isotope ^{133}Cs [200]. The development of optical frequency combs has enabled new frequency standards based on narrow transitions in the visible spectral range [201]. Because the achievable precision increases with the frequency of the reference transition, optical atomic clocks can reach much higher accuracies [202], and the future time standard will possibly be based on “nuclear clocks”, i.e. XUV frequency combs locked to nuclear transitions.

COMMENTS ON THE PAPERS

I Spectrally Resolved Maker Fringes in High-Order Harmonic Generation

This paper investigates transient phase matching effects in HHG which are mapped out into the spectral domain, focusing on characteristics of the long electron trajectory contribution. We identify the macroscopic origin of spatial and spectral structures in HHG spectra. I designed and built the experimental setup, measured and analyzed the experimental data, developed the theoretical model, and wrote the manuscript.

II High-Order Harmonic Generation with μJ Laser Pulses at High Repetition Rates

This paper analyzes the scaling of macroscopic parameters for the generation of high-order harmonics in tight focus geometries. Experimental results obtained with the high-repetition rate HHG setup at the University of Marburg are analyzed in the context of the theoretical model developed. In particular, it was found that the HHG conversion efficiency does not necessarily decrease for tight focus geometries. I designed and built the experimental setup, measured and analyzed the experimental data, developed the theoretical scaling model and wrote the manuscript.

III Carrier–Envelope Phase Dependent High-Order Harmonic Generation with a High-Repetition Rate OPCPA-System

We present the high repetition rate high-order harmonic source in Lund, which is driven by an OPCPA laser system. Characteristic spectral features measured as function of the CEP of the driving laser field indicate that this HHG source approaches the isolated attosecond pulse regime. I prepared the conceptual design for the HHG setup, contributed to setting up the experiment and to initial test measurements. I also helped with the interpretation of the experimental data.

IV High-Order Harmonic Generation Using a High-Repetition Rate Turnkey Laser

In this paper we experimentally investigate HHG using a compact turn-key fiber laser system, operating at 1030 nm. High-order harmonics are generated at up to 400 kHz repetition rate and photon energies exceeding 90 eV are reached. I prepared the conceptual design for the HHG setup, and contributed to setting up the experiment, data acquisition and manuscript writing.

V Attosecond Pulse Walk-Off in High-Order Harmonic Generation

In this paper, we study the influence of the macroscopic generation conditions on the group delay of attosecond pulses in high-order harmonic generation in gases. The group delay relative to the fundamental field is found to decrease with increasing gas pressure in the generation cell. I helped with the interpretation of the experimental findings through feedback and discussions.

VI A High-Flux High-Order Harmonic Source

We present the high-flux high-order harmonic source driven by the 10 Hz laser system in Lund. The optimization of the beam line led to high-order harmonic pulses exceeding the 1 μ J-level, which places this beam line amongst the most intense high-harmonic beam lines in the world. I developed the scaling model used for the beam line design and the data interpretation. I took a major role in the construction of the beam line, data acquisition and analyses, and contributed to writing the manuscript.

VII Conceptual Design Report for a Gas HHG Beam Line at ELI-ALPS

We present a conceptual design for a high-flux XUV beam line at the Extreme Light Infrastructure-Attosecond Light Pulse Source (ELI-ALPS) facility, based on HHG in gases. The beam line will be driven by a laser system with parameters dramatically exceeding those of current laser sources used for HHG. These conditions were taken into account by using a beam line design based on HHG under very loose focusing geometries and low-density gas targets. I developed the loose focusing scheme, including gas target design and overall dimensions. I conceived the idea for the XUV-IR interferometer design, and wrote large parts of the report.

VIII Compression of TW-class Laser Pulses in a Planar Hollow Waveguide for Applications in Strong-Field Physics

In this work, we demonstrate pulse post compression of the TW-class 10 Hz laser system used for the intense harmonics beam line in Lund. A planar, gas-filled, hollow wave guide is used in combination with cylindrical focusing and collimation optics. The compressed 15 fs pulses were used for HHG test experiments. I took a major role in the HHG beam line design and installation, and contributed to the measurements and to the manuscript writing via feedback.

IX Efficient High-Order Harmonic Generation Boosted by Below-Threshold Harmonics

We theoretically and experimentally investigate the effect of low-order harmonics superimposed on the driving laser field in the HHG process, both using a double cell scheme and an interferometric setup. We show that a significant enhancement of the HHG single atom response can be achieved if low-order harmonics, generated in-line in a second gas cell, are added to the fundamental field with the correct phase. I took a major role in the experiments, including setup design and data acquisition, as well as in the theoretical simulations. I wrote large parts of the manuscript.

X Interference Effects in Two-Color High-Order Harmonic Generation

In this work, we study how the HHG process is altered when a weak second harmonic field is added to the driving laser field. In particular, modification of the harmonic dipole phase by the second harmonic field, and its influence on the XUV intensity and beam divergence, are studied experimentally and explained using a simple analytical model. I participated in optimizing the HHG setup, and helped with the interpretation of the experimental findings through feedback and discussions.

XI Digital In-Line Holography on Amplitude and Phase Objects Prepared with Electron Beam Lithography

The intense HHG beam line in Lund is used for digital inline holography measurements. Phase and amplitude information of μm -scale objects produced with electron beam lithography could be retrieved, reaching a spatial resolution of $1.5\ \mu\text{m}$. This paper reports on both sample preparation and holographic characterization. The project was performed at the onset of my PhD work in Lund. I contributed to optimizing the HHG source.

XII Macroscopic Phase Effects in Noncollinear High-Order Harmonic Generation

We study noncollinear HHG driven by a two-color laser field. The generation scheme allows the measurement and control of phase matching effects, and provides access to the intensity-dependent dipole phase. Different types of macroscopic effects are identified and analyzed, and the basic principles of high-order wave mixing are discussed using wave and particle models. I took a major role in setup design and measurements, in conceiving the experiment, and interpreting its results. I wrote the manuscript.

XIII Noncollinear Optical Gating

In this paper, we describe the concept for a new gating method for isolated attosecond pulse generation. The method is based on noncollinear HHG and can be used for angular streaking of attosecond pulse trains. Analytical descriptions and numerical simulations are presented. I conceived the idea, developed major parts of the analytical description, performed the classical simulations, supervised the quantum mechanical calculations and wrote the manuscript.

XIV Gating Attosecond Pulses in a Noncollinear Geometry

The noncollinear optical gating scheme introduced in Paper [XIII](#) is experimentally tested in this paper. Attosecond pulse trains generated with two noncollinearly overlapping driving laser pulses are angularly streaked, resulting in multiple, CEP-dependent XUV beamlets in the recorded far-field XUV spectrogram. I developed the method, led the experiment, and contributed to writing the manuscript.

ACKNOWLEDGEMENTS

During the time I spent in Lund and partly in Marburg, leading to this thesis, a large number of people have contributed to my work and helped me in many different ways.

First of all, I would like to thank my main supervisor Anne L’Huillier for the freedom she gave me to carry out many different projects, and for her stimulating enthusiasm for physics. I am also grateful to my supervisor in Marburg, Ulrich Höfer, who made it possible for my PhD degree to become a joint degree between two universities by giving me the opportunity to carry out a research project in Marburg. I would also like to thank my co-supervisor in Lund, Per Johnsson, for helping with his great expertise and friendliness whenever necessary.

The person who taught me the basics of high-order harmonic generation and who introduced femtosecond laser systems to me, long before the start of my PhD studies, is Xinqu He. Thank you for all your help at this early stage, and thank you for sharing your expertise with me.

Cord Arnold deserves many thanks for always having an open ear and office door, and for his support of the “gating project”, especially towards the end of my PhD. I would also like to give particular thanks to Johan Mauritsson for encouraging me three years ago to cross two laser beams in the lab...

Another person who was involved in my project in Marburg is Jens Güdde who contributed great expertise in lasers and optics, both in Marburg and later on via detailed answers to my questions in numerous emails.

Together with Piotr Rudawski and Fernando Brizuela I spend many fruitful days in the lab: thanks for an always pleasant and enjoyable atmosphere - it was (and is) great working with you! Later on, Linnea Rading joined our 10 Hz team, making sure that sport and Swedish sessions became a regular part of our daily routines. It was Linnea who spent many days with me in the lab, trying to see a first glimpse of a noncollinear gate. Stort tack för det och tack för att du säkerställde att jag bara pratade svenska med dig, från första dagen du kom till labbet!

Other colleagues who contributed to experiments and early or further beam line development in the 10 Hz lab are Per Johnsson, Rafal Rakowski, Jörg Schwenke, Byunghoon Kim, Filippo Campi, and more recently, Bastian Manschwetus, Hampus Nilsson, Miguel Miranda and H el ene Coudert-Alteirac. I worked together with Am elie Jarnac and Aur elien Houard on pulse compression and on the second round of the gating experiments. Thank you very much for your help and for a great time in the lab! The one, who made our work so much easier in the 10 Hz lab is Anders Persson. He kept an eye on our “working horse” and helped whenever necessary.

Many thanks should go to the only theorist in our group, Stefanos Carlström. During the last three years, he was always the right person to talk to whenever I had a complicated problem to solve. You are a great physicist, office mate, sports companion, singer and Swedish teacher! Stefanos gave me a lot of extra work by pointing out how all the text fonts and style settings in this thesis could be optimized. Stort tack för det och tack för att du läste hela avhandlingen! Not only our current, but also our former theorist, Marcus Dahlström deserves many thanks. Your attitude to research (and your music!) is inspiring for me!

Esben Witting-Larsen and Eleonora Lorek deserve many thanks for long but pleasant hours with the “elephant” at the chemical physics department. After being moved back to the physics department, good care was taken of the “elephant” and his laser system by Anne Harth, Piotr Rudawski, Chen Guo, Eleonora Lorek, Miguel Miranda and Arthur Losquin. Anne Harth also deserves many thanks for countless inspiring discussions about interesting physics!

More thanks go to Esben as well as to David Kroon, Samuel Bengtsson, Strubel (Diego Guénot), Marija Kotur and Cord Arnold for building and maintaining a great setup in the Attolab which allowed us to perform the third round of the gating experiments. In this experimental campaign, Maïte Louisy and Miguel Miranda played an important role: they managed to generate and to measure the shortest (pulse), thanks a lot for that! Thank you Miguel for scanning D and for putting water in laser beams! Both Maïte and Cord deserve much thanks for spending many days and nights in the lab, partly together with me, partly alone. Without your help, this experiment had still only been a dream.

Many other former and current colleagues, contributed in one way or another to my work, without being directly involved in projects I was working with: Thomas Fordell, Kathrin Klünder, Aaron von Conta, Jana Preclíková, Matthieu Gisselbrecht, Jenny Karlsson, Diana Serrano, Lovisa Senje, Martin Hansson. Thanks for giving the atomic physics department a great working atmosphere!

The atomic physics department would not be such a pleasant place to work without the Head of Division, Claes-Göran Wahlström, as well as the former and current technical and administrative staff members, Harriett Lindahl, Minna Ramkull, Camilla Nilsson, Anne Petersson Jungbeck, Jakob Testad, Bertil Hermansson and Åke Johansson.

During part of my PhD studies I was financed by the Marie Curie Initial Training Network ATTOFEL, where I got the chance to participate in a number of meetings and conferences and to meet other network fellows from all over the world: Faruk Krecinik, Fabian Lücking, Antoine Moulet, Tran Trung Luu, Emeric Balogh, Aura Ines Gonzales, Nan Lin and Dimitrios Rompotis. Many thanks go to Thomas Pfeifer for being my network supervisor and for inviting me twice to the MPIK in Heidelberg. The open and inspiring atmosphere at MPIK is always motivating!

Last but not least, I would like to thank my family and friends for their support and for showing patience when I disappeared into work, sometimes for many more hours than expected. Similar thanks go to my daughter for making me smile and showing me how fascinating everyday occurrences can be. Special thanks go to my sister, my sister-in-law and my mother-in-law for taking care of my daughter during intense days in the lab, and during intense thesis writing times.

Finally, I would like to thank my wife Charlotte for her love and support and for dragging me away from physics whenever necessary.

CURRICULUM VITAE

Personal information

Name	Christoph M. Heyl
Date of birth	June 9 th 1983, Kassel, Germany
Citizenship	German
Marital Status	Married, one daughter (born 2013)

Academic career

2004 – 2007	Studies in physics , University of Marburg, Germany
2006	Vordiplom in physics , University of Marburg, Germany
2007 – 2008	11 months Erasmus exchange studies in physics, Lund University, Sweden, specialization in photonics & laser physics
2008 – 2010	Studies and diploma project in physics , University of Marburg, Germany
2010	Diplom in physics , University of Marburg, Germany Topic: “High-order harmonic generation at 100 KHz repetition rate for time-resolved two-photon photoemission” Advisor: Prof. Ulrich Höfer
2010 – present	PhD studies in Physics , Lund University, Sweden and University of Marburg, Germany Advisor: Prof. Anne L’Huillier (Lund) and Prof. Ulrich Höfer (Marburg)
2010 – 2013	Fellow of the Marie Curie Initial Training Network ATTOFEL

BIBLIOGRAPHY

1. R.A. Bartels, A. Paul, H. Green, H.C. Kapteyn, M.M. Murnane, S. Backus, I.P. Christov, Y. Liu, D. Attwood and C. Jacobsen. *Generation of spatially coherent light at extreme ultraviolet wavelengths*. Science **297**, 376 (2002).
2. Z. Chang, A. Rundquist, H. Wang, M. M. Murnane and H. C. Kapteyn. *Generation of Coherent Soft X Rays at 2.7 nm Using High Harmonics*. Physical Review Letters **79**, 2967 (1997).
3. Ch. Spielmann, N. H. Burnett, S. Sartania, R. Koppitsch, M. Schnürer, C. Kan, M. Lenzner, P. Wobrauschek and F. Krausz. *Generation of Coherent X-rays in the Water Window Using 5-Femtosecond Laser Pulses*. Science **278**, 661 (1997).
4. R. A. Bartels, A. Paul, H. Green, H. C. Kapteyn, M. M. Murnane, S. Backus, I. P. Christov, Y. Liu, D. Attwood and C. Jacobsen. *Generation of Spatially Coherent Light at Extreme Ultraviolet Wavelengths*. Science **297**, 376 (2002).
5. C. Benko, T.K. Allison, A. Cingöz, L. Hua, F. Labaye, D.C. Yost and J. Ye. *Extreme ultraviolet radiation with coherence time greater than 1 s*. Nature Photonics **8**, 530 (2014).
6. T.H. Maiman. *Stimulated optical radiation in Ruby*. Nature **187**, 493 (1960).
7. P.A. Franken, A.E. Hill, C.W. Peters and G. Weinreich. *Generation of optical harmonics*. Physical Review Letters **7**, 118 (1961).
8. A. McPherson, G. Gibson, H. Jara, U. Johann, T. S. Luk, I. A. McIntyre, K. Boyer and C. K. Rhodes. *Studies of multiphoton production of vacuum-ultraviolet radiation in the rare gases*. Journal of the Optical Society of America B **4**, 595 (1987).
9. M. Ferray, A. L'Huillier, X. F. Li, L. A. Lompré, G. Mainfray and C. Manus. *Multiple-harmonic conversion of 1064 nm radiation in rare gases*. Journal of Physics B **21**, L31 (1988).
10. J. Seres, E. Seres, A.J. Verhoef, G. Tempea, C. Streli, P. Wobrauschek, V. Yakovlev, A. Scrinzi, C. Spielmann and F. Krausz. *Laser technology: Source of coherent kiloelectronvolt X-rays*. Nature **433**, 7026 (2005).

11. T. Popmintchev, M.-C. Chen, D. Popmintchev, P. Arpin, S. Brown, S. Alšauskas, G. Andriukaitis, T. Balčiūnas, O.D. Mücke, A. Pugzlys, A. Baltuška, B. Shim, S.E. Schrauth, A. Gaeta, C. Hernández-García, L. Plaja, A. Becker, A. Jaron-Becker, M.M. Murnane and H.C. Kapteyn. *Bright coherent ultrahigh harmonics in the kev x-ray regime from mid-infrared femtosecond lasers*. *Science* **336**, 1287 (2012).
12. W.E. Lamb Jr. *Theory of an optical maser*. *Physical Review* **134**, A1429 (1964).
13. D. Gabor. *Acoustical quanta and the theory of hearing*. *Nature* **159**, 591 (1947).
14. Anne Harth, Marcel Schultze, Tino Lang, Thomas Binhammer, Stefan Rausch and Uwe Morgner. *Two-color pumped OPCPA system emitting spectra spanning 1.5 octaves from VIS to NIR*. *Optics Express* **20**, 3076–3081 (2012).
15. A.H. Zewail. *Femtochemistry: Atomic-scale dynamics of the chemical bond*. *Journal of Physical Chemistry A* **104**, 5660 (2000).
16. E. Goulielmakis, Z.-H. Loh, A. Wirth, R. Santra, N. Rohringer, V.S. Yakovlev, S. Zherebtsov, T. Pfeifer, A.M. Azzeer, M.F. Kling, S.R. Leone and F. Krausz. *Real-time observation of valence electron motion*. *Nature* **466**, 739 (2010).
17. G. Sansone, F. Kelkensberg, J.F. Pérez-Torres, F. Morales, M.F. Kling, W. Siu, O. Ghafur, P. Johnsson, M. Swoboda, E. Benedetti, F. Ferrari, F. Lépine, J.L. Sanz-Vicario, S. Zherebtsov, I. Znakovskaya, A. Lhuillier, M.Y. Ivanov, M. Nisoli, F. Martín and M.J.J. Vrakking. *Electron localization following attosecond molecular photoionization*. *Nature* **465**, 763 (2010).
18. A.L. Cavalieri, N. Müller, Th. Uphues, V.S. Yakovlev, A. Baltuška, B. Horvath, B. Schmidt, L. Blümel, R. Holzwarth, S. Hendel, M. Drescher, U. Kleineberg, P.M. Echenique, R. Kienberger, F. Krausz and U. Heinzmann. *Attosecond spectroscopy in condensed matter*. *Nature* **449**, 1029 (2007).
19. P. M. Paul, E. S. Toma, P. Breger, G. Mullot, F. Augé, Ph. Balcou, H. G. Muller and P. Agostini. *Observation of a train of attosecond pulses from high harmonic generation*. *Science* **292**, 1689 (2001).
20. M. Hentschel, R. Kienberger, Ch. Spielmann, G.A. Reider, N. Milosevic, T. Brabec, P. Corkum, U. Heinzmann, M. Drescher and F. Krausz. *Attosecond metrology*. *Nature* **414**, 509 (2001).
21. R.J. Jones, K.D. Moll, M.J. Thorpe and J. Ye. *Phase-coherent frequency combs in the vacuum ultraviolet via high-harmonic generation inside a femtosecond enhancement cavity*. *Physical Review Letters* **94**, 193201 (2005).
22. C. Gohle, T. Udem, M. Herrmann, J. Rauschenberger, R. Holzwarth, H.A. Schuessler, F. Krausz and T.W. Hänsch. *A frequency comb in the extreme ultraviolet*. *Nature* **436**, 234 (2005).
23. Jun Ye and Steven T. Cundiff. *Femtosecond Optical Frequency Comb: Principle, Operation, and Applications*. Springer Science + Business Media, Inc. (2005).

24. D.C.Yost. *Development of an Extreme Ultraviolet Frequency Comb for Precision Spectroscopy*. University of Colorado (2011).
25. P. Johnsson, J. Mauritsson, T. Remetter, A. L'Huillier and K.J. Schafer. *Attosecond control of ionization by wave-packet interference*. Physical Review Letters **99**, 233001 (2007).
26. C. Neidel, J. Klei, C.-H. Yang, A. Rouzée, M.J.J. Vrakking, K. Klünder, M. Miranda, C.L. Arnold, T. Fordell, A. L'Huillier, M. Gisselbrecht, P. Johnsson, M.P. Dinh, E. Suraud, P.-G. Reinhard, V. Despré, M.A.L. Marques and F. Lépine. *Probing time-dependent molecular dipoles on the attosecond time scale*. Physical Review Letters **111**, 033001 (2013).
27. J. Mauritsson, P. Johnsson, E. Mansten, M. Swoboda, T. Ruchon, A. L'Huillier and K. J. Schafer. *Coherent Electron Scattering Captured by an Attosecond Quantum Stroboscope*. Physical Review Letters **100**, 073003 (2008).
28. Y. Mairesse, A. de Bohan, L. J. Frasinski, H. Merdji, L. C. Dinu, P. Monchicourt, P. Breger, M. Kovačev, R. Taïeb, B. Carré, H. G. Muller, P. Agostini and P. Salières. *Attosecond synchronization of high-harmonic soft X-rays*. Science **302**, 1540 (2003).
29. K. Klünder, J. M. Dahlström, M. Gisselbrecht, T. Fordell, M. Swoboda, D. Guénot, P. Johnsson, J. Caillat, J. Mauritsson, A. Maquet, R. Taïeb and A. L'Huillier. *Probing Single-Photon Ionization on the Attosecond Time Scale*. Physical Review Letters **106**, 143002 (2011).
30. E. P. Månsson, D. Guénot, C. L. Arnold, D. Kroon, S. Kasper, J. M. Dahlström, E. Lindroth, A. S. Kheifets, A. L'Huillier and M. Sorensen, S. L. Gisselbrecht. *Double ionization probed on the attosecond timescale*. Nature Physics **10**, 207–211 (2014).
31. M. Schultze, M. Fiess, N. Karpowicz, J. Gagnon, M. Korbman, M. Hofstetter, S. Neppl, A.L. Cavalieri, Y. Komninos, Th. Mercouris, C.A. Nicolaides, R. Pazourek, S. Nagele, J. Feist, J. Burgdörfer, A.M. Azzeer, R. Ernstorfer, R. Kienberger, U. Kleineberg, E. Goulielmakis, F. Krausz and V.S. Yakovlev. *Delay in photoemission*. Science **328**, 1658 (2010).
32. S.R. Leone, C.W. Mccurdy, J. Burgdörfer, L.S. Cederbaum, Z. Chang, N. Dudovich, J. Feist, C.H. Greene, M. Ivanov, R. Kienberger, U. Keller, M.F. Kling, Z.-H. Loh, T. Pfeifer, A.N. Pfeiffer, R. Santra, K. Schafer, A. Stolow, U. Thumm and M.J.J. Vrakking. *What will it take to observe processes in 'real time'?* Nature Photonics **8**, 162 (2014).
33. Y. Nabekawa, T. Shimizu, Y. Furukawa, E.J. Takahashi and K. Midorikawa. *Interferometry of attosecond pulse trains in the extreme ultraviolet wavelength region*. Physical Review Letters **102**, 213904 (2009).
34. P. Tzallas, E. Skantzakis, L.A.A. Nikolopoulos, G.D. Tsakiris and D. Charalambidis. *Extreme-ultraviolet pump-probe studies of one-femtosecond-scale electron dynamics*. Nature Physics **7**, 781 (2011).

35. E.J. Takahashi, P. Lan, O.D. Mücke, Y. Nabekawa and K. Midorikawa. *Attosecond nonlinear optics using gigawatt-scale isolated attosecond pulses*. Nature Communications **4**, 2691 (2013).
36. L. Gallmann, J. Herrmann, R. Locher, M. Sabbar, A. Ludwig, M. Lucchini and U. Keller. *Resolving intra-atomic electron dynamics with attosecond transient absorption spectroscopy*. Molecular Physics **111**, 2243 (2013).
37. M. I. Stockman, M. F. Kling, U. Kleineberg and F. Krausz. *Attosecond nanoplasmonic-field microscope*. Nature Photonics **1**, 539–544 (2007).
38. H.N. Chapman, A. Barty, M.J. Bogan, S. Boutet, M. Frank, S.P. Hau-Riege, S. Marchesini, B.W. Woods, S. Bajt, W.H. Benner, R.A. London, E. Plönjes, M. Kuhlmann, R. Treusch, S. Düsterer, T. Tschentscher, J.R. Schneider, E. Spiller, T. Möller, C. Bostedt, M. Hoener, D.A. Shapiro, K.O. Hodgson, D. Van Der Spoel, F. Burmeister, M. Bergh, C. Caleman, G. Hultdt, M.M. Seibert, F.R.N.C. Maia, R.W. Lee, A. Szöke, N. Timneanu and J. Hajdu. *Femtosecond diffractive imaging with a soft-X-ray free-electron laser*. Nature Physics **2**, 839 (2006).
39. A. Mikkelsen, J. Schwenke, T. Fordell, G. Luo, K. Klünder, E. Hilner, N. Anttu, A. A. Zakharov, E. Lundgren, J. Mauritsson, J. N. Andersen, H. Q. Xu and A. L’Huillier. *Photoemission electron microscopy using extreme ultraviolet attosecond pulse trains*. Review Of Scientific Instruments **80**, 123703 (2009).
40. S. H. Chew, F. Süßmann, C. Späth, A. Wirth, J. Schmidt, S. Zherebtsov, A. Guggenmos, A. Oelsner, N. Weber, J. Kapaldo, A. Gliserin, M. I. Stockman, M. F. Kling and U. Kleineberg. *Time-of-flight-photoelectron emission microscopy on plasmonic structures using attosecond extreme ultraviolet pulses*. Applied Physics Letters **100**, 5 (2012).
41. K. Midorikawa, Y. Nabekawa and A. Suda. *XUV multiphoton processes with intense high-order harmonics*. Progress in Quantum Electronics **32**, 43 (2008).
42. P. Tzallas, D. Charalambidis, N.A. Papadogiannis, K. Witte and G.D. Tsakiris. *Direct observation of attosecond light bunching*. Nature **426**, 267 (2003).
43. B. Manschwetus *et al.* *Manuscript in preparation* (2014).
44. T. Haarlammert and H. Zacharias. *Application of high harmonic radiation in surface science*. Current Opinion in Solid State and Materials Science **13**, 13 (2009).
45. M. Bauer, C. Lei, K. Read, R. Tobey, J. Gland, M.M. Murnane and H.C. Kapteyn. *Direct observation of surface chemistry using ultrafast soft-x-ray pulses*. Physical Review Letters **87**, 025501/1 (2001).
46. S. Eich, A. Stange, A.V. Carr, J. Urbancic, T. Popmintchev, M. Wiesenmayer, K. Jansen, A. Ruffing, S. Jakobs, T. Rohwer, S. Hellmann, C. Chen, P. Matyba, L. Kipp, K. Rossnagel, M. Bauer, M.M. Murnane, H.C. Kapteyn, S. Mathias and M. Aeschlimann. *Time- and angle-resolved photoemission spectroscopy with optimized high-harmonic pulses using frequency-doubled Ti:Sapphire lasers*. Journal of Electron Spectroscopy and Related Phenomena **article in press** (2014).

47. E. Turgut, C. La-O-Vorakiat, J.M. Shaw, P. Grychtol, H.T. Nembach, D. Rudolf, R. Adam, M. Aeschlimann, C.M. Schneider, T.J. Silva, M.M. Murnane, H.C. Kapteyn and S. Mathias. *Controlling the competition between optically induced ultrafast spin-flip scattering and spin transport in magnetic multilayers*. Physical Review Letters **110**, 197201 (2013).
48. R. Carley, K. Döbrich, B. Frietsch, C. Gahl, M. Teichmann, O. Schwarzkopf, P. Wernet and M. Weinelt. *Femtosecond laser excitation drives ferromagnetic gadolinium out of magnetic equilibrium*. Physical Review Letters **109**, 057401 (2012).
49. Cheng-Tien Chiang, Alexander Blattermann, Michael Huth, Jurgen Kirschner and Wolf Widdra. *High-order harmonic generation at 4 MHz as a light source for time-of-flight photoemission spectroscopy*. Applied Physics Letters **101**, 071116–071116–4 (2012).
50. S. Hellmann, T. Rohwer, M. Kalläne, K. Hanff, C. Sohrt, A. Stange, A. Carr, M.M. Murnane, H.C. Kapteyn, L. Kipp, M. Bauer and K. Rossnagel. *Time-domain classification of charge-density-wave insulators*. Nature Communications **3**, 1069 (2012).
51. H. Dachraoui, M. Michelswirth, P. Siffalovic, P. Bartz, C. Schäfer, B. Schnatwinkel, J. Mattay, W. Pfeiffer, M. Drescher and U. Heinzmann. *Photoinduced reconfiguration cycle in a molecular adsorbate layer studied by femtosecond inner-shell photoelectron spectroscopy*. Physical Review Letters **106**, 107401 (2011).
52. G.L. Dakovski, Y. Li, S.M. Gilbertson, G. Rodriguez, A.V. Balatsky, J.-X. Zhu, K. Gofryk, E.D. Bauer, P.H. Tobash, A. Taylor, J.L. Sarrao, P.M. Oppeneer, P.S. Riseborough, J.A. Mydosh and T. Durakiewicz. *Anomalous femtosecond quasiparticle dynamics of hidden order state in URu₂Si₂*. Physical Review B - Condensed Matter and Materials Physics **84**, 161103 (2011).
53. K. Ishizaka, T. Kiss, T. Yamamoto, Y. Ishida, T. Saitoh, M. Matsunami, R. Eguchi, T. Ohtsuki, A. Kosuge, T. Kanai, M. Nohara, H. Takagi, S. Watanabe and S. Shin. *Femtosecond core-level photoemission spectroscopy on 1T-TaS₂ using a 60-eV laser source*. Physical Review B - Condensed Matter and Materials Physics **83**, 081104 (2011).
54. J.C. Petersen, S. Kaiser, N. Dean, A. Simoncig, H.Y. Liu, A.L. Cavalieri, C. Cacho, I.C.E. Turcu, E. Springate, F. Frassetto, L. Poletto, S.S. Dhesi, H. Berger and A. Cavalleri. *Clocking the melting transition of charge and lattice order in 1T-TaS₂ with ultrafast extreme-ultraviolet angle-resolved photoemission spectroscopy*. Physical Review Letters **107**, 177402 (2011).
55. R.W. Schoenlein, J.G. Fujimoto, G.L. Eesley and T.W. Capelhart. *Femtosecond relaxation dynamics of image-potential states*. Physical Review B **43**, 4688 (1991).
56. H. Petek and S. Ogawa. *Femtosecond time-resolved two-photon photoemission studies of electron dynamics in metals*. Progress in Surface Science **56**, 239 (1997).

57. M. Aeschlimann, M. Bauer, S. Pawlik, W. Weber, R. Burgermeister, D. Oberli and H.C. Siegmann. *Ultrafast spin-dependent electron dynamics in fcc Co*. Physical Review Letters **79**, 5158 (1997).
58. U. Höfer, I.L. Shumay, Ch. Reuß, U. Thomann, W. Wallauer and Th. Fauster. *Time-resolved coherent photoelectron spectroscopy of quantized electronic states on metal surfaces*. Science **277**, 1480 (1997).
59. N.-H. Ge, C.M. Wong, R.L. Lingle Jr., J.D. McNeill, K.J. Gaffney and C.B. Harris. *Femtosecond dynamics of electron localization at interfaces*. Science **279**, 202 (1998).
60. H. Petek, M.J. Weida, H. Nagano and S. Ogawa. *Real-time observation of adsorbate atom motion above a metal surface*. Science **288**, 1402 (2000).
61. C. Gahl, U. Bovensiepen, C. Frischkorn and M. Wolf. *Ultrafast dynamics of electron localization and solvation in ice layers on Cu(111)*. Physical Review Letters **89**, 1074021 (2002).
62. X.-Y. Zhu. *Electronic structure and electron dynamics at molecule-metal interfaces: Implications for molecule-based electronics*. Surface Science Reports **56**, 1 (2004).
63. T. Fauster, M. Weinelt and U. Höfer. *Quasi-elastic scattering of electrons in image-potential states*. Progress in Surface Science **82**, 224 (2007).
64. J. Güdde, M. Rohleder, T. Meier, S.W. Koch and U. Höfer. *Time-resolved investigation of coherently controlled electric currents at a metal surface*. Science **318**, 1287 (2007).
65. F. Schmitt, P.S. Kirchmann, U. Bovensiepen, R.G. Moore, L. Rettig, M. Krenz, J.-H. Chu, N. Ru, L. Perfetti, D.H. Lu, M. Wolf, I.R. Fisher and Z.-X. Shen. *Transient electronic structure and melting of a charge density wave in TbTe₃*. Science **321**, 1649 (2008).
66. T. Rohwer, S. Hellmann, M. Wiesenmayer, C. Sohrt, A. Stange, B. Slomski, A. Carr, Y. Liu, L.M. Avila, M. Kalläne, S. Mathias, L. Kipp, K. Rossnagel and M. Bauer. *Collapse of long-range charge order tracked by time-resolved photoemission at high momenta*. Nature **471**, 490 (2011).
67. G. Genoud, O. Guilbaud, E. Mengotti, S.-G. Pettersson, E. Georgiadou, E. Pourtal, C.-G. Wahlström and A. L’Huillier. *XUV digital in-line holography using high-order harmonics*. Applied Physics B: Lasers and Optics **90**, 533 (2008).
68. M. Zürich, S. Foertsch, M. Matzas, K. Pachmann, R. Kuth and C. Spielmann. *Apparatus and fast method for cancer cell classification based on high harmonic coherent diffraction imaging in reflection geometry*. Progress in Biomedical Optics and Imaging - Proceedings of SPIE **9033**, 90331O (2014).
69. J. Schwenke, A. Mai, M. Miranda, X. He, G. Genoud, A. Mikkelsen, S.-G. Pettersson, A. Persson and A. L’Huillier. *Single-shot holography using high-order harmonics*. Journal of Modern Optics **55**, 2723–2730 (2008).

-
70. S. Witte, V.T. Tenner, D.W. Noom and K.S. Eikema. *Lensless diffractive imaging with ultra-broadband table-top sources: From infrared to extreme-ultraviolet wavelengths*. *Light: Science and Applications* **3**, 2014.44 (2014).
 71. A. Cingöz, D.C. Yost, T.K. Allison, A. Ruehl, M.E. Fermann, I. Hartl and J. Ye. *Direct frequency comb spectroscopy in the extreme ultraviolet*. *Nature* **482**, 68 (2012).
 72. Ye.V. Baklanov and V.P. Chebotayev. *Narrow resonances of two-photon absorption of super-narrow pulses in a gas*. *Applied Physics* **12**, 97 (1977).
 73. S. Schiller. *Spectrometry with frequency combs*. *Optics Letters* **27**, 766 (2002).
 74. J.C. Berengut, V.A. Dzuba, V.V. Flambaum and A. Ong. *Electron-hole transitions in multiply charged ions for precision laser spectroscopy and searching for variations in alpha*. *Physical Review Letters* **106**, 210802 (2011).
 75. E.E. Eyler, D.E. Chieda, M.C. Stowe, M.J. Thorpe, T.R. Schibli and J. Ye. *Prospects for precision measurements of atomic helium using direct frequency comb spectroscopy*. *European Physical Journal D* **48**, 43 (2008).
 76. M.P. Hehlen, R.R. Greco, W.G. Rellergert, S.T. Sullivan, D. Demille, R.A. Jackson, E.R. Hudson and J.R. Torgerson. *Optical spectroscopy of an atomic nucleus: Progress toward direct observation of the ^{229}Th isomer transition*. *Journal of Luminescence* **133**, 91 (2013).
 77. J. G. Muga, R. S. Mayato and I. L. Egusquiza. *Time in Quantum Mechanics*. Springer Lecture Notes in Physics **734**, 2 (2008).
 78. F. Reiter, U. Graf, E.E. Serebryannikov, W. Schweinberger, M. Fiess, M. Schultze, A.M. Azzeer, R. Kienberger, F. Krausz, A.M. Zheltikov and E. Goulielmakis. *Route to attosecond nonlinear spectroscopy*. *Physical Review Letters* **105**, 243902 (2010).
 79. A. Wirth, M.Th. Hassan, I. Grguraš, J. Gagnon, A. Moulet, T.T. Luu, S. Pabst, R. Santra, Z.A. Alahmed, A.M. Azzeer, V.S. Yakovlev, V. Pervak, F. Krausz and E. Goulielmakis. *Synthesized light transients*. *Science* **334**, 195 (2011).
 80. E. Takahashi, Y. Nabekawa and K. Midorikawa. *Generation of 10- μJ coherent extreme-ultraviolet light by use of high-order harmonics*. *Optics Letters* **27**, 1920 (2002).
 81. A. Vernaleken, J. Weitenberg, T. Sartorius, P. Russbuedt, W. Schneider, S.L. Stebbings, M.F. Kling, P. Hommelhoff, H.-D. Hoffmann, R. Poprawe, F. Krausz, T.W. Hänsch and T. Udem. *Single-pass high-harmonic generation at 20.8 MHz repetition rate*. *Optics Letters* **36**, 3428 (2011).
 82. A.K. Mills, T.J. Hammond, M.H.C. Lam and D.J. Jones. *XUV frequency combs via femtosecond enhancement cavities*. *Journal of Physics B: Atomic, Molecular and Optical Physics* **45**, 142001 (2012).

83. Jean-Claude Diels and Wolfgang Rudolph. *Ultrashort Laser Pulse Phenomena: Fundamental, Techniques, and Applications on a Femtosecond Time Scale*. Academic Press San Diego (1996).
84. S. Akturk, X. Gu, P. Bowlan and R. Trebino. *Spatio-temporal couplings in ultrashort laser pulses*. *Journal of Optics* **12**, 093001 (2010).
85. P. Weinberger. *John Kerr and his effects found in 1877 and 1878*. *Philosophical Magazine Letters* **88**, 897 (2008).
86. P.B. Corkum. *Plasma perspective on strong field multiphoton ionization*. *Physical Review Letters* **71**, 1994 (1993).
87. K. C. Kulander, K. J. Schafer and J. L. Krause. *Dynamics of short-pulse excitation, ionization and harmonic conversion*. In *Super-Intense Laser-Atom Physics*. Plenum Press, New York (1993).
88. K. J. Schafer, B. Yang, L. F. DiMauro and K. C. Kulander. *Above threshold ionization beyond the high harmonic cutoff*. *Physical Review Letters* **70**, 1599 (1993).
89. V.S. Popov. *Tunnel and multiphoton ionization of atoms and ions in a strong laser field (Keldysh theory)*. *Physics-Uspexhi* **47**, 855 (2004).
90. J. L. Krause, K. J. Schafer and K. C. Kulander. *High-order harmonic generation from atoms and ions in the high intensity regime*. *Physical Review Letters* **68**, 3535 (1992).
91. M. Lewenstein, Ph. Balcou, M.Yu. Ivanov, A. L'Huillier and P.B. Corkum. *Theory of high-harmonic generation by low-frequency laser fields*. *Physical Review A* **49**, 2117 (1994).
92. A. L'Huillier, M. Lewenstein, P. Salières, Ph. Balcou, M. Yu. Ivanov, J. Larsson and C. G. Wahlström. *High-order harmonic generation cutoff*. *Physical Review A* **48**, R3433 (1993).
93. M. Dahlström. *Light-Matter Interaction on the Attosecond Timescale*. *Lund Reports on Atomic Physics, LRAP-438* (2011).
94. P. Salières, B. Carre, L. Le Deroff, F. Grasbon, G.G. Paulus, H. Walther, R. Kopold, W. Becker, D.B. Milosevic, A. Sanpera and M. Lewenstein. *Feynman's path-integral approach for intense-laser-atom interactions*. *Science* **292**, 902 (2001).
95. Y. Mairesse, A. De Bohan, L.J. Frasinski, H. Merdji, L.C. Dinu, P. Monchicourt, P. Breger, M. Kovačev, R. Taïeb, B. Carré, H.G. Muller, P. Agostini and P. Salières. *Attosecond Synchronization of High-Harmonic Soft X-rays*. *Science* **302**, 1540 (2003).
96. A.D. Bandrauk, S. Chelkowski, D.J. Diestler, J. Manz and K.-J. Yuan. *Quantum simulation of high-order harmonic spectra of the hydrogen atom*. *Physical Review A - Atomic, Molecular, and Optical Physics* **79**, 023403 (2009).

97. K. Varjú, Y. Mairesse, B. Carré, M.B. Gaarde, P. Johnsson, S. Kazamias, R. Lopez-Martens, J. Mauritsson, K.J. Schafer, Ph. Balcou, A. L'Huillier and P. Salières. *Frequency chirp of harmonic and attosecond pulses*. Journal of Modern Optics **52**, 379 (2005).
98. K. T. Kim, C. M. Kim, M.-G. Baik, G. Umesh and C. H. Nam. *Single sub-50-attosecond pulse generation from chirp-compensated harmonic radiation using material dispersion*. Physical Review A **69**, 051805 (2004).
99. Rodrigo López-Martens, Katalin Varjú, Per Johnsson, Johan Mauritsson, Yann Mairesse, Pascal Salières, Mette B. Gaarde, Kenneth J. Schafer, Anders Persson, Sune Svanberg, Claes-Göran Wahlström and Anne L'Huillier. *Amplitude and Phase Control of Attosecond Light Pulses*. Physical Review Letters **94**, 033001 (2005).
100. P. Salières, Ph. Antoine, A. de Bohan and M. Lewenstein. *Temporal and spectral tailoring of high-order harmonics*. Physical Review Letters **81**, 5544 (1998).
101. G. Sansone, C. Vozzi, S. Stagira, M. Pascolini, L. Poletto, P. Villoresi, G. Tondello, S. De Silvestri and M. Nisoli. *Observation of Carrier-Envelope Phase Phenomena in the Multi-Optical-Cycle Regime*. Physical Review Letters **92**, 113904 (2004).
102. G. Sansone, E. Benedetti, J.-P. Caumes, S. Stagira, C. Vozzi, M. Pascolini, L. Poletto, P. Villoresi, S. De Silvestri and M. Nisoli. *Measurement of Harmonic Phase Differences by Interference of Attosecond Light Pulses*. Physical Review Letters **94**, 193903 (2005).
103. H. R. Telle, G. Steinmeyer, A. E. Dunlop, J. Stenger, D. H. Sutter and U. Keller. *Carrier-envelope offset phase control: A novel concept for absolute optical frequency measurement and ultrashort pulse generation*. Applied Physics B **69**, 327 (1999).
104. A. Baltuška, Th. Udem, M. Uiberacker, M. Hentschel, E. Goulielmakis, Ch. Gohle, R. Holzwarth, V.S. Yakovlev, A. Scrinzi, T.W. Hänsch and F. Krausz. *Attosecond control of electronic processes by intense light fields*. Nature **421**, 611 (2003).
105. M. Nisoli, G. Sansone, S. Stagira, S. De Silvestri, C. Vozzi, M. Pascolini, L. Poletto, P. Villoresi and G. Tondello. *Effects of carrier-envelope phase differences of few-optical-cycle light pulses in single-shot high-order-harmonic spectra*. Physical Review Letters **91**, 213905/1 (2003).
106. E. Mansten, J.M. Dahlström, J. Mauritsson, T. Ruchon, A. L'Huillier, J. Tate, M.B. Gaarde, P. Eckle, A. Guandalini, M. Holler, F. Schapper, L. Gallmann and U. Keller. *Spectral signature of short attosecond pulse trains*. Physical Review Letters **102**, 083002 (2009).
107. C. Ott, M. Schönwald, P. Raith, A. Kaldun, G. Sansone, M. Krüger, P. Hommelhoff, Y. Patil, Y. Zhang, K. Meyer, M. Laux and T. Pfeifer. *Strong-field spectral interferometry using the carrier-envelope phase*. New Journal of Physics **15**, 073031 (2013).

108. M. Krebs, S. Hädrich, S. Demmler, J. Rothhardt, A. Zair, L. Chipperfield, J. Limpert and A. Tünnermann. *Towards isolated attosecond pulses at megahertz repetition rates*. Nature Photonics **7**, 555 (2013).
109. K. Zhao, Q. Zhang, M. Chini, Y. Wu, X. Wang and Z. Chang. *Tailoring a 67 attosecond pulse through advantageous phase-mismatch*. Optics Letters **37**, 3891 (2012).
110. I.J. Sola, E. Mével, L. Elouga, E. Constant, V. Strelkov, L. Poletto, P. Villorosi, E. Benedetti, J.-P. Caumes, S. Stagira, C. Vozzi, G. Sansone and M. Nisoli. *Controlling attosecond electron dynamics by phase-stabilized polarization gating*. Nature Physics **2**, 319 (2006).
111. G. Sansone, E. Benedetti, F. Calegari, C. Vozzi, L. Avaldi, R. Flammini, L. Poletto, P. Villorosi, C. Altucci, R. Velotta, S. Stagira, S. De Silvestri and M. Nisoli. *Isolated single-cycle attosecond pulses*. Science **314**, 443 (2006).
112. F. Ferrari, F. Calegari, M. Lucchini, C. Vozzi, S. Stagira, G. Sansone and M. Nisoli. *High-energy isolated attosecond pulses generated by above-saturation few-cycle fields*. Nature Photonics **4**, 875 (2010).
113. E. Goulielmakis, M. Schultze, M. Hofstetter, V.S. Yakovlev, J. Gagnon, M. Uiberacker, A.L. Aquila, E.M. Gullikson, D.T. Attwood, R. Kienberger, F. Krausz and U. Kleineberg. *Single-cycle nonlinear optics*. Science **320**, 1614 (2008).
114. R. Kienberger, E. Goulielmakis, M. Uiberacker, A. Baltuška, V. Yakovlev, F. Bammer, A. Scrinzi, Th. Westerwalbesloh, U. Kleineberg, U. Heinzmann, M. Drescher and F. Krausz. *Atomic transient recorder*. Nature **427**, 817 (2004).
115. T. Witting, F. Frank, W.A. Okell, C.A. Arrell, J.P. Marangos and J.W.G. Tisch. *Sub-4-fs laser pulse characterization by spatially resolved spectral shearing interferometry and attosecond streaking*. Journal of Physics B: Atomic, Molecular and Optical Physics **45**, 074014 (2012).
116. H. Vincenti and F. Quéré. *Attosecond lighthouses: How to use spatiotemporally coupled light fields to generate isolated attosecond pulses*. Physical Review Letters **108**, 113904 (2012).
117. M. Chini, K. Zhao and Z. Chang. *The generation, characterization and applications of broadband isolated attosecond pulses*. Nature Photonics **8**, 178 (2014).
118. J. Mauritsson, P. Johnsson, E. Gustafsson, A. L'Huillier, K.J. Schafer and M.B. Gaarde. *Attosecond pulse trains generated using two color laser fields*. Physical Review Letters **97**, 013001 (2006).
119. Ximao Feng, Steve Gilbertson, Hiroki Mashiko, He Wang, Sabih D. Khan, Michael Chini, Yi Wu, Kun Zhao and Zenghu Chang. *Generation of Isolated Attosecond Pulses with 20 to 28 Femtosecond Lasers*. Physical Review Letters **103**, 183901 (2009).
120. H. Mashiko, S. Gilbertson, C. Li, S.D. Khan, M.M. Shakya, E. Moon and Z. Chang. *Double optical gating of high-order harmonic generation with carrier-envelope phase stabilized lasers*. Physical Review Letters **100**, 103906 (2008).

121. H. G. Muller. *Reconstruction of attosecond harmonic beating by interference of two-photon transitions*. Applied Physics B **74**, 17 (2002).
122. Y. Mairesse and F. Quéré. *Frequency-resolved optical gating for complete reconstruction of attosecond bursts*. Physical Review A **71**, 011401(R) (2005).
123. R. Kienberger, M. Hentschel, M. Uiberacker, C. Spielmann, M. Kitzler, A. Scrinzi, M. Wieland, T. Westerwalbesloh, U. Kleineberg, U. Heinzmann, M. Drescher and F. Krausz. *Steering attosecond electron wave packets with light*. Science **297**, 1144 (2002).
124. F. Quéré, Y. Mairesse and J. Itatani. *Temporal characterization of attosecond XUV fields*. Journal of Modern Optics **52**, 339 (2005).
125. K.T. Kim, C. Zhang, A.D. Shiner, S.E. Kirkwood, E. Frumker, G. Gariepy, A. Naumov, D.M. Villeneuve and P.B. Corkum. *Manipulation of quantum paths for space-time characterization of attosecond pulses*. Nature Physics **9**, 159 (2013).
126. P. Balcou, P. Salières, A. L’Huillier and M. Lewenstein. *Generalized phase-matching conditions for high harmonics: The role of field-gradient forces*. Physical Review A **55**, 3204–3210 (1997).
127. E. Constant, D. Garzella, P. Breger, E. Mével, Ch. Dorrer, C. Le Blanc, F. Salin and P. Agostini. *Optimizing High Harmonic Generation in Absorbing Gases: Model and Experiment*. Physical Review Letters **82**, 1668 (1999).
128. S. Kazamias, D. Douillet, F. Weihe, C. Valentin, A. Rousse, S. Sebban, G. Grillon, F. Augé, D. Hulin and Ph. Balcou. *Global Optimization of High Harmonic Generation*. Physical Review Letters **90**, 193901 (2003).
129. T. Popmintchev, M.-C. Chen, A. Bahabad, M. Gerrity, P. Sidorenko, O. Cohen, I.P. Christov, M.M. Murnane and H.C. Kapteyn. *Phase matching of high harmonic generation in the soft and hard X-ray regions of the spectrum*. Proceedings of the National Academy of Sciences of the United States of America **106**, 10516 (2009).
130. M.B. Gaarde, J.L. Tate and K.J. Schafer. *Macroscopic aspects of attosecond pulse generation*. Journal of Physics B: Atomic, Molecular and Optical Physics **41** (2008).
131. S. Kazamias, S. Daboussi, O. Guilbaud, K. Cassou, D. Ros, B. Cros and G. Maynard. *Pressure-induced phase matching in high-order harmonic generation*. Physical Review A - Atomic, Molecular, and Optical Physics **83**, 063405 (2011).
132. A. Rundquist, C.G. Durfee III, Z. Chang, C. Herne, S. Backus, M.M. Murnane and H.C. Kapteyn. *Phase-matched generation of coherent soft x-rays*. Science **280**, 1412 (1998).
133. M. Lewenstein, P. Salières and A. Lhuillier. *Phase of the atomic polarization in high-order harmonic generation*. Physical Review A **52**, 4747 (1995).

134. Peter Schwerdtfeger. Table of experimental and calculated static dipole polarizabilities (2008). CTCP, Massey University, Auckland, New Zealand.
135. B.L. Henke, E.M. Gullikson and J.C. Davis. *X-ray interactions: Photoabsorption, scattering, transmission, and reflection at $E = 50\text{-}30,000$ eV, $Z = 1\text{-}92$* . Atomic Data and Nuclear Data Tables **54**, 181 (1993).
136. Eric Gullikson. X-Ray Interactions With Matter (2014). http://henke.lbl.gov/optical_constants/.
137. M. V. Ammosov, N. B. Delone and V. P. Krainov. *Tunnel ionization of complex atoms and of atomic ions in an alternating electromagnetic field*. Soviet Physics - JETP **64**, 1191–1194 (1986).
138. E. Yablonovitch. *Self-phase modulation and short-pulse generation from laser-breakdown plasmas*. Physical Review A **10**, 1888 (1974).
139. A. Couairon and A. Mysyrowicz. *Femtosecond filamentation in transparent media*. Physics Reports **441**, 47 (2007).
140. A. Dubrouil, O. Hort, F. Catoire, D. Descamps, S. Petit, E. Mevel, V.V. Strelkov and E. Constant. *Spatio-spectral structures in high-harmonic beams generated with Terawatt 10-fs pulses*. Nature Physics **6**, 4637 (2014).
141. S. Kazamias, S. Daboussi, O. Guilbaud, K. Cassou, C. Montet, O. Neveu, B. Cros, D. Ros and G. Maynard. *The super-quadratic growth of high-harmonic signal as a function of pressure*. Nature Physics **6**, 12 (2010).
142. P.D. Maker, R.W. Terhune, M. Nisenoff and C.M. Savage. *Effects of dispersion and focusing on the production of optical harmonics*. Physical Review Letters **8**, 21 (1962).
143. J. Rothhardt, M. Krebs, S. Hädrich, S. Demmler, J. Limpert and A. Tünnermann. *Absorption-limited and phase-matched high harmonic generation in the tight focusing regime*. New Journal of Physics **16**, 033022 (2014).
144. A. Zaïr, M. Holler, F. Schapper, J. Biegert, L. Gallmann, U. Keller, A. S. Wyatt, A. Monmayrant, I. A. Walmsley, E. Cormier, T. Auguste, J. P. Caumes and P. Salières. *Quantum Path Interferences in High-Order Harmonic Generation*. Physical Review Letters **100**, 143902–1–4 (2008).
145. E. Brunetti, R. Issac and D. A. Jaroszynski. *Quantum path contribution to high-order harmonic spectra*. Physical Review A **77**, 6 (2008).
146. H. Xu, H. Xiong, Z. N. Zeng, Y. X. Fu, J. P. Yao, R. X. Li, Y. Cheng and Z. Z. Xu. *Fine interference fringes formed in high-order harmonic spectra generated by infrared driving laser pulses*. Physical Review A **78**, 3 (2008).
147. E. Cormier, A. Zaïr, M. Holler, F. Schapper, U. Keller, A. Wyatt, A. Monmayrant, I. Walmsley, T. Auguste and P. Salières. *Direct observation of quantum-path interferences in high order harmonic generation*. European Physical Journal-Special Topics **175**, 191–194 (2009).

148. P. Liu, Z. N. Zeng, Y. X. Li, S. T. Zhao, X. F. Li, R. X. Li and Z. Z. Xu. *Quantum path selection and control in high-order harmonic generation using a spatially shaped laser beam*. Physical Review A **79**, 5 (2009).
149. M. Holler, A. Zaïr, F. Schapper, T. Auguste, E. Cormier, A. Wyatt, A. Monmayrant, I. A. Walmsley, L. Gallmann, P. Salieres and U. Keller. *Ionization effects on spectral signatures of quantum-path interference in high-harmonic generation*. Optics Express **17**, 5716–5722 (2009).
150. A. Zaïr, T. Siegel, S. Sukiasyan, F. Risoud, L. Brugnera, C. Hutchison, Z. Diveki, T. Auguste, J.W.G. Tisch, P. Salières, M.Y. Ivanov and Marangos. *Molecular internal dynamics studied by quantum path interferences in high order harmonic generation*. Chemical Physics **414**, 184 (2013).
151. J. Jiang, P. Wei, Z. Zeng, J. Miao, Y. Zheng, X. Ge, C. Li, R. Li and Z. Xu. *Spatially and spectrally resolved quantum-path tracing in high-order harmonic generation*. Optics Express **22**, 15975 (2014).
152. C.M. Heyl, J. Güdde, A. L’huillier and U. Höfer. *High-order harmonic generation with J laser pulses at high repetition rates*. Journal of Physics B: Atomic, Molecular and Optical Physics **45**, 074020 (2012).
153. C.D. Perciante and J.A. Ferrari. *Fast Hankel transform of n th order with improved performance*. Journal of the Optical Society of America A: Optics and Image Science, and Vision **21**, 1811 (2004).
154. A. Cabasse, G. Machinet, A. Dubrouil, E. Cormier and E. Constant. *Optimization and phase matching of fiber-laser-driven high-order harmonic generation at high repetition rate*. Optics Letters **37**, 4618 (2012).
155. J. Lee, D.R. Carlson and R.J. Jones. *Optimizing intracavity high harmonic generation for XUV fs frequency combs*. Optics Express **19**, 23315 (2011).
156. F. Lindner, W. Stremme, M.G. Schätzel, F. Grasbon, G.G. Paulus, H. Walther, R. Hartmann and L. Strüder. *High-order harmonic generation at a repetition rate of 100 kHz*. Physical Review A - Atomic, Molecular, and Optical Physics **68**, 013814/1 (2003).
157. S. Hädrich, A. Klenke, J. Rothhardt, M. Krebs, A. Hoffmann, O. Pronin, V. Pervak, J. Limpert and A. Tünnermann. *High photon flux table-top coherent extreme-ultraviolet source*. Nature Photonics **8**, 779 (2014).
158. A. L’Huillier, K. J. Schafer and K. C. Kulander. *Theoretical aspects of intense field harmonic-generation*. Journal of Physics B **24**, 3315–3341 (1991).
159. E. Takahashi, Y. Nabekawa, T. Otsuka, M. Obara and K. Midorikawa. *Generation of highly coherent submicrojoule soft x rays by high-order harmonics*. Physical Review A - Atomic, Molecular, and Optical Physics **66**, 021802/1 (2002).
160. W. Boutu, T. Auguste, J.P. Caumes, H. Merdji and B. Carré. *Scaling of the generation of high-order harmonics in large gas media with focal length*. Physical Review A - Atomic, Molecular, and Optical Physics **84**, 053819 (2011).

161. E.J. Takahashi, Y. Nabekawa, H. Mashiko, H. Hasegawa, A. Suda and K. Midorikawa. *Generation of strong optical field in soft X-ray region by using high-order harmonics*. IEEE Journal on Selected Topics in Quantum Electronics **10**, 1315 (2004).
162. S. Kim, J. Jin, Y.-J. Kim, I.-Y. Park, Y. Kim and S.-W. Kim. *High-harmonic generation by resonant plasmon field enhancement*. Nature **453**, 757 (2008).
163. M. Sivis, M. Duwe, B. Abel and C. Ropers. *Nanostructure-enhanced atomic line emission*. Nature **484**, 7397 (2012).
164. M. Sivis, M. Duwe, B. Abel and C. Ropers. *Extreme-ultraviolet light generation in plasmonic nanostructures*. Nature Physics **9**, 304 (2013).
165. E. Seres, J. Seres and C. Spielmann. *Extreme ultraviolet light source based on intracavity high harmonic generation in a mode locked Ti:sapphire oscillator with 9.4 MHz repetition rate*. Optics Express **20**, 6185 (2012).
166. J. Matyschok, T. Lang, T. Binhammer, O. Prochnow, S. Rausch, M. Schultze, A. Harth, P. Rudawski, C.L. Arnold, A. L'Huillier and U. Morgner. *Temporal and spatial effects inside a compact and CEP stabilized, few-cycle OPCPA system at high repetition rates*. Optics Express **21**, 29656 (2013).
167. M. Nisoli, S. De Silvestri and O. Svelto. *Generation of high energy 10 fs pulses by a new pulse compression technique*. Applied Physics Letters **68**, 2793 (1996).
168. C.L. Arnold, B. Zhou, S. Akturk, S. Chen, A. Couairon and A. Mysyrowicz. *Pulse compression with planar hollow waveguides: A pathway towards relativistic intensity with table-top lasers*. New Journal of Physics **12**, 073015 (2010).
169. A. Klenke, S. Breitkopf, M. Kienel, T. Gottschall, T. Eidam, S. Hädrich, J. Rothhardt, J. Limpert and A. Tünnermann. *530 W, 1.3 mJ, four-channel coherent combined femtosecond fiber chirped-pulse amplification system*. Optics Letters **38**, 2283 (2013).
170. A. Dubietis, R. Butkus and A.P. Piskarskas. *Trends in chirped pulse optical parametric amplification*. IEEE Journal on Selected Topics in Quantum Electronics **12**, 163 (2006).
171. P. Rudawski. *Second-generation High-Order Harmonic Sources – From CPA to OPCPA*. Lund Reports on Atomic Physics, LRAP-487 (2014).
172. S. Watanabe, K. Kondo, Y. Nabekawa, A. Sagisaka and Y. Kobayashi. *Two-color phase control in tunneling ionization and harmonic generation by a strong laser field and its third harmonic*. Physical Review Letters **73**, 2692 (1994).
173. Kenichi Ishikawa. *Photoemission and Ionization of He⁺ under Simultaneous Irradiation of Fundamental Laser and High-Order Harmonic Pulses*. Physical Review Letters **91**, 043002 (2003).
174. L.E. Chipperfield, J.S. Robinson, J.W.G. Tisch and J.P. Marangos. *Ideal waveform to generate the maximum possible electron recollision energy for any given oscillation period*. Physical Review Letters **102**, 063003 (2009).

-
175. K. J. Schafer, M. B. Gaarde, A. Heinrich, J. Biegert and U. Keller. *Strong Field Quantum Path Control Using Attosecond Pulse Trains*. Physical Review Letters **92**, 23003 (2004).
176. Mette B. Gaarde, Kenneth J. Schafer, Arne Heinrich, Jens Biegert and Ursula Keller. *Large enhancement of macroscopic yield in attosecond pulse train-assisted harmonic generation*. Physical Review A **72**, 013411 (2005).
177. Eiji J. Takahashi, Tsuneto Kanai, Kenichi L. Ishikawa, Yasuo Nabekawa and Katsumi Midorikawa. *Dramatic Enhancement of High-Order Harmonic Generation*. Physical Review Letters **99**, 053904 (2007).
178. P. B ejot, G. Karras, F. Billard, E. Hertz, B. Lavorel, E. Cormier and O. Faucher. *Harmonic generation and nonlinear propagation: When secondary radiations have primary consequences*. Physical Review Letters **112**, 203902 (2014).
179. N. Dudovich, O. Smirnova, J. Levesque, Y. Mairesse, M.Y. Ivanov, D.M. Villeneuve and P.B. Corkum. *Measuring and controlling the birth of attosecond XUV pulses*. Nature Physics **2**, 781 (2006).
180. T. Popmintchev, M.-C. Chen, P. Arpin, M.M. Murnane and H.C. Kapteyn. *The attosecond nonlinear optics of bright coherent X-ray generation*. Nature Photonics **4**, 822 (2010).
181. U. Teubner and P. Gibbon. *High-order harmonics from laser-irradiated plasma surfaces*. Reviews of Modern Physics **81**, 445 (2009).
182. P. Di Trapani, A. Andreoni, G.P. Banfi, C. Solcia, R. Danielius, A. Piskarskas, P. Foggi, M. Monguzzi and C. Sozzi. *Group-velocity self-matching of femtosecond pulses in noncollinear parametric generation*. Physical Review A **51**, 3164 (1995).
183. A.V. Birulin, V.T. Platonenko and V.V. Strelkov. *High-order harmonic generation in colliding beams*. Quantum Electronics **26**, 377 (1996).
184. S.V. Fomichev, P. Breger, B. Carre, P. Agostini and D.F. Zaretsky. *Non-collinear high-harmonic generation*. Laser Physics **12**, 383 (2002).
185. K.D. Moll, R.J. Jones and J. Ye. *Output coupling methods for cavity-based high-harmonic generation*. Optics Express **14**, 8189 (2006).
186. W. Jian and Z. Heping. *Cavity-enhanced noncollinear high-harmonic generation for extreme ultraviolet frequency combs*. Optics Letters **32**, 3315 (2007).
187. A. Ozawa, A. Vernaleken, W. Schneider, I. Gotlibovych, Th. Udem and T.W. H ansch. *Non-collinear high harmonic generation: A promising outcoupling method for cavity-assisted XUV generation*. Optics Express **16**, 6233 (2008).
188. J.B. Bertrand, H.J. W rner, H.-C. Bandulet, A. Bisson, M. Spanner, J.-C. Kieffer, D.M. Villeneuve and P.B. Corkum. *Ultra-high-order wave mixing in non-collinear high harmonic generation*. Physical Review Letters **106**, 023001 (2011).

189. S. Daboussi, S. Kazamias, K. Cassou, O. Guilbaud, M. Pittman, O. Delmas, O. Neveu, B. Cros, G. Maynard and D. Ros. *Double pulse quasi-collinear high harmonic generation scheme as a tool for X-ray laser plasma gain probing*. Applied Physics B: Lasers and Optics **111**, 7 (2013).
190. K.T. Kim, C. Zhang, A.D. Shiner, B.E. Schmidt, F. Légaré, D.M. Villeneuve and P.B. Corkum. *Petahertz optical oscilloscope*. Nature Photonics **7**, 958 (2013).
191. H. Eichmann, A. Egbert, S. Nolte, C. Momma, B. Wellegehausen, W. Becker, S. Long and J.K. McIver. *Polarization-dependent high-order two-color mixing*. Physical Review A **51**, R3414 (1995).
192. F. Quéré, H. Vincenti, A. Borot, S. Monchoc, T.J. Hammond, K.T. Kim, J.A. Wheeler, C. Zhang, T. Ruchon, T. Auguste, J.F. Hergott, D.M. Villeneuve, P.B. Corkum and R. Lopez-Martens. *Applications of ultrafast wavefront rotation in highly nonlinear optics*. Journal of Physics B: Atomic, Molecular and Optical Physics **47**, 124004 (2014).
193. K.T. Kim, C. Zhang, T. Ruchon, J.-F. Hergott, T. Auguste, D.M. Villeneuve, P.B. Corkum and F. Quéré. *Photonic streaking of attosecond pulse trains*. Nature Photonics **7**, 651 (2013).
194. I. Pupeza, S. Holzberger, T. Eidam, H. Carstens, D. Esser, J. Weitenberg, P. Rußbüldt, J. Rauschenberger, J. Limpert, Th. Udem, A. Tünnermann, T.W. Hänsch, A. Apolonski, F. Krausz and E. Fill. *Compact high-repetition-rate source of coherent 100Å eV radiation*. Nature Photonics **7**, 608 (2013).
195. J.A. Wheeler, A. Borot, S. Monchocé, H. Vincenti, A. Ricci, A. Malvache, R. Lopez-Martens and F. Quéré. *Attosecond lighthouses from plasma mirrors*. Nature Photonics **6**, 829 (2012).
196. D. Garzella, T. Hara, B. Carré, P. Salières, T. Shintake, H. Kitamura and M.E. Couprie. *Using VUV high-order harmonics generated in gas as a seed for single pass FEL*. Nuclear Instruments and Methods in Physics Research, Section A: Accelerators, Spectrometers, Detectors and Associated Equipment **528**, 502 (2004).
197. G. Lambert, T. Hara, D. Garzella, T. Tanikawa, M. Labat, B. Carré, H. Kitamura, T. Shintake, M. Bougeard, S. Inoue, Y. Tanaka, P. Salières, H. Merdji, O. Chubar, O. Gobert, K. Tahara and M.-E. Couprie. *Injection of harmonics generated in gas in a free-electron laser providing intense and coherent extreme-ultraviolet light*. Nat Phys **4**, 296–300 (2008).
198. T. Togashi, E.J. Takahashi, K. Midorikawa, M. Aoyama, K. Yamakawa, T. Sato, A. Iwasaki, S. Owada, T. Okino, K. Yamanouchi, F. Kannari, A. Yagishita, H. Nakano, M.E. Couprie, K. Fukami, T. Hatsui, T. Hara, T. Kameshima, H. Kitamura, N. Kumagai, S. Matsubara, M. Nagasono, H. Ohashi, T. Ohshima, Y. Otake, T. Shintake, K. Tamasaku, H. Tanaka, T. Tanaka, K. Togawa, H. Tomizawa, T. Watanabe, M. Yabashi and T. Ishikawa. *Extreme ultraviolet free electron laser seeded with high-order harmonic of Ti: Sapphire laser*. Optics Express **19**, 317 (2011).

-
199. R.L. Sandberg, D.A. Raymondson, C. La-o vorakiat, A. Paul, K.S. Raines, J. Miao, M.M. Murnane, H.C. Kapteyn and W.F. Schlotter. *Tabletop soft-x-ray Fourier transform holography with 50 nm resolution*. Optics Letters **34**, 1618 (2009).
 200. *The International System of Units (SI)*. Organisation Intergouvernementale de la Convention du Mètre (2006).
 201. N. Hinkley, A. Sherman, N.B. Phillips, M. Schioppo, N.D. Lemke, K. Beloy, M. Pizzocaro, C.W. Oates and A.D. Ludlow. *An atomic clock with 10-18 instability*. Science **341**, 1215 (2013).
 202. W.H. Oskay, S.A. Diddams, E.A. Donley, T.M. Fortier, T.P. Heavner, L. Hollberg, W.M. Itano, S.R. Jefferts, M.J. Delaney, K. Kim, F. Levi, T.E. Parker and J.C. Bergquist. *Single-atom optical clock with high accuracy*. Physical Review Letters **97**, 020801 (2006).

PAPERS

Spectrally Resolved Maker Fringes in High-Order Harmonic Generation

C. M. Heyl, J. Gdde, U. Hfer and A. L'Huillier.

Physical Review Letters **107**, 033903 (2011).

Spectrally Resolved Maker Fringes in High-Order Harmonic Generation

C. M. Heyl,^{1,2} J. Güdde,¹ U. Höfer,^{1,3} and A. L'Huillier²¹Fachbereich Physik, Philipps-Universität Marburg, D-35032 Marburg, Germany²Department of Physics, Lund University, Post Office Box 118, SE-22100 Lund, Sweden³Donostia International Physics Centre (DIPC), Paseo de Manuel Lardizabal 4, 20018 San Sebastian, Spain

(Received 21 February 2011; published 12 July 2011)

We investigate macroscopic interference effects in high-order harmonic generation using a Ti:sapphire laser operating at a 100 kHz repetition rate. The structure and behavior of spectral and spatial interference fringes are explained and analytically described by transient phase matching of the long electron trajectory contribution. Time-frequency mapping due to the temporal chirp of the harmonic emission allows us to observe Maker fringes directly in the spectral domain.

DOI: 10.1103/PhysRevLett.107.033903

PACS numbers: 42.65.Ky, 42.65.Re

High-order harmonic generation (HHG) in gases is nowadays a well established method to generate coherent, extreme ultraviolet (XUV) radiation down to the attosecond time scale [1,2]. The rich physics behind HHG, which combines atoms in strong laser fields and nonlinear optics, has been progressively unraveled during the last 20 years. On the single-atom level, HHG is well described by a semiclassical three-step model: An electron wave packet leaves the atomic potential via tunneling, is accelerated by the external laser field, and recombines back to the ground state, thus emitting a burst of XUV radiation [3,4]. Two families of electron trajectories with different excursion times in the continuum contribute to the harmonic emission. These electron trajectories, or quantum paths, are called “short” and “long,” reflecting the duration of the excursion in the continuum.

Interference phenomena are intimately connected to HHG, determining the harmonic emission both on the single-atom level as well as macroscopically. Interferences between consecutive attosecond bursts lead to harmonic frequency combs, while macroscopic interferences between the fields emitted at different positions in the medium determine the efficiency of the frequency conversion process. The latter effect is commonly used to select a dominant quantum path. When the contributions of short and long trajectories become comparable and overlap, quantum path interferences (QPIs) may occur [5–9]. Such interference effects provide a unique tool for probing the single-atom dipole and may allow direct access to atomic or molecular structures and dynamics.

This Letter reports on interference effects occurring in the emission of individual harmonics. A high repetition rate laser system allows us to measure complex interference phenomena with high signal/noise ratio. We observe

interferences both in the harmonic spectra as a function of intensity and in the spatial far-field profiles. Similar effects have been previously observed and interpreted as QPIs [5,7,10–18]. Using an analytical model as well as numerical simulations, we show that these interferences occur due to the temporal variation of the phase matching conditions [19,20] for only one (the long) quantum path. The frequency modulation (chirp) of the emitted radiation leads to a mapping between time and frequency [5,21,22], which makes it possible to observe temporal Maker fringes directly in the spectral domain [23]. This new interpretation allows us to identify a common origin for several effects often observed in HHG such as spectral [5,7,10–16,25,26] and spatial [11,17] splitting, intensity modulation [7,13,18,27–29], and chirp dependence [5,30].

Generally, the yield S_q of harmonic order q can be expressed as

$$S_q \propto \left| \int_V P_q(\mathbf{r}) \exp(i\Delta\mathbf{k} \cdot \mathbf{r}) d\mathbf{r} \right|^2. \quad (1)$$

$P_q(\mathbf{r})$ denotes the laser-induced polarization in the medium at frequency $q\omega$, where ω is the laser frequency. $\Delta\mathbf{k}$ is the wave vector mismatch between the generated field and $P_q(\mathbf{r})$. In a one-dimensional case, assuming a constant wave vector mismatch and a constant nonlinear polarization strength within a short interaction volume of length L , the above equation reduces to

$$S_q \propto L^2 \text{sinc}^2\left(\frac{\Delta k L}{2\pi}\right). \quad (2)$$

S_q oscillates as a function of Δk , and/or L , leading to an interference pattern known as Maker fringes [31].

For HHG in a nonguiding medium, Δk is the sum of the wave vector mismatch due to the intensity-dependent single-atom dipole phase, Δk_q , the geometrical wave vector mismatch due to focusing, Δk_g , and the difference in wave vectors at frequencies $q\omega$ and ω , due to dispersion in the neutral medium and due to free electrons, Δk_d . The dispersion terms are small in our experimental conditions and will be neglected in the following argumen-

Published by the American Physical Society under the terms of the Creative Commons Attribution 3.0 License. Further distribution of this work must maintain attribution to the author(s) and the published article's title, journal citation, and DOI.

tation. The single-atom dipole phase φ_q can be calculated by considering the classical action along a specific quantum path (i.e., short or long trajectory) for harmonic order q and is well approximated by $\varphi_q = -\alpha_q I$, where I is the fundamental intensity [32]. Consequently, $\Delta k_q = -\alpha_q \partial I / \partial z$. During the laser pulse, I and therefore Δk_q and Δk vary with time. This leads to oscillations of the harmonic yield [33], i.e., Maker fringes in the time domain [34], as illustrated in the simulation presented in Fig. 1(a).

The intensity variation of the dipole phase does not only affect phase matching but also the spectral properties of the radiation. The instantaneous harmonic frequency during the pulse is given by [21,33]

$$\Omega_q(t) = q\omega + \alpha_q \frac{\partial I(t)}{\partial t}. \quad (3)$$

The first term denotes the central harmonic frequency, while the second term describes the variation of the instantaneous frequency due to the single-atom response. The phase modulation process effectively maps time to frequency [Fig. 1(b)], leading to a spectrally broadened harmonic pulse with a blueshifted leading edge and a redshifted trailing edge. Since the harmonic emission is confined to the central part of the light pulse, the mapping process is almost linear. The temporal modulation of the harmonic yield due to Maker fringes appears therefore as a spectral modulation [Fig. 1(c)] [24]. Both processes, the phase matching-induced modulation, as well as the effective mapping into the frequency domain, require α_q to be sufficiently large. Since $\alpha_q \approx 1-5 \times 10^{-14} \text{ cm}^2/\text{W}$ for the short trajectory and $\alpha_q \approx 20-25 \times 10^{-14} \text{ cm}^2/\text{W}$ for the long trajectory [35], Maker fringes are more easily observed for the long trajectory. For sufficiently long pulses

they do not depend on the laser carrier envelope phase (CEP) since both phase matching and time to frequency mapping are pure intensity effects. In conditions where consecutive harmonics overlap spectrally, an additional interference effect may appear which, however, washes out if the CEP is not stable [22,36].

In our experiments, we chose conditions where the long trajectory dominates the generation process. This implies a relatively tight focus geometry, as well as a positioning of the interaction cell close to the laser focus. We use a modified commercial Ti:sapphire laser system [37] delivering 45 fs pulses with energies up to $7 \mu\text{J}$ (without CEP stabilization). The laser beam (5 mm diameter) is focused by an achromatic lens ($f = 60 \text{ mm}$) into a continuous argon gas jet emitted from a nozzle with $100 \mu\text{m}$ inner diameter. A concave XUV grating is used to spectrally separate the harmonic emission onto a microchannel plate assembly. Because of grazing incidence, the grating acts as a spatial window, selecting $\pm 11 \text{ mrad}$ in the horizontal direction (the total divergence is approximately 50 mrad). The microchannel plate records the spectrum in this direction and the central part ($\pm 5 \text{ mrad}$) of the far-field profile in the vertical direction. The gas pressure inside the interaction cell is chosen to be relatively low (a few tens of mbar) to minimize dispersion and absorption effects. The pulse energy fluctuations of the fundamental laser field are less than 1% (rms deviation).

In Fig. 2(a) spatially integrated experimental spectra obtained with a gas jet at the focus (solid black line) and $\approx 0.2 \text{ mm}$ behind the focus (dashed gray line) are shown. In the latter case, the harmonics appear intense and spectrally narrow, which is typical for the short trajectory emission. In contrast the harmonics generated at the focus are spectrally broad, as expected from the long trajectory, and exhibit interference structures. Figure 2(b) presents the corresponding spatially resolved spectrum, with clear splitting of the harmonic lines. The number of additional fringes on each side of the central frequencies $q\omega$ increases with intensity and decreasing harmonic order, as shown in Figs. 2(c) and 2(d). The fringes follow an almost symmetric, nested shape, similar to those observed in [7] under different experimental conditions.

We performed numerical simulations for a time-dependent, three-dimensional harmonic source taking into account dispersion, absorption, and ionization effects. We used a simplified model for the single-atom response, deriving the phase of the dipole moment using classical trajectory calculations [3]. In accordance with previous experimental results, the amplitude of the dipole moment was assumed to scale as $I^{3/2}$ within the plateau [38]. The dependence of the dipole moment with harmonic order was adjusted to reproduce our experimental results. The numerical technique is a three-dimensional integration of Eq. (2) using Fourier-Hankel transform techniques. The integration in the far field is performed in accordance with the experimental geometry. Figure 2(d) presents the results

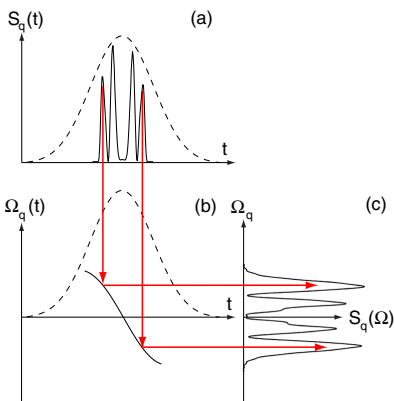


FIG. 1 (color online). Simulation of the mapping process for the 21st harmonic order: any temporal modulation of the harmonic signal $S_q(t)$ is mapped into the frequency domain due to a temporal modulation of the instantaneous harmonic frequency $\Omega_q(t)$. The dashed lines indicate the fundamental intensity profile.

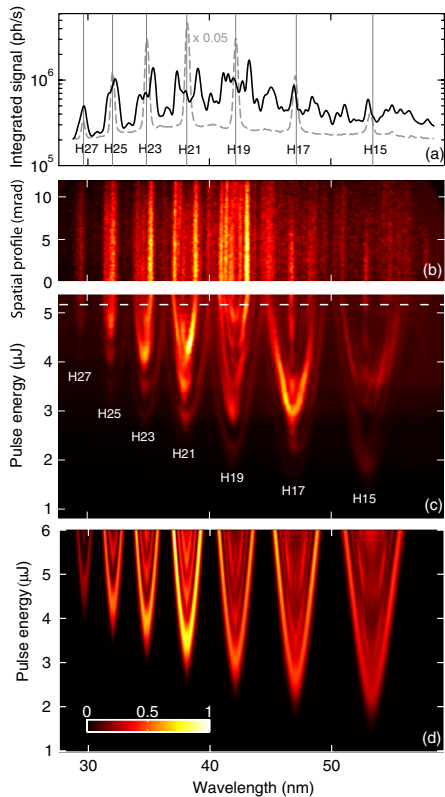


FIG. 2 (color online). Experimental (a–c) and simulated (d) harmonic spectra. (a) Spatially integrated signal measured when the gas jet was placed at the focus (black solid line) and 0.2 mm behind (gray dashed line); the signal strength was reduced by a factor of 0.05. (b) Far-field spatial profiles obtained at 5.2 μJ [white dashed line in (c)]. (c) and (d) show the experimental and simulated spatially integrated harmonic yield as a function of the driving pulse energy. The simulation only includes the long trajectory. (b–d) use the same normalized color scale as shown in (d).

of this simulation, considering only the contribution of the long trajectory. The experimentally observed interference patterns are well reproduced by the simulations.

The shape of the interference structures can be described analytically by examining the intensity dependence of the time-frequency mapping process. During the laser pulse phase matching is transiently optimized at certain intensities I_n , which are reached at given times t_n depending on the peak intensity I_0 . For a Gaussian intensity profile $I_n = I_0 \exp(-t_n^2/\sigma^2)$ where $\sigma = \tau/(2\sqrt{\ln 2})$ defines the temporal width with respect to the full width at half maximum τ . Equation (3) can be evaluated for a certain I_n leading to an equation for the instantaneous harmonic frequency Ω_q as a function of I_0 :

$$\Omega_q(I_0) = q\omega \pm \alpha_q \frac{I_n}{\sigma} 2\sqrt{\ln\left(\frac{I_0}{I_n}\right)}. \quad (4)$$

The equation can be inverted for direct comparison with the experimental spectrum as

$$I_0(\Omega_q) = I_n \exp\left[\frac{\sigma^2(q\omega - \Omega_q)^2}{4\alpha_q^2 I_n^2}\right]. \quad (5)$$

This equation describes the exponential shape of the maximum signal in the harmonic spectrum plotted as a function of the laser intensity (\propto pulse energy). It is indicated as dashed lines on the 21st harmonic signal shown in Fig. 3(a), for different intensities I_n , adjusting α_q for best agreement with the experimental result. Calibrating the intensity reached in our experiment using the cutoff law which defines the maximum photon energy $E_{\text{max}} = I_p + 3.17U_p$ (I_p and U_p are the ionization potential and the ponderomotive energy, respectively), the energy axis can be converted approximately into an intensity axis. We found $\alpha_{17-25} \approx 40 \times 10^{-14} \text{ cm}^2/\text{W}$, which is consistent for the long trajectory, being slightly higher than the values reported in the literature [35].

A consequence of temporal Maker fringes is the modulation of the harmonic signal with intensity. Figure 3(b) shows the spectrally integrated signal as a function of the peak intensity. Both experimental and simulated signals exhibit modulations, due to interference maxima [Fig. 3(a)]. The modulation contrast is limited by spectral and spatial integration. Similar effects have been observed in the past [18,27–29] with various interpretations involving resonances and QPIs. In the case examined in the present work, their origin can be clearly assigned to temporal Maker fringes.

Finally, we calculate in Fig. 4 the spatial properties 4(a)–4(c) and the spectrum as a function of the laser pulse energy 4(d)–4(f) for the 21st harmonic in three different cases. Figures 4(a) and 4(d) refer to the case examined previously, i.e., taking into account only the long trajectory and a nonlinear medium with low density. The intensity dependence of phase matching leads to a similar effect in the spatial domain as in the temporal domain. A mapping

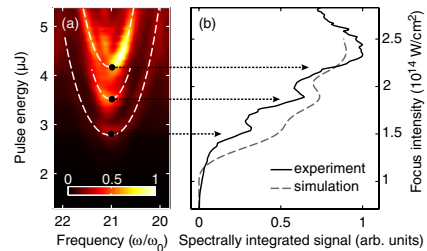


FIG. 3 (color online). Spectrally resolved (a) and integrated (b) harmonic signal as a function of the driving pulse energy for the 21st harmonic order. The white dashed lines are defined by Eq. (5), fitted to the experimental spectrum. Each line indicates a different transient phase matching intensity I_n .

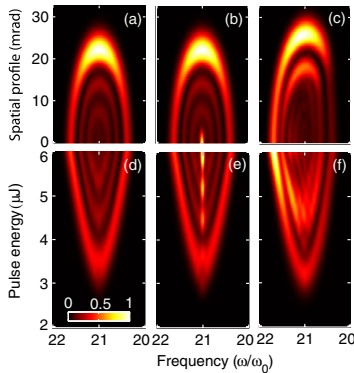


FIG. 4 (color online). (a–c) Spatially and spectrally resolved profiles for the 21st harmonic order calculated for a pulse energy of $6 \mu\text{J}$. (d–f) Spatially integrated (selecting ± 5 mrad of the central part) signal as a function of the driving pulse energy. In (a, c) and (d, f) only the long trajectory is included; in (b) and (e) a contribution from the short trajectory is added. In (c) and (f) the pressure was changed from 50 mbar (other figures) to 500 mbar and the intensity was slightly increased by setting the interaction medium closer to the focus.

between near-field and far-field profiles gives rise to phase matching rings in the far field. Figures 4(b) and 4(e) are calculated using the same conditions as for 4(a) and 4(d), with the addition of the short trajectory. This leads to an increased yield and interferences between both trajectories at the center of the spectral and spatial profiles. A similar feature can be observed in our experimental data (Fig. 2) for the 15th and 17th harmonic. Since the short trajectory contribution leads to well collimated and spectrally narrow harmonics [39], interference effects observed outside these regions involve the long trajectory only.

In Figs. 4(c) and 4(f), we examine the influence of ionization in relation to a higher gas density. Equation (3) can be generalized to include the ionization-induced chirp of the fundamental field by adding on the right $-q\partial\varphi_f/\partial t$, where φ_f denotes the phase of the fundamental pulse envelope, thus modifying the time to frequency mapping. Ionization also changes the phase matching conditions and reduces the number of contributing atoms on the trailing edge of the pulse [20]. Both effects lead to asymmetric temporal and spectral profiles. In general, the time-frequency mapping is modified when the fundamental field is chirped. A positive (negative) chirp decreases (increases) the spectral width of the individual harmonics.

In conclusion, we have identified spectral Maker fringes in HHG which originate from transient phase matching of the long trajectory contribution. This interference effect allows us to analyze and control the phase matching process as well as to spectrally and spatially tune the harmonic emission by changing the intensity and/or chirp of the fundamental pulse. The similarities between our results and previous experiments, where interference effects

were interpreted in terms of QPIs, suggest that macroscopic effects have to be considered. In general, our results beautifully illustrate the fascinating interplay between macroscopic and microscopic effects in HHG.

We thank Pascal Salières for valuable discussions. This research was supported by the Deutsche Forschungsgemeinschaft through HO 2295/1-2 and GRK 790, the European Research Council (ALMA), the Marie Curie Training Network ATTOFEL, the Knut and Alice Wallenberg foundation, and the Swedish Research Council.

- [1] F. Krausz and M. Ivanov, *Rev. Mod. Phys.* **81**, 163 (2009).
- [2] T. Popmintchev *et al.*, *Nat. Photon.* **4**, 822 (2010).
- [3] P. B. Corkum, *Phys. Rev. Lett.* **71**, 1994 (1993).
- [4] K. C. Kulander, K. J. Schafer, and J. L. Krause, in *Super-Intense Laser-Atom Physics* (Plenum Press, New York, 1993).
- [5] Z. Chang *et al.*, *Phys. Rev. A* **58**, R30 (1998).
- [6] K. Schiessl *et al.*, *Phys. Rev. Lett.* **99**, 253903 (2007).
- [7] A. Zaïr *et al.*, *Phys. Rev. Lett.* **100**, 143902 (2008).
- [8] J. Tate *et al.*, *Phys. Rev. Lett.* **98**, 013901 (2007).
- [9] M. V. Frolov, N. L. Manakov, and A. F. Starace, *Phys. Rev. Lett.* **100**, 173001 (2008).
- [10] H. Xu *et al.*, *Phys. Rev. A* **78**, 033841 (2008).
- [11] E. Brunetti, R. Issac, and D. A. Jaroszynski, *Phys. Rev. A* **77**, 023422 (2008).
- [12] M. Holler *et al.*, *Opt. Express* **17**, 5716 (2009).
- [13] E. Cormier *et al.*, *Eur. Phys. J. Special Topics* **175**, 191 (2009).
- [14] T. Auguste *et al.*, *Phys. Rev. A* **80**, 033817 (2009).
- [15] P. Liu *et al.*, *Phys. Rev. A* **79**, 063823 (2009).
- [16] X. He *et al.*, *Phys. Rev. A* **79**, 063829 (2009).
- [17] F. Schapper *et al.*, *Opt. Express* **18**, 2987 (2010).
- [18] J. E. Kruse *et al.*, *Phys. Rev. A* **82**, 033438 (2010).
- [19] S. Kazamias *et al.*, *Phys. Rev. Lett.* **90**, 193901 (2003).
- [20] T. Pfeifer *et al.*, *Opt. Express* **15**, 17120 (2007).
- [21] M. Gaarde *et al.*, *Phys. Rev. A* **59**, 1367 (1999).
- [22] G. Sansone *et al.*, *Phys. Rev. Lett.* **94**, 193903 (2005).
- [23] A similar effect has been observed in the third harmonic generation [24].
- [24] I. A. Heisler *et al.*, *Appl. Phys. Lett.* **92**, 091109 (2008).
- [25] Y. S. Wang *et al.*, *Phys. Rev. A* **62**, 063806 (2000).
- [26] Z. Fangchuan *et al.*, *Phys. Rev. A* **65**, 033808 (2002).
- [27] A. L’Huillier, P. Balcou, and L. A. Lompre, *Phys. Rev. Lett.* **68**, 166 (1992).
- [28] D. C. Yost *et al.*, *Nature Phys.* **5**, 815 (2009).
- [29] J. Seres *et al.*, *Nature Phys.* **6**, 455 (2010).
- [30] D. G. Lee *et al.*, *Phys. Rev. Lett.* **87**, 243902 (2001).
- [31] P. D. Maker *et al.*, *Phys. Rev. Lett.* **8**, 21 (1962).
- [32] M. Lewenstein, P. Salières, and A. L’Huillier, *Phys. Rev. A* **52**, 4747 (1995).
- [33] P. Salières *et al.*, *Adv. At. Mol. Opt. Phys.* **41**, 83 (1999).
- [34] S. Kazamias *et al.*, *Phys. Rev. A* **68**, 033819 (2003).
- [35] K. Varjú *et al.*, *J. Mod. Opt.* **52**, 379 (2005).
- [36] E. Mansten *et al.*, *Phys. Rev. Lett.* **102**, 083002 (2009).
- [37] C. M. Heyl *et al.* (unpublished).
- [38] C. G. Wahlström *et al.*, *Phys. Rev. A* **48**, 4709 (1993).
- [39] C. Lyngå *et al.*, *Phys. Rev. A* **60**, 4823 (1999).

High-Order Harmonic Generation with μJ Laser Pulses at High Repetition Rates

C.M. Heyl, J. Gdde, A. L'Huillier and U. Hfer.

Journal of Physics B **45**, 074020 (2012).

This paper was selected by the journal editors as a "*Highlight article 2012*".

High-order harmonic generation with μJ laser pulses at high repetition rates

C M Heyl^{1,2}, J Güdde¹, A L'Huillier² and U Höfer¹

¹ Fachbereich Physik, Philipps-Universität Marburg, Renthof 5, D-35032 Marburg, Germany

² Department of Physics, Lund University, PO Box 118, SE-22100 Lund, Sweden

E-mail: christoph.hey1@fysik.lth.se

Received 20 November 2011, in final form 19 January 2012

Published 16 March 2012

Online at stacks.iop.org/JPhysB/45/074020

Abstract

We investigate the generation of high-order harmonics using laser pulse energies in the few- μJ range at high repetition rates. We analyse how the conversion efficiency is influenced by the tight focusing geometry required for the generation of high-order harmonics under these conditions. A generalized phase-matching model allows us to discuss macroscopic phase effects independent of focal length. We present experimental results using the example of a 100 kHz laser system to generate harmonics up to the 27th order in Ar with a photon flux up to 3×10^9 photons s^{-1} into one harmonic order. High-repetition-rate femtosecond or even attosecond light sources open new possibilities for a broad range of applications such as time-resolved photoelectron spectroscopy and microscopy in the extreme ultraviolet regime.

(Some figures may appear in colour only in the online journal)

1. Introduction

High-order harmonic generation (HHG) in gases makes it possible to produce extreme ultraviolet (XUV) pulses on the femtosecond or even attosecond timescale that is of interest for a broad range of experiments in different fields of physics and chemistry [1, 2]. Since the generation itself requires intensities in the range of 10^{14} W cm^{-2} , high-power laser systems are normally used to drive this highly nonlinear light conversion process. Due to average power limitations, the repetition rate of such laser systems is usually low, i.e. less than a few kHz. However, many experiments would benefit greatly from a higher repetition rate, in the 100 kHz or even MHz range. In particular, there are a number of applications where ultrashort XUV pulses at high repetition rates are required without demanding a very high photon flux or XUV photon energies that could only be generated in very high harmonic orders.

This work was mainly motivated by the application of time-resolved photoelectron spectroscopy for studies of ultrafast dynamics in solids and at solid surfaces. In the last two decades, the use of visible or near-ultraviolet femtosecond pump and probe pulses in the so-called two-photon photoemission (2PPE) has enabled many novel experiments, probing the ultrashort lifetime of electronic excitations in

metals and at metal surfaces [3–7], the dynamics of adsorbate motion [8], electron localization and solvation at surfaces [9, 10], charge-transfer processes at molecular interfaces [11], coherently controlled electron currents [12], phase transitions and other ultrafast processes in solids [13]. These types of experiments can benefit from higher probe photon energies for a variety of reasons. First of all, the dynamics of holes, in addition to that of electrons, become more easily accessible [14]. Second, the range of detectable electron momenta can cover the complete surface Brillouin zone [15]. Last but not the least, variable photon energies allow—like in ultraviolet photoelectron spectroscopy (UPS) with synchrotron radiation—the suppression or enhancement of selected states due to energy-dependent photoemission cross-sections [16]. Unlike in time-resolved core-level spectroscopy employing high-harmonic sources [17], photon energies in excess of 40 eV are usually not required or even desirable. The signal-to-noise ratio, however, greatly benefits from high repetition rates since the number of emitted electrons per pulse has to be limited in order to avoid space charge effects. This is also important for time-resolved photoelectron microscopy studies [18, 19], where the spatial resolution of an photoelectron emission microscope could be combined with the temporal resolution of attosecond pulses. A high-repetition-rate high-harmonic source would, e.g., allow the

investigation of surface plasmons on attosecond timescales with a high signal-to-noise ratio [20].

A high repetition rate to improve statistics, while keeping the number of events per pulse at a very low level is also required for all kinds of coincidence measurements where more than one detected particle needs to be linked to the same excitation event. Typical examples are experiments where electrons and ions or ionized molecules are detected using a reaction microscope [21, 22] or experiments on correlated two-electron emission from solids [23]. A further application is the generation of frequency combs in the XUV range for high-resolution spectroscopy [24, 25]. Since the line spacing of a frequency comb is inversely proportional to the repetition rate, a high repetition rate allows a mode spacing in the comb that is large enough for high-resolution spectroscopy. A promising approach would be Fourier-transform spectroscopy in the XUV regime [26].

To date, a few groups reported the generation of high-order harmonics at repetition rates above a few tens of kHz [24, 27–31, 33, 34]. In order to reach the high intensities required for the HHG process using pulses with a few μJ energy, three different schemes have been applied. In the first one, the amplified laser is focused using either a mirror or an achromatic lens with short focal length (free focus geometry) [27]. In the second scheme, a high-finesse optical resonator that contains the nonlinear interaction medium is used. Intracavity enhancement enables the generation of XUV pulses at the high repetition rate of the seed laser oscillator. The generation geometry in this scheme is typically very similar to the free focus geometry. This technique suffers, however, from the difficulty of extracting the generated pulses [35]. A third scheme utilizes the local field enhancement induced by resonant plasmons within a metallic nanostructure [28, 36]. This interesting method has been experimentally demonstrated but not applied yet in a reproducible manner.

In this work, we investigate HHG under tight focusing conditions using a free focus geometry. In section 2, we analyse the macroscopic effects in HHG by introducing a generalized phase-matching model valid for all the focal length³. We further specify the conditions needed for efficient generation using a tight focus geometry. In section 3, we show results of an experiment with a 100 kHz laser system and pulse energies of only 6 μJ . Spectrally narrow and spatially confined high-order harmonics are generated even under non-phase-matched conditions.

2. HHG from a macroscopic point of view

2.1. Brief summary of macroscopic phase effects

The properties of a harmonic signal depend both on the single-atom response as well as on macroscopic effects such as phase matching and the generation geometry. From a single-atom point of view, the HHG process can be described by a semi-classical three-step model [37, 38]: the electron wave packet

leaves the atom via tunnelling being accelerated by the external laser field and recombines with its ion, emitting a burst of XUV radiation. Two different kinds of electron trajectories can be identified. Reflecting the duration of the excursion in the continuum they are called ‘short’ and ‘long’. Both trajectories contribute with different phases to the harmonic emission and are therefore affecting the macroscopic conditions differently [39]. In general, the single-atom response does not directly depend on macroscopic parameters. On the other hand, macroscopic effects play an essential role for HHG with low driving pulse energies since a tight focus geometry is typically required under these conditions. We therefore concentrate here on macroscopic effects.

The yield S_q of harmonic order q depends on the wave vector mismatch $\Delta\mathbf{k}$ between the laser-induced polarization $P_q(\mathbf{r})$ at the frequency $q\omega$ and the generated field. In the HHG process, $\Delta\mathbf{k}$ consists of four different terms: the wave vector mismatch due to the intensity-dependent single-atom dipole phase [40], $\Delta\mathbf{k}_q$; the geometrical wave vector mismatch due to focusing, $\Delta\mathbf{k}_g$; and the difference in wave vectors at frequencies ω and $q\omega$ [41], due to dispersion in the neutral medium, $\Delta\mathbf{k}_n$, and due to free electrons, $\Delta\mathbf{k}_p$. We neglect non-adiabatic phase-matching effects relevant for few cycle laser pulses as investigated in [42] as well as a possible reshaping of the fundamental laser pulse envelope. In order to generate the harmonic signal fully phase matched, the four contributions have to compensate each other for all radial (r) and longitudinal (z) positions within the nonlinear medium, for all times t . Since the emission from all atoms has to add up constructively along the propagation axis in order to maximize the harmonic yield of a collimated beam, we consider in the following only the longitudinal component of the wave vectors $\Delta k_z = \partial\Delta\varphi/\partial z$, where $\Delta\varphi$ is the corresponding phase mismatch⁴:

$$0 = \Delta k_z(r, z, t) = \underbrace{\Delta k_q}_{\substack{<0 \text{ for } z < 0 \\ >0 \text{ for } z > 0}} + \underbrace{\Delta k_g}_{<0} + \underbrace{\Delta k_n}_{>0} + \underbrace{\Delta k_p}_{<0}. \quad (1)$$

Here, $z < 0$ ($z > 0$) denotes the condition where the nonlinear medium is placed before (behind) the focus. The first and last terms on the right-hand side depend on both time and spatial coordinates, whereas the second and third terms can be treated as constant in time, depending only on the position in the nonlinear medium. The first term can be well approximated as $\Delta k_q = -\alpha_q \partial I / \partial z$, where I is the laser intensity [40]. The proportionality constant α_q is positive; it is small for the short trajectories and large for the long trajectories [40, 43]. In order to achieve phase matching at the focus ($\Delta k_q \approx 0$), the neutral dispersion has to compensate the negative plasma dispersion as well as the geometrical Gouy phase term Δk_g . With increasing distance to the focus, Δk_g as well as $\partial(\Delta k_g)/\partial z$ decreases. This makes it easier to compensate for Δk_g and leads to a larger phase-matched generation volume. For $z > 0$, the dipole phase contributes as an additional positive term [40] that leads typically to better phase-matching conditions for the short

³ We restrict our analysis to the conditions where scalar and paraxial approximations can be applied, neglecting the influence of longitudinal field components at high numerical apertures.

⁴ The signs of the different components of $\Delta\mathbf{k}$ are consistent within this paper. The overall sign, however, is different in some publications due to a different definition of $\Delta\mathbf{k}$.

trajectory behind the focus [39]. For the long trajectory, Δk_q contributes as a dominant positive term behind the focus but leads to strongly time-dependent phase-matching conditions [44].

2.2. Phase matching at short confocal parameters

At a given focusing geometry, phase matching can be typically achieved by adjusting the gas pressure p and laser pulse energy E_f . Providing that the intensity is low enough to ensure that the negative plasma dispersion does not dominate the positive contributions in (1), phase matching occurs at a certain pressure p_{match} called phase-matching pressure [45]. Driving the HHG process at high repetition rates and therefore with low pulse energies requires typically a tight focus geometry. In order to understand how the macroscopic parameters have to be chosen in order to achieve phase matching under such conditions, we analyse the scaling of the relevant parameters with the focal length f and pulse energy. We thereby refer to the focal length as a scaling parameter, considering a fixed beam diameter D before focusing instead of the more general confocal parameter b . Throughout this paper, we use Gaussian optics, where b and f are related through $b = 2z_0 = 8\lambda f_{\#}^2/\pi$, where z_0 is the Rayleigh range and $f_{\#} = f/D$ is the f -number of the focused beam with the central wavelength λ .

As f decreases, the wave vector mismatch due to the Gouy phase Δk_g increases rapidly since it scales as $\Delta k_g \propto 1/f^2$ at the focus. Consequently, it seems to prevent a phase-matched generation. It is, however, possible to obtain identical phase-matching conditions at long or short focal lengths if E_f and p are scaled appropriately with f . This can be seen by modifying (1). The wave vector mismatch due to dispersion can be rewritten as $\Delta k_{n,p} = p \cdot \partial(\Delta k_{n,p})/\partial p$, the partial derivatives being independent on pressure. Considering the scaling of Δk_g with the focal length, we can treat $(\Delta k_g \cdot f^2)$ as independent of f . At the focus where Δk_q vanishes and at an intensity sufficient to generate harmonics, but such that $|\Delta k_n| \geq |\Delta k_p|$, we obtain

$$\frac{(\Delta k_g \cdot f^2)}{f^2} + p_{\text{match}} \left[\frac{\partial(\Delta k_n)}{\partial p} + \frac{\partial(\Delta k_p)}{\partial p} \right] = 0, \quad (2)$$

for $p = p_{\text{match}}$. p_{match} is proportional to $1/f^2$, provided we scale the pulse energy appropriately in order to maintain the intensity distribution within the interaction volume. For a Gaussian laser pulse with the pulse length τ , the peak intensity in the focus is given by

$$I_0 = \frac{\pi}{2\tau\lambda^2} \frac{E_f}{f_{\#}^2}. \quad (3)$$

Scaling E_f as f^2 ensures a constant focus intensity, and consequently, a constant degree of ionization. Figure 1 illustrates this scaling for the generation of harmonic 21 in argon at the focus. The phase-matching pressure is represented as a function of focal length, for different degrees of ionization. The dispersion data for the 21st harmonic were taken from [46]. In general, the negative dispersion due to free electrons and the Gouy phase shift can be compensated by the neutral dispersion as long as the free electron dispersion does not exceed the dispersion in the neutral gas. Depending on the

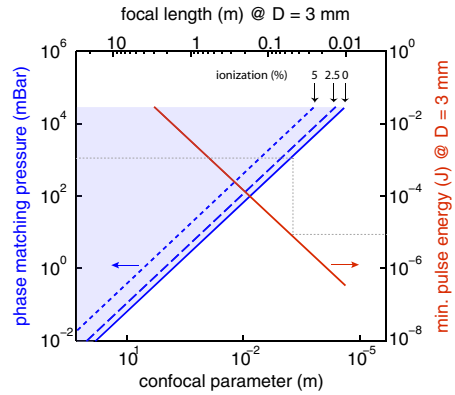


Figure 1. Scaling of phase-matching pressure with a confocal parameter for different ionization levels in argon. Additionally, the corresponding minimum laser pulse energy required is shown (right axis). For the simulations, the following parameters were used: beam diameter before focusing, $D = 3$ mm, and gas cell position, at the focus, central wavelengths of 800 nm, $q = 21$. The required pulse energy was calculated assuming a peak intensity of 1.5×10^{14} W cm $^{-2}$ and a pulse length of 45 fs.

gas, this happens typically at an ionization level of a few per cent. For $|\Delta k_n| \geq |\Delta k_p|$, an increased ionization level leads to a higher phase-matching pressure. Under conditions where higher ionization levels are reached, phase matching can still be reached in the leading edge of the laser pulse.

We also show in figure 1, the minimum pulse energy E_f required to reach an intensity of 1.5×10^{14} W cm $^{-2}$ assuming a pulse length of 45 fs. Using a laser pulse with for instance 10 μ J pulse energy, a focal length of approximately 6 cm is needed for a Gaussian beam with 3 mm diameter before focusing. Under these conditions, with a degree of ionization less than 1%, a pressure of approximately 1 bar is necessary in order to achieve phase matching.

The above argumentation considers the phase-matching situation at the focus. More generally, it is possible to express phase-matching conditions that are independent of focal length within a generating volume. We consider the generation volume with the length L_{max} and radial diameter D_{max} in which the laser intensity I exceeds the threshold intensity I_t to generate a certain harmonic order q , i.e. such that $q\hbar\omega \leq I_p + 3.17U_p(I)$, where I_p is the ionization potential and U_p the ponderomotive energy. I_t is therefore given by

$$I_t(q) = \frac{2m\omega^2 c_0 \epsilon_0 (q\hbar\omega - I_p)}{e^2 \cdot 3.17}, \quad (4)$$

where m , c_0 , ϵ_0 and e denote electron mass, speed of light, dielectric constant and electron charge, respectively. Assuming Gaussian optics, it is straightforward to derive the following relations:

$$L_{\text{max}} = \frac{8\lambda}{\pi} f_{\#}^2 \sqrt{\frac{I_0}{I_t} - 1}, \quad (5)$$

$$D_{\text{max}} = \frac{\lambda}{\pi} f_{\#} \sqrt{8 \ln \left(\frac{I_0}{I_t} \right)}. \quad (6)$$

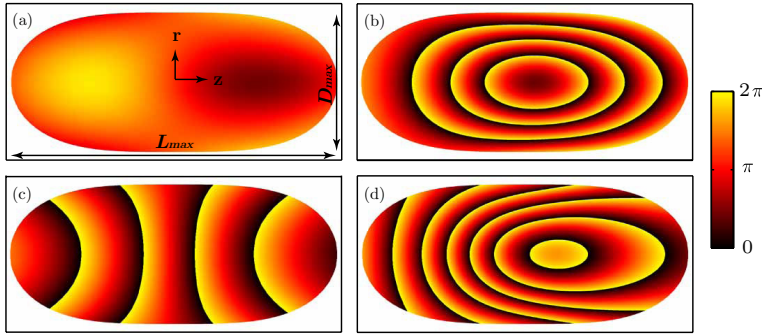


Figure 2. Generalized phase-matching map for short (a), (c) and long (b), (d) trajectories under two different conditions using the example of the 17th harmonic order. While the phase-matching condition was optimized for the short trajectory in (a) and (b), the conditions where dispersion terms are negligibly small are visualized in (c) and (d). The total phase mismatch $\Delta\varphi$ modulo 2π is plotted as a function of the spatial coordinates r and z centred at the focus at $t = 0$. The peak intensity is $1.5 \times 10^{14} \text{ W cm}^{-2}$ and the pulse length is 45 fs, which leads to an ionization level below 1%.

Equations (5) and (6) show that the length of the generation volume scales as $L_{\text{max}} \propto f^2$ and its radial diameter as $D_{\text{max}} \propto f$. Scaling the driving pulse energy as $E_f \propto f^2$ leads to a constant intensity distribution within the considered volume. Since the longitudinal dimension of this volume scales with f^2 , Δk_q follows the same scaling law. Therefore, equation (2) can be generalized to $z \neq 0$, by including a term ($\Delta k_q \cdot f^2$).

In figure 2, we show a generalized phase-matching map valid for all the focal lengths. In contrast to previous work [47, 48], where the degree of phase matching was represented graphically via the coherence length $L_{\text{coh}} = \pi/\Delta k$ over which the harmonic field can be built up constructively, we plot simply $\Delta\varphi$ modulo 2π as a function of r and z centred at the focus and in time ($t = 0$) at the maximum of the fundamental laser pulse envelope. The dipole phase is calculated within the approximation of classical trajectories in order to define the proportionality constants α_q . For $q = 17$, as considered in figure 2, $\alpha_{17} = 2.4 \times 10^{-13} \text{ cm}^2 \text{ W}^{-1}$ for the long and approximately zero for the short trajectory. For higher harmonic orders, α_q increases for the short trajectory, being, however, significantly smaller than for the long trajectory. While the dipole phase as well as the Gouy phase can be calculated directly as a function of r and z , the dispersion terms are calculated via integration of Δk_n and Δk_p along the propagation axis. In figure 2(a), the phase-matching condition is approximately optimized for the short trajectory for two areas before and behind the focus, indicated by an almost constant value of $\Delta\varphi$. For $f_{\#} = 20$ and $10 \mu\text{J}$ pulse energy (the same example as above), the corresponding phase-matching pressure is 600 mbar. A slightly higher pressure would lead to optimized conditions at the focus which would correspond to the situation in figure 1. For the same conditions, $\Delta\varphi$ varies strongly for the long trajectory, as shown in figure 2(b).

In figures 2(c) and (d), we show the situation where the dispersion terms are negligibly small which is typically the case when the gas pressure is too low. Under these conditions, the geometrical phase leads to strong phase modulations along

z , which results in a reduced signal strength for the short trajectory. The spatial and temporal properties of the generated harmonic beam are, however, not significantly affected by a longitudinal phase mismatch. Spatial phase and intensity modulations in the far-field typically arise due to radial phase modulations in the generation volume, which lead to a distorted wave front, whereas temporal modulations occur if the phase-matching situation is time dependent. Since only small phase modulations occur in the radial direction the emitted beam is spatially well confined even under these non-phase-matched generation conditions. Additionally, only weak temporal variations of the phase mismatch can be expected for the short trajectory. The typical phase-matching problem at short focal lengths does limit the overall efficiency but still allows for a high beam quality. In contrast, strong spatial intensity modulations are expected for the long trajectory due to a strong radial variation of $\Delta\varphi$. Furthermore, the strongly intensity-dependent dipole phase leads to temporal phase variations that can lead to complicated temporal and spectral structures [32].

Aside from phase matching, we have to consider absorption effects within the generation volume. Increasing the pressure up to the phase-matching pressure would typically lead to conditions where the absorption length ($L_{\text{abs}} = 1/\sigma\rho$, where ρ is the gas density and σ is the ionization cross section) is significantly shorter than the medium length L_{med} . Following the argumentation in [49], the optimum is reached for $L_{\text{coh}} > 5L_{\text{abs}}$ and $L_{\text{med}} > 3L_{\text{abs}}$. In order to avoid re-absorption of the emitted XUV photons behind the generation volume, L_{med} should not exceed L_{max} . Therefore, we obtain

$$L_{\text{max}} > L_{\text{med}} > 3L_{\text{abs}}. \quad (7)$$

Although the theoretical considerations above show that in principle, the same phase-matching conditions can be reached with long as well as with short focal lengths so that (7) can be fulfilled, technical constraints typically set the limits at tight focus geometries. At focal lengths of a few centimeter, the gas medium has to be confined to a size below 1 mm,

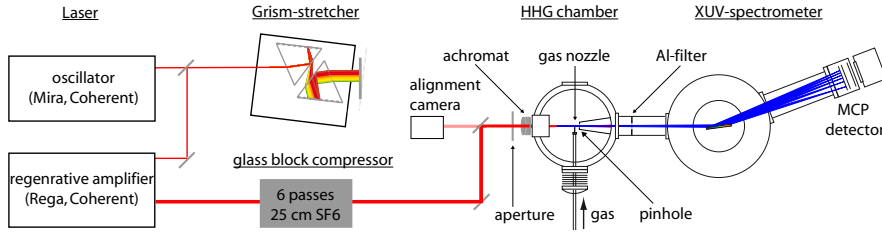


Figure 3. Experimental setup: the laser pulses generated in the oscillator are stretched using a Grism-based stretcher, amplified by a regenerative amplifier and re-compressed via multiple passes through a SF6 glass block. An achromat ($f = 6$ cm) is used to focus the beam into a continuous gas jet. The generated harmonics are spectrally and spatially filtered and imaged onto an MCP detector.

while allowing a pressure of a few bar. For $p \ll p_{\text{match}}$ (7) cannot be fulfilled. Since the amount of contributing atoms within the generation volume as well as L_{coh} is very small under these conditions, this leads to a dramatically reduced HHG signal. As explained above, this should, however, not deteriorate the spatial and temporal coherence properties for the short-trajectory emission significantly.

Furthermore, it is very important to minimize the ionization level when generating high-order harmonics under tight focusing conditions in order to keep the phase-matching pressure as low as possible. A possible way to achieve such a situation, while still reaching high harmonic orders would be to use longer driving wavelengths in the μm range [50].

2.3. Geometrical scaling

Aside from a possible influence due to phase matching, the geometrical scaling of the generation volume limits the generated photon flux at short focal lengths. A general expression can be formulated by considering the number of atoms n contributing to the harmonic emission [51]. n can be expressed as a product of the pressure p and the maximum dimensions of the nonlinear medium: $n \propto pL_{\text{max}}D_{\text{max}}^2$. According to the above argumentation, we have to scale p as $\propto 1/f^2$ in order to maintain the phase-matching conditions. Considering further the scaling relations for L_{max} and D_{max} , we obtain $n \propto f^2$. Since E_f has to be scaled in the same way in order to maintain the intensity, the amount of fundamental pulse energy per contributing atom is independent of focal length. For a certain phase-matching situation, we therefore achieve a conversion efficiency $\eta_q = E_h/E_f$, which is independent of f . Consequently, the harmonic pulse energy E_h follows the same scaling relation as E_f and we obtain

$$E_h \propto f^2. \quad (8)$$

This equation is valid not only for a phase-matched generation but in general for all phase-matching conditions as long as the generation parameters are scaled appropriately. This implies a sufficiently long medium or a scaling of the medium length with L_{max} and therefore as $L_{\text{med}} \propto f^2$. All relevant scaling relations are summarized in table 1, showing f , as well as E_f , as a scaling parameter.

In contrast to possible phase-matching problems that can, in principle, be solved even at a short focal length, the geometrical scaling relations described above set a general

Table 1. Scaling relations: a scaling of the given experimental parameters f , E_f , p and L_{med} with f or E_f , as shown on the left side of the table, causes the scaling behaviour of L_{max} , D_{max} , n , E_h and η_q shown on the right side.

Scaling parameter	f	E_f	p	L_{med}	L_{max}	D_{max}	n	E_h	η_q
f	–	f^2	$1/f^2$	f^2	f^2	f	f^2	f^2	Const.
E_f	$\sqrt{E_f}$	–	$1/E_f$	E_f	E_f	$\sqrt{E_f}$	E_f	E_f	Const.

limit for the harmonic yield. Due to a geometrical scaling of the interaction volume, the laser pulse energy that can be up-converted into high harmonic radiation scales quadratically with focal length. This indicates that the focal length should always be chosen as long as possible when a high XUV photon flux is required. At short focal lengths, technical constraints typically limit the pressure to values well below p_{match} . This leads to a reduced signal due to a deteriorated phase-matching situation and a reduced number of contributing atoms. For many applications, however, the photon flux is not a limitation. Instead, good coherence as well as good spatial and spectral properties are often more important and can be achieved easily even at short focal lengths.

3. Experimental setup

The average power of current femtosecond laser systems is typically limited to a few watts. Therefore, a high repetition rate is always linked to a low-pulse energy. Consequently, a short focal length is necessary to generate high-order harmonics at high repetition rates in order to reach the intensities required for the generation process.

An overview of the experimental setup is shown in figure 3. The laser system used in our experiments delivers pulses up to $7 \mu\text{J}$ with a pulse duration of 45 fs full-width at half-maximum, centred at 800 nm. It is based on a commercial system from Coherent Inc., consisting of a titanium–sapphire oscillator (Mira) and a regenerative amplifier (Rega). The latter is continuously pumped by a 10 W neodymium:yttrium–vanadium solid-state laser (VERDI-V10). The repetition rate of the amplifier can be adjusted between 10 and 250 kHz. For the HHG experiments, a repetition rate of 100 kHz was chosen. For higher repetition rates, the pulse energy starts to decrease considerably. By replacing the standard stretcher and

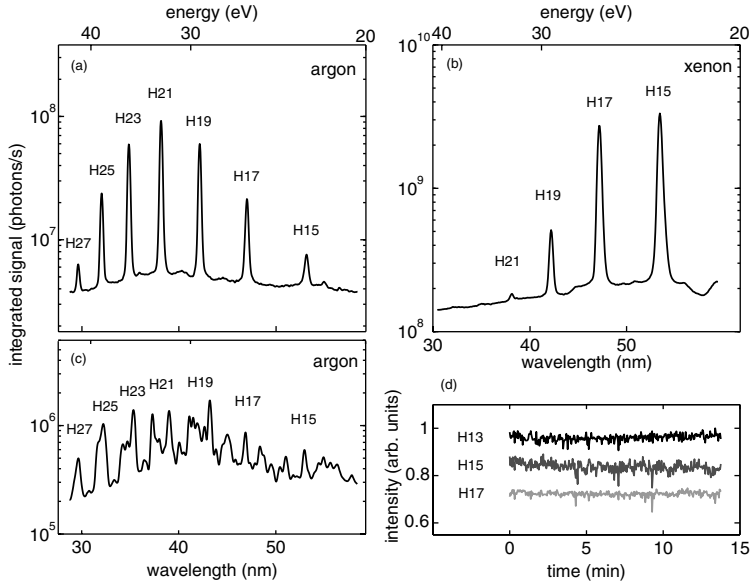


Figure 4. Measured harmonic spectra in argon (a), (c) and xenon (b). In (a) and (b), the nozzle was placed approximately $200\ \mu\text{m}$ behind the focus, and in (c), the position is at the focus. The harmonic signal was integrated over $\pm 11\ \text{mrad}$ with respect to the optical axis. The spectra were recorded with $1\ \text{s}$ exposure time. In (d), spatially and spectrally integrated harmonic signal generated in argon as a function of time using an integration time of $0.5\ \text{s}$ is shown.

compressor unit, the system was changed to down chirped pulse amplification (DPA) operation [52]. The employed Grism stretcher [53, 54] stretches the incoming laser pulses by a factor of around 350 to a pulse length of several picoseconds, introducing a negative chirp of around $-400\,000\ \text{fs}^2$. The amplified laser pulses are then re-compressed by passing a SF₆ glass block of $25\ \text{cm}$ length six times. By using this amplification scheme, the compressor transmission could be increased to above 90%, while avoiding the introduction of pulse front distortions due to a misaligned compressor. This leads to a significantly better beam quality and a 30% higher pulse energy after compression. Furthermore, a Grism-based stretcher allows for a precise chirp compensation up to the third order [54]. Even large additional dispersion due to dispersive elements in the beam path behind the compressor can easily be compensated.

The linear polarized amplified laser pulses are focused with an achromatic lens ($f = 60\ \text{mm}$) into the interaction gas. The gas is supplied by a thin nozzle, consisting of a stainless steel tube with an inner diameter of $90\ \mu\text{m}$. In the experiment, two different kinds of nozzle geometries were used. The laser was focused either through two $50\ \mu\text{m}$ holes into the nozzle (configuration A) or directly in front of the open nozzle (configuration B). The nozzle was mounted on a three-dimensional translation stage for precise positioning within the focus. A camera was used to image the nozzle on axis through a dielectric mirror. This is important since the laser beam has to be adjusted with a precision of $10\ \mu\text{m}$ relative to the nozzle.

The emitted harmonics pass a pinhole ($0.5\ \text{mm}$ diameter) used for differential pumping and located directly behind the interaction volume. A $200\ \text{nm}$ thick aluminium foil is used to block the fundamental beam, while transmitting the harmonics. A concave XUV grating (Hitachi, Grating 001-0639, $600\ \text{l mm}^{-1}$) is used for spectral imaging onto a microchannel plate (MCP) assembly in the horizontal plane. In the vertical plane, the grating reflects the harmonics without any refocusing, allowing us to image spectral and spatial profiles simultaneously.

4. Results and discussion

Typical harmonic spectra generated in argon and xenon are shown in figures 4(a) and (b). In both spectra, we observe the typical comb structure of high contrast peaks occurring at odd multiples of the driving laser frequency. The vertical axis displays the estimated spatially integrated photon flux per harmonic order. The calibration was done by extrapolating single-photon counts at low intensities taking into account the efficiency of the grating and the MCP as well as the transmission through the filter. We achieve a photon flux of up to 10^8 in argon and 3×10^9 photons s^{-1} in xenon. This is comparable to the photon flux used in [15] for time-resolved 2PPE, where, however, a high-power 3 kHz system was employed. The spectra were recorded when the gas cell was placed approximately $200\ \mu\text{m}$ behind the focus. Under these conditions, a dominant contribution from the short trajectory can be expected [39]. As typical for the short trajectory,

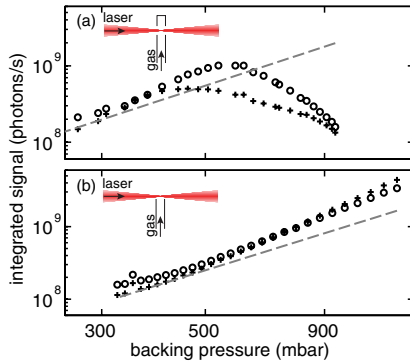


Figure 5. Spatially integrated signal of harmonic 15 (+) and 17 (o) generated in xenon for two different nozzle geometries: (a) the laser beam was focused through the perforated nozzle and (b) the focus is placed directly in front of an open nozzle. The dashed grey line is shown for reference, indicating a signal that increases quadratically with pressure.

the harmonics appear spatially well confined (approximately 30 mrad divergence) and spectrally narrow (approximately 250 meV at harmonic 21) even though we cannot assume a phase-matched generation due to a pressure well below the calculated phase-matching pressure. This is in good agreement with our theoretical considerations as presented above (see figure 2(c)).

At the focus, phase matching for the short trajectory is worse but it improves considerably for the long trajectory. This can be seen when comparing the longitudinal phase variations close to and behind the focus in figures 2(c) and (d). In the experiment, we observe a weaker, more divergent and spectrally broadened signal at the focus that we interpret as due to a dominant contribution from the long trajectory. The spectral and spatial characteristics can be explained as due to the dipole phase that varies strongly in time and in space within the generation volume. A strong variation of the dipole phase in radial direction across the focus leads to a divergent beam and intensity modulations in the spatial profile. The phase variation in time leads to a spectral splitting of the individual harmonic lines [32]. A strong temporal intensity modulation can therefore be expected under these conditions. We observe these phenomena for argon as well as for xenon. In accordance with previous results [27] and due to a lower ionization potential, the harmonics generated in xenon are characterized by a higher yield and a less pronounced plateau extension. However, no further qualitative differences have been observed.

In figure 4(c), the temporal stability of the harmonic signal generated in argon is shown. As in a typical application where integration times in the order of 1 s are common, the spectrally and spatially integrated signal was time averaged over 0.5 s. We then compute a RMS deviation of only 2.5%.

We have further investigated the influence of different target sizes and geometries. A pressure-dependent signal measured with two different gas nozzles is shown in figure 5.

The conditions here are similar to those shown in figure 4(b). In configuration A (figure 5(a)), where the laser beam passes through the nozzle, the gas flow is directed along the beam axis. In configuration B (figure 5(b)), where the beam is focused directly in front of the open nozzle, the gas flow occurs perpendicular to the beam axis. Although we expect a higher gas density in the generation volume in configuration A, the highest yield was measured with configuration B. We interpret this result as follows: due to the gas flow geometry, the gas medium in configuration A extends far behind the generation volume. Absorption of the generated harmonics leads to a dropping signal at higher pressures. In configuration B, no absorption effects are visible.

In both configurations, a signal that increases more than quadratically with pressure can be observed. Measuring the harmonic yield as a function of the pressure gives direct information about the phase-matching conditions. In general, a quadratic growth indicates that the phase-matching situation does not change with increasing pressure, which is typically the case at low pressure conditions well below the phase-matching pressure. A super quadratic growth indicates improving phase-matching conditions [45]. The opposite behaviour can be expected if phase matching deteriorates or if absorption starts to play a role. Following this argumentation, a clear indication for an improving phase-matching situation is visible in figure (5). A comparison with our simulations suggests that the phase-matching pressure needed in our experimental conditions lies in the range of 1 bar, while gas flow estimations yield a pressure of 50 mbar in the interaction volume at 800 mbar backing pressure. At 50 mbar, L_{abs} is smaller than 1 mm for harmonics 15 and 17, supporting our interpretation for an absorption limited signal in configuration A. Assuming that the intensity is below the critical limit where plasma dispersion would prevent phase matching, the harmonic yield could be increased dramatically and phase matching could be achieved by increasing the pressure in the interaction volume. Using the classical cut-off law, the peak intensity in our experimental conditions was estimated to approximately $1.5 \times 10^{14} \text{ W cm}^{-2}$. At this intensity, the estimated ionization level at the peak of the pulse is below 1% (estimated with a modified Ammosov–Delone–Krainov model using the correction factors introduced in [48]), and therefore, a phase-matched generation should be possible.

While absorption sets the limit in configuration A, the limit in B is simply given by the pressure in the vacuum chamber (the chamber was pumped using a 500 l s^{-1} turbomolecular pump) that has to be limited to avoid a damage of the MCP detector. As expected for a higher refractive index, the phase-matching conditions improve faster with increasing pressure for the 15th harmonic than for the 17th. Furthermore, the absorption limit sets in earlier for harmonic 15 due to a shorter absorption length. Both effects are clearly visible in figure 5. In both configurations, the highest yield was measured with the smallest gas nozzle. The reason is a relatively short coherence length well below the length of the gas volume due to a gas pressure well below the phase-matching pressure.

5. Conclusion and outlook

In conclusion, we have systematically analysed the generation of high-order harmonics for different focusing geometries. A generalized macroscopic model allows us to specify the conditions for the efficient generation of high-order harmonics using tight focus geometries. We identify a simple geometrical scaling for the maximum harmonic yield as a function of focal length and pulse energy. Scaling the focal length with $\sqrt{E_f}$, the medium length with E_f and the pressure as $1/E_f$ allows for the generation of high-order harmonics with the same phase-matching conditions and the same conversion efficiency. Considering the situation where the average laser power does not depend on the repetition rate, this implies a repetition rate-independent average power for the generated XUV beam.

Using a 100 kHz laser system, we generate high-order harmonics in argon and xenon with a laser pulse energy of only a few μJ . Measuring the harmonic spectral and spatial profiles at different focus positions allows us to identify contributions from different trajectories. We show experimentally and theoretically that our harmonics are not generated phase matched. A phase-matched generation could, however, be expected at much higher gas densities. Nevertheless, spatially well-confined, spectrally narrow harmonics are generated with a photon flux up to 3×10^9 photons s^{-1} (conversion efficiency 10^{-8}) into one harmonic order, which is sufficient for a typical photoemission experiment. The efficiency is comparable to the value reported in [31] where the authors claim a phase-matched generation. In contrast, we show that we achieve similar results under non-phase matched conditions, which implies the possibility of increasing the efficiency (and the photon flux) considerably, by using smaller gas volumes at higher densities.

Our results clearly show that the generation of high-order harmonics is possible even with relatively low pulse energies, which opens the way for high-repetition-rate attosecond XUV sources. We show further that there are no fundamental differences between HHG with high-energy laser pulses and the generation with μJ pulses. With the currently available laser systems, this implies the possibility for the generation of single attosecond pulses at MHz repetition rates.

Acknowledgments

This research was supported by the Deutsche Forschungsgemeinschaft through HO 2295/1-2 and GRK 790, the European Research Council (ALMA), the Marie Curie Training Network ATTOFEL, the Knut and Alice Wallenberg foundation and the Swedish Research Council.

References

- [1] Krausz F and Ivanov M 2009 Attosecond physics *Rev. Mod. Phys.* **81** 163
- [2] Popmintchev T, Chen M-C, Arpin P, Murnane M M and Kapteyn H C 2010 The attosecond nonlinear optics of bright coherent x-ray generation *Nature Photon.* **4** 822
- [3] Schoenlein R W, Fujimoto J G, Eesley G L and Capehart T W 1991 Femtosecond relaxation dynamics of image-potential states *Phys. Rev. B* **43** 4688
- [4] Petek H and Ogawa S 1997 Femtosecond time-resolved two-photon photoemission studies of electron dynamics in metals *Prog. Surf. Sci.* **56** 239
- [5] Aeschlimann M, Bauer M, Pawlik S, Weber W, Burgermeister R, Oberli D and Siegmann H C 1997 Ultrafast spin-dependent electron dynamics in fcc Co *Phys. Rev. Lett.* **79** 5158
- [6] Höfer U, Shumay I L, Reuß C, Thomann U, Wallauer W and Fauster T 1997 Time-resolved coherent photoelectron spectroscopy of quantized electronic states on metal surfaces *Science* **277** 1480
- [7] Fauster T, Weinelt M and Höfer U 2007 Quasi-elastic scattering of electrons in image-potential states *Prog. Surf. Sci.* **82** 224
- [8] Petek H, Weida M J, Nagano H and Ogawa S 2000 Real-time observation of adsorbate atom motion above a metal surface *Science* **288** 1402
- [9] Ge N H, Wong C M, Lingle R L, McNeill J D, Gaffney K J and Harris C B 1998 Femtosecond dynamics of electron localization at interfaces *Science* **279** 202
- [10] Gahl C, Bovensiepen U, Frischkorn C and Wolf M 2002 Ultrafast dynamics of electron localization and solvation in ice layers on Cu(111) *Phys. Rev. Lett.* **89** 107402
- [11] Zhu X Y 2004 Electronic structure and electron dynamics at molecule-metal interfaces: implications for molecule-based electronics *Surf. Sci. Rep.* **56** 1
- [12] Güdde J, Rohleder M, Meier T, Koch S W and Höfer U 2007 Time-resolved investigation of coherently controlled electric currents at a metal surface *Science* **318** 1287
- [13] Schmitt F *et al* 2008 Transient electronic structure and melting of a charge density wave in TbTe_3 *Science* **321** 1649
- [14] Baeumlér M and Haight R 1991 Ultrafast electron dynamics at the $\text{Ge}(111)2 \times 1$ surface *Phys. Rev. Lett.* **67** 1153
- [15] Rohwer T *et al* 2011 Collapse of long-range charge order tracked by time-resolved photoemission at high momenta *Nature* **471** 490
- [16] Haarlammert T and Zacharias H 2009 Application of high harmonic radiation in surface science *Curr. Opin. Solid State Mater. Sci.* **13** 13
- [17] Siffalovic P, Drescher M and Heinzmann U 2002 Femtosecond time-resolved core-level photoelectron spectroscopy tracking surface photovoltage transients on p-GaAs *Europhys. Lett.* **60** 924
- [18] Schmidt O, Bauer M, Wiemann C, Porath R, Scharte M, Andreyev O, Schönhense G and Aeschlimann M 2002 Time-resolved two-photon photoemission electron microscopy *Appl. Phys. B* **74** 223
- [19] Kubo A, Pontius N and Petek H 2007 Femtosecond microscopy of surface plasmon polariton wave packet evolution at the silver/vacuum interface *Nano Lett.* **7** 470
- [20] Stockman M I, Kling M F, Kleineberg U and Krausz F 2007 Attosecond nanoplasmonic-field microscope *Nature Photon.* **1** 539
- [21] Ullrich J, Moshhammer R, Dorn A, Dörner R, Schmidt L P H and Schmidt-Böcking H 2003 Recoil-ion and electron momentum spectroscopy: reaction-microscopes *Rep. Prog. Phys.* **66** 1463
- [22] Singh K P *et al* 2010 Control of electron localization in deuterium molecular ions using an attosecond pulse train and a many-cycle infrared pulse *Phys. Rev. Lett.* **104** 023001
- [23] Schumann F O, Winkler C and Kirschner J 2007 Correlation effects in two electron photoemission *Phys. Rev. Lett.* **98** 257604
- [24] Gohle C, Udem T, Herrmann M, Rauschenberger J, Holzwarth R, Schuessler H A, Krausz F and Hänsch T W 2005 A frequency comb in the extreme ultraviolet *Nature* **436** 234

- [25] Kandula D Z, Gohle C, Pinkert T J, Ubachs W and Eikema K S 2010 Extreme ultraviolet frequency comb metrology *Phys. Rev. Lett.* **105** 063001
- [26] Kovačev M *et al* 2005 Extreme ultraviolet Fourier-transform spectroscopy with high-order harmonics *Phys. Rev. Lett.* **95** 223903
- [27] Lindner F, Stremme W, Schätzel M G, Grasbon F, Paulus G G, Walther H, Hartmann R and Strüder L 2003 High-order harmonic generation at a repetition rate of 100 kHz *Phys. Rev. A* **68** 013814
- [28] Kim S, Jin J, Kim Y-J, Park I-Y, Kim Y and Kim S-W 2008 High-harmonic generation by resonant plasmon field enhancement *Nature* **453** 757
- [29] Yost D C, Schibli T R, Ye J, Tate J L, Hostetter J, Gaarde M B and Schafer K J 2009 Vacuum-ultraviolet frequency combs from below-threshold harmonics *Nature Phys.* **5** 815
- [30] Boullet J, Zaouter Y, Limpert J, Petit S, Mairesse Y, Fabre B, Higuert J, Mével E, Constant E and Cormier E 2009 High-order harmonic generation at a megahertz-level repetition rate directly driven by an ytterbium-doped-fiber chirped-pulse amplification system *Opt. Lett.* **34** 1489
- [31] Chen M C, Gerrity M R, Backus S, Popmintchev T, Zhou X, Arpin P, Zhang X, Kapteyn H C and Murnane M M 2009 Spatially coherent, phase matched, high-order harmonic EUV beams at 50 kHz *Opt. Express* **17** 17376
- [32] Heyl C M, Güdde J, Höfer U and L'Huillier A 2011 Spectrally resolved maker fringes in high-order harmonic generation *Phys. Rev. Lett.* **107** 033903
- [33] Vernaleken A *et al* 2011 Single-pass high-harmonic generation at 20.8 MHz repetition rate *Opt. Lett.* **36** 3428
- [34] Hädrich S, Krebs M, Rothhardt J, Carstens H, Demmler S, Limper J and Tünnermann A 2011 Generation of μ W level plateau harmonics at high repetition rate *Opt. Express* **19** 19374
- [35] Yost D C, Schibli T R and Ye J 2008 Efficient output coupling of intracavity high-harmonic generation *Opt. Lett.* **33** 1099
- [36] Park I-Y, Kim S, Choi J, Lee D-H, Kim Y-J, Kling M F, Stockman M I and Kim S-W 2011 Efficient output coupling of intracavity high-harmonic generation *Nature Photon.* **5** 577
- [37] Corkum P B 1993 Plasma perspective on strong-field multiphoton ionization *Phys. Rev. Lett.* **71** 1994
- [38] Schafer K J, Yang B, DiMauro L F and Kulander K C 1993 Above threshold ionization beyond the high harmonic cutoff *Phys. Rev. Lett.* **70** 1599
- [39] Lyngå C, Gaarde M B, Delfin C, Bellini M, Hänsch T W, L'Huillier A and Wahlström C-G 1999 Studies of the temporal coherence of high-order harmonics *Phys. Rev. A* **60** 4823
- [40] Lewenstein M, Salières P and L'Huillier A 1995 Phase of the atomic polarization in high-order harmonic generation *Phys. Rev. A* **52** 4747
- [41] Durfee C G III, Rundquist A R, Backus S, Herne C, Murnane M M and Kapteyn H C 1995 Phase matching of high-order harmonics in hollow waveguides *Phys. Rev. Lett.* **83** 2187
- [42] Geissler M, Tempea G and Brabec T 2000 Phase-matched high-order harmonic generation in the nonadiabatic limit *Phys. Rev. A* **62** 033817
- [43] Varju K *et al* 2005 Frequency chirp of harmonic and attosecond pulses *J. Mod. Opt.* **52** 379
- [44] Kazamias S, Douillet D, Weihe F, Valentin C, Rousse A, Sebban S, Grillon G, Augé F, Hulin D and Balcou Ph 2003 Global optimization of high harmonic generation *Phys. Rev. Lett.* **90** 193901
- [45] Kazamias S, Daboussi S, Guilbaud O, Cassou K, Ros D, Cros B and Maynard G 2011 Pressure-induced phase matching in high-order harmonic generation *Phys. Rev. A* **83** 063405
- [46] Henke B L, Gullikson E M and Davis J C 1993 X-ray interactions: photoabsorption, scattering, transmission, and reflection at $E = 50$ -30000 eV, $Z = 1$ -92 *At. Data Nucl. Data Tables* **54** 181
- [47] Balcou P, Salières P, L'Huillier A and Lewenstein M 1997 Generalized phase-matching conditions for high harmonics: the role of field-gradient forces *Phys. Rev. A* **55** 3204
- [48] Gaarde M B, Tate J L and Schafer K J 2008 Macroscopic aspects of attosecond pulse generation *J. Phys. B* **41** 132001
- [49] Constant E, Garzella D, Breger P, Mével E, Dorrer Ch, Le Blanc C, Salin F and Agostini P 1999 Optimizing high harmonic generation in absorbing gases: model and experiment *Phys. Rev. Lett.* **82** 1668
- [50] Colosimo P *et al* 2008 Scaling strong-field interactions towards the classical limit *Nature Phys.* **4** 386
- [51] L'Huillier A, Schafer K F and Kulander K C 1991 Theoretical aspects of intense field harmonic-generation *J. Phys. B: At. Mol. Opt. Phys.* **24** 3315
- [52] Gaudiosi D M, Lytle A L, Kohl P, Murnane M M, Kapteyn H C and Backus S 2004 11-W average power Ti:sapphire amplifier system using down chirped pulse amplification *Opt. Lett.* **29** 2665
- [53] Kane S and Squier J 1997 Grism-pair stretcher-compressor system for simultaneous second- and third-order dispersion compensation in chirped-pulse amplification *J. Opt. Soc. Am. B* **14** 661
- [54] Zheng J and Zacharias H 2009 Design considerations for a compact Grism stretcher for non-collinear optical parametric chirped-pulse amplification *Appl. Phys. B* **96** 445

PAPER III

Carrier–Envelope Phase Dependent High-Order Harmonic Generation with a High-Repetition Rate OPCPA-System

P. Rudawski, A. Harth, C. Guo, E. Lorek, M. Miranda, C. M. Heyl,
E. W. Larsen, J. Ahrens, O. Prochnow, T. Binhammer, U. Morgner,
J. Mauritsson, A. L’Huillier and C. L. Arnold.

Submitted for publication.

EPJ manuscript No.
(will be inserted by the editor)

Carrier-envelope phase dependent high-order harmonic generation with a high-repetition rate OPCPA-system

P. Rudawski¹, A. Harth¹, C. Guo¹, E. Lorek¹, M. Miranda¹, C. M. Heyl¹, E. W. Larsen¹, J. Ahrens², O. Prochnow², T. Binhammer², U. Morgner³, J. Mauritsson¹, A. L'Huillier¹, and C. L. Arnold¹

¹ Department of Physics, Lund University, P. O. Box 118, SE-22100 Lund, Sweden

² VENTÉON Laser Technologies GmbH, Hertzstrasse 1b, D-30827 Garbsen, Germany

³ Institut of Quantum Optics, Leibniz Universität Hannover, Welfengarten 1, D-30167 Hannover, Germany

Received: date / Revised version: date

Abstract We study high-order harmonic generation with a high-repetition rate (200 kHz), few-cycle, driving laser, based on optical parametric chirped pulse amplification. The system delivers carrier-envelope phase stable, 8 fs, 10 μ J pulses at a central wavelength of 890 nm. High-order harmonics, generated in a high-pressure Ar gas jet, exhibit a strong CEP-dependence over a large spectra range owing to excellent stability of the driving laser pulses. This range can be divided into three spectral regions with distinct CEP influence. The observed spectral interference structures are explained by an analytical model based upon multiple pulse interferences.

PACS. 42.65.Yj Optical parametric oscillators and amplifiers – 42.65.Ky Frequency conversion; harmonic generation – 32.80.Rm Multiphoton ionization and excitation to highly excited states

1 Introduction

The development of attosecond science strongly relies on the progress of ultrafast laser sources. Over more than twenty years, Chirped-Pulse Amplification (CPA) systems based on Titanium:Sapphire (Ti:Saph) technology have been used to drive XUV attosecond sources at repetition rates up to a few kHz. Optical Parametric Chirped Pulse Amplification (OPCPA) systems [1, 2] are based on three-wave mixing in a nonlinear crystal, using as input waves, a stretched broadband seed pulse and narrowband pump pulse of matched duration. The seed pulse is amplified, while an idler pulse is generated. The current limitations in conventional amplifiers, such as gain-narrowing and thermal lensing, are avoided in parametric amplification. OPCPA technology allows for the amplification of few-cycle pulses with TW peak power [3] at low repetition rates and is particularly advantageous at high-repetition rate from hundreds of kHz [4, 5, 6] to few MHz [7, 8, 9]. Recently, OPCPA systems producing CEP-stable few-cycle pulses at high-repetition rate have been successfully used for high-order harmonic generation (HHG). Tünnermann and coworkers approached the single attosecond pulse limit [10] and generated high-order harmonics in Ar with high average power [11].

In this work, we present a HHG source driven by a compact OPCPA laser producing CEP-stable 8 fs, 10 μ J pulses, at 890 nm central wavelength, and 200 kHz repetition rate [6]. To achieve sufficiently high intensity for efficient HHG in Ar, the laser beam is tightly focused

($f=5$ cm) into a high pressure effusive Ar gas jet. The generated HHG spectra exhibit a strong CEP-dependence covering the spectral region from 25 to 45 eV.

CEP-dependent effects in HHG have been observed in previous works [10, 12, 13, 14, 15, 16, 17], but have often been limited to specific spectral regions, such as the cut-off [10, 12, 14] or the region between consecutive harmonic spectral peaks [15, 16]. The interpretation of the observed CEP effects vary from quantum path interferences to interference between consecutive attosecond pulses. In the latter case, several effects have been discussed: the number of interfering pulses [13], the variation of timing between these pulses as well as the phase difference between consecutive pulses. Here, we develop a simple model consisting in coherently adding the spectra from the number of emitted attosecond pulses, which is estimated to be three in the present experiment, taking into account the variation of the spectral phase with the laser CEP. The good agreement between the results of this model and the experimental data indicates that the physics of the interference structures is contained in the variation of the spectral phase of consecutive attosecond pulses and not only in the number of interfering pulses.

The OPCPA system and the HHG source are described in Sections 2 and 3. The CEP-dependent harmonic spectra are presented in Section 4 and interpreted in Section 5.

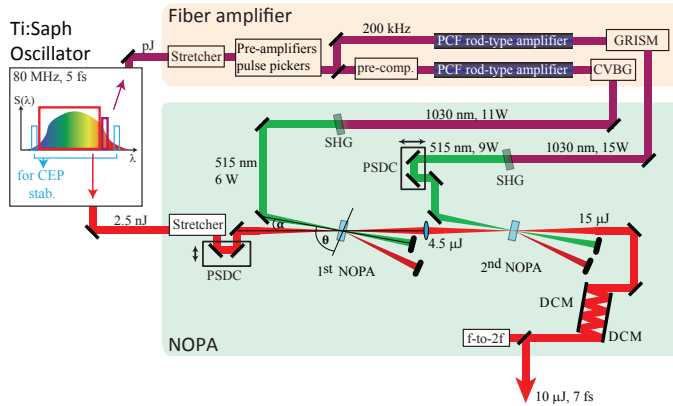


Figure 1. The OPCPA system; PCF - photonic crystal fiber, CVBG - chirp volume Bragg grating, SHG - second harmonic generation in BBO crystals, PSDC - pump-signal delay control, NOPA non-collinear optical parametric amplification in BBO crystals, α - non-collinear angle, θ - phase-matching angle, DCM - double chirp mirror.

2 Experimental setup: OPCPA

The HHG setup is driven by an OPCPA system [6], sketched in Figure 1. The system comprises three main units: a broadband Ti:Saph oscillator (VENTEON), a pumping laser based on an Yb-doped fiber amplifier, and a two-stage Non-collinear Optical Parametric Amplifier (NOPA). The Ti:Saph oscillator produces an octave-spanning spectrum, supporting CEP stable pulses with duration below 5 fs. The rms phase noise, corresponding to a power spectral density integrated from 3 Hz to 1 MHz, is measured to be below 80 mrad [18]. A small part of the oscillator spectrum around 1030 nm serves as seed for the fiber laser, whereas the main part of the spectrum (600-1020 nm, 2.5 nJ, <6 fs) seeds the NOPA. Optical seeding of the fiber pump laser intrinsically synchronizes pump and seed in the NOPA stages. The fiber pump laser chain, CPA-based, mainly consists of two Yb-doped photonic crystal rod-type fiber amplifiers which provide 11 and 15 W IR-average power, respectively (see Fig. 1). The fiber output pulses are frequency doubled to 515 nm and pump two NOPA-stages consisting of two 5 mm-long Type-I BBO crystals configured for Poynting-Vector-Walk-off Compensation (PVWC) geometry [19]. The signal from the oscillator is stretched to match the pump pulse duration, amplified in the two NOPA-stages, and finally compressed to below 7 fs using chirped mirrors. The output beam has an energy of 10 μ J per pulse at 200 kHz repetition rate.

3 Experimental setup: HHG

The CEP-stable pulses from the OPCPA are sent into a HHG setup, illustrated in Figure 2. The setup comprises two chambers: one for the generation and one for the detection of XUV radiation, separated from each other by a small conical expanding hole for differential pumping. Thus, the pressure in the generation chamber can be as high as 10^{-2} mbar (with gas load), while the pressure in the detection chamber remains below 10^{-7} mbar.

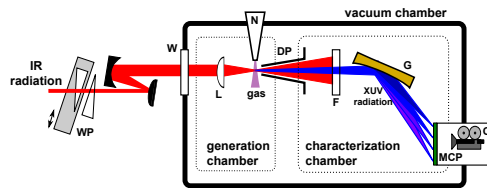


Figure 2. Experimental setup for HHG including a wedge pair (WP), a telescope, and a vacuum chamber composed of a generation chamber and a characterization chamber hosting the XUV spectrometer. W-window, L-lens, N-gas nozzle, DP-differential pumping hole, F-filter, G-grating, MCP-multiphoton channel plate, C-camera.

The pulses from the OPCPA are negatively chirped to pre-compensate additional dispersion of optical components used in the HHG setup, *i.e.* the vacuum window and the focusing lens. Fine tuning of the dispersion

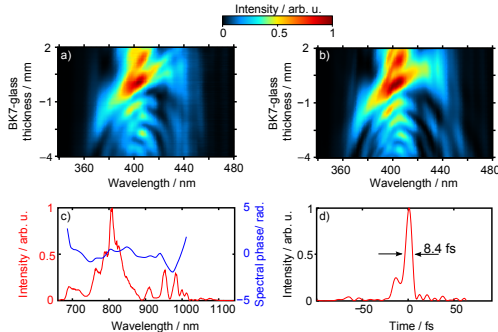


Figure 3. Temporal characterization of the pulse after the lens with d-scan. a) Measured and b) retrieved d-scan traces. c) Reconstructed spectral phase of the IR-pulse (blue) and measured spectral intensity of the pulse (red). b) Reconstructed temporal pulse (for zero BK7-glass thickness) with a full width at half maximum of 8.4 fs.

is carried out by a pair of BK7, anti-reflection coated wedges mounted on a motorized translation stage. After the wedge-pair, the beam propagates through an all-reflective telescope, where the beam diameter is expanded from 2 to 5 mm. Afterwards, it enters the vacuum chamber through a 0.5 mm-thick anti-reflection coated window. The fundamental beam is focused with an achromatic lens ($f = 5$ cm) into an effusive Ar gas jet. Due to the large bandwidth of the pulses a small effect of chromatic aberration remains. According to the design data of the lens, the position of the focus varies by about $60 \mu\text{m}$ within a wavelength range from 650 to 1000 nm, which is comparable to the estimated Rayleigh length ($50 \mu\text{m}$).

Figure 3 shows the spectral phase of the pulse obtained from a dispersion-scan measurement (d-scan) after the lens and its reconstructed temporal pulse profile. The d-scan technique [20] is based on modifying the pulse spectral phase by propagation through wedges, frequency doubling and measuring the obtained spectra as a function of dispersion (propagation distance in the wedges). The spectral phase is then iteratively reconstructed from the dispersion scan. With the central wavelength of 890 nm and a measured pulse duration of 8.4 fs the pulse includes three optical cycles under its full width at half maximum. The achromat was chosen mostly for the benefit of simple alignment. Moreover, obvious alternatives to focus the beam, i.e. spherical mirrors and metallic off-axis parabolic mirrors, were tried, but ruled out by either the strong astigmatism of short focal length spherical mirrors or by the often poor surface quality of metallic off-axis parabolas. In the future, a custom-made, dielectric focusing parabola might be the solution to obtain a diffraction limited spot size without impact on the pulse duration.

The Ar gas jet originates from a $90 \mu\text{m}$ diameter nozzle, with 4 bar backing pressure. The nozzle is positioned as closely as possible to the laser beam by using a three-

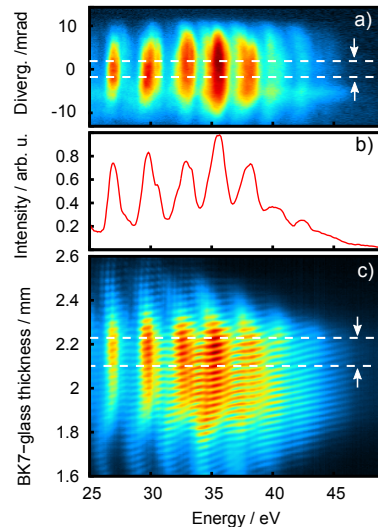


Figure 4. a) Spatially-resolved HHG spectrum recorded by imaging the MCP phosphor screen with a camera. The integration of the spatial profile (using only the marked region) leads to the HHG spectrum shown in b). c) Integrated HHG spectrum vs. BK7 wedge thickness. The influence of the change of the carrier-envelope phase over the whole HHG spectrum is clearly visible as well as the influence of the material dispersion on the IR pulse duration.

axis translation stage. Tight focusing results in a short Rayleigh length, a small interaction volume, and a steep Gouy-phase gradient with consequences for HHG phase matching [21]. In order to compensate for both small volume and steep Gouy-phase gradient, a high generation gas density is needed. Focusing the fundamental beam with an f -number around 10 implies that a generation pressure of a few bars is needed to achieve phase matching [22, 23]. The gas pressure used in the present setup is limited by the pumping system and is estimated to be below 1 bar in the interaction region. Thus, high-order harmonics are not generated fully phase-matched. The gas target is located behind the laser focus, so that the short trajectory contribution to HHG is selected [24].

The generated high-order harmonic radiation and the fundamental IR laser pulses enter the characterization chamber through the differential pump hole. The HHG beam can be separated from the fundamental by metallic filters, e.g. 200 nm-thick aluminum or titanium filters, installed in a motorized filter mount. The XUV radiation is recorded with a spectrometer consisting of a cylindrical diffraction grating (Hitachi, 600 lines/mm), a Micro Channel Plate (MCP), and a phosphor screen. The MCP is coated with a CsI layer in order to extend its sensitiv-

ity range in the VUV spectral range. Spatially-resolved harmonic spectra are recorded by imaging the phosphor screen with a CCD camera. The spectra are calibrated in photon energy using the well known transmission edges of different filters [25].

4 Results

Figure 4 (a) shows a typical, spatially-resolved harmonic spectrum generated in Ar in the photon energy range from 25 to 45 eV. A spectrum integrated over the central region (indicated by the dashed white lines) is presented in Figure 4 (b). The harmonics are spectrally broad, especially in the cut-off region above 40 eV.

Figure 4 (c) presents the integrated HHG spectrum as a function of the wedge thickness (see wedge pair in Fig. 2). Translating one wedge with respect to the other changes both the carrier-envelope phase of the IR-pulses and the overall dispersion of the pulse, affecting the pulse duration and the intensity. Such a scan takes less than a minute, and laser instabilities are therefore negligible. A change of thickness of $\sim 30 \mu\text{m}$ BK7 glass shifts the carrier-envelope phase by π , while the simultaneous change in pulse duration is negligible. The scan shown in Figure 4 (c) spans over a variable glass thickness of 1 mm. Both CEP and intensity effects are clearly visible. Below 1.8 and above 2.4 mm the pulse is considerably chirped and the laser intensity is too low to efficiently generate high-order harmonics. HHG is efficient within a range of about 0.5 mm of BK7, corresponding to the shortest pulses. Most remarkable in the recorded HHG spectra is the strong CEP dependence, which is not limited to the cut-off region, but is clearly observable in the presented spectrum.

The behavior seen in our experiment is shown in more detail in Figure 5 (a) [a zoom to the area between the dashed, white lines in Figure 4 (c)]. The plotted range corresponds to a change of BK7-glass thickness of $120 \mu\text{m}$; the impact on the change of pulse duration can be neglected, CEP effects clearly dominate. Figure 5 (b) presents two lineouts from Figure 5 (a) with a change of CEP of $\Delta\varphi = \pi/2$ between them. Three different regions can be distinguished: In region I, in the cut-off (above 40 eV), spectral peaks shift from odd to even harmonics as the CEP changes by $\pi/2$. In region III (low harmonic orders), the position of the harmonic peaks does not change, but their amplitude depends on the CEP. For example, the 17th and 19th harmonics reach a maximum for different CEP values. In between, in region II, the harmonic spectrum shows non trivial dynamics upon CEP change; spectral peaks are not located at multiple orders of the laser frequency and their position shift with CEP.

5 Discussion

To interpret the complex spectra shown in Fig. 5 (a), we develop a model based upon interferences of multiple pulses. A Fourier transformation of the spectra, assuming

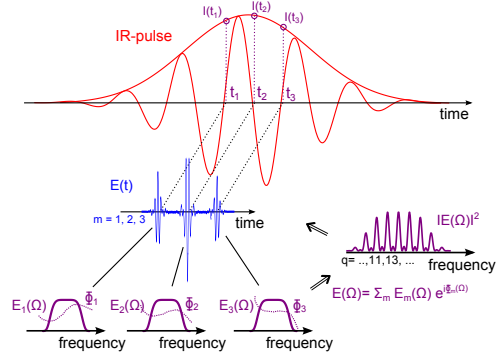


Figure 6. Sketch of the multipulse interference mode. A IR driving pulse generates three attosecond pulses leading to an attosecond pulse train. Every attosecond pulse in time can be described with a spectral amplitude and phase in the Fourier domain. The coherent superposition of the three complex spectra leads to the high-order harmonic spectrum $E(\Omega)$.

a constant spectral phase, indicates that the number of pulses in the train is approximately three, as illustrated in Fig. 6. The next step consists in coherently summing the complex spectra of these attosecond pulses, taking into account the CEP-dependent spectral phase,

$$E(\Omega) = \sum_{m=1}^3 E_m(\Omega) e^{i\Phi_m(\Omega)}, \quad (1)$$

with

$$\Phi_m(\Omega) = m\pi + \Omega t_m + \alpha_{\Omega} I(t_m). \quad (2)$$

The first term comes from the symmetry of HHG: two consecutive pulses are opposite in sign. In the second term, t_m indicates the (periodic) timing of the XUV attosecond pulses in the train. Two consecutive pulses are separated in time by half a laser period: $t_{m+1} - t_m = T/2$. Finally the third term reflects the influence of the generation process with a phase contribution which depends on the driving laser intensity at t_m [26]. This term will lead to a phase variation of the attosecond pulse as well as to a slight change of timing of the attosecond pulses (not included in t_m). The laser profile is assumed to be Gaussian with duration $\tau = 7$ fs and peak intensity $I_0 = 1.5 \times 10^{14}$ W/cm².

Fig. 5 (b) shows $|E(\Omega)|^2$ as a function of the laser CEP and Ω . In our model, the laser CEP influences the timing of the attosecond pulses in the train and therefore, for short enough pulses, the spectral phase which depends on $I(t_m)$. The experimental results are well reproduced in all three spectral regions. To understand better how our simple model [Eq. (2)] leads to the interference structure

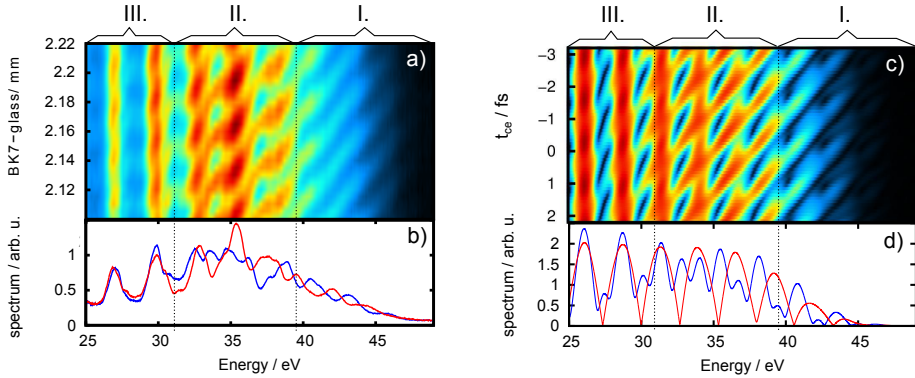


Figure 5. Measured a) and simulated c) HHG spectra as a function of the carrier-envelope phase of the driver. Corresponding to a) and c), figures b) and d) present two lineouts with a change of the CEP of $\Delta\varphi = \pi/2$ between them. Three regions are marked in the figures: region I, II and III, which indicate different types of CEP dependence.

shown in Fig. 5 (b), we calculate the phase difference between two consecutive attosecond pulses:

$$\Delta\Phi(\Omega) = \pi + \frac{\Omega T}{2} + \alpha_\Omega \left[I\left(t_1 + \frac{T}{2}\right) - I(t_1) \right]. \quad (3)$$

For long IR pulses, $I(t_1 + T/2) \approx I(t_1)$, so that $\Delta\Phi \equiv 0 \pmod{2\pi}$ when $\Omega = q\omega$, where q is an odd integer. Destructive interferences lead to the extinction of the XUV emission at all frequencies except those at odd multiple orders of the laser frequency and the CEP does not affect the HHG spectrum. For short pulses, the laser intensity changes between consecutive half cycles and the interference pattern becomes more complex. By Taylor expanding $I(t)$ around $t = 0$, Eq. (3) becomes

$$\Delta\Phi(\Omega) \approx \pi + \frac{\Omega T}{2} - \frac{4 \ln 2 T}{\tau^2} \left(t_1 + \frac{T}{4} \right) \alpha_\Omega I_0. \quad (4)$$

We can relate t_1 , or equivalently $t_1 + T/4$ to the carrier-envelope phase of the IR field through the equation $t_1 + T/4 = \phi_{ce} T / 2\pi$. ϕ_{ce} represents the phase difference between $t_1 + T/4$ and the pulse center (We are only concerned here with the relative value of the CEP). Eq. (4) becomes

$$\Delta\Phi(\Omega) \approx \pi + \frac{\Omega T}{2} - \frac{2 \ln 2 T^2 \phi_{ce} \alpha_\Omega I_0}{\pi \tau^2}. \quad (5)$$

It is interesting to consider the variation of $\Delta\Phi$ with respect to ϕ_{ce} .

$$\frac{\partial \Delta\Phi}{\partial \phi_{ce}} = -\frac{2 \ln 2 T^2 \alpha_\Omega I_0}{\pi \tau^2}. \quad (6)$$

For long pulses, low intensities or low photon energy such that α_Ω is small [27], $\partial \Delta\Phi / \partial \phi_{ce} \approx 0$, which implies that

the position of the harmonics does not depend on the CEP (region III). If $\partial \Delta\Phi / \partial \phi_{ce} \approx 1$, $\Delta\Phi$ varies by π when ϕ_{ce} changes by π and the position of the harmonic peaks moves from an odd to an even multiple of the laser frequency (region I). More generally, when $\partial \Delta\Phi / \partial \phi_{ce} \neq 0 \pmod{2}$, the position of the harmonic peaks will move with CEP. This variation increases with frequency as α_Ω increases towards the cutoff. When $\partial \Delta\Phi / \partial \phi_{ce}$ is not close to an integer, the interference pattern will exhibit discontinuities as the CEP is varied and the spectrum will have a complex behavior as is the case in region II.

6 Summary

This article presents studies of high-order harmonic generation, driven by a high-repetition rate OPCPA laser system. In spite of the low available IR energy per pulse (10 μJ), there is no difficulty in generating harmonics in Ar. This is achieved in a tight focusing geometry and with high generation pressure. Many applications in attosecond science should benefit from attosecond sources operating at higher repetition rates, i.e. in the MHz range [22,28,29,30,31,32]. Examples of such applications are coincidence detection of two or more particles, which require a low number of events per laser shot [33], but a large number of events per second to build up statistics, photoelectron spectroscopy and microscopy in solids and on solid surfaces [34,35] where space charge effects can be a serious obstacle.

The excellent CEP-stability of the system allows us to study in detail the HHG spectrum as a function of the CEP of the driving pulses. We find that the HHG spectrum strongly depends on the CEP, over the whole spectral range from 25 to 45 eV. In the cutoff region, the harmonic peaks shift from odd to even orders, while at low

energy, the CEP only affects the amplitudes of the peaks. In an intermediate region between 32 and 40 eV, the spectra becomes nontrivial and the number of spectral peaks increases. We developed a simple model which reproduces well the experimental observations. Our interpretation is that in our experiment, the spectra are affected by the CEP-dependence of the spectral phase difference between contributing attosecond pulses. We also provide an analytical derivation of the structure of the interference pattern. Precise CEP-dependent HHG spectra could be used in the future to get information on the atomic or molecular systems used for the generation, which would be extremely useful e.g. for tomographic reconstruction.

7 Acknowledgments

P. Rudawski and A. Harth contributed to this work equally. This research was supported by the Marie Curie Research Training Network ATTOFEL, the European Research Council (ALMA, PALP), the Knut and Alice Wallenberg foundation, the Swedish Foundation for Strategic Research, and the Swedish Research Council.

References

1. A. Dubietis, G. Jonušauskas, and A.P. Piskarskas. Powerful femtosecond pulse generation by chirped and stretched pulse parametric amplification in BBO crystal. *Opt. Commun.*, 88, (4-6), 437-440 (1992). 0030-4018.
2. A. Vaupel, N. Bodnar, B. Webb, L. Shah, M. Richardson. Concepts, performance review, and prospects of table-top, few-cycle optical parametric chirped-pulse amplification. *Opt. Eng.*, 53(5), 051507, December 2013.
3. D. Herrmann, L. Veisz, R. Tautz, F. Tavella, K. Schmid, V. Pervak, and F. Krausz. Generation of sub-three-cycle, 16 TW light pulses by using noncollinear optical parametric chirped-pulse amplification. *Opt. Lett.* 34, 2459-2461 (2009).
4. M. Schultze, T. Binhammer, G. Palmer, M. Emons, T. Lang, and U. Morgner. Multi- μJ , CEP-stabilized, two-cycle pulses from an OPCPA system with up to 500 kHz repetition rate. *Opt. Express*, 18(26):27291-27297, Dec 2010.
5. A. Harth, M. Schultze, T. Lang, T. Binhammer, S. Rausch, and U. Morgner. Two-color pumped OPCPA system emitting spectra spanning 1.5 octaves from VIS to NIR. *Opt. Express*, 20(3):3076-3081, Jan 2012.
6. J. Matyschok, T. Lang, T. Binhammer, O. Prochnow, S. Rausch, M. Schultze, A. Harth, P. Rudawski, C. L. Arnold, A. L'Huillier, and U. Morgner. Temporal and spatial effects inside a compact and CEP stabilized, few-cycle OPCPA system at high repetition rates. *Opt. Express*, 21(24):29656-29665, Dec 2013.
7. R. Riedel, A. Stephanides, M. Prandolini, B. Gronloh, B. Jungbluth, T. Mans, and F. Tavella. Power scaling of supercontinuum seeded megahertz-repetition rate optical parametric chirped pulse amplifiers. *Opt. Lett.*, 39, 1422-1424 (2014).
8. J. Nillon, O. Crégut, C. Bressler, and S. Haacke. Two MHz tunable non collinear optical parametric amplifiers with pulse durations down to 6 fs. *Opt. Express*, 22, 14964-14974 (2014).
9. J. Rothhardt, S. Demmler, S. Hädrich, J. Limpert, and A. Tünnermann. Octave-spanning OPCPA system delivering CEP-stable few-cycle pulses and 22 W of average power at 1 MHz repetition rate. *Opt. Express*, 20(10):10870-10878, May 2012.
10. M. Krebs, S. Hädrich, S. Demmler, J. Rothhardt, A. Zaïr, L. Chipperfield, J. Limpert, and A. Tünnermann. Towards isolated attosecond pulses at megahertz repetition rates. *Nature Photonics*, 7:555-559, 2013.
11. S. Hädrich, A. Klenke, J. Rothhardt, M. Krebs, A. Hoffmann, O. Pronin, V. Pervak, J. Limpert, and A. Tünnermann. High photon flux table-top coherent extreme-ultraviolet source. *Nature Photonics*, 8:779-783, 2014.
12. A. Baltuška, Th. Udem, M. Uiberacker, M. Hentschel, E. Goulielmakis, Ch. Gohle, R. Holzwarth, V. S. Yakovlev, A. Scrinzi, T. W. Hänsch, and F. Krausz. Attosecond control of electronic processes by intense light fields. *Nature*, 421:611, 2003.
13. E. Mansten, J. M. Dahlström, J. Mauritsson, T. Ruchon, A. L'Huillier, J. Tate, M. B. Gaarde, P. Eckle, A. Guedali, M. Holler, F. Schapper, L. Gallmann, and U. Keller. Spectral signature of short attosecond pulse trains. *Phys. Rev. Lett.*, 102(8):083002, Feb 2009.
14. M. Nisoli, G. Sansone, S. Stagira, S. De Silvestri, C. Vozzi, M. Pascolini, L. Poletto, P. Villoresi, G. Tondello. Effects of Carrier-Envelope Phase Differences of Few-Optical-Cycle Light Pulses in Single-Shot High-Order-Harmonic Spectra. *Phys. Rev. Lett.*, 91(21):213905, Nov 2003.
15. G. Sansone, C. Vozzi, S. Stagira, M. Pascolini, L. Poletto, P. Villoresi, G. Tondello, S. De Silvestri, and M. Nisoli. Observation of carrier-envelope phase phenomena in the multi-optical-cycle regime. *Phys. Rev. Lett.*, 92:113904, 2004.
16. G. Sansone, E. Benedetti, J.-P. Caumes, S. Stagira, C. Vozzi, M. Pascolini, L. Poletto, P. Villoresi, S. De Silvestri, and M. Nisoli. Measurement of harmonic phase differences by interference of attosecond light pulses. *Phys. Rev. Lett.*, 94:193903, 2005.
17. C. Ott, M. Schönwald, P. Raith, A. Kaldun, G. Sansone, M. Krüger, P. Hommelhoff, Y. Patil, Y. Zhang, K. Meyer, M. Laux, and T. Pfeifer. Strong-field spectral interferometry using the carrier-envelope phase. *New Journal of Physics*, 15(7):073031, 2013.
18. S. Rausch, T. Binhammer, A. Harth, F. X. Kärtner, and U. Morgner. Few-cycle femtosecond field synthesizer. *Optics Express*, 16(22):17410-17419, 2008.
19. T. Lang, A. Harth, J. Matyschok, T. Binhammer, M. Schultze, and U. Morgner. Impact of temporal, spatial and cascaded effects on the pulse formation in ultra-broadband parametric amplifiers. *Opt. Express*, 21(1):949-959, Jan 2013.
20. M. Miranda, T. Fordell, C. Arnold, A. L'Huillier, and H. Crespo. Simultaneous compression and characterization of ultrashort laser pulses using chirped mirrors and glass wedges. *Opt. Express*, 20(1):688-697, Jan 2012.
21. A. L'Huillier, X. F. Li, and L. A. Lompré. Propagation effects in high-order harmonic generation in rare gases. *JOSA B*, 7:527-536, 1990.

22. C. M. Heyl, J. Güdde, A. L'Huillier, and U. Höfer. High-order harmonic generation with μJ laser pulses at high repetition rates. *Journal of Physics B: Atomic, Molecular and Optical Physics*, 45(7):074020, 2012.
23. J. Rothhardt, M. Krebs, S. Hädrich, S. Demmler, J. Limpert, and A. Tünnermann. Absorption-limited and phase-matched high harmonic generation in the tight focusing regime. *New Journal of Physics*, 16(3):033022, 2014.
24. P. Salières, A. L'Huillier, and M. Lewenstein. Coherence control of high-order harmonics. *Phys. Rev. Lett.*, 74:3776, 1995.
25. B.L. Henke, E.M. Gullikson, and J.C. Davis. X-ray interactions: Photoabsorption, scattering, transmission, and reflection at $e = 50\text{--}30,000\text{ eV}$, $z = 1\text{--}92$. *Atomic Data and Nuclear Data Tables*, 54(2):181 – 342, 1993.
26. M. Lewenstein, K. C. Kulander, K. J. Schafer, and P. H. Bucksbaum. Rings in above-threshold ionization: A quasiclassical analysis. *Phys. Rev. A*, 51:1495, 1995.
27. K. Varjú, Y. Mairesse, B. Carre, M. B. Gaarde, P. Johnson, S. Kazamias, R. Lopez-Martens, J. Mauritsson, K. J. Schafer, Ph. Balcou, A. L'Huillier, and P. Salières. Frequency chirp of harmonic and attosecond pulses. *J. Mod. Opt.*, 52:379, 2005.
28. J. Bouillet, Y. Zaouter, J. Limpert, S. Petit, Y. Mairesse, B. Fabre, J. Higuët, E. Mével, E. Constant, and E. Cormier. High-order harmonic generation at a megahertz-level repetition rate directly driven by an ytterbium-doped-fiber chirped-pulse amplification system. *Opt. Lett.*, 34(9):1489–1491, May 2009.
29. C. Chiang, A. Blättermann, M. Huth, J. Kirschner, and W. Widdr. High-order harmonic generation at 4 MHz as a light source for time-of-flight photoemission spectroscopy. *Appl. Phys. Lett.*, 101:071116, Jun 2012.
30. O. H. Heckl, C. R. E. Baer, C. Kränkel, S. V. Marchese, F. Schapper, M. Holler, T. Südmeyer, J. S. Robinson, J. W. G. Tisch, F. Couny, P. Light, F. Benabid, and U. Keller. High harmonic generation in a gas-filled hollow-core photonic crystal fiber. *Applied Physics B*, 97(2):369–373, 2009.
31. F. J. Furch, S. Birkner, F. Kelkensberg, A. Giree, A. Anderson, C. P. Schulz, and M. J. J. Vrakking. Carrier-envelope phase stable few-cycle pulses at 400 kHz for electron-ion coincidence experiments. *Opt. Express*, 21(19):22671–22682, Sep 2013.
32. E. Lorek, E. Witting-Larsen, C. M. Heyl, S. Carlström, D. Paleček, D. Zigmantas, J. Mauritsson. High-order harmonic generation using a high-repetition-rate turnkey laser. *arXiv:1409.2725*.
33. E. P. Månsson, D. Guénot, C. L. Arnold, D. Kroon, S. Kasper, J. M. Dahlström, E. Lindroth, A. S. Kheifets, A. L'Huillier, S. L. Sorensen, and M. Gisselbrecht. Double ionization probed on the attosecond timescale. *Nat Phys*, 10, 2014.
34. T. Haarlammert, H. Zacharias. Application of high harmonic radiation in surface science. *Current Opinion in Solid State and Materials Science*, 13, 13-27, 2009.
35. A. Mikkelsen, J. Schwenke, T. Fordell, G. Luo, K. Klünder, E. Hilner, N. Anttu, A. A. Zakharov, E. Lundgren, J. Mauritsson, J. N. Andersen, H. Q. Xu, and A. L'Huillier. Photoemission electron microscopy using extreme ultraviolet attosecond pulse trains. *Review of Scientific Instruments*, 80:123703, 2009.

PAPER IV

High-Order Harmonic Generation Using a High-Repetition Rate Turnkey Laser

E. Lorek, E. W. Larsen, C. M. Heyl, S. Carlström, D. Paleček,
D. Zigmantas, and J. Mauritsson.

Submitted for publication.

High-order harmonic generation using a high-repetition-rate turnkey laser

E. Lorek,^{1,*} E. W. Larsen,¹ C. M. Heyl,¹ S. Carlström,¹ D. Paleček,² D. Zigmantas,² and J. Mauritsson^{1,†}

¹*Department of Physics, Lund University, Box 118, 221 00 Lund, Sweden*

²*Department of Chemical Physics, Lund University, Box 124, 221 00 Lund, Sweden*

(Dated: September 8, 2014)

We generate high-order harmonics at high pulse repetition rates using a turnkey laser. High-order harmonics at 400 kHz are observed when argon is used as target gas. In neon we achieve generation of photons with energies exceeding 90 eV (~ 13 nm) at 20 kHz. We measure a photon flux of $4.4 \cdot 10^{10}$ photons per second per harmonic in argon at 100 kHz. Many experiments employing high-order harmonics would benefit from higher repetition rates, and the user-friendly operation opens up for applications of coherent extreme ultra-violet pulses in new research areas.

I. INTRODUCTION

Coherent extreme ultra-violet (XUV) pulses, providing excellent temporal and spatial resolution, can be produced by a process called high-order harmonic generation (HHG) [1]. The harmonic spectrum typically consists of odd harmonic orders of the driving field frequency that form a plateau extending over a large energy range up to high photon energies [2]. By isolating a single harmonic order, high spatial resolution can be obtained [3]. While an isolated harmonic order has a duration on the order of the driving field, the total harmonic spectrum corresponds to a train of pulses with hundreds of attoseconds in duration [4]. By applying various temporal confinement schemes isolated attosecond pulses can also be obtained [5]. These attosecond pulses have been fruitfully used, *e.g.* for studies of the motion of electrons on their natural timescale [6–12].

High-order harmonics are produced by focusing a laser into a gas. The process is usually described with a simplified semi-classical three-step model [13, 14], where the electric field distorts the Coulomb potential of the atom allowing an electron to 1) tunnel out; 2) be accelerated by the electric field; and 3) recombine with its parent ion, leading to emission of coherent XUV light. Since this process is repeated every half-cycle of the laser field, interference between consecutive pulses results in odd high-order harmonics of the fundamental frequency and, in the time-domain, an attosecond pulse train (APT). By increasing the duration of the driving field the number of pulses in the APT is increased, leading to a spectral narrowing of the harmonic orders allowing for an improved spectral resolution while the pulse duration of the individual attosecond pulses may be unaffected, thereby maintaining the possibility for very high temporal resolution.

HHG requires laser intensities on the order of 10^{14} W/cm² to distort the Coulomb potential and allowing the electron to tunnel out and get accelerated to high energies. Such fields are usually obtained by energetic pulses with short time durations, produced by large high power laser systems. Due to the limitations in average

power of such systems, high energy pulses are obtained at the cost of repetition rate. Traditionally, HHG has therefore been limited to low pulse repetition rates, not exceeding a few kHz. Many experiments using HHG would, however, benefit from higher repetition rates. Examples include time-resolved photoemission electron spectroscopy and microscopy, two techniques that are limited in the number of emitted photoelectrons per pulse by space charge effects and therefore need a higher repetition rate in order to provide better statistics. Other experiments where coherent XUV pulses at a high repetition rate are needed include coincidence measurements [15–17] and the generation of frequency combs in the XUV range for high-resolution spectroscopy [18–20].

The fact that high power laser systems are used for HHG has not only limited the repetition rates but also the availability to relatively few laboratories with the right equipment and expertise to run the systems. Generating high-order harmonics with a more compact and user-friendly laser system than those traditionally used, could increase the availability. Examples of fields potentially benefiting from accessible HHG include, apart from attosecond science itself, femtochemistry, nanophysics [21] and surface science [22].

Both the issue of the traditionally limited repetition rates and the issue of limited accessibility of HHG light are addressed in this paper. Several recent studies report the generation of high-order harmonics at high-repetition rates (50 kHz–25 MHz) [18, 20, 22–34]. The general approach is to use a laser system with a high repetition rate, either an oscillator or an amplified system. In order to achieve the required intensity for HHG, despite the low pulse energy, three schemes have been applied. The first scheme [23–30], investigated in detail by [31, 32], uses a tight-focusing geometry where the laser light is focused by a mirror or lens with short focal length onto the gas medium, effectively producing a high intensity at the focus. The second scheme [18, 20, 33] uses a high-finesse optical resonator that contains the medium for HHG. In this intra-cavity scheme, high-order harmonics are produced at the high repetition rate of the seed oscillator. This technique is, however, experimentally challenging. The third scheme exploits the local field enhancement induced by resonant plasmons within a metallic nanostructure to achieve the intensity needed for HHG [34]. If this is actually a viable route to generate harmonics has,

* eleonora.lorek@fysik.lth.se

† johan.mauritsson@fysik.lth.se

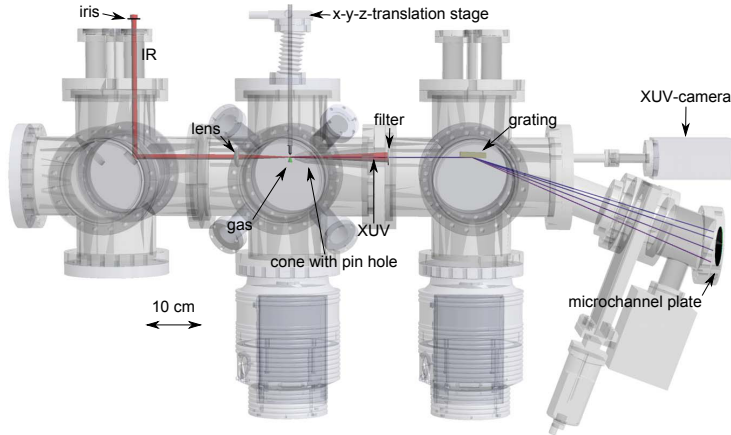


FIG. 1: The experimental HHG setup including the beam path. The beamsizes are exaggerated. To allow room for a future interferometer enabling attosecond pump-probe experiments, the beam path is off-centered. A full 3D model of the HHG setup in pdf-format can be found as supplementary material. (Multimedia view)

however, been questioned [35].

In a recent work [22], not only the traditionally limited repetition rates for HHG was addressed but also the accessibility of HHG light. HHG with energies between 13 eV and 45 eV from a turnkey laser at repetition rates of 0.2–25 MHz is reported.

In this work we perform a more detailed investigation of HHG using a high-repetition-rate turnkey laser. Using this compact, stable and user-friendly laser in a tight focusing-scheme, we can achieve generation up to 92.7 eV (13.4 nm) at 20 kHz in neon. An XUV photon flux of up to $4.4 \cdot 10^{10}$ photons/s per harmonic order using argon and 100 kHz is measured. We can generate harmonics at up to 400 kHz repetition rate in argon.

In section II the experimental method and setup are presented. Section III is devoted to a presentation of our results followed by a conclusion in Section IV.

II. EXPERIMENTAL METHOD AND SETUP

The main challenge with HHG at high repetition rates is the limited energy per pulse, setting constraints for reaching the intensities needed while keeping macroscopic generation conditions optimized. The three schemes mentioned above address this limitation in different ways, using power or intensity enhancement approaches in combination or solely with a tight-focusing geometry. In this work, we employ the straightforward tight-focusing approach in a single-pass configuration.

The tight-focus geometry leads to a small interaction volume, demanding a high gas density for efficient HHG [31]. Confining a high density gas target to a small interaction volume while limiting the backing pressure in the vacuum chamber in order to avoid re-absorption of the

generated XUV radiation, is technically challenging [32]. The tight focusing also leads to a very divergent harmonic beam, which makes the manipulation and transport of the beam for further experiments more difficult. It is therefore desirable to focus the fundamental laser beam as loosely as possible, while still reaching sufficient generation intensities. The necessary laser intensity, I_L , can be estimated from the cut-off law [36], which defines the highest harmonic order q of the plateau harmonics that typically can be observed:

$$\hbar q \omega = I_p + 3.17 U_p. \quad (1)$$

Here, ω is the laser angular frequency, I_p the ionization potential of the atoms used for HHG and $U_p \sim I_L \lambda^2$ the ponderomotive energy with λ denoting the laser wavelength. The cut-off law predicts that the ponderomotive energy, and thereby the cut-off energy, can be increased by increasing either I_L or λ . However, it has been shown that the efficiency scales very unfavorably with increasing wavelength [37]. Nevertheless, increasing the driving wavelength from the typically used 800 nm to 1030 nm allows us to relax the intensity requirement while still reaching high cut-off energies and good conversion efficiencies at high repetition rates.

The laser used to drive HHG is a commercially available ("PHAROS", Light Conversion), compact Yb:KGW laser ($640 \times 360 \times 212$ mm), which is both user-friendly and stable in its operation (pulse energy, pointing and pulse duration). The wavelength is 1030 nm and the repetition rate is tunable between 1 kHz and 600 kHz and, in addition, a number of pulses can be removed using a pulse picker. With changed repetition rate, the pulse energy can be varied between 0.5 mJ and 10 μ J. Note that the average power is not constant over the tunability range. The pulse duration is 170 fs.

The experimental setup, including the beam path and the vacuum chambers, is presented in Fig. 1 (Multimedia view). The laser light is sent into the chamber and focused by an achromatic lens with 100 mm focal length. The target gas (argon, neon or air) is supplied by an open-ended, movable gas nozzle with 90 μm inner diameter. The generated XUV light then propagates, together with the IR light, through a small pinhole placed close after the generation location. The pinhole separates the generation part of the chamber from the detection part, each pumped by a turbo pump with a capacity of 500 l/s (Oerlikon Leybold vacuum, MAG W600). The small pinhole allows for a very steep pressure gradient with up to 10^{-2} mbar in the generation part of the chamber while maintaining 10^{-7} mbar in the detection part. After the generation the IR light is removed by a 200 nm thin aluminum filter.

The generated harmonic emission is detected using a flat-field grazing-incidence XUV spectrometer based on a blazed, varied-line-space XUV grating (Hitachi, Grating 001-0639) with 600 lines/mm, which is placed on a rotation stage and a linear translation stage. The grating diffracts and focuses the harmonics along the dispersive plane and reflects them in the perpendicular direction onto a 78 mm diameter microchannel plate (MCP) (Photonis). This allows us to study both the spectral contents of the emission and the divergence of the individual harmonics. The MCP is finally imaged by a CCD camera (Allied Vision Technologies, Pike F-505B). By removing the grating from the beam path with the linear stage the photon flux can be measured in the forward direction using an X-ray camera (Andor, iKon-L DO936N-M0W-BN). The spectrometer was calibrated using the grating equation with the known geometry of the setup and the grating constant as inputs. The calibration was verified by two atomic lines in argon and two atomic lines in neon. The argon lines used are 104.82 nm [38] and 106.67 nm [39] corresponding to the transitions $3p^5(^2P_{1/2})4s \rightarrow 3p^6(^1S_0)$ and $3p^5(^2P_{3/2})4s \rightarrow 3p^6(^1S_0)$, while the two neon lines are 73.590 nm and 74.372 nm corresponding to transitions $2s^22p^5(^2P_{1/2}^o)3s \rightarrow 2s^22p^6$ and $2s^22p^5(^2P_{3/2}^o)3s \rightarrow 2s^22p^6$ [40].

III. RESULTS

Using the experimental setup described in Section II, high-order harmonics were successfully generated in both argon and neon, but conveniently also in air (mainly nitrogen). The use of air at a backing pressure of 1 atm is a very convenient experimental trick as it does not require any gas bottles or connections.

Figure 2 shows a typical spectrum, obtained at 20 kHz repetition rate in argon. Typical for harmonic spectra generated with 170 fs long laser pulses is that the harmonics are spectrally well defined. This spectral resolution enables a very clear separation of two different contributions to each of the lower harmonics, coming from two different electron trajectories leading to the same final

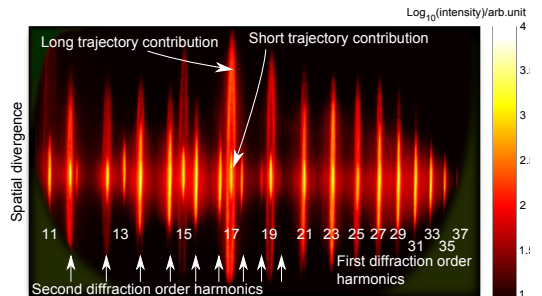


FIG. 2: A typical high-order harmonic spectrum, generated from argon at 20 kHz with 69.5 μJ pulses.

Examples of a short and a long trajectory electron contribution are indicated. The harmonics in the first diffraction order are identified and those in the second diffraction order indicated by arrows.

Repetition rate/kHz	Laser pulse energy/ μJ	Harmonic order	Photon energy/eV
20	<175	41	49.4
50	<90	35	42.1
100	54	33	39.7
200	30	27	32.5
300	20	21	25.3
400	15	19	22.9

TABLE I: The highest observed harmonic orders and corresponding photon energies generated in argon for different repetition rates and pulse energies.

energy [41]. Electrons escaping early after the maximum of the electric field experience a longer time in the continuum and follow a so-called long trajectory while those escaping later follow a shorter one.

Since the long trajectory electrons spend more time in the continuum than the short trajectory electrons and therefore acquire more intensity-dependent phase, the generated light will have a more curved wavefront than the light from the short trajectory electrons. The emission is therefore more divergent than the emission from short trajectory electrons. This is clearly seen for harmonic orders 11–29 where the more divergent contribution from the long trajectory electrons surround a central spot being the contribution of the short trajectory electrons. For even higher harmonic orders (31 and higher), within the cut-off region, the two trajectories merge into one with a decreasing divergence as the energy increases.

Exploiting the variable repetition rate of the laser, we investigated the maximum repetition rate at which our setup can provide high-order harmonics in argon. Table I shows the highest observed harmonic order for various repetition rates and pulse energies. The generation conditions were individually optimized, with different iris opening diameters and with different positions of the gas jet. As can be seen in the table, HHG up to a rate of

400 kHz was possible.

In order to estimate the generated photon flux and conversion efficiency we have to correct for the losses induced in the measurement. Assuming a total aluminum oxide layer of 15 nm [42] on the aluminum filter [43] and compensating for the diffraction efficiency of the grating and the quantum efficiency of the XUV camera, the flux of the generated XUV photons in argon was estimated for 20 and 100 kHz repetition rates. For each of these measurements the pulse picker was set to remove a number of laser pulses in order to not saturate the detection, and Table II lists the fluxes that would have been obtained, had all the laser pulses been used, together with the corresponding conversion efficiencies for each harmonic order. As can be seen in the table, up to $4.2 \cdot 10^{11}$ photons/s per harmonic order were generated at 20 kHz and a pulse energy of 175 μ J, corresponding to a conversion efficiency of $4.9 \cdot 10^{-7}$. At 100 kHz and a pulse energy of 54 μ J, up to $4.4 \cdot 10^{10}$ photons/s were generated per order, corresponding to a conversion efficiency $3.9 \cdot 10^{-8}$.

High-order harmonics were also generated in neon. Since neon has a higher ionization potential than argon (21.56 eV compared to 15.76 eV) the laser intensity can be increased without completely ionizing the gas and saturating the HHG process, and thereby higher cut-off energies are reached. The yield is, however, strongly reduced compared to when using argon.

Since our grating was not optimized for the short wavelengths obtained when generating harmonics in neon, several diffraction orders overlapped (see Fig. 3) and the harmonics had to be sorted into their respective diffraction order. The different diffraction orders can easily be identified from the change in divergence as the harmonic cut-off is approached (see Fig. 3). The cut-off part for both the first and the second diffraction order were outside the range of the detector and there is unfortunately a partial overlap between the harmonic orders in the first and the third diffraction orders. This is why we had to use the fourth diffraction order to identify the highest achievable harmonic order. The highest harmonic order we observed in neon was 77 (92.7 eV or 13.4 nm) obtained at 20 kHz repetition rate with a pulse energy of 170 μ J.

IV. CONCLUSION

In conclusion we have demonstrated high-order harmonic generation using a high-repetition-rate turnkey laser. We have performed a technical investigation of our system and demonstrated that high-order harmonics could be generated at up to 400 kHz repetition rate in argon. A flux of up to $4.2 \cdot 10^{11}$ and $4.4 \cdot 10^{10}$ XUV photons/s per harmonic order was measured for 20 kHz and 100 kHz, respectively. This corresponds to the conversion efficiencies of $4.9 \cdot 10^{-7}$ and $3.9 \cdot 10^{-8}$. High-order harmonic generation using this compact, user-friendly and stable laser was achieved in argon, neon and air. In neon harmonic orders as high as 77 were generated, which cor-

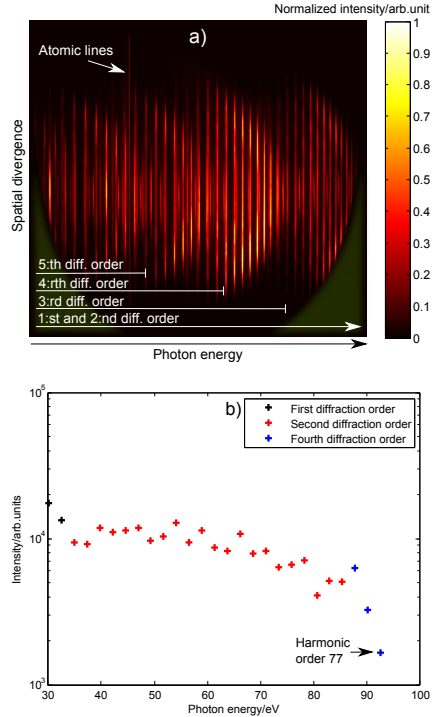


FIG. 3: A neon harmonic spectrum, obtained at 20 kHz, is shown in a). The two atomic lines used for calibration are indicated, together with the diffraction orders present in the image. A lineout is performed on a) along the photon energy axis and at the center of the spectrum in the spatial divergence direction. The values of the peaks corresponding to the identified harmonic orders are shown in b). The efficiency of the grating is different for different diffraction orders and the harmonic amplitudes of the first and fourth diffraction orders were adjusted to fit the harmonic amplitudes of the second diffraction order. Photon energies above 90 eV can be observed.

responds to 13.4 nm or 92.7 eV. This study shows that high-order harmonics, and hence attosecond pulses, can be generated at high repetition rate, flux and photon energy with a turnkey laser. This can be of interest to all attoscience experiments benefiting from high repetition rate HHG, but could also invite researchers from new fields to start using high-order harmonics.

Harmonic order	Photon energy/eV	20 kHz		100 kHz	
		Number of photons generated/s · 10 ¹¹	Conversion efficiency · 10 ⁻⁷	Number of photons generated/s · 10 ¹⁰	Conversion efficiency · 10 ⁻⁸
13	15.6	0.5	0.3	-	-
15	18.1	0.5	0.4	0.4	0.2
17	20.5	2.3	2.2	3.0	1.9
19	22.9	3.0	3.1	3.9	2.7
21	25.3	4.2	4.9	4.1	3.1
23	27.7	2.3	3.0	4.2	3.4
25	30.1	2.3	3.1	4.4	3.9
27	32.5	1.8	2.7	4.1	4.0
29	34.9	1.4	2.2	3.5	3.7
31	37.3	1.4	2.3	1.3	1.5
33	39.7	0.9	1.7	0.1	0.1
35	42.1	0.4	0.7	-	-
37	44.5	0.1	0.2	-	-
39	46.9	0.03	0.07	-	-
Total		21.1	27.0	29.0	24.3

TABLE II: The number of XUV photons per second as well as conversion efficiencies for the different harmonic orders generated in argon at 20 kHz and 100 kHz repetition rate. The pulse energy was 175 μ J and 54 μ J at the two repetition rates.

ACKNOWLEDGMENTS

This research was supported by the Swedish Foundation of Strategic research, the Marie Curie program AT-

TOFEL (ITN), the Swedish Research Council and the Knut and Alice Wallenberg Foundation.

- [1] M. Ferray, A. L'Huillier, X. F. Li, G. Mainfray, and C. Manus, *J. Phys. B* **21**, L31 (1988).
- [2] T. Popmintchev, M.-C. Chen, D. Popmintchev, P. Arpin, S. Brown, S. Alisauskas, G. Andriukaitis, T. Balciunas, O. D. Mücke, A. Pugzlys, A. Baltuska, B. Shim, S. E. Schrauth, A. Gaeta, C. Hernandez-Garcia, L. Plaja, A. Becker, A. Jaron-Becker, M. M. Murnane, and H. C. Kapteyn, *Science* **336**, 1287 (2012).
- [3] R. A. Bartels, A. Paul, H. Green, H. C. Kapteyn, M. M. Murnane, S. Backus, I. P. Christov, Y. Liu, D. Attwood, and C. Jacobsen, *Science* **297**, 376 (2002).
- [4] P. M. Paul, E. S. Toma, P. Breger, G. Mullot, F. Augé, P. Balcou, H. G. Muller, and P. Agostini, *Science* **292**, 1689 (2001).
- [5] M. Hentschel, R. Kienberger, C. Spielmann, G. A. Reider, N. Milosevic, T. Brabec, P. Corkum, U. Heinzmann, M. Drescher, and F. Krausz, *Nature* **414**, 509 (2001).
- [6] M. Drescher, M. Hentschel, R. Kienberger, M. Uiberacker, V. Yakovlev, A. Scrinzi, T. Westerwalbesloh, U. Kleineberg, U. Heinzmann, and F. Krausz, *Nature* **419**, 803 (2002).
- [7] A. L. Cavalieri, N. Müller, T. Uphues, V. S. Yakovlev, A. Baltuska, B. Horvath, B. Schmidt, L. Blümel, R. Holzwarth, S. Hendel, M. Drescher, U. Kleineberg, P. M. Echenique, R. Kienberger, F. Krausz, and U. Heinzmann, *Nature* **449**, 1029 (2007).
- [8] J. Mauritsson, P. Johnsson, E. Mansten, M. Swoboda, T. Ruchon, A. L'Huillier, and K. J. Schafer, *Phys. Rev. Lett.* **100**, 073003 (2008).
- [9] G. Sansone, F. Kelkensberg, J. F. Pérez-Torres, F. Morales, M. F. Kling, W. Siu, O. Ghafur, P. Johnsson, M. Swoboda, E. Benedetti, F. Ferrari, F. Lépine, J. L. Sanz-Vicario, S. Zherebtsov, I. Znakovskaya, A. L'Huillier, M. Y. Ivanov, M. Nisoli, F. Martin, and M. J. J. Vrakking, *Nature* **465**, 763766 (2010).
- [10] M. Schultze, M. Fie, N. Karpowicz, J. Gagnon, M. Korbman, M. Hofstetter, S. Neppl, A. L. Cavalieri, Y. Komninos, T. Mercouris, C. A. Nicolaides, R. Pazourek, S. Nagele, J. Feist, J. Burgdrfer, A. M. Azzeer, R. Ernstorfer, R. Kienberger, U. Kleineberg, E. Goulielmakis, F. Krausz, and V. S. Yakovlev, *Science* **328**, 1658 (2010).
- [11] J. Mauritsson, T. Remetter, M. Swoboda, K. Klunder, A. L'Huillier, K. J. Schafer, O. Ghafur, F. Kelkensberg, W. Siu, P. Johnsson, M. J. J. Vrakking, I. Znakovskaya, T. Uphues, S. Zherebtsov, M. F. Kling, F. Lepine, E. Benedetti, F. Ferrari, G. Sansone, and M. Nisoli, *Phys. Rev. Lett.* **105**, 053001 (2010).
- [12] F. Krausz and M. Ivanov, *Reviews of Modern Physics* **81**, 163 (2009).
- [13] P. B. Corkum, *Phys. Rev. Lett.* **71**, 1994 (1993).
- [14] K. J. Schafer, B. Yang, L. F. DiMauro, and K. C. Kulander, *Phys. Rev. Lett.* **70**, 1599 (1993).
- [15] J. Ullrich, R. Moshhammer, A. Dorn, R. Dörner, L. P. H. Schmidt, and H. Schmitt-Böcking, *Reports on Progress in Physics* **66**, 1463 (2003).
- [16] K. P. Singh, F. He, P. Ranitovic, W. Cao, S. De, D. Ray, S. Chen, U. Thumm, A. Becker, M. M. Murnane, H. C. Kapteyn, I. V. Litvinyuk, and C. L. Cocke, *Phys. Rev. Lett.* **104**, 023001 (2010).
- [17] F. O. Schumann, C. Winkler, and J. Kirschner, *Phys. Rev. Lett.* **98**, 257604 (2007).

- [18] C. Gohle, T. Udem, M. Herrmann, J. Rauschenberger, R. Holzwarth, H. A. Schuessler, F. Krausz, and T. W. Hänsch, *Nature* **436**, 234 (2005).
- [19] D. Z. Kandula, C. Gohle, T. J. Pinkert, W. Ubachs, and K. S. E. Eikema, *Phys. Rev. Lett.* **105** (2010).
- [20] R. J. Jones, K. D. Moll, M. J. Thorpe, and J. Ye, *Phys. Rev. Lett.* **94**, 193201 (2005).
- [21] A. Mikkelsen, J. Schwenke, T. Fordell, G. Luo, K. Klünder, E. Hilner, N. Anttu, A. A. Zakharov, E. Lundgren, J. Mauritsson, J. N. Andersen, H. Q. Xu, and A. L'Huillier, *Review Of Scientific Instruments* **80**, 123703 (2009).
- [22] M. Huth, C.-T. Chiang, A. Trützschler, F. O. Schumann, J. Kirschner, and W. Widdra, *Appl. Phys. Lett.* **104**, 061602 (2014).
- [23] F. Lindner, W. Stremme, M. G. Schätzel, F. Grasbon, G. G. Paulus, H. Walther, R. Hartmann, and L. Strüder, *Phys. Rev. A* **68**, 013814 (2003).
- [24] M. C. Chen, M. R. Gerrity, S. Backus, T. Popmintchev, X. Zhou, P. Arpin, X. Zhang, H. C. Kapteyn, and M. M. Murnane, *Opt. Exp.* **17**, 17376 (2009).
- [25] J. Bouillet, Y. Zaouter, J. Limpert, S. Petit, Y. Mairesse, B. Fabre, J. Higuët, E. Mevel, E. Constant, and E. Cormier, *Opt. Lett.* **34**, 1489 (2009).
- [26] S. Hädrich, M. Krebs, J. Rothhardt, H. Carstens, S. Demmler, J. Limpert, and A. Tünnermann, *Opt. Express* **19**, 19374 (2011).
- [27] A. Vernaleken, J. Weitenberg, T. Sartorius, P. Russbuedt, W. Schneider, S. L. Stebbings, M. F. Kling, P. Hommelhoff, H.-D. Hoffmann, R. Poprawe, F. Krausz, T. W. Hänsch, and T. Udem, *Opt. Lett.* **36**, 3428 (2011).
- [28] C.-T. Chiang, A. Blattermann, M. Huth, J. Kirschner, and W. Widdra, *Appl. Phys. Lett.* **101**, 071116 (2012).
- [29] M. Krebs, S. Hädrich, S. Demmler, J. Rothhardt, A. Zar, L. Chipperfield, J. Limpert, and A. Tünnermann, *Nature Photonics* **7**, 555 (2013).
- [30] S. Fuchs, C. Rödel, M. Krebs, S. Hädrich, J. Bierbach, A. E. Paz, S. Kuschel, M. Wünsche, V. Hilbert, U. Zastrau, E. Förster, J. Limpert, and G. G. Paulus, *Review of Scientific Instruments* **84**, 023101 (2013).
- [31] C. M. Heyl, J. Güdde, A. L'Huillier, and U. Höfer, *Journal of Physics B: Atomic, Molecular and Optical Physics* **45**, 074020 (2012).
- [32] J. Rothhardt, M. Krebs, S. Hädrich, S. Demmler, J. Limpert, and A. Tünnermann, *New Journal of Physics* **16**, 033022 (2014).
- [33] D. C. Yost, T. R. Schibli, J. Ye, J. L. Tate, J. Hostetter, M. B. Gaarde, and K. J. Schafer, *Nature Physics* **5**, 815 (2009).
- [34] S. Kim, J. Jin, Y.-J. Kim, I.-Y. Park, Y. Kim, and S.-W. Kim, *Nature* **453**, 757 (2008).
- [35] M. Sivilis, M. Duwe, B. Abel, and C. Ropers, *Nature* **485**, E1 (2012).
- [36] J. L. Krause, K. J. Schafer, and K. C. Kulander, *Phys. Rev. Lett.* **68**, 3535 (1992).
- [37] J. Tate, T. Augustine, H. G. Muller, P. Salières, P. Agostini, and L. F. DiMauro, *Phys. Rev. Lett.* **98**, 013901 (2007).
- [38] I. Velchev, W. Hogervorst, and W. Ubachs, *J. Phys. B* **32**, L511 (1999).
- [39] L. Minnhagen, *J. Opt. Soc. Am.* **63**, 1185 (1973).
- [40] E. B. Saloman and C. J. Sansonetti, *Journal of Physical and Chemical Reference Data* **33**, 1113 (2004).
- [41] M. Lewenstein, P. Balcou, M. Ivanov, A. L'Huillier, and P. B. Corkum, *Phys. Rev. A* **49**, 2117 (1994).
- [42] R. López-Martens, K. Varjú, P. Johnsson, J. Mauritsson, Y. Mairesse, P. Salières, M. B. Gaarde, K. J. Schafer, A. Persson, S. Svanberg, C.-G. Wahlström, and A. L'Huillier, *Phys. Rev. Lett.* **94**, 033001 (2005).
- [43] B. Henke, E. Gullikson, and J. Davis, *Atomic Data and Nuclear Data Tables* **54**, 181 (1993).

PAPER V

Attosecond Pulse Walk-Off in High-Order Harmonic Generation

D. Kroon, D. Guénot, M. Kotur, E. Balogh, E. W. Larsen,
C. M. Heyl, M. Miranda, M. Gisselbrecht, J. Mauritsson, P. Johnsson,
K. Varjú, A. L'Huillier and C. L. Arnold.

Optics Letters **39**, 2218 (2014).

Attosecond pulse walk-off in high-order harmonic generation

D. Kroon,^{1,*} D. Guénot,¹ M. Kotur,¹ E. Balogh,² E. W. Larsen,¹ C. M. Heyl,¹ M. Miranda,¹ M. Gisselbrecht,¹ J. Mauritsson,¹ P. Johnsson,¹ K. Varjú,² A. L'Huillier,¹ and C. L. Arnold¹

¹Department of Physics, Lund University, P.O. Box 118, 22100 Lund, Sweden

²Department of Optics and Quantum Electronics, University of Szeged, Dóm tér 9, 6720 Szeged, Hungary

*Corresponding author: david.kroon@fysik.lth.se

Received January 8, 2014; revised March 5, 2014; accepted March 6, 2014;
posted March 7, 2014 (Doc. ID 204087); published March 31, 2014

We study the influence of the generation conditions on the group delay of attosecond pulses in high-order harmonic generation in gases. The group delay relative to the fundamental field is found to decrease with increasing gas pressure in the generation cell, reflecting a temporal walk-off due to the dispersive properties of the nonlinear medium. This effect is well reproduced using an on-axis phase-matching model of high-order harmonic generation in an absorbing gas. © 2014 Optical Society of America

OCIS codes: (320.7110) Ultrafast nonlinear optics; (020.2649) Strong field laser physics; (020.4180) Multiphoton processes.

<http://dx.doi.org/10.1364/OL.39.002218>

The nonlinear interaction between a focused high-power laser beam and a gas target generates broadband light bursts emitted once every half cycle of the driving field [1,2]. In the spectral domain, the half-cycle periodicity and symmetry properties of the target gas result in peaks centered at the odd-order harmonics of the driving pulse carrier frequency. The large bandwidth combined with the coherence of the process, inherited from the generating field, yields pulses with a time duration on the attosecond scale [3,4]. The intrinsic synchronization of the attosecond pulses with the generating field [5] allows for pump-probe experiments on an ultrafast time scale.

By cross correlating the attosecond pulse train (APT) with a weak copy of the generating pulse in a detection gas, while monitoring the generated photoelectron spectrum, the phase difference between consecutive harmonic orders can be extracted [5]. Combined with a measurement of the relative spectral amplitudes, this information allows for a reconstruction of the average time structure of the pulses in the train. This is the well-known RABITT scheme (reconstruction of attosecond beating by interference of two-photon transition) for characterization of APTs.

This technique has recently gained a lot of interest since the comparison of RABITT measurements in different systems, for example, different atomic shells, allows for the determination of their relative photoionization delays [6]. These experiments demand high interferometric stability, on the order of tens of attoseconds, and require control of the timing of the attosecond pulses relative to the fundamental field. In some early implementations of the RABITT scheme [5,7,8], the probe pulse and the generation pulse were both propagated through the generation medium, making it possible to encode the phase relation between the generating and the probing field into the recorded electron spectrogram, but at the same time perturbing the regularity of the pulse train.

In this work, we perform RABITT measurements using an actively stabilized interferometer. We present an experimental study of the group delay of the attosecond

pulses relative to the generating field as a function of the gas density in the generation cell. Our results show that the detected pulse train advances by almost 200 as, relative to the fundamental field, as the pressure is increased by a factor of three. This observation is interpreted as a temporal walk-off of the attosecond pulses due to dispersion in the medium and simulated using an on-axis phase-matching model.

The experiments were performed with a Ti:Sapphire femtosecond laser emitting pulses with 20 fs (FWHM) duration, centered around 800 nm, with 1 kHz repetition rate and a pulse energy of 3 mJ. A beam splitter divides the laser output into the probe and the pump arm of a Mach-Zehnder interferometer [see Fig. 1(a)]. The pump pulse is focused into a 6 mm long cylindrical cell by a 45 cm focal length parabolic mirror. A pulsed gas valve, synchronized with the laser pulses, releases Ar gas into the cell where the XUV light is generated. The instantaneous gas pressure in the cell is stabilized by monitoring the background pressure in the chamber and controlling the valve opening with a feedback loop. The actual pressure in the generation cell is unknown and is assumed to scale linearly with the background pressure. A 200 nm thick aluminium filter blocks the fundamental radiation and acts as an amplitude and phase filter for the harmonic radiation. The probe arm and the generation arm of the interferometer are recombined using a holey

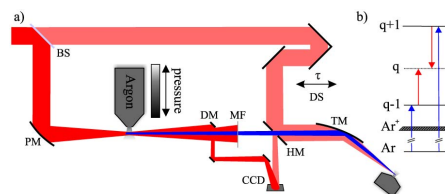


Fig. 1. Schematic outline of (a) the experimental setup and (b) the principle of the measurement. The optical elements are a beam splitter (BS), a parabolic mirror (PM), a d-shaped mirror (DM), a metallic filter (MF), a holey mirror (HM), a toroidal mirror (TM), and a delay stage (DS).

mirror, which transmits the XUV APT and reflects the outer portion of the probe beam. A gold coated toroidal mirror focuses both beams into the sensitive region of a magnetic bottle electron spectrometer, where an effusive gas jet provides argon as the detection gas.

The delay is monitored by forming spatial interference fringes between the generation beam and probe beam on the CCD chip of a camera. For this purpose, a small portion of the generation beam is split off with a d-shaped mirror prior to the metallic filter; for the probe beam the portion going through the hole in the recombination mirror is used. A computer program extracts the phase of the spatial fringes and sends a feedback signal to a piezoelectric delay stage in the probe arm. Any perturbation of the optical path length introduced in either of the interferometer arms is, thus, actively compensated for. Furthermore, laser beam-pointing drifts, which could be interpreted as a relative length change of the interferometer arms, are avoided by active beam-pointing stabilization before the interferometer. The precision of the delay stabilization was tested in an out-of-loop measurement. A comparison between the active delay stabilization being turned off and on shows that the standard deviation of the extracted phase delay between the pump and probe pulses drops from 200 as to 50 as, for a measurement taken over 400 s.

The experiment consisted of recording spectrograms of the photoelectron energy as a function of the delay (τ) between the APTs and the infrared (IR) probe field. Sidebands appear between the harmonic peaks in the photoelectron spectrogram due to absorption of a harmonic ($q-1$) and an IR photon, or by absorption of the next harmonic ($q+1$) and emission of an IR photon [see Fig. 1(b)]. The sideband intensity oscillates as a function of delay [3], according to

$$S(\tau, q) = A + B \cos[2\omega(\tau - \tau_q)], \quad (1)$$

where A and B are quantities that depend on the probability amplitudes of the two processes leading to the same final state and ω is the fundamental angular frequency. The quantity extracted from the measurement, τ_q , is a time offset equal to

$$\tau_q = \frac{\phi_{q+1} - \phi_{q-1}}{2\omega} \approx \left. \frac{\partial \phi_{\Omega}}{\partial \Omega} \right|_{\Omega=q\omega}, \quad (2)$$

where ϕ_{q+1} and ϕ_{q-1} are the accumulated phases along the two quantum paths shown in Fig. 1(b). ϕ_{q+1} is the sum of the phase of the $(q+1)$ th harmonic field and the phase accumulated in the two-photon ionization process [6]. τ_q can thus generally be written as a sum of two terms, one representing the group delay of the average attosecond pulse in the train and a second term originating from the electronic transition. On the right-hand side of Eq. (2), the finite difference is approximated as the derivative of the phase with respect to the angular frequency, $\Omega = q\omega$.

Figure 2 summarizes the experimental results presented in this Letter. Figure 2(a) shows photoelectron spectra obtained at four different pressures in the harmonic generation cell. Each of the spectra has been

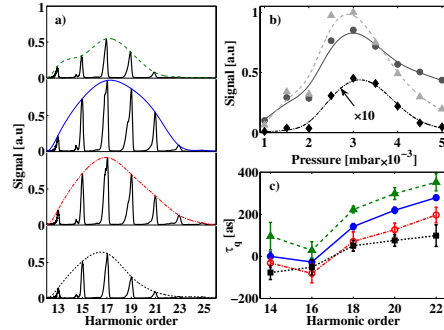


Fig. 2. Summary of the experimental results. (a) Photoelectron spectra from Ar atoms, ionized by a train of XUV pulses generated at generation pressures corresponding to 1.5×10^{-3} , 2.5×10^{-3} , 3.5×10^{-3} , and 4.5×10^{-3} mbar background pressure. An estimate of the spectral envelope, by interpolation between the peak values, is indicated. (b) Spectral amplitudes of harmonics 15 (solid circles), 19 (triangles) and 23 (diamonds, $\times 10$) as a function of pressure. (c) Relative group delays at the same pressures as in (a). The line types and colors match those in (a). The group delay at sideband order 14 at the pressure 2.5×10^{-3} mbar has been arbitrarily set to zero.

corrected for the absorption cross section to reflect the spectral properties of the pulse train. In Fig. 2(b) the spectral amplitudes of harmonics 15, 19, and 23 are plotted as a function of the background pressure. High-order harmonics exhibit a greater sensitivity to a pressure change than low-orders. This leads to a bandwidth narrowing and a shift of the spectral envelope toward lower photon energies with increasing pressure. Finally, Fig. 2(c) shows the spectrally-resolved group delay extracted from the sideband oscillations, in the energy range 22–34 eV. The data points were obtained by alternating measurements at a particular pressure and a reference pressure of 2.5×10^{-3} mbar. The error bars were estimated by considering the variation in five such consecutive measurements. A few important features can be observed. For a given pressure, the group delay increases with harmonic order, meaning that high-order harmonics are delayed relative to low orders (positive chirp). This behavior indicates that the harmonics are dominantly generated from short electron trajectories [5,9]. The Al filter exhibit negative group delay dispersion in this spectral range and partly compensates for the chirp. The anomalous behavior of sideband 16 can be attributed to the 26.6 eV, $3s^23p^6 \rightarrow 3s3p^64p$ resonant transition to an autoionizing state [10], affecting the phase of the two-photon ionization process. Finally, over the entire spectral range there is a negative shift of the group delay with increasing generation pressure. Understanding this effect is the focus of this Letter.

We rewrite τ as $\phi_p/\omega = [(q+1)\phi_p - (q-1)\phi_p]/2\omega$, where ϕ_p is the (variable) phase of the probe field. Since ϕ_p is related to the phase of the pump field, ϕ_1 , by a constant, δ , which does not depend on the generating conditions and in particular not on the pressure in the generating medium, we replace ϕ_p by ϕ_1 and Eq. (1) becomes

$$S(\tau, q) = A + B \cos(\Delta\phi_{q-1} - \Delta\phi_{q+1} + 2\delta), \quad (3)$$

where $\Delta\phi_q = \phi_q - q\phi_1$ is the phase mismatch, i.e., the relative phase between the generated field and the polarization of the medium at the same frequency ($q\omega$). The phase mismatch is the sum of several contributions. It includes the phase of the atomic (microscopic) dipole moment, which is related to the accumulated time the electron spends in the continuum [5] as well as the dispersion of the metallic filter. It also includes macroscopic contributions from the upconversion process, such as dispersion in the generation medium and the Gouy phase due to focusing.

For simplicity, we initially assume that the chirp induced by the single atom response (“atto-chirp”) is approximately compensated for by an adequate filter. We also assume a homogeneous medium of length, L , and loose focusing, so that the variation of the Gouy phase can be approximated by a linear term. The first part of the argument of the cosine function in Eq. (3) can then be approximated by $2\omega\tau_w$, with

$$\tau_w = \frac{\Delta\phi_{q+1} - \Delta\phi_{q-1}}{2\omega} \approx \frac{\partial\Delta\phi_\Omega}{\partial\Omega} \approx \frac{\partial\phi_\Omega}{\partial\Omega} - \frac{\phi_1}{\omega}. \quad (4)$$

Equation (4) has a simple physical interpretation. The right-hand side represents the frequency-resolved *temporal walk-off* of the attosecond pulse relative to the half-cycle of the fundamental field. In the simple case where absorption can be neglected, $\Delta\phi_q \approx \Delta k_q L/2$, where Δk_q represents the wave-vector mismatch between the generated harmonic field and the component of the nonlinear polarization of frequency $q\omega$. The harmonics are, on average, generated in the middle of the medium, which explains the factor $1/2$. $2\tau_w/L$ is then the difference between the inverse of the group velocity ($\partial k_\Omega/\partial\Omega$) of the attosecond pulse at frequency, Ω , and the inverse of the phase velocity at the fundamental frequency (k_1/ω). In the more realistic case, where absorption is considered, the effective interaction length depends on frequency and the temporal walk-off cannot simply be expressed in terms of velocities, but rather delays.

Including absorption and assuming a 1D geometry [11,12], the phase mismatch can be expressed as

$$\Delta\phi_q = \Delta k_q \frac{L}{2} - \arctan \left[\frac{\tan \left(\frac{\Delta k_q \frac{L}{2}}{\tanh \left(\kappa_q \frac{L}{2} \right)} \right)}{\tanh \left(\kappa_q \frac{L}{2} \right)} \right] + \arctan \left[\frac{\Delta k_q}{\kappa_q} \right], \quad (5)$$

where κ_q is the absorption coefficient at frequency $q\omega$. Figure 3(a) shows numerical estimates of different contributions to Δk_q as a function of frequency, using parameters mimicking the experiment (1% degree of ionization, corresponding to a peak intensity of 1×10^{14} W/cm², and a confocal parameter of 1.3 cm, with the focus in the center of the 6 mm long cell). The Gouy phase leads to a pressure-independent positive and approximately linear term (dashed-dotted line). The wave vector mismatches due to dispersion in the neutral medium and because of the generated free electrons are shown in solid and dashed lines, respectively. The respective influences of the three contributions change with varying pressure,

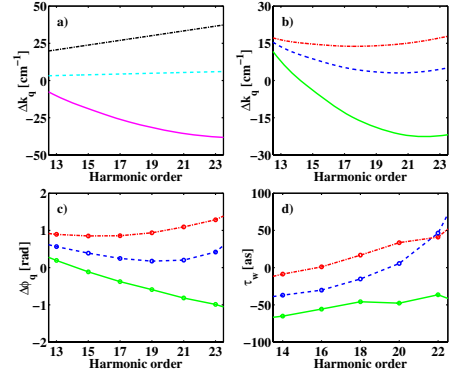


Fig. 3. (a) Contributions to the wave-vector mismatch at a gas pressure of 44 mbar: dispersion of the neutral Ar gas (solid line), dispersion of the plasma generated by the driving pulse (dashed line), and contribution from the geometrical phase (dashed-dotted line). (b) Sum of all the contributions at three different generation pressures (dashed-dotted, 27 mbar; dashed, 44 mbar; solid, 80 mbar). (c) Phase mismatch calculated using Eq. (5). (d) τ_w , as defined in Eq. (4).

as shown in Fig. 3(b). At low pressures, Δk_q is dominated by the positive Gouy phase contribution. At higher pressures, it becomes more and more influenced by neutral dispersion, leading to a characteristic decreasing curve. Figure 3(c) shows $\Delta\phi_q$ at three different pressures. The difference between (b) and (c) arises from absorption, which influences mainly the low harmonic orders, as well as from the coherent buildup process itself, when $\Delta k_q \neq 0$ and the coherence length is less than the medium length [see Eq. (5)]. The slope of $\Delta\phi_q$ changes from positive when the Gouy phase is the dominant contribution to Δk_q , negative when, instead, dispersion is most important. The group delay therefore decreases over the whole spectral range when the pressure increases, as can be seen in Fig. 3(d).

Figure 4 shows the results of our 1D simulation. The model reproduces qualitatively the main experimental observations. The harmonic spectral envelope shifts to lower photon energies as the pressure increases [Fig. 4(a)]. The amplitude exhibits a maximum at the “phase matching” pressure [13,14], where the phase mismatch is zero [Fig. 4(b)] and the phase matching pressure is almost independent of order. Finally, the group delay decreases by about 80 as from the lowest to the highest pressure [Figs. 4(b) and 4(c)]. This variation represents the temporal walk-off of the attosecond pulses relative to the fundamental field as the pressure is varied. As explained, it originates from the dispersion properties of the generating medium and, in particular, the decrease of the refractive index of argon gas for photon energies above the ionization threshold. Its magnitude depends also on the interplay of absorption and phase matching, limiting the effective generation length. The physical length of the generation medium which, under our experimental conditions, could be slightly dependent on the pressure, plays a subordinate role as the accumulated phase mismatch is determined by the absorption length

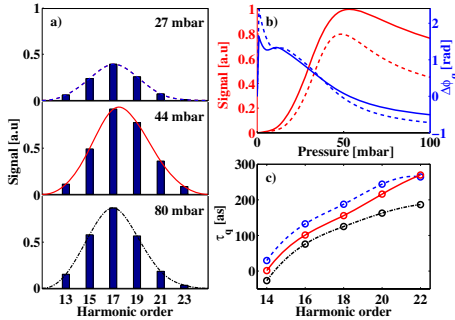


Fig. 4. 1D simulations. (a) Calculated spectral amplitudes at three different generation pressures. (b) Amplitudes of harmonics 17 (solid lines) and 19 (dashed lines) as a function of pressure. (c) Relative attosecond group delay, at the same pressures as in (a), including the “atto chirp” and the metallic filter dispersion.

rather than the physical length of the medium. A more quantitative description of our experimental results would require the inclusion of temporal and 3D effects, which is beyond the scope of this Letter.

In conclusion, we find that, with increasing generation pressure, the harmonic spectral envelope shifts toward lower energy and the APT acquires a negative group delay, which we interpret as a temporal walk-off. Consequently, attosecond pump-probe experiments require not only mechanical stability but also a constant pressure in the generation region. Conversely, group delay measurements, such as those presented in this work, give new insights into the generation process, highlighting the role of phase matching on the attosecond time scale.

This research was supported by the Marie Curie program ATTOFEL (ITN), the European Research Council (ALMA), the Swedish Foundation for Strategic Research, the Swedish Research Council, and the Knut and Alice Wallenberg Foundation. KV and EB acknowledge support from the Bolyai Grant of the Hungarian Academy

of Sciences and the Hungarian Scientific Research Fund (OTKA project NN 107235).

References

1. P. B. Corkum, *Phys. Rev. Lett.* **71**, 1994 (1993).
2. K. J. Schafer, B. Yang, L. F. DiMauro, and K. C. Kulander, *Phys. Rev. Lett.* **70**, 1599 (1993).
3. P. M. Paul, E. S. Toma, P. Breger, G. Mullot, F. Augé, P. Balcou, H. G. Muller, and P. Agostini, *Science* **292**, 1689 (2001).
4. M. Hentschel, R. Kienberger, C. Spielmann, G. A. Reider, N. Milosevic, T. Brabec, P. Corkum, U. Heinzmann, M. Drescher, and F. Krausz, *Nature* **414**, 509 (2001).
5. Y. Mairesse, A. de Bohan, L. J. Frasinski, H. Merdji, L. C. Dinu, P. Monchicourt, P. Breger, M. Kovačev, R. Taïeb, B. Carré, H. G. Muller, P. Agostini, and P. Salières, *Science* **302**, 1540 (2003).
6. K. Klünder, J. M. Dahlström, M. Gisselbrecht, T. Fordell, M. Swoboda, D. Guénot, P. Johnsson, J. Caillat, J. Mauritsson, A. Maquet, R. Taïeb, and A. L’Huillier, *Phys. Rev. Lett.* **106**, 143002 (2011).
7. L. C. Dinu, H. G. Muller, S. Kazamias, G. Mullot, F. Augé, P. Balcou, P. M. Paul, M. Kovačev, P. Breger, and P. Agostini, *Phys. Rev. Lett.* **91**, 063901 (2003).
8. S. A. Aseyev, Y. Ni, L. J. Frasinski, H. G. Muller, and M. J. J. Vrakking, *Phys. Rev. Lett.* **91**, 223902 (2003).
9. K. Varjú, Y. Mairesse, B. Carre, M. B. Gaarde, P. Johnsson, S. Kazamias, R. Lopez-Martens, J. Mauritsson, K. J. Schafer, P. Balcou, A. L’Huillier, and P. Salières, *J. Mod. Opt.* **52**, 379 (2005).
10. R. P. Madden, D. L. Ederer, and K. Codling, *Phys. Rev.* **177**, 136 (1969).
11. T. Ruchon, C. P. Hauri, K. Varjú, E. Mansten, M. Swoboda, R. López-Martens, and A. L’Huillier, *New J. Phys.* **10**, 025027 (2008).
12. E. Constant, D. Garzella, P. Breger, E. Mével, C. Dorrer, C. L. Blanc, F. Salin, and P. Agostini, *Phys. Rev. Lett.* **82**, 1668 (1999).
13. S. Kazamias, D. Douillet, F. Weihe, C. Valentin, A. Rousse, S. Sebban, G. Grillon, F. Augé, D. Hulin, and P. Balcou, *Phys. Rev. Lett.* **90**, 193901 (2003).
14. P. Rudawski, C. M. Heyl, F. Brizuela, J. Schwenke, A. Persson, E. Mansten, R. Rakowski, L. Rading, F. Campi, B. Kim, P. Johnsson, and A. L’Huillier, *Rev. Sci. Instrum.* **84**, 073103 (2013).

PAPER VI

A High-Flux High-Order Harmonic Source

P. Rudawski, C. M. Heyl, F. Brizuela, J. Schwenke, A. Persson,
E. Mansten, R. Rakowski, L. Rading, F. Campi, B. Kim, P. Johansson
and A. L'Huillier.

Review of Scientific Instruments **84**, 073103 (2013).



A high-flux high-order harmonic source

P. Rudawski,^{1,a)} C. M. Heyl,¹ F. Brizuela,¹ J. Schwenke,¹ A. Persson,¹ E. Mansten,²
R. Rakowski,¹ L. Rading,¹ F. Campi,¹ B. Kim,¹ P. Johnsson,¹ and A. L'Huillier¹

¹Department of Physics, Lund University, P.O. Box 118, SE-221 00 Lund, Sweden

²MAX-lab, Lunds Universitet, P.O. Box 118, SE-221 00 Lund, Sweden

(Received 12 March 2013; accepted 11 June 2013; published online 9 July 2013)

We develop and implement an experimental strategy for the generation of high-energy high-order harmonics (HHG) in gases for studies of nonlinear processes in the soft x-ray region. We generate high-order harmonics by focusing a high energy Ti:Sapphire laser into a gas cell filled with argon or neon. The energy per pulse is optimized by an automated control of the multiple parameters that influence the generation process. This optimization procedure allows us to obtain energies per pulse and harmonic order as high as 200 nJ in argon and 20 nJ in neon, with good spatial properties, using a loose focusing geometry ($f_{\#} \approx 400$) and a 20 mm long medium. We also theoretically examine the macroscopic conditions for absorption-limited conversion efficiency and optimization of the HHG pulse energy for high-energy laser systems. © 2013 Author(s). All article content, except where otherwise noted, is licensed under a Creative Commons Attribution 3.0 Unported License. [<http://dx.doi.org/10.1063/1.4812266>]

I. INTRODUCTION

High-order harmonics generated by the nonlinear interaction of an intense ultrashort laser pulse with atoms or molecules are now used in many fields of physics. The interest in the generated radiation results from unique features like tunability over the extreme ultraviolet (XUV) and soft x-ray (SXR) spectral regions (reaching several keV^{1,2}), excellent beam quality,³ and ultrashort pulse duration down to the attosecond range.⁴ High-order harmonic generation (HHG) sources are well established in many research areas such as attosecond science⁵ or femtosecond spectroscopy⁶ and have become interesting for high-resolution imaging,^{7,8} free-electron-laser seeding,⁹ and nonlinear optics in the XUV range.^{10,11}

Most applications of HHG sources benefit from harmonic pulses with high pulse energy. This requirement is difficult to achieve due to the low conversion efficiency of the generation process. Since the discovery of the HHG process over two decades ago,^{12,13} its conversion efficiency has been progressively improved by optimizing the macroscopic phase-matching conditions and the microscopic single atom response. High-order harmonic generation has been carried out in different conditions, such as high-pressure jets,¹⁴ gas cells,¹⁵ semi-infinite media, and capillaries.¹⁶ Phase-matching optimization using loosely focused (possibly self-guided) fundamental fields has led to conversion efficiencies of $\sim 10^{-7}$ in neon,¹⁵ $\sim 10^{-5}$ in argon,¹⁷ and slightly below 10^{-4} in xenon.^{18,19} By modifying the generation field, e.g., by combining the fundamental field with one or more of its harmonics, the microscopic single atom response has been controlled on the subcycle level leading to enhanced HHG signals and/or generation of even-order harmonics.^{20–22}

In this article, we describe a high-flux HHG source operating in the photon energy range up to 100 eV. The HHG

setup is designed to work in a loose focusing geometry (up to 5 m focal length) and is driven by a high energy femtosecond laser system delivering up to 100 mJ per pulse. The optimization of the signal is performed using an automated scan of the main parameters that contribute to phase-matching (e.g., driving pulse intensity, gas pressure, etc.). Using this technique we have obtained a total energy per pulse in argon of a microjoule and a few hundred nJ in neon, in a geometry with an f-number $f_{\#} = f/D \approx 400$ and $f_{\#} \approx 133$, respectively, and a 20 mm long gas cell. Beam profiles were measured using an XUV-camera and the coherence properties were estimated in a Young's double-slit experiment. The article is organized as follows. Section II presents theoretical considerations for HHG under loose focusing. The HHG setup together with the methods for characterization and optimization are described in Sec. III. Results obtained with the high-energy, ultrashort laser system at the Lund Laser Centre are presented in Sec. IV. Section V presents a summary of the work and a discussion about scaling to extremely long focal lengths.

II. MODEL FOR LOOSE FOCUSING HHG

High-order harmonic generation with high conversion efficiency requires optimization of both the microscopic and macroscopic properties of the process. The microscopic response is well described by a semi-classical three-step model.^{23,24} In every half-cycle of the driving wave, electrons can tunnel through the distorted atomic potential barrier, being then accelerated in the intense laser field. Depending on the release time into the continuum, the electrons may return to the parent ion and recombine, emitting an XUV photon. The trajectories of these electrons can be divided into two groups called short and long, depending on the excursion time in the continuum. HHG requires laser intensities in the range of 10^{14} W/cm²– 10^{15} W/cm² depending on the selected gas.

^{a)}Electronic mail: piotr.rudawski@fysik.lth.se



Macroscopically, the total HHG signal is a coherent sum of the photons emitted from different atoms in the medium. For a given harmonic order q , constructive addition occurs along the propagation direction over the so-called coherence length $L_{\text{coh}} = \pi/\Delta k$. Here, $\Delta k = qk_1 - k_q$ is the wave-vector mismatch along the propagation direction between the generated field and the laser-induced polarization at frequency $q\omega$. In order to maximize the coherence length, the wave-vector mismatch must be minimized. In a non-guiding focus geometry this can be done through the interplay between the four sources of wave-vector mismatch,

$$\Delta k = \underbrace{\Delta k_g}_{<0} + \underbrace{\Delta k_n}_{>0} + \underbrace{\Delta k_p}_{<0} + \underbrace{\Delta k_d}_{\begin{matrix} <0 \text{ for } z < 0 \\ >0 \text{ for } z > 0 \end{matrix}}. \quad (1)$$

The negative contribution Δk_g originates from the Gaussian beam phase gradient along the propagation direction (z). Δk_n and Δk_p describe the neutral and free-electron dispersion which have opposite sign and are proportional to the gas pressure. To explicitly outline this linear dependence, we write $\Delta k_{n,p} = p \partial(\Delta k_{n,p})/\partial p$, where the partial derivative is now pressure independent in the following. Δk_d is the gradient of the so-called dipole phase which is proportional to the intensity gradient and is small for the short trajectories but large for the long ones.²⁵

Under our experimental conditions, the short trajectories dominate the HHG process. If only these trajectories are considered in Eq. (1), the dipole phase contribution can be neglected and the wave-vector mismatch can be minimized by canceling the plasma dispersion and Gaussian beam phase gradient with the neutral dispersion. For a fixed generation geometry, the degree of ionization in the medium determines the pressure, p_{match} , for which the system is phase matched.^{26,27} For each harmonic order, p_{match} is defined as

$$p_{\text{match}} = - \frac{\Delta k_g}{\frac{\partial(\Delta k_n)}{\partial p} + \frac{\partial(\Delta k_p)}{\partial p}}. \quad (2)$$

For a given medium, harmonic order, and focal length, the only variable parameter is the free-electron contribution which is proportional to the degree of ionization ($\partial\Delta k_p/\partial p \propto r_{\text{ion}}$), and consequently can be adjusted by changing the laser intensity. The equation requires the intensity to be low enough so that the contribution due to neutral dispersion dominates over the free-electron dispersion. This defines a maximum ionization degree ($r_{\text{ion}}^{\text{max}}$), typically a few percent, above which phase-matched generation is not possible.

Figure 1 shows the variation of p_{match} in argon as a function of the degree of ionization for three harmonic orders and two different focusing geometries. p_{match} tends towards infinity when r_{ion} reaches $r_{\text{ion}}^{\text{max}}$. At low degree of ionization, the phase-matching pressure varies little both with pressure and with harmonic order. Considering that the dipole response is highest at the highest intensity, one could assume that the most efficient generation is possible at high pressures and at intensities that support an ionization degree around $r_{\text{ion}}^{\text{max}}$. High intensities, however, lead to steep gradients of r_{ion} in the longitudinal and radial directions within the generation volume, confining phase-matched generation to a small volume and leading to transient phase-matching.²⁷ In spite of a

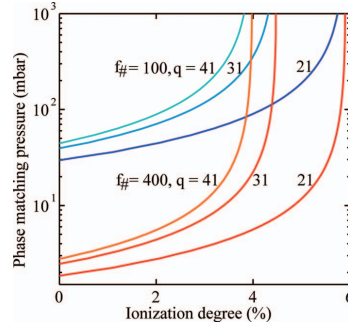


FIG. 1. Phase matching pressure in Ar as a function of ionization degree for different harmonic orders, q , and different focus geometries $f_{\#} = 100$, blue, and $f_{\#} = 400$, red. The central wavelength is 800 nm and the generation cell is placed at the focus of the fundamental beam.

higher single atom response at high intensity, those effects can reduce the overall efficiency. An optimum ionization degree should assure phase-matched HHG over a broad bandwidth and a large volume. The ionization level should be such that the phase-matching pressure is approximately constant for a broad range of high-order harmonics, potentially leading to short and intense attosecond pulses. This phase-matching bandwidth increases with decreasing ionization degree yet at the same time the single atom response as well as the conversion efficiency decrease. As a rule of thumb, the optimum value for the ionization degree can be taken as $\sim r_{\text{ion}}^{\text{max}}/2$ for the highest harmonic in the considered HHG bandwidth. Under the conditions of Figure 1, this corresponds to $\sim 2\%$ ionization and a laser intensity of $\sim 1.1 \times 10^{14}$ W/cm².

When the coherence length, L_{coh} , is maximized, the harmonic emission is limited by re-absorption in the generation gas. The absorption length, L_{abs} , is defined by

$$L_{\text{abs}}(p) = \frac{kT}{p\sigma_{\text{ion}}}, \quad (3)$$

where k is the Boltzmann constant, T the temperature, and σ_{ion} the ionization cross-section. Following the argumentation of Constant *et al.*,²⁸ the harmonic yield is then maximized when the medium length, L_{med} , is at least three times the absorption length. This allows to define an optimum medium length under phase-matched conditions, $L_{\text{med}}^{\text{opt}} = 3L_{\text{abs}}(p_{\text{match}})$. For example for the 21st harmonic in Ar, and $f_{\#} = 400$, $T = 300$ K, $\sigma_{\text{ion}} = 2 \times 10^{-21}$ m², $p_{\text{match}} \approx 5$ mbar, and consequently $L_{\text{med}}^{\text{opt}}$ should be chosen to be at least 12 mm.

For high-energy laser systems, an increase of the absorption-limited HHG intensity can be achieved by scaling up the $f_{\#}$, i.e., by increasing the focal length for a certain initial beam diameter. The conversion efficiency can be held constant when changing the focal length if the laser pulse energy, the gas pressure, and the medium length are scaled appropriately. Using Gaussian optics and Eqs. (2) and (3), we derive the following scaling relations: E_f (laser energy) $\propto f^2$ in order to keep the same intensity at focus, $p_{\text{match}} \propto 1/f^2$ since $\Delta k_g \propto 1/f^2$, and $L_{\text{med}} \propto f^2$. This ensures constant conversion

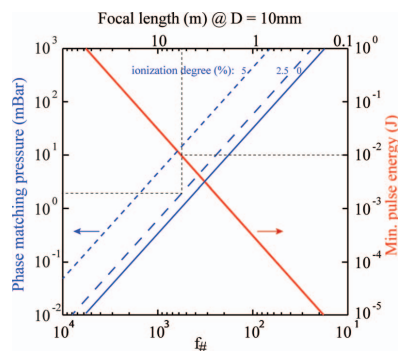


FIG. 2. Scaling of the phase matching pressure and the required laser pulse energy with focal length (or $f_{\#}$) for different ionization levels in argon. The corresponding minimum laser pulse energy required is shown in red. For the simulations, the following parameters were used: beam diameter before focusing: $D = 10$ mm, gas cell position: at the focus, central wavelength of 800 nm, harmonic order $q = 21$. The required pulse energy was calculated assuming a peak intensity of 1.5×10^{14} W/cm² and a pulse length of 45 fs.

efficiency, independent of the focusing geometry,²⁷ and the harmonic energy $E_h \propto f^2$.

Figure 2 illustrates these scaling relations in the case of argon, with the following parameters: 800 nm wavelength, a 45 fs pulse duration, an intensity of 1.5×10^{14} W/cm² at focus, and an initial beam diameter of 10 mm. A laser pulse energy of 10 mJ requires a focal length of approximately 5 m and a generation pressure of a few mbar to efficiently generate harmonics.

III. HIGH-ORDER HARMONIC EXPERIMENTAL SETUP

Our HHG setup consists of three sections: generation, diagnostics, and application (see Figure 3). The sections are connected by vacuum tubes with a diameter $\phi = 40$ mm. The generation section is mounted on stiffly connected optical tables. The diagnostics section together with the application chamber are mounted on a rail system. This allows us to adjust the distance between the vacuum chambers depending

on the focusing geometry in order to avoid damage of optical elements placed after the generation by the fundamental laser field. It also provides vibration isolation and high stability.

High-order harmonics are generated by loosely focusing a high energy laser beam into a noble gas. The fundamental laser beam is apertured down by a variable diameter iris (I), typically between 9 and 30 mm and focused by a lens (L). Control of the beam size allows for re-adjustments of the focusing geometry ($f_{\#}$) as well as laser energy and intensity distribution at focus. Thus it allows us to optimize phase-matching in a simple way. Directly after the focusing optics, the beam enters the generation chamber. The entrance UV fused silica window is mounted at a small angle to avoid back propagation of the reflected light to the laser system. The beam propagates inside a 100 mm diameter vacuum tube and is folded by mirrors (M) mounted on small breadboards placed in 6-way crosses. Alternatively, the laser beam can be focused by a mirror at near-normal incidence placed in one of the vacuum crosses. The focused beam interacts with the noble gas confined in a cell (PGC). The cylindrical cell has a diameter of typically 0.5 mm and a length between 3 mm and 20 mm. The gas is released at the repetition rate of the laser by a valve²⁹ driven by a piezo-electric actuator and synchronized with the laser pulse. The opening and closing times are optimized for maximum harmonic signal. Simulating the gas distribution in the cell, we found a small pressure gradient from the middle of the cell, where the gas is injected, towards the ends of the cell, where the pressure abruptly drops. The cell is mounted on an XY motorized stage. Additionally, two motorized actuators control the tilt of the cell with respect to the incoming beam. In order to optimize the position of the cell relative to the laser focus the gas cell is additionally placed on a 6 cm long-range translation stage moving along the propagation direction (Z).

The generation chamber is designed to work simultaneously with up to two gas cells. The cells can be mounted in parallel or in series. The parallel configuration allows for the generation of two independent harmonic beams³⁰ while the serial configuration can be used for the enhancement of the HHG process using low-order harmonics generated in the first cell.²² In both configurations, the generated harmonic beam propagates collinearly with the fundamental radiation in vacuum (10^{-6} mbar) to the diagnostics chamber. Elimination

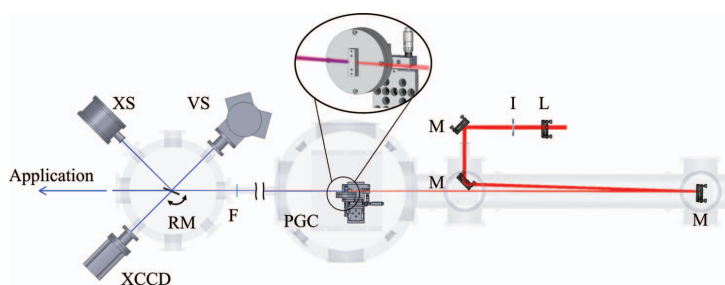


FIG. 3. HHG setup in the 4 m focusing configuration; L - focusing lens, I - iris, M - folding mirrors, PGC - pulsed gas cell, F - aluminum filters, RM - rotating mirror, XS - XUV spectrometer, VS - VUV spectrometer, and XCCD - XUV CCD camera.

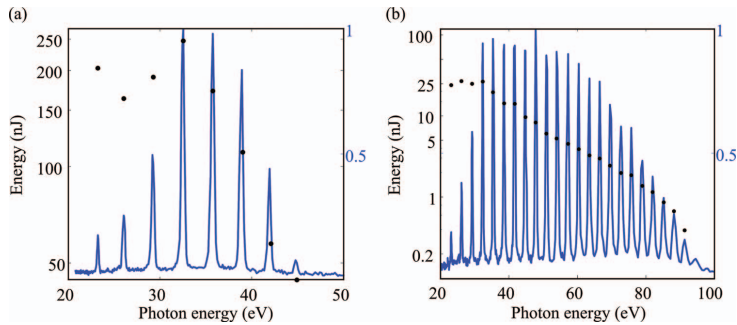


FIG. 4. High-order harmonic spectra in argon (a) and neon (b) gas. The pulse energy per individual harmonics, shown as dots, was obtained by combining total energy measurements with the spectral response from the XUV spectrometer.

of the fundamental is achieved by using 200 nm thick aluminum filters (F). The filters are mounted on a manual translation stage placed at the entrance of the diagnostics chamber, and controlled from the outside of the vacuum chamber.

The alignment of the setup is based on the beam position at the entrance iris and a reference point inside the diagnostics chamber. The precise alignment of the gas cell with respect to the laser beam is done by motorized control of the cell's four axes (XY and two tilts). The reference point and gas cell are monitored by cameras equipped with variable focal length objectives.

At the center of the diagnostics chamber, a gold-coated flat mirror (RM) mounted on a rotation stage is used to send the XUV beam to the different instruments or, when the mirror is removed, towards the application chamber (Fig. 3). The HHG spectra are measured by a flat-field grating spectrometer (XS, Jobin-Yvon PGM-PGS 200). The spectrometer detects spectrally-resolved far-field spatial profiles of individual high-order harmonics in the XUV spectral range. Low-order harmonics are detected using a vacuum ultraviolet monochromator (VS, McPherson 234/302). The vacuum ultraviolet spectrometer is equipped with an MCP detector coated with CsI allowing HHG diagnostics in a range from 50 to 250 nm. Additionally, spatial profiles and energy measurements are carried out using a back-illuminated XUV-CCD (Andor iKon-L) camera (XCCD). To attenuate the HHG beam for these measurements we use one or two 200 nm thick aluminum filters.

IV. RESULTS

This section presents measurements of high-order harmonics generated in argon and neon. The driving laser system is a high-power Ti:Sapphire chirped-pulse-amplification-based laser system delivering 45 fs pulses with up to 100 mJ energy at 10 Hz repetition rate. Before compression, the laser beam is spatially filtered with a conical pinhole mounted in a vacuum chamber. The pinhole waist, approximately 500 μm , is placed in a focal plane of a 1.7 m focal length lens. The laser beam diameter is 30 mm at the entrance to the har-

monic setup. The laser beam position and angle are actively stabilized.

Figure 4 presents typical integrated harmonic spectra for (a) argon and (b) neon, recorded by the XUV spectrometer. The driving laser beam, with 20 mJ energy in case of argon and 24 mJ in case of neon, was focused by a 4 m lens in a 20 mm long cell. The HHG cut-off energy is 45 eV (29th harmonic) in argon whereas in neon it reaches 91.5 eV (59th harmonic). Under these conditions the total measured harmonic energy per laser shot is 1.15 μJ for argon and 0.23 μJ for neon. These values correspond to conversion efficiencies of 5×10^{-5} for argon and 8×10^{-6} for neon. Due to the high sensitivity of the XUV camera to the infrared radiation, the harmonic beam energy is measured within the aluminum filter's transmission window, i.e., between 14 eV and 71 eV, corresponding to harmonic orders between 11 and 45. The measurement procedure, similar to the one described by Erny *et al.*,³¹ is based on XUV-CCD recorded background-subtracted images. The images are integrated to obtain the total number of counts. The total number of photons is estimated based on a calibration curve from the manufacturer. The individual harmonic energy is obtained by multiplying the total HHG beam energy with the relative intensity of each harmonic measured by the spectrometer. The spectrum is corrected for the folding mirror reflection (based on data from Henke *et al.*³²), the grating efficiency, and the measured aluminum filter transmission. The estimated pulse energy per harmonic is shown as dots in Figure 4. The most prominent harmonic, both in argon and neon is the 21st harmonic (32.5 eV). Its energy is 250 nJ in argon and 30 nJ in neon. These values are comparable to previous results obtained by Takahashi *et al.*^{15,17}

To find the optimum high-order harmonic energies an automated optimization procedure was carried out. This procedure is briefly summarized here. The important parameters to control are: fundamental beam energy and diameter (before focusing), gas pressure, and gas cell position relative to the laser focus. The energy of the fundamental beam is varied by an attenuator consisting of a half-wave plate mounted on a motorized rotation stage and a polarizer. We use a motorized

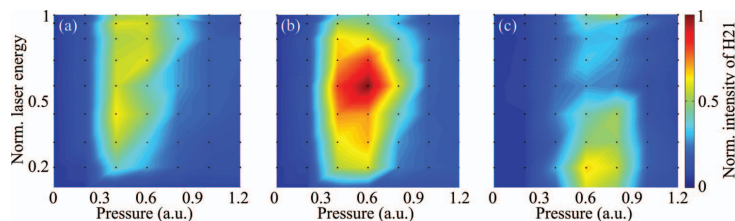


FIG. 5. Intensity of the 21st harmonic generated in argon as a function of driving laser energy and generation gas pressure. The measurements were carried out for a gas cell placed at the laser focus for three iris sizes: (a) $\phi = 22$ mm, (b) $\phi = 24$ mm, and (c) $\phi = 32$ mm. The values of a harmonic intensity between the measured points, shown as black dots, were interpolated.

variable iris to change the diameter of the fundamental beam before focusing. The distance between the center of the cell and the fundamental beam waist is varied by moving the cell. Finally, the gas pressure in the cell is adjusted by controlling a voltage applied to the cell nozzle's piezoelectric disks. We record a set of harmonic spectra while varying these four parameters in an automated way. Either the total HHG energy or the energy of a single harmonic can be optimized. Our optimization procedure allows us to routinely obtain HHG energies at the level of several hundred nJ in argon and a few tens of nJ in neon.

An example of the automated optimization is presented in Figure 5, where we investigated the dependence of the intensity of the 21st harmonic generated in argon as a function of the laser energy and gas pressure for three iris diameters. The signal is normalized to the maximum obtained for 21st harmonic. The recorded data show that for increasing iris size (decreasing $f_{\#}$), the required laser energy decreases and the phase matching pressure increases in agreement with our model prediction (see Fig. 1). Similar optimization in neon shows, as expected, a higher p_{match} . The optimum iris diameter corresponds to the longest Rayleigh range (the highest $f_{\#}$) for which the phase-matching conditions can be achieved, while keeping a high enough intensity at focus. It assures the highest HHG beam energy as is shown in Sec. II.

Figure 6(a) shows the spatial profile of high-order harmonics generated in argon and transmitted through an aluminum filter. The corresponding orders are between 11 and

45. The back-panel shows that the intensity distribution is almost perfectly Gaussian. Similar high quality Gaussian beams were generated in neon. The high spatial quality of the generated beams is due partly to the spatial quality of the driving beam, and partly to optimized phase-matching along the propagation axis. In our conditions, IR and XUV beams distortion due to nonlinear and plasma effects are negligible.

The generated beams divergence carries information about the contribution from the electronic trajectories. The divergence of the “short trajectory” harmonic beam is usually much smaller than for the “long trajectory” harmonics. For the 21st harmonic generated in argon, the divergence of the beam resulting from the long trajectory is 14 times higher than that from the short trajectory.³⁶ The different divergence is a consequence of a larger accumulated phase on the long trajectories. The analysis of the harmonic beam divergence shows that the main contribution to HHG in our conditions comes from the short trajectories. The contribution from the long trajectories is visible on the analyzed CCD images as a weak background.³⁰

To estimate the spatial coherence of the HH beam, we performed a double-slit experiment. The degree of coherence of the HHG beam can be estimated from the fringe contrast in the diffraction pattern.^{33,34} The slits used in this experiment had a width of 40 μm , a slit separation of 400 μm , and were located 1.5 m from the source. Figure 6(b) shows a cross-section of the double-slit diffraction pattern obtained with a single shot exposure. The experimental data were fitted with

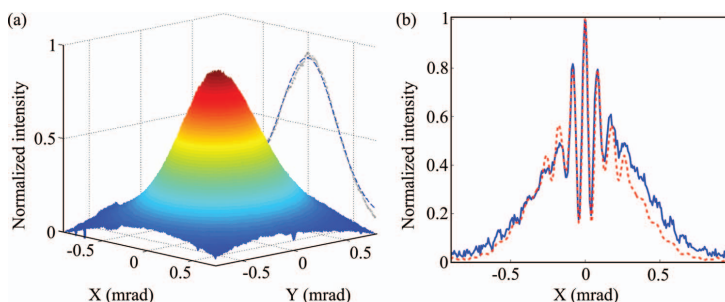


FIG. 6. (a) Spatial profile of the harmonic beam generated in Ar by focusing fundamental radiation with 2 m focal length lens into a 10 mm long cell, recorded with an x-ray CCD camera. The back-panel shows the cross-section of the beam (gray, dotted line), and a fitted intensity distribution (blue, dashed line). (b) Diffraction pattern created in a double-slit experiment, experimental data (blue, solid line), and fitted intensity distribution (red, dashed line).

a theoretical intensity function formed by the sum of diffraction patterns of the different harmonic wavelengths within the transmission window of the filter. The best fit was found with a degree of coherence of 0.8, in good agreement with previous measurements.³⁵

V. SUMMARY AND OUTLOOK

We have developed a high-energy HHG setup, working in a loose focusing geometry, generating a total energy per laser pulse of a microjoule in argon and a few hundred nJ in neon. The source is designed for future studies of nonlinear processes in the XUV spectral range. The high harmonic pulse energies together with their high spatial coherence allow us to reach high peak intensities. For example, an intensity of 2×10^{14} W/cm² per harmonic pulse could be reached by focusing the HHG beam generated in argon using a broadband grazing-incident mirror, assuming a 3 μ m focal spot size, 20 fs duration, and 30% transmission after reflection and filtering by an Al filter.

Our theoretical analysis of phase-matching in the absorption-limited case provides a simple guide for scaling HHG properties to high laser energies. For example we estimate that with $E_f = 1$ J, $f = 50$ m, $p = 0.01$ mbar, and $L_{\text{med}} = 6$ m, harmonic pulses with energy as high as 70 μ J could be reached.

Further increase in energy could be achieved by modifying the single atom response, e.g., using a double-cell scheme.²² Our current beam line includes the option to drive the HHG process with two cells or to use an interferometric setup in order to combine the fundamental with itself, its second or third harmonic (ω/ω , $\omega/2\omega$, and $\omega/3\omega$), thus providing a large range of options for modifying the driving field.

Our experimental results combined with the above considerations show that HHG has the potential to provide intense ultrashort pulses reaching the intensity levels required for nonlinear experiments in the XUV spectral range.

ACKNOWLEDGMENTS

This research was supported by the Marie Curie program ATTOFEL (ITN), the European Research Council (ALMA), the Joint Research Programme ALADIN of Laserlab-Europe II, the Swedish Research Council, the Swedish Foundation for Strategic Research, and the Knut and Alice Wallenberg Foundation.

- ¹C. Spielmann, N. H. Burnett, S. Sartania, R. Koppitsch, M. Schnürer, C. Kan, M. Lenzner, P. Wobrowschek, and F. Krausz, "Generation of coherent x-rays in the water window using 5-femtosecond laser pulses" *Science* **278**, 661 (1997).
- ²T. Popmintchev, M.-C. Chen, D. Popmintchev, P. Arpin, S. Brown, S. Alisaukas, G. Andriukaitis, T. Balciunas, O. D. Mücke, A. Pugzlys, A. Baltuska, B. Shim, S. E. Schrauth, A. Gaeta, C. Hernández-García, L. Plaja, A. Becker, A. Jaron-Becker, M. M. Murnane, and H. C. Kapteyn, "Bright coherent ultrahigh harmonics in the keV x-ray regime from mid-infrared femtosecond lasers," *Science* **336**, 1287–1291 (2012).
- ³Y. Tamaki, J. Itatani, M. Obara, and K. Midorikawa, "Highly coherent soft x-ray generation by macroscopic phase matching of high-order harmonics," *Jpn. J. Appl. Phys.* **40**, L1154–L1156 (2001).
- ⁴E. Goulielmakis, M. Schultze, M. Hofstetter, V. S. Yakovlev, J. Gagnon, M. Uiberacker, A. L. Aquila, E. M. Gullikson, D. T. Attwood, R. Kienberger,

- F. Krausz, and U. Kleineberg, "Single-cycle nonlinear optics," *Science* **320**, 1614 (2008).
- ⁵F. Krausz and M. Ivanov, "Attosecond physics," *Rev. Mod. Phys.* **81**, 163–234 (2009).
- ⁶S. L. Sorensen, O. Bjørneholm, I. Hjelte, T. Kihlgrén, G. Ohrwall, S. Sundin, S. Svensson, S. Buil, D. Descamps, and A. L'Huillier, "Femtosecond pump-probe photoelectron spectroscopy of predissociative states in acetylen," *J. Chem. Phys.* **112**, 8038 (2000).
- ⁷R. L. Sandberg, C. Song, P. W. Wachulak, D. A. Raymondson, A. Paul, B. Amirbekian, E. Lee, A. E. Sakdinawat, C. La-O-Vorakiat, M. C. Marconi, C. S. Menoni, M. M. Murnane, J. J. Rocca, H. C. Kapteyn, and J. Miao, "High numerical aperture tabletop soft x-ray diffraction microscopy with 70-nm resolution," *Proc. Natl. Acad. Sci. U.S.A.* **105**, 24–27 (2008).
- ⁸J. Schwenke, E. Lorek, R. Rakowski, X. He, A. Kvennefors, A. Mikkelsen, P. Rudawski, C. M. Heyl, I. Maximov, S.-G. Pettersson, A. Persson, and A. L'Huillier, "Digital in-line holography on amplitude and phase objects prepared with electron beam lithography," *J. Microsc.* **247**, 196–201 (2012).
- ⁹G. Lambert, T. Hara, D. Garzella, T. Tanikawa, M. Latat, B. Carre, H. Kitamura, T. Shintake, M. Bougeard, S. Inoue, Y. Tanaka, P. Salieres, H. Merdji, O. Chubar, O. Gobert, K. Tahara, and M.-E. Couprie, "Injection of harmonics generated in gas in a free-electron laser providing intense and coherent extreme-ultraviolet light," *Nat. Phys.* **4**, 296–300 (2008).
- ¹⁰E. P. Benis, D. Charalambidis, T. N. Kitsopoulos, G. D. Tsakiris, and P. Tzallas, "Two-photon double ionization of rare gases by a superposition of harmonics," *Phys. Rev. A* **74**, 051402(R) (2006).
- ¹¹K. Ishikawa and K. Midorikawa, "Two-photon ionization of He⁺ as a nonlinear optical effect in the soft-x-ray region," *Phys. Rev. A* **65**, 043405 (2002).
- ¹²M. Ferray, A. L'Huillier, X. F. Li, G. Mainfray, and C. Manus, "Multiple-harmonic conversion of 1064 nm radiation in rare gases," *J. Phys. B* **21**, L31 (1988).
- ¹³A. McPherson, G. Gibson, H. Jara, U. Johann, T. S. Luk, I. A. McIntyre, K. Boyer, and C. K. Rhodes, "Studies of multiphoton production of vacuum-ultraviolet radiation in the rare gases," *J. Opt. Soc. Am. B* **4**, 595 (1987).
- ¹⁴T. Brabec and F. Krausz, "Intense few-cycle laser fields: Frontiers of nonlinear optics," *Rev. Mod. Phys.* **72**, 545 (2000).
- ¹⁵E. J. Takahashi, Y. Nabekawa, and K. Midorikawa, "Low-divergence coherent soft x-ray source at 13 nm by high-order harmonics," *Appl. Phys. Lett.* **84**, 4–6 (2004).
- ¹⁶T. Popmintchev, M. C. Chen, P. Arpin, M. M. Murnane, and H. C. Kapteyn, "The attosecond nonlinear optics of bright coherent x-ray generation," *Nat. Photonics* **4**, 822–832 (2010).
- ¹⁷E. Takahashi, Y. Nabekawa, T. Otsuka, M. Obara, and K. Midorikawa, "Generation of highly coherent submicrojoule soft x rays by high-order harmonics," *Phys. Rev. A* **66**, 021802(R) (2002).
- ¹⁸E. Takahashi, Y. Nabekawa, and K. Midorikawa, "Generation of 10- μ J coherent extreme-ultraviolet light by use of high-order harmonics," *Opt. Lett.* **27**, 1920 (2002).
- ¹⁹J.-F. Hergott, M. Kovacev, H. Merdji, C. Hubert, Y. Mairesse, E. Jean, P. Breger, P. Agostini, B. Carré, and P. Salieres, "Extreme-ultraviolet high-order harmonic pulses in the microjoule range," *Phys. Rev. A* **66**, 021801(R) (2002).
- ²⁰J. Mauritsson, P. Johnsson, E. Gustafsson, A. L'Huillier, K. J. Schafer, and M. B. Gaarde, "Attosecond pulse trains generated using two color laser fields," *Phys. Rev. Lett.* **97**, 013001 (2006).
- ²¹D. Shafir, H. Soifer, B. D. Bruner, M. Dagan, Y. Mairesse, S. Patchkovskii, M. Yu. Ivanov, O. Smirnova, and N. Dudovich, "Resolving the time when an electron exits a tunneling barrier," *Nature (London)* **485**, 343–346 (2012).
- ²²F. Brizuela, C. M. Heyl, P. Rudawski, D. Kroon, L. Rading, J. M. Dahlström, J. Mauritsson, P. Johnsson, C. L. Arnold, and A. L'Huillier, "Efficient high-order harmonic generation boosted by below-threshold harmonics," *Sci. Rep.* **3**, 1410 (2013).
- ²³P. B. Corkum, "Plasma perspective on strong-field multiphoton ionization," *Phys. Rev. Lett.* **71**, 1994 (1993).
- ²⁴K. J. Schafer, B. Yang, L. F. DiMauro, and K. C. Kulander, "Above threshold ionization beyond the high harmonic cutoff," *Phys. Rev. Lett.* **70**, 1599 (1993).
- ²⁵P. Salieres, A. L'Huillier, and M. Lewenstein, "Coherence control of high-order harmonics," *Phys. Rev. Lett.* **74**, 3776 (1995).
- ²⁶S. Kazamias, D. Douillet, F. Weihe, C. Valentin, A. Rousse, S. Sebban, G. Grillon, F. Augé, D. Hulin, and P. Balcou, "Global optimization of high harmonic generation," *Phys. Rev. Lett.* **90**, 193901 (2003).

- ²⁷C. M. Heyl, J. Gudde, A. L'Huillier, and U. Hofer, "High-order harmonic generation with μJ laser pulses at high repetition rates," *J. Phys. B* **45**, 074020 (2012).
- ²⁸E. Constant, D. Garzella, P. Breger, E. Mevel, C. Dorrer, C. L. Blanc, F. Salin, and P. Agostini, "Optimizing high harmonic generation in absorbing gases: Model and experiment," *Phys. Rev. Lett.* **82**, 1668 (1999).
- ²⁹Attotech HB.
- ³⁰C. Lynga, M. B. Gaarde, C. Delfin, M. Bellini, A. L'Huillier, T. W. Hansch, and C.-G. Wahlstrom, "Studies of the temporal coherence of high-order harmonics," *Phys. Rev. A* **60**, 4823 (1999).
- ³¹C. Erny, E. Mansten, M. Gisselbrecht, J. Schwenke, R. Rakowski, X. He, M. B. Gaarde, S. Werin, and A. L'Huillier, "Metrology of high-order harmonics for free-electron laser seeding," *New J. Phys.* **13**, 073035 (2011).
- ³²B. L. Henke, E. M. Gullikson, and J. C. Davis, "X-ray interactions: Photoabsorption, scattering, transmission, and reflection at $E = 50\text{--}30000\text{ eV}$, $Z = 1\text{--}92$," *At. Data Nucl. Data Tables* **54**, 181–342 (1993).
- ³³M. Born and E. Wolf, *Principles of Optics* (Cambridge University Press, 1999).
- ³⁴B. E. A. Saleh and M. C. Teich, *Fundamentals of Photonics* (John Wiley and Sons, 2007).
- ³⁵R. A. Bartels, A. Paul, H. Green, H. C. Kapteyn, M. M. Murnane, S. Backus, I. P. Christov, Y. Liu, D. Attwood, and C. Jacobsen, "Generation of spatially coherent light at extreme ultraviolet wavelengths," *Science* **297**, 376 (2002).
- ³⁶X. He, M. Miranda, J. Schwenke, O. Guilbaud, T. Ruchon, C. Heyl, E. Georgadiou, R. Rakowski, A. Persson, M. B. Gaarde, and A. L'Huillier, "Spatial and spectral properties of the high-order harmonic emission in argon for seeding applications," *Phys. Rev. A* **79**, 063829 (2009).

PAPER VII

Conceptual Design Report for a Gas HHG Beam Line at ELI-ALPS

C. M. Heyl, P. Rudawski, F. Brizuela, P. Johnsson, C. L. Arnold and
A. L'Huillier.

Report ELI-ALPS, (2012).

Conceptual Design Report for a gas HHG beamline at ELI-ALPS

Christoph M. Heyl, Piotr Rudawski, Fernando Brizuela, Per Johnsson,
Cord L. Arnold, and Anne L'Huillier

Physics Department, Lund University, PO Box 118, SE-221 00 Lund, Sweden,

November 21, 2012

1. Aim of the CDR

The aim of the CDR is specified below:

Preparing a conceptual design of the gas HHG beamline to be driven by the SYLOS laser of the ELI-ALPS facility with the driver source parameters provided in two phases: *phase 1*: 1 kHz, ~30 mJ, <10 fs, CEP stabilized, *phase 2*: 1 kHz, ~100 mJ, <5 fs, CEP stabilized. If isolated attosecond pulses cannot be produced with the given parameters, gating techniques have to be foreseen. Characterization of the produced attosecond pulses has to be included. The design should address the question of HHG source development needs vs. user availability and that both types of experiments will have to be performed during facility operation. The design also involves a planned layout, laboratory space and supply requirement estimates, and a full equipment list including necessary diagnostic equipment.

Additional information was provided by ELI-ALPS during the confection of this CDR:

- Estimated laser beam diameter: 30 mm
- Estimated laser spatial profile quality: $M^2 = 1.1$
- Damage threshold for mirrors: 200 mJ/cm² for *phase 1* and 500 mJ/cm² for *phase 2*

The performance of the laser for the two phases is summarized in Table 1.

	Pulse energy (mJ)	Pulse duration (fs)	estimated beam diameter (mm)	repetition rate (kHz)	Average power (W)
<i>phase 1</i>	30	<10	30	1	30
<i>phase 2</i>	100	<5	30	1	100

Table 1: SYLOS laser parameters.

2. System overview and general requirements

The main layout of the proposed setup is shown in Figure 1. The system is separated into four units connected by vacuum tubes. The distances between the individual units can be changed in order to ensure the optimum performance of the system in its different phases (viz. *phase 1* and 2). In the following, we make a few general comments on the laser beam requirements, followed by a brief overview of the system while a more detailed description of the individual units is given in Section 3.

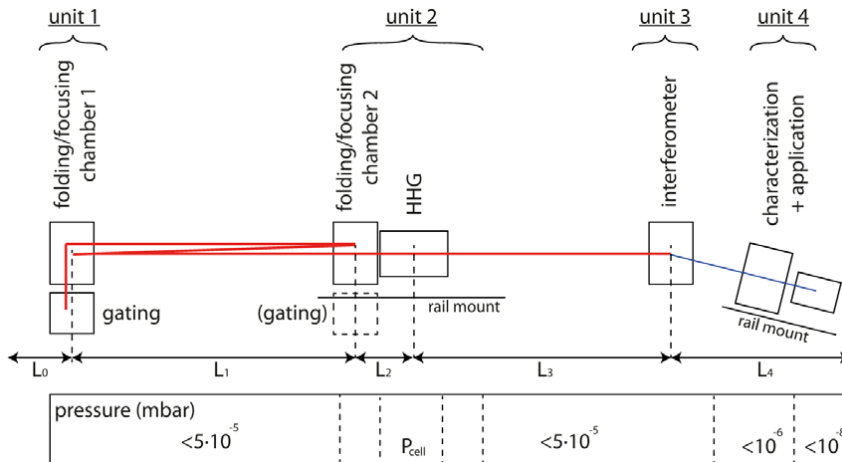


Figure 1: System overview and vacuum specifications. The given distances are labeled as follows: L_0 : space before the first focusing/folding chamber to center of this chamber; L_1 : center of first focusing/folding chamber to center second focusing/folding chamber; L_2 : center of first focusing/folding chamber to HHG cell center; L_3 : HHG cell center to center of interferometer chamber; L_4 : center of interferometer chamber to end of the beamline (including characterization & application area).

The large scale of the system and the extreme laser parameters set high requirements for beam propagation and focusing, and on the reflective optics. Due to the high average power, a very good *heat transfer management* has to be ensured for all optics in the beam path. The long beam propagation distances will require high beam pointing stability. Since the distance from the laser output to the beamline is not defined, we define the pointing stability as a lateral displacement of the center of mass of the beam at the generation or application point, which should be kept below 100 μm . If such stability is not provided by the laser, an *active beam pointing stabilization* system should be implemented before entering the HHG setup. Further, *variation of the pulse energy* should be possible. The presented setup requires an *s-polarized* (vertically polarized) laser field (see also Section 3.3). A number of *alignment cameras* have to be foreseen along the beamline. As a minimum, we suggest two points to be imaged for alignment: one in *unit 4* (as described in Section 3.4) and another which images the entrance of the gas cell in *unit 2*. Both cameras can be mounted outside the vacuum system and image through viewports.

After the compressor, the laser beam should propagate under vacuum into a first vacuum chamber at *unit 1* where it can pass an optical setup modifying the beam for gating purposes (Section 3.2). Alternatively it can enter at *unit 2* (in this case, the gating setup would be located here), depending on the focusing geometry. Another vacuum chamber at *unit 1* contains a focusing mirror and beam folding mirror(s). The second part of the beam folding setup is located in the first vacuum chamber at *unit 2* which is connected to another chamber which acts as an entrance to the HHG gas cell. The HHG cell is located at the center of *unit 2* at the focus of the laser beam. Another vacuum chamber acts as the exit from the HHG cell. Both entrance and exit chambers ensure differential pumping between the gas cell and the connecting beamline tubes. The fundamental and harmonic beams co-propagate to *unit 3* which contains an interferometric setup as well as filters in order to be able to

- (i) separate the fundamental and harmonic beams,
- (ii) adjust the time delay between the fundamental and attosecond pulses,
- (iii) filter the harmonic spectrum, and
- (iv) possibly compress the attosecond pulses.

Unit 4 contains spectrometers and detectors to temporally, spectrally and spatially characterize the produced pulses. From *unit 4*, the generated attosecond pulses can be sent to user setups.

Besides the general layout, Figure 1 specifies upper limits for the vacuum pressure. Due to the relatively long beam propagation distances, the pressure inside the straight tube sections has to be kept at least below $5 \cdot 10^{-5}$ mbar. The HHG cell pressure is discussed in Section 3.1. The pressure at *unit 4* should be seen as an upper limit for the characterization chamber. Depending on the application, a much lower pressure might be necessary in the application chamber.

In the following, we give a detailed description of our design, in four sections: Focusing and HHG cell, Gating, Interferometer, and Characterization.

3 Detailed description of the design

3.1 Focusing & HHG cell

The HHG beamline is based on a loose focusing concept allowing for the generation of attosecond pulses with high efficiency. Phase matching considerations suggest a long, non-guiding generation medium with low density¹. The concept upscales well-known HHG beamline design considerations at much shorter focal geometries where short gas cells are typically used.

¹ Heyl, C. et al., J. Phys. B, **45**:074020 (2012).

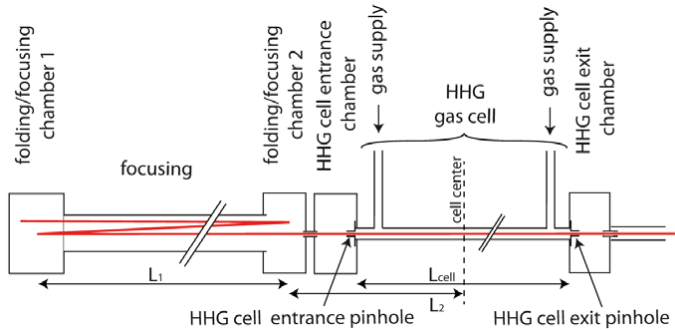


Figure 2: Focusing and gas cell layout. As an example, a beam folded into three sections ($N = 3$) is shown.

Focusing layout

We consider two different operation modes which imply different system optimization parameters in order to achieve single attosecond pulse generation (*operation mode 1*) or highest possible XUV flux (*operation mode 2*).

Operation mode 1, which is based on ionization gating² (Section 3.2), requires an intensity which is approximately one order of magnitude higher than for *operation mode 2*. We therefore consider different focusing geometries for the two operation modes in order to achieve the best efficiency. Further, different focusing geometries are considered for *phase 1* and *phase 2*. In the suggested design, a switch between the two modes is possible by changing the focal length and the cell length (L_{cell}), while adjusting the number of beam folding sections to keep the distances between the units fixed. In order to allow for very loose focusing geometry while limiting the total size of the system, the focused laser beam can be folded, as shown in Figure 2. Instead of folding the focused beam, a telescope setup could be used to reduce the beam size and reach a loose focusing geometry over a shorter distance. The main limitation in both configurations, which imposes the length of the focusing section L_1 , is the intensity at the last optical element before the focus. A telescope setup does not provide any major advantages, but might complicate changing the focal geometry. We therefore suggest focusing with long focal length optics and folding the focused laser beam. In addition, a *variable aperture* should be placed before the focusing optics, to fine tune the focusing geometry. If the estimated beam quality parameter for the laser cannot be achieved, we suggest implementing *adaptive optics* (e.g. a mirror before the focusing element as well as a wave front sensor behind) to compensate for non-perfect focusing of the laser beam in the gas cell.

Generation cell

The generation cell consists of a straight tube, mounted between an entrance and an exit chamber. The beam enters and exits the cell through a short tube section with a diameter of a

² Ferrari, F. et al., Nature Photonics, 4:857 (2010).

few millimeters. We suggest using two short tube sections instead of simple pinholes in order to improve the differential pumping situation between the cell and the vacuum tubes. The width of the short tube sections (as well as of the cell in general) has to be chosen large enough to avoid clipping the laser beam, taking into account beam pointing fluctuations which are difficult to estimate at the current status. For differential pumping purposes and in order to limit the gas flow into the long connecting tube section along L_1 , another thin tube section should separate the HHG cell entrance chamber and the last folding mirror chamber. A fourth thin tube section after the HHG cell exit chamber ensures a low gas pressure in the tube along L_3 .

All chambers of *unit 2* (including the HHG cell) should be mounted on a rail system. The cell itself consists of either several tube sections or alternatively, a long bellow. Changing the cell length simply requires a movement of entrance and exit chamber plus adjustment of the relevant tubing. Further, the exact position of *unit 2* can easily be adjusted by moving the entire unit on the rail system. In the current design, considering the very loose focusing geometry, we expect only a very weak dependence of the generated XUV emission on the focus position. The focus is therefore placed in the center of the gas medium. Furthermore, due to this geometry, we expect that phase matching can be achieved without using quasi phase matching techniques or a guiding cell geometry. We therefore suggest a gas cell geometry with constant pressure and constant diameter that exceeds the size of the focused beam.

Pressure and gas cell length were estimated by scaling up known experimental parameters at much shorter focusing geometries³ as well as by theoretical simulations. The given gas pressure should be considered as an approximate value, which should to be adjusted once the system is in operation. The gas pressure depends not only on the focusing geometry, but also on other parameters like the gas type (typically xenon, argon, neon, helium), the laser intensity, and the generated wavelength of interest.

System parameters

The estimated system parameters are listed in Table 2. The focal length for *operation mode 1* (*operation mode 2*) was calculated considering a peak intensity around $5 \cdot 10^{15}$ W/cm² ($5 \cdot 10^{14}$ W/cm²), for a perfectly focused Gaussian beam. The required intensities for both operation modes are typically less than these values. We consider higher values in order to take into account non-perfect focusing.

³ Heyl, C. et al., J. Phys. B, **45**:074020 (2012).

	focal length (m) $\sim L_1 \times N + L_2$	L_1 (m)	number of folding sections (N)	L_2 (m)	gascell length (m)	peak fluence at last mirror (mJ/cm ²)	min L_3 (m)	expected XUV beam divergence (μ rad)	P_{cell} (mbar)
<i>phase 1</i>									
<i>Operation mode 1</i>	~12	4,9	2	1,7	0,16	26	2	75	2
<i>Operation mode 2</i>	~36	4,9	7	1,7	1,4	170	6	25	0,2
<i>phase 2</i>									
<i>Operation mode 1</i>	~30	12,2	2	5	1	82	6	30	0,3
<i>Operation mode 2</i>	~90	12,2	7	5	9	428	15	10	0,03

Table 2: Main system parameters for the different phases and operation modes.

The folding geometry was chosen in order to

- (i) minimize L_1 while keeping the peak fluence at the last folding mirror below the damage threshold values provided in Section 1,
- (ii) ensure easy conversion⁴ between *operation mode 1* and 2, and
- (iii) keep the focal length as long as possible in order to maximize the XUV flux.

The system layout can also accommodate intermediate situations between the two modes, by changing the number of folding sections and gas cell length.

As an estimate for the damage threshold, we assume the maximum peak fluence values given in Section 1. Two different values are considered since a further mirror development between *phase 1* and *phase 2* is planned. We further note that the peak fluence should only be seen as one limiting factor. Thermal load due to the very high average power must also be considered. The folding geometry as well as the length L_3 were calculated considering the above mentioned peak fluence values, assuming a 45° angle of incidence at the interferometer (see Section 3.3).

The conversion efficiency depends on the generation gas. In argon, for example, for *operation mode 1* we expect a conversion efficiency for each harmonic order of $\sim 10^{-5}$. For *operation mode 2*, where a continuum spectrum is generated, we expect a conversion efficiency of $\sim 10^{-6}$ into the plateau region. Using lighter gases (Ne or He) which enable to achieve higher photon energies, the conversion efficiency is approximately one order of magnitude less.

3.2 Gating

Single attosecond pulse (SAP) generation requires the confinement of the high-order harmonic emission to only one half-cycle of the IR field (1.3 fs). We propose to use ionization gating⁵ as the main technique for both *phase 1* and *phase 2*, based on the high laser intensity

⁴ Conversion between operation modes requires changing the focusing optics, number of folding sections, and gas cell length, without changing the distances between the units.

⁵ Ferrari, F. et al., Nature Photonics, 4:857 (2010).

and the short pulse duration of the source. The required peak intensity for ionization gating is well above the saturation intensity, at which most of the medium ionizes. In this regime, the field strength increases rapidly in the rising edge of the pulse, resulting in a steep ionization front. Only one half-cycle contributes significantly to HHG, whereas the generation from the following sub-cycles is suppressed due to depletion of the generation medium. There are two main requirements for the ionization gating technique:

- (i) Short pulse duration and high laser intensity in order to allow for efficient HHG during only one half-cycle of the laser.
- (ii) Selection by spectral filtering of the continuous part of the HHG spectrum.

Requirement (i) is easily achieved by the performance of the laser system. In *operation mode 1* the intensity in the gas cell largely exceeds that necessary for HHG. The description of the focusing geometry required for this *operation mode* for both phases was presented in Section 3.1. Requirement (ii) can be achieved either by using metallic filters (Section 3.3) or multilayer mirrors (Section 3.4).

As an alternative method for SAP generation in *phase 1*, we propose the Double Optical Gating (DOG)⁶ technique, which combines polarization gating⁷ and two-color HHG. The basic idea of polarization gating is that the fundamental field is made elliptical during most of the pulse except during a short time at the center of the pulse, thus suppressing HHG. Using a combination of fundamental and its second harmonic, attosecond pulses are generated in one half-cycle of the fundamental field⁸. The DOG technique requires thin transmissive optics (less than 0.5 mm to keep the B-integral below 1 in *phase 1*) making it unsuited for *phase 2*.

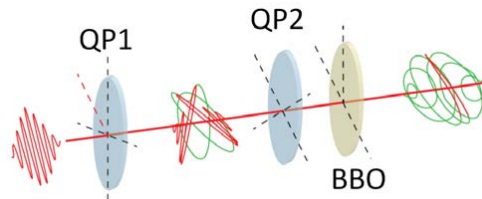


Figure 3: Double optical gating setup, from ref.⁹. QP1 and QP2 - quartz plates, BBO – barium borate crystal.

A DOG setup can easily be inserted in the fundamental beam. Since it uses transmission optics, dispersion precompensation is required.

The experimental setup (Figure 3) includes two quartz plates (QP1 and QP2) and a barium borate crystal (BBO). The first quartz plate (QP1), with optical axis at 45° with respect to the incoming pulse, creates two orthogonally polarized and delayed components. When the two components overlap, the polarization is circular. The second quartz plate (QP2) combined with the BBO crystal act as a quarter waveplate, changing the linearly polarized part into

⁶ Mashiko et al. Phys. Rev. Lett. **100**:103906 (2008).

⁷ Tcherbakoff et al. Phys. Rev. A **68**:043804 (2003).

⁸ Mauritsson et al. Phys. Rev. Lett. **97**:013001 (2006).

⁹ Sansone et al. Nat. Phot. **5**:655 (2011).

circularly polarized and vice versa. The type I BBO crystal generates the second harmonic. Fine tuning of the sub-cycle delay is achieved by tilting the second quartz plate.

3.3 Interferometer

After HHG, the fundamental IR field must be separated from the harmonic beam. One way of efficiently doing so is by using fused silica plates with antireflection (AR) coatings for the infrared¹⁰. By using these plates near grazing incidence, the harmonic spectrum is reflected while the IR field is transmitted. Depending on the application, the harmonic spectra might need to be further filtered to remove low-order harmonics or to select cutoff spectral region in order to generate single attosecond pulses. This can be achieved through the use of thin metallic filters whose thickness and material composition determine the transmitted bandwidth¹¹. These filters can also provide some temporal compression of attosecond pulses by compensating intrinsic HHG chirp¹². The time duration of the attosecond pulses can be measured by cross correlation using a fraction of the residual IR field, with a variable delay relative to the attosecond pulses, as described in Section 3.4. We propose a compact (40 cm × 20 cm) interferometer to separate the harmonic spectrum from the IR, filter appropriately the spectrum, and combine the IR and XUV pulses with a controlled time delay. A schematic of this setup is shown in Figure 4.

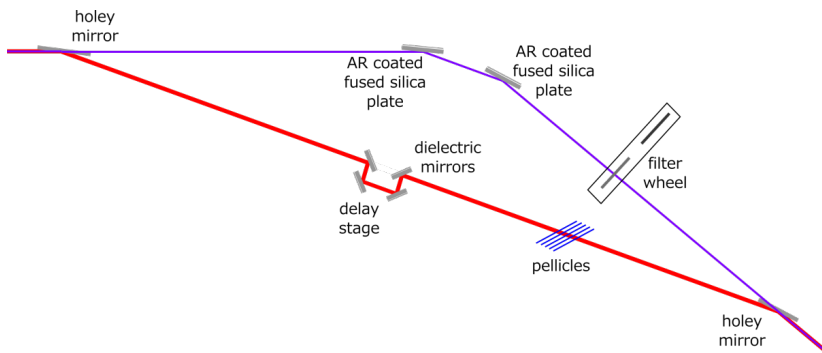


Figure 4: Interferometric setup for attosecond pulse generation and measurement.

The different divergence of the IR and harmonic beams provides a simple way of separating and recombining them using holey mirrors. In one arm of the interferometer, the harmonic beam, which is very collimated, passes through a hole in the mirror and is reflected off two AR-coated fused silica plates at grazing incidence (e.g. 10 degrees incidence angle). The hole should be larger than the expected XUV beam size at this point. The beam size for *Operation mode 2* should be considered in each phase to avoid changing the mirror when switching modes. The combination of the holey mirror and the two fused silica plates with AR coating for the fundamental, ensures the complete elimination of the IR beam in this arm. The XUV

¹⁰ Gustafsson et al. Opt. Lett. **32**:1353 (2007).

¹¹ Bourassin-Bouchet et al. New J. Phys. **14**:023040 (2012).

¹² López-Martens et al. Phys. Rev. Lett. **94**:033001 (2005).

reflectivity of the coated fused silica plates ranges from 40% to 20% per reflection in the spectral range of 20 eV to 100 eV for a 10 degree incidence angle. After the second plate, a wheel with thin metallic film filters is placed providing appropriate filtering of the harmonic spectrum. The dielectric holey mirror reflects the more divergent IR beam in the second arm of the interferometer. In this arm, a piezo-controlled delay stage is added to adjust the optical path difference between the two arms. The delay stage should be able to scan 30 μm with a precision better than 5 nm during measurements. In the case of generating harmonics with the DOG technique described in Section 3.2, pellicles at Brewster angle can be added to this arm to remove the residual circularly polarized light which is unwanted in the cross correlation measurements (in the figure the pellicles have been drawn at a different angle for clarity). The distance between the generation cell and the interferometer is dictated by the damage threshold of the first holey mirror and fused silica plate and is listed as L_3 in Table 2 for the different stages and operation modes.

3.4 Characterization

This Section describes the spatial, spectral, and temporal characterization of the radiation produced in the generation chamber. The central element here is an arrangement of three (or more) mirrors, mounted on a translation and rotation stage, with the purpose of redirecting the incoming VUV, XUV, and IR radiation towards different application and characterization stations, arranged circularly around the deflection mirrors. In particular, single attosecond pulses (SAPs) as well as attosecond pulse trains (APTs) can be directly characterized at their application ports. The layout is sketched in Figure 5. For the purpose of redirecting the radiation to different ports, we envisage a metallic coated mirror (e.g. gold) which features a very broad reflection range in the VUV, visible, and IR spectral regions at both grazing and normal incidence and high reflectivity in the XUV at grazing incidence.

Furthermore, we suggest XUV multilayer coatings to, depending on the application, select a spectral region, extract a particular harmonic, or to temporally compress SAPs. The multilayer XUV mirrors which are designed for specific wavelength ranges and small angles (close to normal incidence) will direct the radiation to application ports 1 and 2. Metallic mirrors address the rest of the ports. The highest possible XUV flux is obtained at port 5, as no deflection is required; in this case the mirrors are moved completely out of the beam path. Ports 1 and 2 and ports 3 and 4, respectively are designed symmetrically, meaning that each pair of ports shares exactly the same properties. This offers great flexibility to users and operators, as e.g. the XUV radiation send to experiments in one application port can be characterized at its symmetric counterpart and vice versa. The total arrangement of five application and characterization ports provides a large variety of possibilities for user applications.

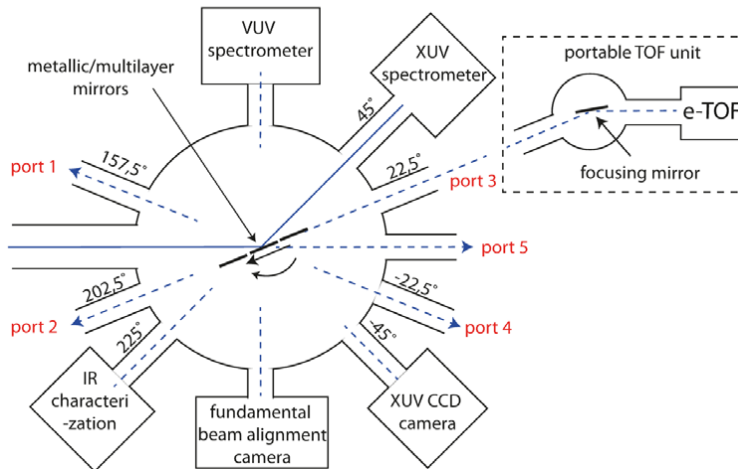


Figure 5: Beam characterization: Mirrors with different coatings on a rotation and translation stage send the incoming VUV, XUV, and IR radiation to different application and diagnostic end-stations.

For spectral characterization we envisage a VUV spectrometer ($\sim 5 - 20$ eV) for low-order harmonics (sub ionization threshold harmonics) and a high resolution XUV spectrometer (20 – 200 eV) for high-order harmonics from different generation gases. A spectral resolution below 1 nm is sufficient for this application. The spectrometers should be one-dimensional imaging spectrometers, which provide valuable insight also into the spatial properties of the beam. Different suitable types of such imaging spectrometers are commercially available. A CsI-coated imaging MCP should be used as the detector for the VUV spectrometer. For the XUV spectrometer, either an imaging MCP or an XUV CCD can be used. These diagnostic tools will be important for tuning the gating parameters for the generation of single attosecond pulses. Moreover, we suggest a calibrated back-illuminated XUV CCD camera to characterize the spatial beam profile and to measure the XUV pulse energy¹³. We recommend a 2048 x 2048 array with a 13.5 μm pixel size, to ensure high spatial resolution and ample field of view.

Ionization cross-correlations with the IR field obtained from the pump-probe interferometer will be performed to characterize the temporal properties of the generated XUV single attosecond pulses and attosecond pulse trains. The generated photo-electron spectra are recorded with an electron time-of-flight (e-TOF) spectrometer while the IR field is temporally swept through the XUV field. A toroidal mirror at grazing incidence focuses the XUV and IR fields into the sensitive region of the e-TOF where a suitable detection gas is provided. The cross-correlations can be performed in different modes; the streaking method¹⁴ will be applied to SAPs, while the RABBIT¹⁵ scheme¹⁶ will be used for attosecond pulse trains. The e-TOF should feature a narrow electron acceptance angle in order to perform reliable streaking

¹³ Erny et al, N. J. Phys., **13**:073035 (2011).

¹⁴ Hentschel et al, Nature, **414**:509 (2001).; Kienberger et al, Nature, **427**:817 (2004).

¹⁵ RABBIT - Reconstruction of attosecond beating by interference of two-photon transitions

¹⁶ Paul et al, Science **292**:1689 (2001).

measurements. In addition, it should provide an energy resolution better than 100 meV for photoelectrons with energies up to 100 eV. Depending on the length of the streaking trace, the single attosecond pulse and/or the IR streaking pulse can be reconstructed¹⁷. The unit composed of the toroidal mirror and subsequent e-TOF can be moved to different application and diagnosis ports. In this way the radiation at each port can be characterized either directly or at its symmetric counterpart.

Finally, we envisage two more ports for diagnostics: One port for alignment purposes, and another port from which the IR beam can be extracted and directed to characterization devices suited to measure the temporal profile of few- to single-cycle laser pulses, such as special versions of FROG¹⁸ or SPIDER¹⁹.

4 Summary

Laboratory space estimates

As shown in Figure 1, the entire system consists of several units, separated by connecting vacuum tubes. Little transversal space is needed for the straight tube sections. The main size limitation is the length of the system. Considering a length of $L_0 = 2$ m along the beamline before *unit 1*, L_1 , L_2 and L_3 as discussed in Section 3.1 and a length of 8 m for L_4 (space for characterization and application area), a total length, L_{total} , of approximately 23 m and 42 m are needed for phase 1 and phase 2 respectively (Table 3). Our estimations include some work space around the system. The given values of L_1 and L_3 should be seen as an estimate of the minimum required lengths. This implies the possibility to increase these values for *phase 1* (while keeping the total focal length unchanged) in order to fit the dimensions for *phase 2*.

(m)	L_0	L_1	L_2	L_3	L_4	L_{total}
<i>phase 1</i>	2	4,9	1,7	6	8	22,6
<i>phase 2</i>	2	12,2	5	15	8	42,2

Table 3: System length.

We further note that it might be of interest from an application point of view to increase the beam propagation distance before the application area significantly (e.g. the distance between *unit 3* and *4*). This is especially relevant for applications where the XUV beam is refocused in order to reach a high XUV intensity. Minimizing the number of mirrors in the XUV beam while achieving a tight focus geometry requires the expansion of the divergent XUV beam before refocusing.

¹⁷ Itatani et al, Phys. Rev. Lett., **88**(17):173903 (2002); Mairesse et al, Phys. Rev. A, **71**(1):011401 (2005); Quéré et al, J. Mod. Opt., 52(2-3):339 (2005); Chini et al, Opt. Express, 18(12):13006 (2010).

¹⁸ FROG - Frequency Resolved Optical Gating.

¹⁹ SPIDER - Spectral Phase Interferometry for Direct Electric-field Reconstruction.

Our size estimations for the individual units are given in Table 4. Again, the actual chamber size plus some work space around are considered.

length x transverse size (m x m)	Unit 1	Unit 2	Unit 3	Unit 4 (including application area)
phase 1	3 x 3	3 x 3	3 x 3	7 x 8
phase 2	3 x 3	10 x 3	3 x 3	7 x 8

Table 4: Dimensions of the individual sub-systems.

The minimum floor space required for each phase is schematically shown in Figure 6. The proposed floor plan fits within the laboratory space at ELI labeled 100KHZ-ISO 7, AU1-ISO 7, AU2-ISO 7, and AU3-ISO 7 in the ‘Layout for Technology 2012.08.27’ document. We also note that *unit 4* can be set up equivalently to the right or the left of the beamline. Changing from the left to the right requires building a mirrored interferometer (Figure 4).

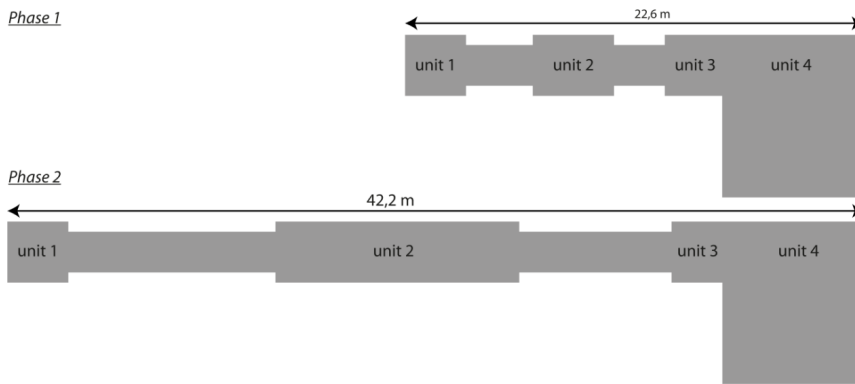


Figure 6: Estimated footprint of the setup for both phases

Source development needs and user availability

The system allows further source development even during operation periods dedicated for users. This is ensured by a design which allows fast switching between sending the generated attosecond pulses for characterization and to user stations.

The beamline dimensions and other system parameters greatly exceed the parameters of any known operating attosecond beamlines. We therefore foresee a large amount of time necessary for testing and initial source development during the first six months of the system operation. In the long run, 15% operation time for further source development should be sufficient.

Estimated construction time

We estimate a construction time of 17 man months for the detailed design, 8 months for delivery of all items, and 19 man months for setup and installation. This estimation does not include “testing and initial source development” mentioned above.

PAPER VIII

Compression of TW-class Laser Pulses in a Planar Hollow Waveguide for Applications in Strong-Field Physics

A. Jarnac, F. Brizuela, C. M. Heyl, P. Rudawski, F. Campi, B. Kim, L. Rading, P. Johnsson, A. Mysyrowicz, A. L'Huillier, A. Houard and C. L. Arnold.

Accepted for publication in European Physics Journal D.

Compression of TW class laser pulses in a planar hollow waveguide for applications in strong-field physics

A. Jarnac,¹ F. Brizuela,² C. M. Heyl,² P. Rudawski,² F. Campi,² B. Kim,² L. Rading,²
P. Johnsson,² A. Mysyrowicz,¹ A. L'Huillier,² A. Houard,¹ and C. L. Arnold²

¹Laboratoire d'Optique Appliquée, FR-91762 Palaiseau, France

²Department of Physics, Lund University, P.O. Box 118, 22100 Lund, Sweden

compiled: June 14, 2014

We demonstrate pulse post compression of a TW class chirped pulse amplification laser employing a gas-filled planar hollow waveguide. A waveguide throughput of 80% is achieved for 50 mJ input pulse energy. Good focusability of the output mode is demonstrated and after compression with chirped mirrors sub-15 fs pulse duration is obtained. The viability of the planar hollow waveguide compression scheme for applications in strong-field physics is demonstrated by generating high-order harmonics in a pulsed Ar gas cell.

OCIS codes: (320.5520) Pulse compression; (320.7110) Ultrafast nonlinear optics; (020.2649) Strong field laser physics

<http://dx.doi.org/10.1364/XX.99.099999>

Few-cycle laser pulses have become indispensable tools in optics and related sciences, such as High-order Harmonic Generation (HHG) [1] and attosecond science [2], strong-field physics [3], and acceleration of particles [4]. While low-energy, few-cycle pulses can today routinely be obtained from Titanium:Sapphire (Ti:Saph) based ultrafast oscillators [5], the output of chirped pulse amplification (CPA) lasers hardly reaches below 20 fs pulse duration, mostly due to gain-bandwidth-narrowing. Typical Ti:Saph based CPA lasers, found in research laboratories today, have pulse duration in the range of 25-100 fs and pulse energies in the mJ to hundreds of mJ range. Thus, there is a strong need for pulse post compression.

The two most prominent schemes for pulse compression to the few-cycle regime are based on strong spectral broadening due to nonlinear propagation in either a noble gas filled hollow capillary [6] or in a self-guided filament [7] and subsequent compression with chirped mirrors. Due to ionization inside the capillary and nonlinear coupling to higher order capillary modes (with stronger attenuation) the output pulse energy of a hollow capillary compressor rarely exceeds 1 mJ. Attempts to increase the energy output require advanced optical [8] or advanced capillary engineering [9] and often exhibit low efficiency [10].

Pulse compression employing self-guiding in laser filaments, which form as consequence of a dynamic equilibrium between self-focusing and plasma defocusing [11], in practice is also limited to output pulse energies of about 1 mJ, mainly due to the onset of multiple filamentation, spatial chirp, and angular dispersion [12].

A scheme that potentially scales much more favorably to high pulse energy than hollow capillaries and filamentation was proposed by Nurbuda and Midorikawa [13]. By use of planar hollow waveguides for post compression, the pulse energy can easily be up-scaled by increasing the beam size in one spatial direction, while keeping the intensity inside the waveguide at levels benefiting efficient self-phase modulation, but limiting ionization. In the first implementation, strong deterioration of the beam profile along the unguided direction was observed due to one-dimensional, small-scale self-focusing [14]. Shortly after, some of the authors showed that by carefully controlling experimental parameters, such as gas pressure and waveguide length, a balance between spectral broadening and beam deterioration can be achieved. Pulse compression at the 10 mJ level and good focusability was demonstrated [15, 16]. A theoretical model for further up-scaling of the planar hollow waveguide compression scheme was introduced [16, 17].

In the current work, we present pulse post compression of a TW class CPA laser in a gas-filled planar hollow waveguide with up to 50 mJ input pulse energy. The compressed pulses are fully characterized in terms of beam profile, focusability, and pulse duration. We demonstrate the benefit of such pulses for applications in strong-field physics by performing HHG in Ar as generation gas. The harmonic cut-off is significantly increased compared to that obtained with longer driving pulses.

The experimental setup is sketched in Fig. 1. Pulses of up to 50 mJ pulse energy at 10 Hz repetition rate and pulse duration of 45 fs, centered around 800 nm are focused with a cylindrical focusing mirror ($f=2$ m) onto

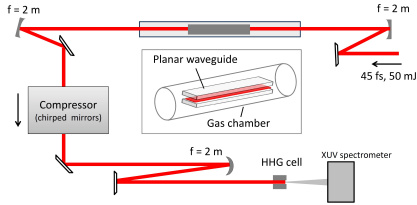


Fig. 1. Sketch of the experimental setup.

the input of a planar hollow waveguide. The waveguide consists of two parallel, highly polished glass slabs (Plan Optik GmbH) made of Borofloat with dimensions $500 \times 40 \times 10 \text{ mm}^3$ and a gap of $2a = 127 \mu\text{m}$ between them. The gap is matched to the width of the line-shaped laser focus at the waveguide entrance $w_{\text{foc}} \approx 0.735a$, where w_{foc} is the Gaussian half-width ($1/e^2$); this condition facilitates maximum coupling efficiency into the fundamental waveguide mode. The waveguide is located inside a transparent tube with thin (2.2 mm), broadband anti-reflection coated fused silica windows at both ends. The tube is approximately 3 m long in order to avoid detrimental nonlinear interaction with the windows. The output beam of the waveguide is collimated with an identical cylindrical mirror and passed through a chirped mirror compressor. After compression the beam is sent to a HHG setup and generated harmonic spectra are recorded with a flat-field, XUV photon spectrometer [18].

The tube, in which the waveguide is located, is filled with Ar at pressures up to one atmosphere. The waveguide throughput is higher than 80% in vacuum (86% in theory), proving good coupling to the fundamental mode. It does not decrease up to 400 mbar of Ar, indicating that losses due to ionization and nonlinear coupling to higher order modes are small.

Fig. 2a) shows the spectra observed at the input and output of the waveguide for pulse energy of 50 mJ at vacuum and 200 and 400 mbar of Ar. For the evacuated waveguide, the spectrum slightly broadens, probably due to parasitic nonlinear interaction with the windows. At 400 mbar of Ar, an about four-fold increase of the spectral width is observed with the wings spanning from 700-900 nm. The broadening is only slightly blue-shifted, identifying self-phase modulation as the main source of spectral broadening with only small contribution from plasma related blue-shifting [19]. The spectrum obtained at 400 mbar supports a transform limited pulse duration of 13 fs. The spectra were measured at the center of the output beam. It should be noted that along the unguided waveguide direction, spectral broadening is maximum at the beam center and smaller at the wings. Inhomogeneous spectral broadening leads to different transverse pulse duration after compression, with the shortest pulse obtained at the beam center and longer pulse duration at the wings [16].

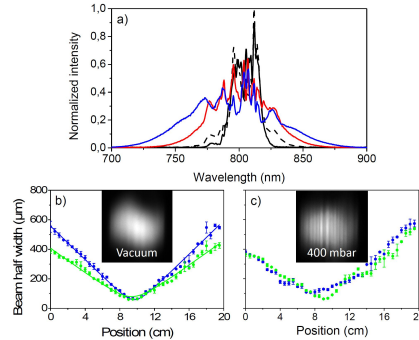


Fig. 2. a) Spectra observed at the waveguide input (solid black) and output (dashed black) for vacuum and for 200 (red) and 400 mbar (blue) of Ar. b, c) Focusability of the guided (green) and free (blue) waveguide directions, illustrated in terms of beam caustics for the waveguide under vacuum (b) and at 400 mbar (c). M^2 -fits are plotted in (b). The insets show the output modes in the corresponding conditions.

Transverse beam profile and focusability are important criteria for pulse compression in planar hollow waveguides. If the waveguide output is not focusable to a small spot size, pulse post compression will not result in an increase of the peak intensity. As discussed in [16], the focusability in the non-guided waveguide direction inevitably diminishes; first, due to the transversely inhomogeneous spectrum and second, due to a pulse front deformation resulting from the beam center propagating slower (due to the Kerr-effect) than the wings. The second effect essentially introduces an astigmatism, which however can easily be compensated by translating the collimating cylindrical mirror. Finally, modulational instability from one-dimensional self-focusing deteriorates the mode along the unguided waveguide direction. The insets in Fig. 2b) and 2c) show the transverse mode observed at the output of the gas cell in case of vacuum (b) and 400 mbar of Ar (c). It was shown in [16] that the transverse mode structure does not reduce the focusable intensity significantly. However, for an Ar pressure exceeding 500 mbar the transverse mode breaks up into a number of filaments, unusable for pulse compression. As self-phase modulation and self-focusing are the spectral and spatial manifestations of the Kerr-nonlinearity, transverse beam break-up ultimately limits the maximum spectral broadening and thus the shortest achievable compressed pulse duration [16]. To delay the onset of break-up, the laser beam profile is spatially filtered before the grating compressor of our CPA chain.

The focusability is investigated by focusing the beam, after careful attenuation with reflections from uncoated wedges, with a thin lens ($f=2 \text{ m}$) onto the chip of a CCD camera, which is moved along the optical axis in the vicinity of the geometrical focus. Fig. 2b) and c) show

the beam half width as a function of position for the guided and the free waveguide directions for the evacuated waveguide (b) and filled with 400 mbar of Ar (c). The beam size is extracted from the images by computing second order moments $\sigma_{x,y}$. For Gaussian beams $2\sigma_{x,y} = w_{x,y}$, where $w_{x,y}$ is the Gaussian half width ($1/e^2$). Indeed, the beam sizes obtained by moment theory are very close to those resulting from fitting a Gaussian profile, indicating that the focal spot is single-peaked and close to Gaussian shape. The focusability in terms of a M^2 -parameter is obtained by fitting a parabola to the beam caustic (beam size vs. propagation direction) [20]. For the case of vacuum, $M^2 \approx 1.28$ and $M^2 \approx 1.32$ in the guided and free waveguide directions are obtained, respectively. For a filling pressure of 400 mbar, the focusability in the guided direction remains approximately unchanged, while in the free direction the minimum beam size increases by a factor of ≈ 1.6 . At the same time, the focal position moves towards the lens, exhibiting a slight astigmatism, which however is easily removed by moving the collimation mirror.

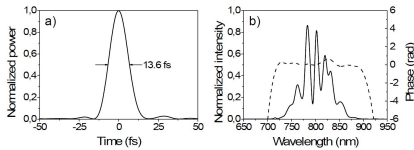


Fig. 3. Temporal pulse profile (a) and spectral intensity and phase (b) obtained from SPIDER measurement.

The waveguide output is compressed with chirped mirrors from Layertec and VENTÉON. The compressed pulses are characterized with a commercial, few-cycle SPIDER (VENTÉON). A pair of AR-coated fused silica wedges is used to fine-tune dispersion. Fig. 3 shows a SPIDER measurement in optimized conditions for 50 mJ pulse energy at the waveguide input and 400 mbar of Ar. Individual measurements exhibit a large spread in retrieved pulse duration due to shot-to-shot pulse energy fluctuations, typical for low repetition rate TW class lasers. We performed ten SPIDER measurements, with retrieved duration spreading from 13.4 fs to 17 fs; the average pulse duration was 14.3 fs. The retrieved spectral phase (Fig. 3b) is reasonably flat, indicating that the chirped mirror compressor is well suited to compress the waveguide output.

Having demonstrated strong spectral broadening, high throughput, good focusability, and sub-15 fs pulse duration, we use the compressed pulses to drive HHG, where short pulse duration and high focal intensity (exceeding $10^{14} \text{ W cm}^{-2}$) are inevitable ingredients. A HHG spectrum is comprised of discrete odd order harmonics of the driving field frequency, whereas the spectral width of individual harmonics decreases with increasing number of half-cycles contributing to harmonic genera-

tion. The highest energy E_{max} in a HHG spectrum is related to the driving field intensity by the cut-off law $E_{\text{max}} = 3.17U_P + I_P$ [21], where U_P is the ponderomotive energy (average energy of an electron in an AC field with $U_P \propto I_{\text{max}}$), I_P is the ionization potential of the gas, and I_{max} is the peak intensity of the driving field.

In practice, for multi-cycle driving pulses the cut-off energy is rather determined by macroscopic phase-matching and propagation effects. Strong ionization of the gas medium leads both to reshaping of the fundamental field due to plasma-defocusing as well as to termination of HHG due to plasma-related unfavorable phase-matching conditions. Thus generating with shorter pulses, two main effects should be observed: first, a broadening of the individual harmonics due to fewer half-cycles contributing to the generation process and second a higher cut-off energy due to higher peak intensity as well as due to plasma-related effects setting in later for shorter pulses.

It should be noted that the compressed pulse energy reaching the HHG setup is distinctively lower than the waveguide output. While $\approx 40 \text{ mJ}$ are obtained at the output of the waveguide (50 mJ at the input), the compressed pulse energy available for HHG is $\approx 20 \text{ mJ}$. The losses are mostly due to clipping on the limited apertures of vacuum windows and chirped mirrors. The compressed waveguide output is loosely focused with a spherical mirror ($f=2 \text{ m}$) into a Ar gas cell. Fig. 4 shows HHG spectra obtained in two different situations, using long pulses $\approx 45 \text{ fs}$, circumventing the waveguide setup (blue), or using the waveguide compressor with 400 mbar of Ar (red). The pulse energy in both cases is $\approx 20 \text{ mJ}$. With the waveguide compressor the individual harmonics become broader and the cut-off energy increases, indicating that the pulses are significantly shorter and more intense. Furthermore, the harmonics feature rich transverse spatial structure (see inset), where each of the harmonics exhibits a 'V'-shape with higher XUV photon energy on-axis compared to the wings. Such behavior is not observed with the long pulses. It might be related to either a spatial variation in the dipole phase [22] or to propagation effects. The transversely varying spectrum and pulse duration of the waveguide output can lead to complicated spatio-temporal couplings upon focusing in combination with nonlinear propagation. Although interesting in itself the particular shape of the harmonics is beyond the scope of this article.

In conclusion, we have demonstrated that pulse post compression in planar hollow waveguides is a viable tool to approach the few-cycle pulse duration regime with typical TW CPA lasers. In this work 50 mJ input pulses could be compressed to sub-15 fs pulse duration with 40% total efficiency (input-to-experiment). A carefully designed chirped mirror compressor should in the future allow for 70%. The pulse energy range presented here currently is and most likely will remain not easily accessible with competing compression schemes. Furthermore, the planar hollow waveguide still bears great

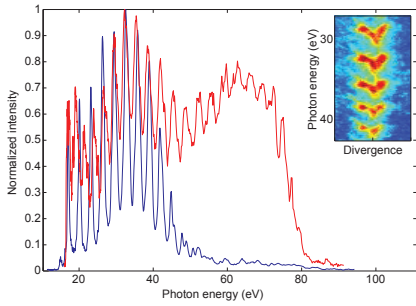


Fig. 4. HHG spectrum with (red) and without (blue) waveguide compressor at ≈ 20 mJ pulse energy. The inset shows the spatial shape for a range of harmonics generated from the waveguide compressed pulses.

potential for energy up-scaling.

Up-scaling can most easily be discussed in terms of the B-integral, acquired by the beam during nonlinear propagation inside the waveguide,

$$B = \int_{z=0}^L k_0 I(z) n_2 P z dz \approx k_0 I_0 n_2 P L \quad (1)$$

where k_0 is the wavenumber at the carrier frequency, I_0 is the intensity at the waveguide input, n_2 is the nonlinear refractive index for Ar at atmospheric pressure, P is the gas pressure in atmospheres, and L is the length of the waveguide. For the current experiment $B \approx 8$. While a higher B-integral would lead to stronger spectral broadening, inevitably the transverse beam profile would disintegrate, resulting in an unusable beam. Consequently, energy up-scaling must be achieved, while keeping the B-integral constant. Increasing the beam size in the unguided direction provides a trivial way to up-scale the pulse energy. Further control knobs are intensity, pressure, length of the waveguide, and type of gas. The intensity however should be kept below a level of strong ionization (here $\approx 7 \times 10^{13} \text{ Wcm}^{-2}$) to avoid plasma-related absorption and nonlinear coupling to higher waveguide modes. For Ne and He as filling gases the pulse energy can be increased by factors of ≈ 3 and ≈ 5 , respectively, while keeping comparable relative ionization [23]. The lower nonlinearity (≈ 7 times for Ne and ≈ 33 times for He) has to be compensated by higher pressure inside the waveguide. Considering the degrees of freedom sketched above, an up-scaling to input pulse energies in the range of hundreds of mJ seems straight forward, offering a possibility to expand the concept of pulse post compression to lasers with tens of TW peak power.

This research was supported by the European Research Council (ALMA, PALP), the Swedish Research Council, the Crafoord Foundation, the Knut and Alice Wallenberg Foundation, and the Swedish Foundation for Strategic Research. A.J. and A.H. acknowledge support

from DGA, the European Science Foundation (SILMI) and the European Cooperation in Science and Technology (COST).

References

- [1] A. L’Huillier, T. Auguste, P. H. Balcou, B. Carre, P. Monot, P. Salières, C. Altucci, M. B. Gaarde, J. Larsson, E. Mével, T. Starczewski, S. Svanberg, C. G. Wahlström, K. S. Zerne, R. Budil, T. Ditmire, and M. D. Perry, *J. Nonl. Opt. Phys. Mat.* **4**, 647–665 (1995).
- [2] F. Krausz and M. Ivanov, *Rev. Mod. Phys.* **81**, 163–234 (2009).
- [3] T. Brabec and F. Krausz, *Rev. Mod. Phys.* **72**, 545–591 (2000).
- [4] E. Esarey, C. B. Schroeder, and W. P. Leemans, *Rev. Mod. Phys.* **81**, 1229–1285 (2009).
- [5] S. Rausch, T. Binhammer, A. Harth, E. Schulz, M. Siegel, and U. Morgner, *Opt. Express* **17**, 14341–14352 (2009).
- [6] M. Nisoli, S. De Silvestri, O. Svelto, R. Szipöcs, K. Ferencz, C. Spielmann, S. Sartania, and F. Krausz, *Opt. Lett.* **22**, 522–524 (1997).
- [7] C. Hauri, W. Kornelis, F. Helbing, A. Heinrich, A. Couairon, A. Mysyrowicz, J. Biegert, and U. Keller, *Appl. Phys. B* **79**, 673–677 (2004).
- [8] X. Chen, A. Malvache, A. Ricci, A. Jullien, and R. Lopez-Martens, *Fib. Opt.* **21**, 198–201 (2011).
- [9] F. Böhle, M. Kretschmar, A. Jullien, M. Kovacs, M. Miranda, R. Romero, H. Crespo, U. Morgner, P. Simon, R. Lopez-Martens, and T. Nagy, *Las. Phys. Lett.* (accepted) (2014).
- [10] C. Fourcade Dutin, A. Dubrouil, S. Petit, E. Mével, E. Constant, and D. Descamps, *Opt. Lett.* **35**, 253–255 (2010).
- [11] A. Couairon and A. Mysyrowicz, *Phys. Rep.* **441**, 47–189 (2007).
- [12] A. Zair, A. Guandalini, F. Schapper, M. Holler, J. Biegert, L. Gallmann, U. Keller, A. Couairon, M. Franco, and A. Mysyrowicz, *Opt. Express* **15**, 5394–5404 (2007).
- [13] M. Nurhuda, A. Suda, S. Bohman, S. Yamaguchi, and K. Midorikawa, *Phys. Rev. Lett.* **97**, 153902 (2006).
- [14] J. Chen, A. Suda, E. J. Takahashi, M. Nurhuda, and K. Midorikawa, *Opt. Lett.* **33**, 2992–2994 (2008).
- [15] S. Akturk, C. L. Arnold, B. Zhou, and A. Mysyrowicz, *Opt. Lett.* **34**, 1462–1464 (2009).
- [16] C. L. Arnold, B. Zhou, S. Akturk, S. Chen, A. Couairon, and A. Mysyrowicz, *N. J. Phys.* **12**, 073015 (2010).
- [17] C. L. Arnold, S. Akturk, M. Franco, A. Couairon, and A. Mysyrowicz, *Opt. Express* **17**, 11122–11129 (2009).
- [18] P. Rudawski, C. M. Heyl, F. Brizuela, J. Schwenke, A. Persson, E. Mansten, R. Rakowski, L. Rading, F. Campi, B. Kim, P. Johnsson, and A. L’Huillier, *Rev. Sci. Instrum.* **84**, 073103 (2013).
- [19] A. Brodeur and S. L. Chin, *Phys. Rev. Lett.* **80**, 4406–4409 (1998).
- [20] A. Siegman, *OSA TOPS* **17**, 184–199 (1997).
- [21] P. B. Corkum, *Phys. Rev. Lett.* **71**, 1994–1997 (1993).
- [22] E. Constant, A. Dubrouil, O. Hort, S. Petit, D. Descamps, and E. Mével, *J. Phys. B* **45**, 074018 (2012).
- [23] A. M. Perelomov, V. S. Popov, and M. V. Terent’ev, *Sov. Phys. JETP* **23**, 924–934 (1966).

References

- [1] A. L'Huillier, T. Auguste, P. H. Balcou, B. Carre, P. Monot, P. Salieres, C. Altucci, M. B. Gaarde, J. Larson, E. Mével, T. Starczewski, S. Svanberg, C. G. Wahlström, K. S. Zerne, R. Budil, T. Ditmire, and M. D. Perry, "High-order harmonics - a coherent source in the xuv range," *J. Nonl. Opt. Phys. Mat.* **4**, 647–665 (1995).
- [2] F. Krausz and M. Ivanov, "Attosecond physics," *Rev. Mod. Phys.* **81**, 163–234 (2009).
- [3] T. Brabec and F. Krausz, "Intense few-cycle laser fields: Frontiers of nonlinear optics," *Rev. Mod. Phys.* **72**, 545–591 (2000).
- [4] E. Esarey, C. B. Schroeder, and W. P. Leemans, "Physics of laser-driven plasma-based electron accelerators," *Rev. Mod. Phys.* **81**, 1229–1285 (2009).
- [5] S. Rausch, T. Binhammer, A. Harth, E. Schulz, M. Siegel, and U. Morgner, "Few-cycle oscillator pulse train with constant carrier-envelope phase and 65 as jitter," *Opt. Express* **17**, 14341–14352 (2009).
- [6] M. Nisoli, S. De Silvestri, O. Svelto, R. Szipöcs, K. Ferencz, C. Spielmann, S. Sartania, and F. Krausz, "Compression of high-energy laser pulses below 5 fs," *Opt. Lett.* **22**, 522–524 (1997).
- [7] C. Hauri, W. Kornelis, F. Helbing, A. Heinrich, A. Couairon, A. Mysyrowicz, J. Biegert, and U. Keller, "Generation of intense, carrier-envelope phase-locked few-cycle laser pulses through filamentation," *Appl. Phys. B* **79**, 673–677 (2004).
- [8] X. Chen, A. Malvache, A. Ricci, A. Jullien, and R. Lopez-Martens, "Efficient hollow fiber compression scheme for generating multi-mj, carrier-envelope phase stable, sub-5 fs pulses," *Fib. Opt.* **21**, 198–201 (2011).
- [9] F. Böhle, M. Kretschmar, A. Jullien, M. Kovacs, M. Miranda, R. Romero, H. Crespo, U. Morgner, P. Simon, R. Lopez-Martens, and T. Nagy, "Compression of CEP-stable multi-mj laser pulses down to 4 fs in long hollow fibers," *Las. Phys. Lett.* (accepted) (2014).
- [10] C. Fourcade Dutin, A. Dubrouil, S. Petit, E. Mével, E. Constant, and D. Descamps, "Post-compression of high-energy femtosecond pulses using gas ionization," *Opt. Lett.* **35**, 253–255 (2010).
- [11] A. Couairon and A. Mysyrowicz, "Femtosecond filamentation in transparent media," *Phys. Rep.* **441**, 47–189 (2007).
- [12] A. Zair, A. Guandalini, F. Schapper, M. Holler, J. Biegert, L. Gallmann, U. Keller, A. Couairon, M. Franco, and A. Mysyrowicz, "Spatio-temporal characterization of few-cycle pulses obtained by filamentation," *Opt. Express* **15**, 5394–5404 (2007).
- [13] M. Nurhuda, A. Suda, S. Bohman, S. Yamaguchi, and K. Midorikawa, "Optical pulse compression of ultrashort laser pulses in an argon-filled planar waveguide," *Phys. Rev. Lett.* **97**, 153902 (2006).
- [14] J. Chen, A. Suda, E. J. Takahashi, M. Nurhuda, and K. Midorikawa, "Compression of intense ultrashort laser pulses in a gas-filled planar waveguide," *Opt. Lett.* **33**, 2992–2994 (2008).
- [15] S. Akturk, C. L. Arnold, B. Zhou, and A. Mysyrowicz, "High energy ultrashort laser pulse compression in hollow planar waveguides," *Opt. Lett.* **34**, 1462–1464 (2009).
- [16] C. L. Arnold, B. Zhou, S. Akturk, S. Chen, A. Couairon, and A. Mysyrowicz, "Pulse compression with planar hollow waveguides: a pathway towards relativistic intensity with table-top lasers," *N. J. Phys.* **12**, 073015 (2010).
- [17] C. L. Arnold, S. Akturk, M. Franco, A. Couairon, and A. Mysyrowicz, "Compression of ultrashort laser pulses in planar hollow waveguides: a stability analysis," *Opt. Express* **17**, 11122–11129 (2009).
- [18] P. Rudawski, C. M. Heyl, F. Brizuela, J. Schwenke, A. Persson, E. Mansten, R. Rakowski, L. Rading, F. Campi, B. Kim, P. Johnsson, and A. L'Huillier, "A high-flux high-order harmonic source," *Rev. Sci. Instrum.* **84**, 073103 (2013).
- [19] A. Brodeur and S. L. Chin, "Band-gap dependence of the ultrafast white-light continuum," *Phys. Rev. Lett.* **80**, 4406–4409 (1998).
- [20] A. Siegman, "How to (maybe) measure laser beam quality," *OSA TOPS* **17**, 184–199 (1997).
- [21] P. B. Corkum, "Plasma perspective on strong field multiphoton ionization," *Phys. Rev. Lett.* **71**, 1994–1997 (1993).
- [22] E. Constant, A. Dubrouil, O. Hort, S. Petit, D. Descamps, and E. Mével, "Spatial shaping of intense femtosecond beams for the generation of high-energy attosecond pulses," *J. Phys. B* **45**, 074018 (2012).
- [23] A. M. Perelomov, V. S. Popov, and M. V. Terent'ev, "Ionization of atoms in an alternating electric field," *Sov. Phys. JETP* **23**, 924–934 (1966).

PAPER IX

Efficient High-Order Harmonic Generation Boosted by Below-Threshold Harmonics

F. Brizuela*, C. M. Heyl*, P. Rudawski*, D. Kroon, L. Rading,
J. M. Dahlström, J. Mauritsson, P. Johnsson, C. L. Arnold and
A. L'Huillier; (* authors contributed equally).

Scientific Reports **3**, 1410 (2013).



Efficient high-order harmonic generation boosted by below-threshold harmonics

SUBJECT AREAS:
ATTOSECOND SCIENCE
NONLINEAR OPTICS
APPLIED PHYSICS
X-RAYS

F. Brizuela¹, C. M. Heyl¹, P. Rudawski¹, D. Kroon¹, L. Rading¹, J. M. Dahlström², J. Mauritsson¹, P. Johansson¹, C. L. Arnold¹ & A. L'Huillier¹

¹Department of Physics, Lund University, P. O. Box 118, SE-22100 Lund, Sweden, ²Atomic Physics, Fysikum, Stockholm University, AlbaNova University Center, SE-10691 Stockholm, Sweden.

Received
12 February 2013

Accepted
13 February 2013

Published
11 March 2013

Correspondence and
requests for materials
should be addressed to
A.L. (anne.lhuillier@
fysik.lth.se)

High-order harmonic generation (HHG) in gases has been established as an important technique for the generation of coherent extreme ultraviolet (XUV) pulses at ultrashort time scales. Its main drawback, however, is the low conversion efficiency, setting limits for many applications, such as ultrafast coherent imaging, nonlinear processes in the XUV range, or seeded free electron lasers. Here we introduce a novel scheme based on using below-threshold harmonics, generated in a “seeding cell”, to boost the HHG process in a “generation cell”, placed further downstream in the focused laser beam. By modifying the fundamental driving field, these low-order harmonics alter the ionization step of the nonlinear HHG process. Our dual-cell scheme enhances the conversion efficiency of HHG, opening the path for the realization of robust intense attosecond XUV sources.

The interaction of intense laser pulses with atomic or molecular gas media leads to the generation of harmonics of the laser light, up to very high orders¹. These harmonics are locked in phase, giving rise to attosecond bursts of XUV light. The simplicity of the experimental technique, together with the progress in ultrafast laser technology, has promoted HHG sources as essential tools in many laboratories; opening, in particular, the field of attosecond science². However, HHG suffers from low conversion efficiency, owing partly to phase mismatches in the nonlinear medium that prevent efficient build up of the macroscopic field^{3–6}, but mostly to the weak response of the individual atoms to the field.

The atomic response to an external driving field can be described by a three-step model [Fig. 1(a)]: First, a bound electron tunnel-ionizes into the continuum; second, it is accelerated by the laser field; and finally, it recombines with the parent ion upon field reversal, emitting an XUV photon^{7,8}. The electron trajectories can be grouped in two families, named the long and the short, depending on the excursion time of the electron and generated in intervals II and III of Fig. 1(a), respectively. The most interesting from a practical point-of-view are the short trajectories, which lead to collimated and spectrally narrow emission. Unfortunately, these trajectories start at times close to the zero-crossings of the driving electric field, suffering from very low quantum-tunneling probability.

Altering the driving electric field at the subcycle level⁹ provides a way of modifying the single atom response. This has been investigated mainly by adding the second harmonic field^{10–13}, thus breaking the symmetry between consecutive half cycles. In contrast, odd-order harmonics modify the HHG process while maintaining the half-cycle symmetry. In a pioneering work, Watanabe and coworkers¹⁴ investigated the influence of the third harmonic (TH) on single ionization and HHG in Ar, obtaining an enhancement of up to a factor of ten for the 27–31 harmonics. Also, a few theoretical works discuss the influence of the TH on the enhancement of the yield^{15,16} and/or the extension of the cutoff energy^{17–19}. Another approach to enhance the signal by modify the single atom response is to control the time of ionization by using attosecond pulse trains to initialize the three-step process via single photon absorption^{20–23}.

In this letter, we demonstrate a simple and robust, yet powerful enhancement scheme based on a dual gas-cell setup [Fig. 1(b)]. We study HHG in neon using a high-energy (~20 mJ), near-infrared fundamental field, loosely focused in a long gas cell, resulting in high-order harmonics in the 40–100 eV range, with a typical energy of 10 nJ per harmonic order. The addition of a high-pressure Ar gas cell before the generation cell produces a large enhancement in the Ne signal, as seen in Fig. 1(c). We experimentally and theoretically show that the observed enhancement is due to below-threshold, low-order harmonics which modify the fundamental field in such a way that the contribution of the short trajectories is increased.

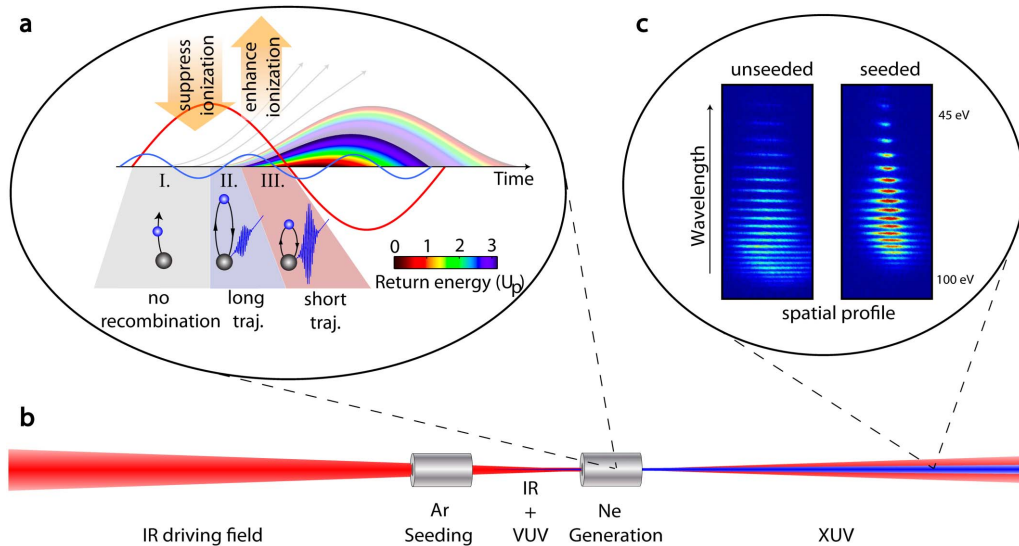


Figure 1 | HHG in a dual gas-cell. (a) Schematic classical trajectories for a sinusoidal driving field (red line). The colors indicate the return energy of the electrons in units of the ponderomotive energy U_p . Modifying the driving field by adding an odd harmonic field (blue line) can lead to an enhanced ionization probability for short trajectories (interval III) while suppressing the ionization of non-contributing electrons (intervals I and II), as indicated by the arrows. (b) Schematic experimental setup. Low-order harmonics generated in the seeding cell co-propagate with the fundamental into the generation cell and modify the HHG process. (c) Comparison of a typical HHG spectrum from a neon-filled generation cell obtained using only the fundamental field; and a spectrum obtained combining the fundamental field with low-order harmonics generated in the argon-filled seeding cell. In the latter case, the harmonic yield for the plateau harmonics is enhanced while the cutoff energy and the divergence are reduced.

Results

In our experiment, the generation cell is placed approximately at the laser focus while the seeding cell is located a few centimeters before (see Methods). The gas pressures in the cells can be independently adjusted and are typically a few mbar in the generation cell (Ne) and up to tens of mbar in the seeding cell (Ar). In Fig. 2(a–c), HHG spectra from neon are plotted as a function of the seeding pressure for three different driving intensities. When no gas is present in the seeding cell, standard Ne spectra are obtained. As the seeding pressure increases, the signal from the neon cell decreases until it is almost completely suppressed. At higher pressures, the neon spectra reappear and are significantly enhanced in the 50–80 eV region

while the maximum photon energy slightly shifts to lower harmonic orders.

Figure 2(d) shows harmonics generated in the seeding cell. Harmonics with energies above the ionization threshold are not present at pressures where the enhancement in the generation cell occurs, and therefore are not responsible for the signal boost through single-photon ionization^{20–23}. At these pressures, only low-order harmonics are efficiently generated in the seeding cell, indicating that they are responsible for the seeding process.

In order to validate our interpretation, we performed numerical simulations for both cells. In the generation cell, we simulated the seeded HHG process using the strong-field approximation

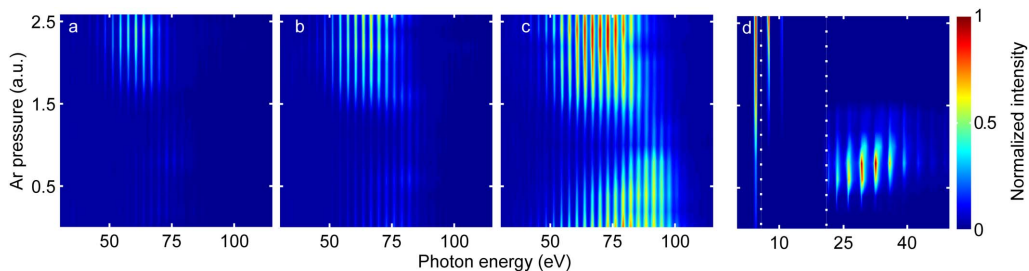


Figure 2 | Experimental HHG spectra. (a–c) Spectra from the generation cell as a function of the pressure in the seeding cell at three driving intensities 2.7, 3.5, and 4.4×10^{14} W/cm², respectively. The spectra were obtained using argon in the seeding cell and neon, at a fixed pressure, in the generation cell. The data were normalized to the most intense enhanced neon spectrum. (d) Low- (3–7) and high-order harmonics from the seeding cell as a function of Ar pressure. The dotted lines indicate regions measured independently with different detectors. Each region was normalized to the highest intensity in the corresponding spectral range.

(SFA)^{15,16,24,25} (see Methods). The total field can be written as

$$E(t) = E_0 \left[\sin(\omega t) + \sum_{q\omega < I_p} r_q \sin(q\omega t + \Delta\phi_q) \right], \quad (1)$$

where E_0 is the amplitude of the fundamental field, ω its frequency, I_p the ionization energy, r_q the ratio between the fundamental and q th harmonic field, and $\Delta\phi_q$ their relative phase. Although all harmonics below the ionization threshold of Ar may influence the enhancement phenomenon, we considered only the TH, which is the most intense one (we omit the subscript 3 below). A simulated HHG spectrum in neon with $|r|^2 = 0.01$, is shown in Fig. 3(a) as a function of $\Delta\phi$. A relative phase of ~ 1 rad leads to an enhanced ionization probability, since the electrical field is increased at the time where the short electron trajectories are born [interval III in Fig. 1(a)]. Furthermore, the electric field amplitude is reduced around the peak of the fundamental field leading to suppressed probability for non-contributing trajectories (intervals I, II) and to an improved macroscopic situation since plasma dispersion and depletion effects are minimized^{4,5}. When $\Delta\phi \approx 1 \pm \pi$, the situation is reversed and HHG is suppressed compared to the unseeded case.

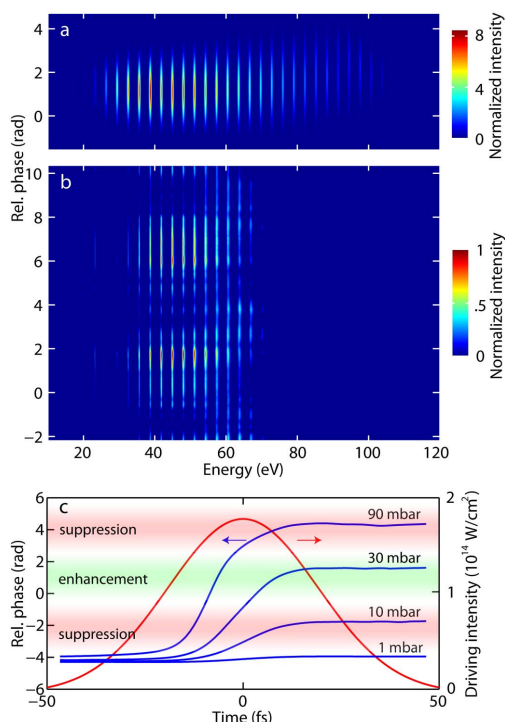


Figure 3 | Influence of the relative (ω , 3ω) phase in HHG. (a) SFA spectra as a function of $\Delta\phi$ in the generation cell, normalized to the unseeded spectrum. Only the contribution of the short trajectory is considered. An effective grating response is included to mimic the experimental conditions. (b) Experimental results with the TH generated in a crystal, normalized to the highest signal. (c) Propagation simulations in the seeding cell: $\Delta\phi$ at the exit of the cell as a function of time for different pressures.

We experimentally confirmed the dependence of the HHG signal on $\Delta\phi$ by studying HHG using a combination of the fundamental and the TH generated in a crystal¹⁴. To control the delay between the two fields, we used a Michelson interferometer with the TH produced in one arm. Our results, plotted in Fig. 3(b), show a strong delay dependence of the harmonic yield. However, we could not increase the overall HHG efficiency compared to the dual-cell scheme, since a large fraction of the fundamental field was needed for the TH generation and consequently lost for HHG.

In the seeding cell, we examined the pressure dependence of both low-order and high-order harmonic generation. Our calculations²⁶ confirm the experimental observation that HHG in Ar peaks at a certain pressure (~ 10 mbar) which corresponds to optimized phase matching²⁷, while below-threshold harmonics continue to increase up to pressures as high as 100 mbar. We also investigated the propagation of the fundamental and TH fields in a high pressure cell²⁸ (see Methods). This allowed us to examine their phase relation after the seeding cell and to eliminate the relatively weak reshaping of the fundamental field in our experimental conditions as possible cause for the enhancement. As Fig. 3(c) shows, for high enough seeding pressures, $\Delta\phi$ will be between 0 and 2 radians during part of the laser pulse, leading to a gated enhancement mechanism.

Discussion

As in any enhancement scheme, a key question is whether our method is advantageous over “usual” HHG optimization, which can be achieved for example by using looser focusing, optimizing the position of the focus in the cell, or adjusting the pressure in the gas cell^{1,29,30}. Ideally, one would like to compare optimized HHG and optimized seeded HHG for a given fundamental pulse energy. This is not easy to realize experimentally, so we choose to benchmark seeded HHG against optimized unseeded HHG, with ~ 10 nJ at 63 eV (41st harmonic).

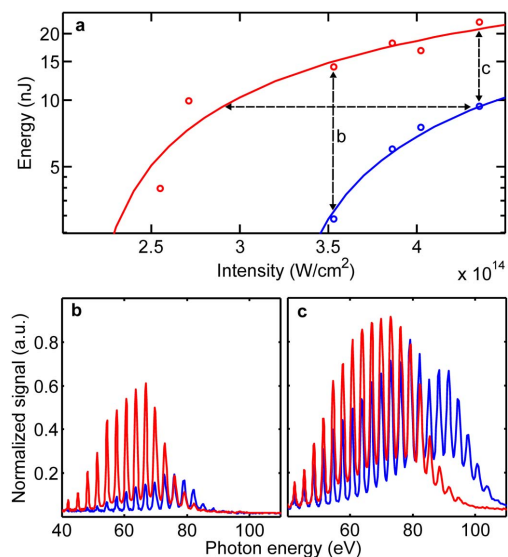


Figure 4 | Optimization of HHG. (a) 41st harmonic energy as a function of the driving intensity for seeded (red) and unseeded (blue) HHG. Unseeded HHG is optimized at the maximum intensity. (b, c) Corresponding experimental spectra at 3.5 and 4.4×10^{14} W/cm², respectively.

Figure 4(a) compares the 41st harmonic signal in the seeded and unseeded cases as a function of the driving intensity. The intensity required for saturating seeded HHG is only half that needed for unseeded HHG. This explains the reduction of the cutoff energy and the lower divergence for the harmonics. The enhancement factor depends on the driving intensity [Fig. 4(b,c)]. For the 41st harmonic, it varies from five at 3.5×10^{14} W/cm² (and even higher at lower intensity) to two at 4.4×10^{14} W/cm². By further optimizing seeded HHG (e.g. by changing the focusing conditions) one should be able to obtain an even larger increase compared to unseeded HHG. The higher efficiency together with the lower divergence leads to a brighter source of XUV light.

In summary, we have studied the effect of seeding HHG using harmonics generated in a separate gas cell and showed that low-order harmonics are responsible for the resulting enhancement. The combined electric field preferentially enhances the short trajectories while suppressing depletion and plasma dispersion effects. The required phase difference between the fundamental and the low-order harmonics is obtained by adjusting the pressure in the seeding cell, thus modifying the free-electron dispersion. Our method is not limited to the gas combination presented here. Experimentally we have observed an increased harmonic yield for a variety of gas combinations, and even when the same gas is used in both cells. Our simulations show that the enhancement can be scaled far above one order of magnitude by increasing the low-order harmonic intensity, for example by using longer cells, higher pressures or gases with higher nonlinearities. This also leads to a shorter temporal gate, of interest for single attosecond pulse generation.

Methods

Experimental setup. The harmonics were generated using 45 fs pulses, centered at 800 nm. The gas cells used in this setup were 1 cm long with a diameter of 1 mm. The injection of gas into the cell was synchronized with the laser repetition rate (10 Hz) and the delay between the gas injection and the laser pulse was optimized for each cell. In the experiments, seeding cell pressure and pulse energy were the parameters investigated. The generation cell pressure was set for the best phase-matching conditions for Ne at the highest laser intensity (4.4×10^{14} W/cm²), corresponding to less than 10 mbar. The focus position was adjusted in order to optimize HHG in the generation cell. The cell separation was 15 mm with the generation-cell located at focus ($f = 4$ m). Nevertheless, larger separations, up to 50 mm yielded similar results. The cells were mounted on motor-controlled XYZ stages with motorized XY tilt capabilities. The cells could be removed completely from the IR field. A CCD camera was used to align each cell to the laser and observation of the spectra at the best phase-matching conditions were used to evaluate the tilt of each cell. The same Ne spectra from the generation cell could be obtained through the evacuated seeding cell or with the seeding cell removed from the beam path. The same was true for the seeding cell where Ar spectra could be obtained under both conditions. The pressure and intensity controls were automated to scan the region of interest. At each experimental condition 10 single-shot spectra were measured and averaged. The harmonic orders were calibrated using the absorption edge of an Al-foil filter. The fundamental intensity was estimated from the cutoff of the unseeded Ne spectra.

Numerical simulations. Generation cell. The influence of a weak third harmonic field on the HHG process was simulated by solving the time-dependent Schrödinger Equation within the strong field approximation. The quasi-classical action for the electron motion in the continuum

$$S(\vec{p}, t, t_0) = \int_{t_0}^t dt' \left(\frac{\vec{p} - e\vec{A}(t')}{2m} + I_p \right) \quad (2)$$

is calculated for a combined vector potential of the fundamental field and a weak parallel auxiliary field consistent with the field definition in Eq. (1). t_0 and t correspond to the tunneling and recombination times for an electron with canonical momentum \vec{p} . I_p is the ionization potential, and \vec{A} the vector potential of the field. We approximate the HHG dipole as²⁴

$$\begin{aligned} x(t) = i \int_0^\infty d\tau \left(\frac{\pi}{\epsilon + i\tau/2} \right)^{3/2} & d_x^*(p_x(t, \tau) - A_x(t)) \\ & \times d_x(p_x(t, \tau) - A_x(t - \tau)) E(t - \tau) \\ & \times \exp(-iS_{cl}(t, \tau)) F(\tau) + c.c., \end{aligned} \quad (3)$$

where a stationary phase approximation is performed over momentum, with $p_x(t, \tau) = |E(t) - E(t - \tau)|\tau$, where $\tau = t - t_0$ is the excursion time in the continuum.

We also insert a filter function $F(\tau)$ to select the short trajectory: $F(\tau) \approx 1$ for $\tau < 0.65T$ and $F(\tau) \approx 0$ for $\tau > 0.65T$, where $0.65T$ corresponds to the position of the cutoff. The integral in Eq. (3) is then evaluated numerically on a finite grid followed by a numerical Fourier transform for the dipole emission.

Seeding cell. We performed calculations which combine the solution of the time-dependent Schrödinger equation in a single-active electron approximation and propagation in a partially ionized medium^{26,3} using a slowly-varying envelope approximation. Our main goal was to examine the influence of the pressure both for low-order and high-order harmonic generation in conditions mimicking the experiment. We found a maximum for HHG at around 10 mbar, while below-threshold, low-order harmonics which are not reabsorbed in the medium continue to increase up to very high pressures (100 mbar).

The generation of the third harmonic in the seeding cell was simulated using a (3 + 1)-dimensional, unidirectional, nonlinear envelope equation²⁸. The complete frequency dependent dispersion relation is considered, enabling to propagate the fundamental and the third harmonic simultaneously. It is numerically integrated using a split-step technique, where the linear contributions, such as dispersion and diffraction are treated in k -transverse frequency space, while the nonlinear part, taking into account the Kerr effect, third-harmonic generation as well as plasma dispersion and plasma defocusing is treated in normal space. The method is described in detail in²⁹. The calculated phase variation is mainly due to plasma dispersion effects. There are also small contributions from the geometrical phase acquired along the seeding cell as well pressure-dependent third harmonic phase matching.

1. Popmintchev, T. *et al.* Bright Coherent Ultrahigh Harmonics in the keV X-ray Regime from Mid-Infrared Femtosecond Lasers. *Science* **336**, 1287–1291 (2012).
2. Krausz, F. & Ivanov, M. Attosecond Physics. *Rev. Mod. Phys.* **81**, 163 (2009).
3. Constant, E. *et al.* Optimizing High Harmonic Generation in Absorbing Gases: Model and Experiment. *Phys. Rev. Lett.* **82**, 1668 (1999).
4. Kazamias, S. *et al.* Global Optimization of High Harmonic Generation. *Phys. Rev. Lett.* **90**, 193901 (2003).
5. Gaarde, M. B., Tate, J. L. & Schafer, K. J. Macroscopic aspects of attosecond pulse generation. *J. Phys. B* **41**, 132001 (2008).
6. Willner, A. *et al.* Efficient control of quantum paths via dual-gas high harmonic generation. *New J. Phys.* **13**, 113001 (2011).
7. Corkum, P. B. Plasma perspective on strong field multiphoton ionization. *Phys. Rev. Lett.* **71**, 1994–1997 (1993).
8. Schafer, K. J., Yang, B., DiMauro, L. F. & Kulander, K. C. Above threshold ionization beyond the high harmonic cutoff. *Phys. Rev. Lett.* **70**, 1599 (1993).
9. Wirth, A. *et al.* Synthesized Light Transients. *Science* **334**, 195–200 (2011).
10. Eichmann, H. *et al.* Polarization-dependent high-order two-color mixing. *Phys. Rev. A* **51**, R3414 (1995).
11. Mauritsson, J. *et al.* Attosecond Pulse Trains Generated Using Two Color Laser Fields. *Phys. Rev. Lett.* **97**, 013001 (2006).
12. Kim, I. J. *et al.* Highly Efficient High-Harmonic Generation in an Orthogonally Polarized Two-Color Laser Field. *Phys. Rev. Lett.* **94**, 243901 (2005).
13. Raz, O., Pedatzur, O., Bruner, B. D. & Dudovich, N. Spectral caustics in attosecond science. *Nat. Phot.* **6**, 170 (2012).
14. Watanabe, S., Kondo, K., Nabekawa, Y., Sagisaka, A. & Kobayashi, Y. Two-Color Phase Control in Tunneling Ionization and Harmonic Generation by a Strong Laser Field and Its Third Harmonic. *Phys. Rev. Lett.* **73**, 2692 (1994).
15. Kondo, K., Kobayashi, Y., Sagisaka, A., Nabekawa, Y. & Watanabe, S. Tunneling ionization and harmonic generation in two-color fields. *J. Opt. Soc. Am. B* **13**, 424–429 (1996).
16. Pi, L. W., Shi, T. Y. & Qiao, H. X. Enhancement of Bichromatic High-Order Harmonic Generation by a Strong Laser Field and Its Third Harmonic. *Chin. Phys. Lett.* **23**, 1490 (2006).
17. Ishikawa, K. Photoemission and Ionization of He⁺ under Simultaneous Irradiation of Fundamental Laser and High-Order Harmonic Pulses. *Phys. Rev. Lett.* **91**, 043002 (2003).
18. Ivanov, I. A. & Kheifets, A. S. Tailoring the waveforms to extend the high-order harmonic generation cutoff. *Phys. Rev. A* **80**, 023809 (2009).
19. Chipperfield, L. E., Robinson, J. S., Tisch, J. W. G. & Marangos, J. P. Ideal waveform to generate the maximum possible electron recollision energy for any given oscillation period. *Phys. Rev. Lett.* **102**, 063003 (2009).
20. Schafer, K. J., Gaarde, M. B., Heinrich, A., Biegert, J. & Keller, U. Strong Field Quantum Path Control Using Attosecond Pulse Trains. *Phys. Rev. Lett.* **92**, 230003 (2004).
21. Gaarde, M. B., Schafer, K. J., Heinrich, A., Biegert, J. & Keller, U. Large enhancement of macroscopic yield in attosecond pulse train-assisted harmonic generation. *Phys. Rev. A* **72**, 013411 (2005).
22. Heinrich, A. *et al.* Enhanced VUV-assisted high harmonic generation. *J. Phys. B* **39**, S275 (2006).
23. Takahashi, E. J., Kanai, T., Ishikawa, K. L., Nabekawa, Y. & Midorikawa, K. Dramatic Enhancement of High-Order Harmonic Generation. *Phys. Rev. Lett.* **99**, 053904 (2007).
24. Lewenstein, M., Salières, P. & L’Huillier, A. Phase of the atomic polarization in high-order harmonic generation. *Phys. Rev. A* **52**, 4747 (1995).



25. Dahlström, J. M., L'Huillier, A. & Mauritsson, J. Quantum mechanical approach to probing the birth of attosecond pulses using a two-colour field. *J. Phys. B* **44**, 095602 (2011).
26. Erny, C. *et al.* Metrology of high-order harmonics for free-electron laser seeding. *New J. Phys.* **13**, 073035 (2011).
27. Heyl, C. M., Gütde, J., L'Huillier, A. & Höfer, U. High-order harmonic generation with μJ laser pulses at high repetition rates. *J. Phys. B* **45**, 074020 (2012).
28. Arnold, C. L. *et al.* Pulse compression with planar hollow waveguides: a pathway towards relativistic intensity with table-top lasers. *N. J. Phys.* **12**, 073015 (2010).
29. Takahashi, E., Nabekawa, Y. & Midorikawa, K. Generation of 10- μJ coherent extreme-ultraviolet light by use of high-order harmonics. *Opt. Lett.* **27**, 1920 (2002).
30. Salières, P., L'Huillier, A. & Lewenstein, M. Coherence control of high-order harmonics. *Phys. Rev. Lett.* **74**, 3776 (1995).

Acknowledgements

We thank Erik Mansten, Jörg Schwenke, and Rafal Rakowski for their early contribution to the project, and Byunghoon Kim for his contribution to the $\omega/3\omega$ measurements. This research was supported by the Marie Curie program ATTOFEL (ITN), the European

Research Council (ALMA), the Joint Research Programme ALADIN of Laserlab-Europe II, the Swedish Research Council, the Swedish Foundation for Strategic Research, the Knut and Alice Wallenberg Foundation.

Author contributions

F.B., C.M.H. and P.R. contributed equally to this work. F.B., C.M.H., P.R. and L.R. performed the experiments. D.K. and C.L.A. performed the propagation calculations. C.M.H. and J.M.D. performed the SFA calculations. J.M., P.J., A.L. and all the other authors helped with the interpretation and the writing of the article.

Additional information

Competing financial interests: The authors declare no competing financial interests.

License: This work is licensed under a Creative Commons Attribution-NonCommercial-NoDerivs 3.0 Unported License. To view a copy of this license, visit <http://creativecommons.org/licenses/by-nc-nd/3.0/>

How to cite this article: Brizuela, F. *et al.* Efficient high-order harmonic generation boosted by below-threshold harmonics. *Sci. Rep.* **3**, 1410; DOI:10.1038/srep01410 (2013).

PAPER X

Interference Effects in Two-Color High-Order Harmonic Generation

X. He, M. Dahlström, R. Rakowski, C. M. Heyl, A. Persson,
J. Mauritsson, and A. L'Huillier.

Physical Review A **82**, 033410 (2010).

Interference effects in two-color high-order harmonic generation

X. He,¹ J. M. Dahlström,¹ R. Rakowski,¹ C. M. Heyl,^{1,2} A. Persson,¹ J. Mauritsson,¹ and A. L'Huillier¹

¹*Department of Physics, Lund University, P. O. Box 118, SE-221 00 Lund, Sweden*

²*Department of Physics, University of Marburg, Marburg, Germany*

(Received 5 May 2010; published 13 September 2010)

We study high-order harmonic generation in argon driven by an intense 800 nm laser field and a small fraction of its second harmonic. The intensity and divergence of the emitted even and odd harmonics are strongly modulated as a function of the relative delay between the two fields. We provide a detailed analysis of the underlying interference effects. The interference changes drastically when approaching the cutoff region due to a switch of the dominant trajectory responsible for harmonic generation.

DOI: [10.1103/PhysRevA.82.033410](https://doi.org/10.1103/PhysRevA.82.033410)

PACS number(s): 32.80.Rm, 32.80.Qk, 42.65.Ky

High-order harmonic generation (HHG) from the interaction of an intense infrared (IR) laser field and a gas target provides a coherent table-top radiation source in the extreme ultraviolet (XUV) range, of interest for a number of applications, in particular the production of attosecond light pulses [1,2]. The underlying physics of HHG is well described by the so-called three-step model [3–5]: an electron wave packet is created by tunneling through the Coulomb barrier deformed by the laser field; it is subsequently accelerated by the laser field; and returns to the atom where it recombines to the ground state, leading to the production of an XUV light burst. This process is repeated every half-cycle of the IR laser field, resulting in an attosecond pulse train (APT) with a pulse separation of one-half IR period and to a spectrum of odd harmonics.

There is a growing interest to achieve even better control of the generation process [6], e.g., to obtain higher conversion efficiency or to tailor attosecond pulses or pulse trains for specific applications. Two-color HHG driven by an IR laser and its second harmonic (blue) provides subcycle control of the generating electric field, with the interesting property that two consecutive half-cycles become different, and not simply opposite in sign. This breakdown of the electric field inversion symmetry has been used for several applications, e.g., the generation of even and odd high-harmonics with increased conversion efficiency [7,8] and the production of attosecond pulse trains with one pulse per IR cycle [9,10]. In some conditions, when the intensity of the second harmonic is much weaker than that of the fundamental laser field, even harmonics can be used to provide information about the generation process [11–13].

In this article, we investigate both experimentally and theoretically high-order harmonic generation driven by a two-color laser field consisting of a 800 nm fundamental and a fraction of its second harmonic. The even and odd harmonic intensities are found to be modulated as a function of IR-blue delay, forming in some cases a rich interference pattern (Fig. 1). We investigate how these oscillations depend on harmonic energy and intensity of the blue field and how the spatial profiles of the emitted harmonics are affected. We provide an interpretation based on quasiclassical calculations.

Experiments were performed using an amplified 10 Hz titanium sapphire laser system delivering 40 fs pulses at 800 nm with energy up to 1 J. The results presented in this article are obtained with only a small fraction (less than 10 mJ)

of this energy. The laser beam was sent through a 1.3 mm-thick type I KDP (potassium dihydrogen phosphate) crystal to generate the second harmonic. A Michelson interferometer was used to separate and delay the second harmonic and to make the polarizations of the two laser fields parallel to each other. The relative delay was adjusted with a 500 μm -thick glass plate. After recombination of the two colors, the beam was focused by a spherical mirror with a 2 m focal length into a cylindrical gas cell with 1 mm diameter and 15 mm length, filled with Ar gas. Variable apertures were placed in the fundamental and second harmonic beams to adjust intensities and focusing geometries. These conditions are such that phase matching is optimized and pulse energies per harmonic reaching 100 nJ have been measured. The harmonic spectra were detected by a flat-field XUV spectrometer, located 1.5 m from the source and allowing us to obtain spatial and spectral information simultaneously [14].

Figures 1(a)–1(c) presents the spectra of the 21st to 24th harmonics as a function of relative delay (τ) in units of the period of the blue field $T_B = 1.3$ fs. The color code indicates the intensity of the emitted light. When the blue intensity is less than a percent of the IR [panel (a)], the odd and even harmonics oscillate with opposite phase twice per blue cycle [11–13]. When the blue intensity is increased to a few percent [Figs. 1(b) and 1(c)], even and odd harmonics become comparable in strength and vary more strongly with the IR-blue delay.

Figure 2 compares the intensities of the 22nd (a) and 23rd (b) harmonics as a function of τ for the three different intensities of the blue field used in Fig. 1. At low intensity (thin red line), the odd and even harmonics oscillate out of phase. When the blue intensity is increased, the patterns become more complex, exhibiting multiple maxima per half blue period. The number and position of these maxima depend on the blue intensity, as well as harmonic order. These results arise from the interferometric nature of the HHG process, which will be analyzed in more detail in the following.

To understand the interference structure shown in Figs. 1 and 2, let us consider the radiation emitted every IR cycle over a certain energy range. It comprises predominantly two bursts, one each half-cycle. In absence of the blue field, they are identical except for a change of sign. We further assume that the emitted bursts are identical from one IR cycle to the next. The radiation emitted from the interaction of an intense laser field comprising n periods with an atom can be generally

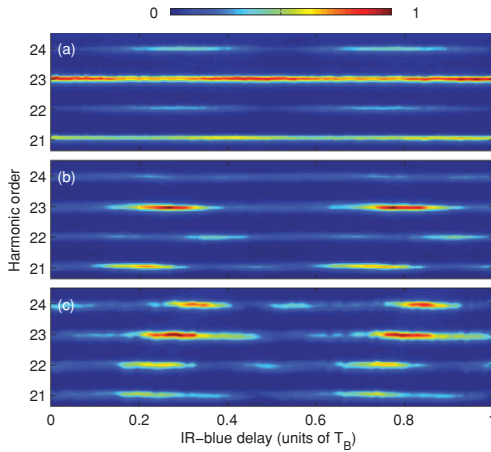


FIG. 1. (Color online) 21st to 24th harmonic spectra as a function of the relative delay between the IR and blue fields for different intensity ratios, increasing from about half a percent in (a) to a few percent in (b) and (c). The IR intensity is estimated to be 1.8×10^{14} W/cm², based on the cutoff position. The color code indicates the harmonic intensities in arbitrary units.

expressed as

$$s(t) = \sum_{j=1}^{j=n} a_+(t) \otimes \delta(t - jT) + a_-(t) \otimes \delta\left(t - jT - \frac{T}{2}\right), \quad (1)$$

where $a_+(t)$ and $a_-(t)$ are the fields emitted in the first and second half period, respectively, and T is the IR field period. If the blue field is weak, it mainly affects the phase of the emitted radiation. $a_{\pm}(t) \approx \pm a(t) \exp[\pm i\sigma(t)]$, where $a(t)$ is the pulse emitted from the first (positive) half period due to the interaction with the fundamental field only, and $\sigma(t)$ is a slow function over time. The Fourier transform of the pulse train can then be approximated as

$$S(\Omega) \approx A(\Omega) \sum_{j=1}^{j=n} e^{ij\Omega T + i\sigma(\Omega)} - e^{ij\Omega T + i\frac{\Omega T}{2} - i\sigma(\Omega)}, \quad (2)$$

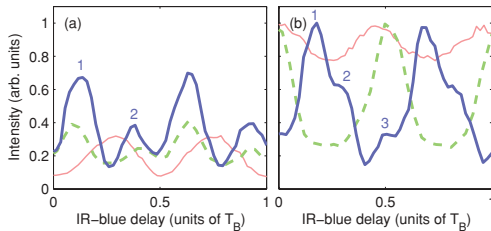


FIG. 2. (Color online) Intensities of the 22nd (a) and 23rd (b) harmonics, normalized to the maximum value of the 23rd harmonic for the three cases in Fig. 1. The thin red line, green dashed line, and thick blue line correspond to (a), (b), and (c).

where $A(\Omega)$ is the Fourier transform of $a(t)$ and $\sigma(\Omega) = \sigma[t_r(\Omega)]$. $t_r(\Omega)$ represents the time at which the component at frequency Ω of the light burst is emitted, i.e., the return time of the corresponding classical electron trajectory. The Ω dependence accounts for the chirp of the emitted radiation [15]. The power spectrum reduces to the form

$$|S(\Omega)|^2 \approx 4 |A(\Omega)|^2 \left| \frac{\sin\left(\frac{n\Omega T}{2}\right)}{\sin\left(\frac{\Omega T}{2}\right)} \right|^2 \left| \sin\left[\frac{\Omega T}{4} - \sigma(\Omega)\right] \right|^2, \quad (3)$$

which has a straightforward interpretation. The first factor is the spectrum emitted by a single attosecond pulse, the second factor modulates this broad spectrum, leading to a comb of even and odd harmonics. Finally the last factor cancels the even harmonic components when there is no second harmonic ($\sigma = 0$). When a second harmonic field is present, it modulates the amplitude of both even and odd harmonics. For the even harmonics ($\Omega = q\omega$ where ω is the IR frequency and q is an even integer), $|S(q\omega)|^2 \propto |\sin[\sigma(q\omega)]|^2$, while for the odd harmonics (q odd), $|S(q\omega)|^2 \propto |\cos[\sigma(q\omega)]|^2$.

The phase change induced by the blue field can be estimated using the classical limit, $I_p \rightarrow 0$. By treating the blue field as a perturbation, $\sigma(\Omega)$ is found to be [13]

$$\sigma(\Omega) = \frac{e}{\hbar} \int_{t_i}^{t_r} dt' x_R(t_r, t') E_B(t'), \quad (4)$$

where t_i is the ionization time and e the electron charge. x_R denotes the position at time t' of an electron that starts its motion in the IR field [$E_R(t) = E_R^0 \sin(\omega t)$] at time t_i . Finally, E_B is the second harmonic field $E_B(t) = E_B^0 \sin(2\omega t + \phi_B)$. Equation (4) can be rewritten as

$$\sigma(\Omega) = \sigma_0 \sin[\phi_B + \delta(\Omega)], \quad (5)$$

with $\sigma_0 = eE_B^0 \Delta(\Omega)/\hbar$. $\Delta(\Omega)$ and $\delta(\Omega)$ are the frequency-dependent modulus and argument of the Fourier transform at 2ω of the electron trajectory in the IR field.

Figures 3(a) and 3(b) shows the calculated intensity of two consecutive harmonics (even and odd) as a function of σ_0 and delay, expressed here as $(\phi_B + \delta)/2\pi$, while (c), (d) present lineouts at three different σ_0 , indicated by the corresponding lines in (a) and (b). The odd and even harmonic intensities strongly varies with delay in opposite phase with each other, so that the total intensity remains constant. The number of maxima increases with σ_0 , i.e., with the blue field intensity.

When the blue field is weak ($\sigma_0 \ll 1$), the intensity of the even harmonic varies as $|\sigma_0 \sin(\phi_B + \delta)|^2$, while the odd harmonic intensity varies as $1 - |\sigma_0 \sin(\phi_B + \delta)|^2$ [thin red line in Fig. 3(d)]. At moderate blue intensity, corresponding to the conditions of Fig. 1(b), the even harmonic intensity (green dashed line) show two peaks of equal strength over a delay of $T_B/2$, while the odd harmonics show one strong and one weak peak. This behavior compares well to that observed experimentally in Fig. 2 where two (one) peaks are visible in the even (odd) harmonics. We estimate σ_0 to be just above $\pi/2$ in this case. At higher blue intensity, as in Fig. 1(c), the even harmonic intensity (thick blue line) show two peaks (1,2), while the odd harmonics presents a broad peak with two maxima (1,2) and an additional sharp peak (3). The same qualitative behavior is observed experimentally

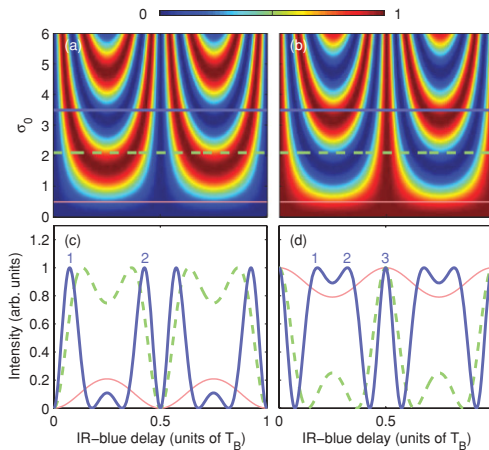


FIG. 3. (Color online) Harmonic intensity as a function of σ_0 and IR-blue delay for even (a) and odd (b) harmonics. The σ_0 corresponding to the intensities used in Figs. 1(a)–1(c) are indicated by the thick blue solid (1a), green dashed (1b), and thin red lines (1c). (c) and (d) show the corresponding lineouts.

(blue line in Fig. 2). σ_0 is thus estimated to be slightly above π . From this analysis, we can estimate the ratios of the blue to IR intensities to be 0.4, 5, and 20 % in Figs. 1(a), 1(b), and 1(c). The relative strength of the experimental peaks in Fig. 2 is not accurately modeled using Eq. (3) since we include neither amplitude effects nor propagation in our calculation. In addition, experimental effects, such as dephasing between the IR and the blue, could lead to decrease in contrast.

Complementary information on the generation process can be obtained by studying the spatial distribution [16]. In Figs. 4(a) and 4(b) we show the spatial distribution of the 22nd and 23rd harmonics. In the one-color case, the divergence of the q th harmonic Θ_q can be estimated using Gaussian optics by the simple expression [14],

$$\Theta_q = \frac{\lambda_q}{\pi w_q} \sqrt{1 + 4\alpha_q^2 I_R^2 \frac{w_q^4}{w_R^4}} \approx |\alpha_q| I_R \frac{\lambda_q w_q}{\pi w_R^2}, \quad (6)$$

where I_R is the peak IR intensity, w_R , w_q are the radii of the IR and q th harmonic fields and λ_q the q th harmonic wavelength. $\alpha_q I_R$ is the single-atom phase, corresponding to the phase accumulated by the electron on its trajectory, often called “dipole phase”. When $\alpha_q I_R$ is large, it dominates the diffraction limit in Eq. (6) and the divergence takes the simple expression shown on the right side in Eq. (6). For the short trajectory, we have $|\alpha_q| \approx 2.7 \times 10^{-14}$ cm²/W for the 23rd harmonic [14,17].

As shown in Eq. (2), the addition of a weak blue field affects the phase of each half-cycle contribution by $\pm\sigma$. The divergence of the q th harmonic is then expected to vary between $\Theta_q(1 \pm \sigma/|\alpha_q|I_R)$, the limits being reached when one half-cycle is dominant. These limits are indicated by the grey lines in Figs. 4(c) and 4(d), calculated by using the experimentally determined one-color divergence $\Theta_q = 0.33$ mrad. The two

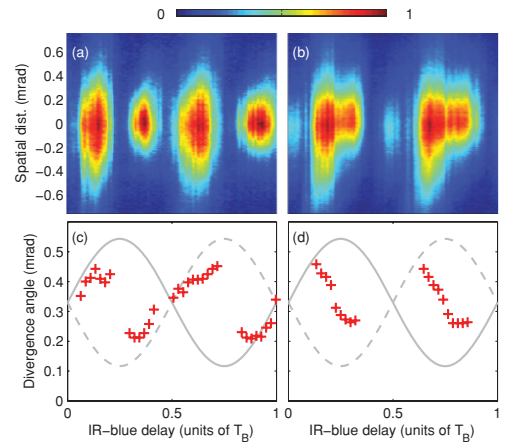


FIG. 4. (Color online) Spatial profiles for the 22nd (a) and 23rd (b) harmonics as a function of delay, in the conditions of Fig. 1(c). The experimental divergence angles (red symbols) are compared to the theoretical half-cycle divergences in (c) and (d) for the 22nd and 23rd harmonics, respectively.

lines (solid and dashed) show the variation of the divergence for two (positive or negative) half-cycles. Our experimental results for the 22nd and the 23rd harmonics are indicated by the red symbols. As expected, the measured divergence angles are comprised between the theoretical values for two consecutive half-cycle contributions. The variation of the measured divergence can be interpreted as follows: In (c), one half-cycle (corresponding to the dashed line) is dominant from $\tau = 0.3T_B$ to $0.7T_B$, while the other half-cycle prevails for the other delays. In contrast in (d), the measured divergence does not indicate preferential emission during one particular half cycle since it is well within the expected half-cycle values for almost all delays.

Finally, we investigate how the interference pattern depends on Ω , i.e., harmonic order, from the plateau to the cutoff region. Figure 5(a) shows the harmonic spectra as a function of delay, in the weak blue intensity case [corresponding to Fig. 1(a)]. The nodes of the oscillations of the even harmonics are indicated by the white crosses. The position of the nodes varies approximately linearly from harmonic order 22 to 28, in agreement with the prediction of the simple model presented above (see also [11,13]), for the short trajectory (see red line). In Fig. 5(b), we examine the behavior of higher-order harmonics, approaching the cutoff region. Surprisingly, the 30th harmonic hardly oscillates, while the 32nd and 34th oscillate almost out of phase with the 28th. To understand the apparent lack of oscillation of the 30th harmonic, we analyze its spatial profile. In Fig. 5(c), we present the 30th harmonic intensity obtained by integrating over the outer (central) part of the spatial profile, plotted as a thick blue (thin red) line. This allows us to unravel two different oscillations almost opposite in phase [see also + and * symbols in Fig. 5(a)]. The phase obtained by integrating the outer part of the spatial profile is close to that obtained for the 32nd and 34th harmonics in Fig. 5(b).

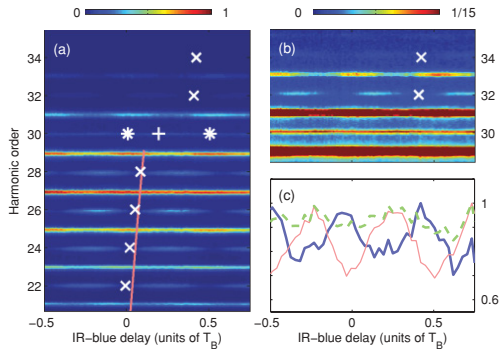


FIG. 5. (Color online) (a) Harmonic spectra as a function of delay. (b) Corresponding high energy region using a saturated color scale. The white crosses indicate the position of the nodes of the oscillations. The red curve in (a) is $\delta(\Omega)$ for the short branch. (c) 30th harmonic intensity as a function of delay, spatially integrated (green dashed), integrated over the central part (thick blue line); and over the outer part (thin red line) of the spatial profile. The + and * symbols in (a) refer to the nodes of the central and outer part, respectively.

We interpret this result as due to the long trajectory which becomes more important when approaching the cutoff region. The switch between the two trajectories seems to occur at the 30th harmonic in our experiment. If this harmonic has comparable (and approximately out of phase) contributions from the two trajectories, it would only weakly oscillate with τ , which is what is observed experimentally. Phase matching calculations performed using our experimental conditions show a progressive switch from the short trajectory to the long trajectory when approaching the cutoff region and thus confirm this interpretation.

In summary, we have experimentally identified and theoretically analyzed interference effects in two-color HHG. Adding a weak blue field allows us to control the intensity and divergence of the harmonic emission. An interesting switch between the short and long trajectories of the harmonic emission has been identified when approaching the cutoff region.

This research was supported by the Marie Curie Incoming International Fellowship OHIO, the European Research Council (ALMA), the Knut and Alice Wallenberg Foundation, the Joint Research Programme ALADIN of Laserlab-Europe II, and the Swedish Research Council.

- [1] P. M. Paul *et al.*, *Science* **292**, 1689 (2001).
- [2] M. Hentschel *et al.*, *Nature* **414**, 509 (2001).
- [3] K. J. Schafer, B. Yang, L. F. DiMauro, and K. C. Kulander, *Phys. Rev. Lett.* **70**, 1599 (1993).
- [4] P. B. Corkum, *Phys. Rev. Lett.* **71**, 1994 (1993).
- [5] M. Lewenstein, P. Balcou, M. Y. Ivanov, A. L'Huillier, and P. B. Corkum, *Phys. Rev. A* **49**, 2117 (1994).
- [6] C. Winterfeldt, C. Spielmann, and G. Gerber, *Rev. Mod. Phys.* **80**, 117 (2008).
- [7] I. J. Kim, C. M. Kim, H. T. Kim, G. H. Lee, Y. S. Lee, J. Y. Park, D. J. Cho, C. H. Nam, *Phys. Rev. Lett.* **94**, 243901 (2005).
- [8] T. T. Liu, T. Kanai, T. Sekikawa, and S. Watanabe, *Phys. Rev. A* **73**, 063823 (2006).
- [9] J. Mauritsson, P. Johnsson, E. Gustafsson, A. L'Huillier, K. J. Schafer, M. B. Gaarde, *Phys. Rev. Lett.* **97**, 013001 (2006).
- [10] J. Mauritsson, P. Johnsson, E. Mansten, M. Swoboda, T. Ruchon, A. L'Huillier, K. J. Schafer, *Phys. Rev. Lett.* **100**, 073003 (2008).
- [11] N. Dudovich *et al.*, *Nature Phys.* **2**, 781 (2006).
- [12] G. Doumy, J. Wheeler, C. Roedig, R. Chirla, P. Agostini, L. F. DiMauro, *Phys. Rev. Lett.* **102**, 093002 (2009).
- [13] J. M. Dahlstrom, T. Fordell, E. Mansten, T. Ruchon, M. Swoboda, K. Klunder, M. Gisselbrecht, A. L'Huillier, J. Mauritsson, *Phys. Rev. A* **80**, 033836 (2009).
- [14] X. He *et al.*, *Phys. Rev. A* **79**, 063829 (2009).
- [15] We assume that there is one dominant trajectory contributing (one saddle point).
- [16] N. Dudovich, J. L. Tate, Y. Mairesse, D. M. Villeneuve, P. B. Corkum, and M. B. Gaarde, *Phys. Rev. A* **80**, 011806(R) (2009).
- [17] K. Varju *et al.*, *J. Mod. Opt.* **52**, 379 (2005).

PAPER XI

Digital In-Line Holography on Amplitude and Phase Objects Prepared with Electron Beam Lithography

J. Schwenke, E. Lorek, R. Rakowski, X. He, A. Kvennefors, A. Mikkelsen, P. Rudawski, C. M. Heyl, I. Maximov, S. G. Pettersson, A. Persson, and A. L'Huillier.

Journal of Microscopy **247**, 196201 (2012).

Digital in-line holography on amplitude and phase objects prepared with electron beam lithography

J. SCHWENKE*, †, E. LOREK*, R. RAKOWSKI*, X. HE*,
A. KVENNEFORS ‡, A. MIKKELSEN §, P. RUDAWSKI*,
C. M. HEYL*, I. MAXIMOV †, S.-G. PETERSSON*,
A. PERSSON* & A. L'HUILLIER*

*Division of Atomic Physics, Lund University, SE-221 00 Lund, Sweden

†MAX-lab, Lund University, SE-221 00 Lund, Sweden

‡Division of Solid State Physics/Nanometer Structure Consortium, Lund University, SE-221 00, Lund, Sweden

§Synchrotron Radiation Research, Lund University, SE-221 00, Lund, Sweden

Key words. Electron beam lithography, high-order harmonic generation, holography, spin-coating, thin films.

Summary

We report on the fabrication and characterization of amplitude and phase samples consisting of well defined Au or Al features formed on ultrathin silicon nitride membranes. The samples were manufactured using electron beam lithography, metallization and a lift-off technique, which allow precise lateral control and thickness of the metal features. The fabricated specimens were evaluated by conventional microscopy, atomic force microscopy and with the digital in-line holography set-up at the Lund Laser Centre. The latter uses high-order harmonic generation as a light source, and is capable of recovering both the shape and phase shifting properties of the samples. We report on the details of the sample production and on the imaging tests with the holography set-up.

Introduction

An ultrashort light pulse in the X-ray regime can penetrate and interact with a structurally intact biological sample or macromolecule to yield a high resolution image, before the sample is destroyed by the very same pulse (Neutze *et al.*, 2000; Bergh *et al.*, 2008). The requirements for such an experiment are stringent: The light pulse needs to be of high intensity, because the interaction efficiency is low, and the tolerable pulse duration is just a few femtoseconds, limited by the onset of the Coulomb explosion caused

by the intense electromagnetic field of the pulse (Howells *et al.*, 2009). To achieve high spatial resolution, and to image biological samples in their natural state, the photon energy needs to be in the X-ray regime. The absorption of X-rays in matter prohibits the use of glass-based lenses and therefore hinders the application of conventional imaging methods. Despite the difficulties, an experimental implementation is by all means feasible, as has been demonstrated by Chapman *et al.* in 2006, in a groundbreaking experiment at the FLASH Free-Electron Laser (FEL) in Hamburg, Germany (Chapman *et al.*, 2006). In this experiment, a test sample was imaged by diffraction with a coherent soft X-ray pulse of 25 femtoseconds (fs) duration. The method used, coherent diffraction imaging (CDI; Chapman & Nugent, 2010), retrieves the diffraction pattern and requires an iterative algorithm to reconstruct an image of the sample, because of the loss of phase information. Coherent diffractive imaging is also used at the Linac Coherent Light Source FEL at the SLAC National Accelerator Laboratory in the United States (Seibert *et al.*, 2011). Although FELs provide an excellent combination of high degree of coherence, short-pulse duration and high intensity, they are large-scale facilities with limited user access. In recent years, laser-based sources have emerged as an alternative. A very promising light source for these kinds of experiments is high-order harmonic generation (McPherson *et al.*, 1987; Ferray *et al.*, 1988), a process which generates coherent light pulses of ultrashort duration in a medium, i.e. inert gas (Krausz & Ivanov, 2009). The short time duration can be used for time-resolved, single-shot measurements such as CDI, and indeed it was shown that the achievable flux is sufficient for this application (Ravasio *et al.*, 2009). Furthermore, the good coherence of the pulse allows for alternative imaging methods that do not require

Correspondence to: Anne L'Huillier, Division of Atomic Physics, Lund University, P.O. Box 118, SE-221 00 Lund, Sweden. Tel: +46-46-222-7661; fax: +46-46-222-4250; e-mail: Anne.LHuillier@fysik.lth.se

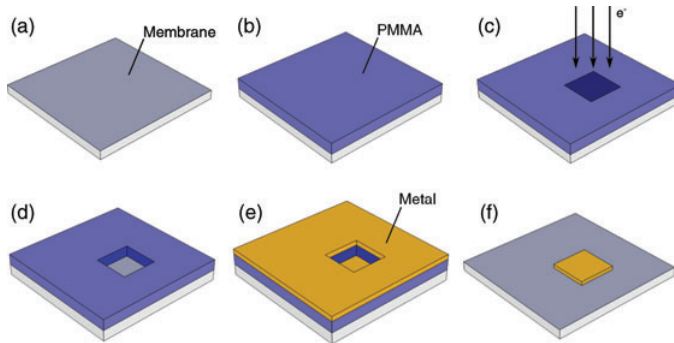


Fig. 1. Schematic of sample fabrication using electron beam lithography (EBL) and lift-off: (a) the membrane is prepared for resist deposition, (b) spin-coating of silicon nitride membrane by PMMA resist, (c) EBL exposure of the resist, (d) removal of the exposed resist in development, (e) thermal evaporation of a thin metal layer and (f) lift-off in acetone to form metal feature.

iterative algorithms to reconstruct an image. In digital in-line holography, the phase information is present in the recorded hologram, and a more direct way of retrieving the object image is available (Gabor, 1948). The method retrieves both the amplitude and phase properties of the sample, and can be used to image a large variety of free-standing objects. Digital in-line holography using high-order harmonic generation has been demonstrated by several groups, including our own (Bartels *et al.*, 2002; Morlens *et al.*, 2006; Genoud *et al.*, 2007). In this paper, we report on the production of test samples for this kind of experiment, in which we used electron beam lithography (EBL) to pattern various materials on ultrathin silicon nitride membranes. Samples on membranes as thin as 20 nm were successfully produced. The method is relevant for all applications that require high transmission in the extreme ultraviolet (XUV) range (30–100 eV). This paper is structured as follows: The next section will describe the sample production in detail as well as the characterization with conventional microscopy. In digital holography section, the holographic imaging set-up is described. The result section shows the experimental results from the produced samples. A summary is given in summary and conclusions section.

Sample fabrication

The patterning of the membrane was performed in the clean room of Lund Nano Lab at the Division of Solid State Physics, Lund University. Before exposure of the membrane in EBL, the sample was spin-coated with a thin layer of polymethyl methacrylate (PMMA). The PMMA layer works as a positive electron beam sensitive resist, i.e. after irradiation by high-energy electrons and development, the resist is locally removed resulting in a well-defined pattern. Subsequent evaporation of a thin metal layer onto the membrane and dissolution of unexposed resist in acetone (lift-off technique) leads to

formation of the metal features with precisely controlled shape and thickness (Broers *et al.*, 1996; Vieu *et al.*, 2000). This approach allows fabrication of metal features with lateral size as small as 15 nm, but in the present work we limit the lateral size to $2 \mu\text{m}$.

In our experiments we used a commercially available EBL system Raith 150 (Raith GmbH, Germany), thermal evaporation tools for deposition of the metal layers as well as Zeiss AxioVision (Carl Zeiss Microimaging GmbH, Göttingen, Germany) optical microscopes for sample inspection. The 20 nm thick, $500 \times 500 \mu\text{m}^2$ large silicon nitride (Si_3N_4) membrane, supported by a solid Si frame up to $3 \times 3 \text{mm}^2$ in size, was bought ready-made from SPI Supplies (Structure Probe, Inc., West Chester, PA, U.S.A.). The sample with the membrane was glued onto a stainless steel support structure using melted indium. For spin coating, the rectangular support structure was temporarily attached to a 2" silicon wafer. The samples were spin-coated with a thin layer of PMMA resist, 950KD, dissolved in anisole. After deposition of the resist and its soft baking, the resist was exposed to the electron beam in the EBL machine using acceleration voltage 20 kV and a dosage of $340 \mu\text{C cm}^{-2}$ for the amplitude object, and $810 \mu\text{C cm}^{-2}$ for the phase object. The exposed PMMA was developed in a mixture of methyl-isobutylketone and isopropanol (MIBK:IPA), rinsed in IPA and nitrogen blow dried. In the following steps, a thin layer of Au or Al was evaporated and carefully lifted-off to make metal features on the silicon nitride membrane. The sample fabrication steps are shown in Figure 1. Microscope images of the samples used in this work are shown in Figure 2. The first example, Figure 2(a), shows a membrane covered with a 20 nm thick layer of gold. The formed pattern consists of squares of varying size, 16, 8, 4 and $2 \mu\text{m}$ side lengths. Figure 2(b) shows the second sample, where the membrane is covered with aluminium in various shapes. This sample is designed to introduce a phase shift to the

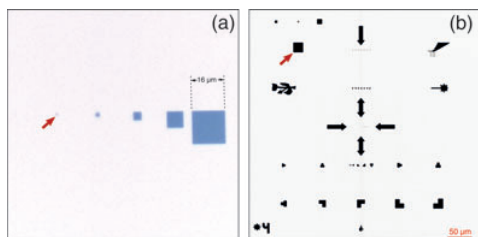


Fig. 2. Sample images taken with an optical microscope. The images were edited to increase the contrast. (a) Layer of Au shaped as squares of varying size. The smallest square with a side length of $2\ \mu\text{m}$ is marked with a red arrow. (b) Layer of Al in various shapes. The red arrow marks the shape used for the phase property measurement. The black arrows are part of the Al layer.

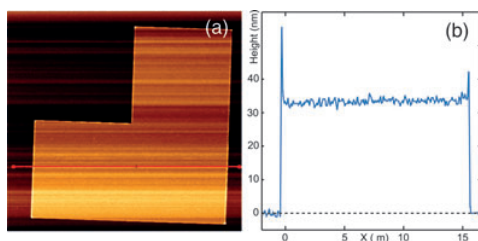


Fig. 3. Details of the phase sample analysed with an atomic force microscope (AFM). (a) Shows a magnified view of one of the produced shapes and (b) shows the height trace along the red line in (a).



Fig. 4. Schematic of the imaging set-up. The XUV pulses from the HHG source are refocused with a Schwarzschild objective (SWO). The focal point is the source for the holography set-up. The hologram is detected with a combination of a microchannel plate (MCP) and a charge-coupled device (CCD) detector.

transmitted XUV pulse. The produced samples were examined with an optical microscope and an electron microscope. The Al sample was also examined with an atomic force microscope (AFM), to measure the thickness of the layer. The layer was determined to be $34\ \text{nm}$ thick (Fig. 3). This method has been demonstrated on Si_3N_4 films before, yet on thicker membranes (Fischbein & Drndic, 2006).

Digital holography

The produced samples were imaged with the digital in-line holography set-up at the Lund Laser Centre, which uses XUV pulses produced in a high-order-harmonic generation (HHG)

set-up. The HHG process takes place when an intense laser pulse is focused into a gas medium. The interaction of the laser pulse with the gas atoms results in the emission of overtones of the fundamental frequency. The laser system used in this experiment operates at a wavelength of $800\ \text{nm}$, and Ar is used as a target medium. The generated spectrum reaches into the extreme ultraviolet regime, up to the 29th harmonic at $27.6\ \text{nm}$. More details on the HHG set-up can be found in He *et al.* (He *et al.*, 2009). The XUV pulse is refocused tightly, to get a divergent pulse for the in-line holography scheme (Fig. 4, see Schwenke *et al.*, 2008 for more details). The samples are imaged in transmission, which means that the beam must transmit through the membrane to interact with the sample layer. This requires a sufficient transmittance of the membrane for the XUV. During the experiment, a transmittance of about 46% at $38\ \text{nm}$ wavelength was measured. The photon flux from the source of about 3×10^{10} photons per pulse per harmonic (He *et al.*, 2009) allow for single-shot imaging, as has been demonstrated previously (Schwenke *et al.*, 2008). The quality of the holograms is, however, improved by acquiring an image during a few seconds, about 30 shots at a $10\ \text{Hz}$ repetition rate.

The fringes of the hologram reveal both the spatial composition of the diffracted light as well as the phase shift relative to the reference part of the beam. A reconstruction of the field in the sample plane can be achieved by applying a numerical algorithm to the recorded hologram. A detailed description of the algorithm can be found in Genoud *et al.* (Genoud *et al.*, 2007). Of particular interest in this work is the correction for the twin-image blurring, which arises from the ambiguity of the interference fringes in the hologram. We apply an iterative algorithm suggested by Litychevskaia and Fink (Litychevskaia & Fink, 2007), which successively recovers the phase information lost in the recording process. This improves the contrast of the reconstructed object image, and can potentially yield the true values of the complex object properties. The spatial resolution of the reconstructed images is limited, because information can only be obtained in the overlap region between the reference wave and the object wave, which is restricted by the divergence of the source. In this set-up, the limit for the spatial resolution is calculated to be about $1.2\ \mu\text{m}$.

Results

The sample production method allows for a wide range of different designs and materials to be used. For this work, various sample structures made of single layers of Au ($20\ \text{nm}$ thickness) or Al ($21.7\ \text{nm}$; and also Cr, $26.7\ \text{nm}$) were produced. A double-layer sample of Au ($15.1\ \text{nm}$) and Ni ($6\ \text{nm}$) was produced as well. Here Ni served as an adhesive to the silicon nitride membrane. We found that once a proper handling protocol was in place, the lithographic process could reliably be applied on membranes as thin as $20\ \text{nm}$. Variations

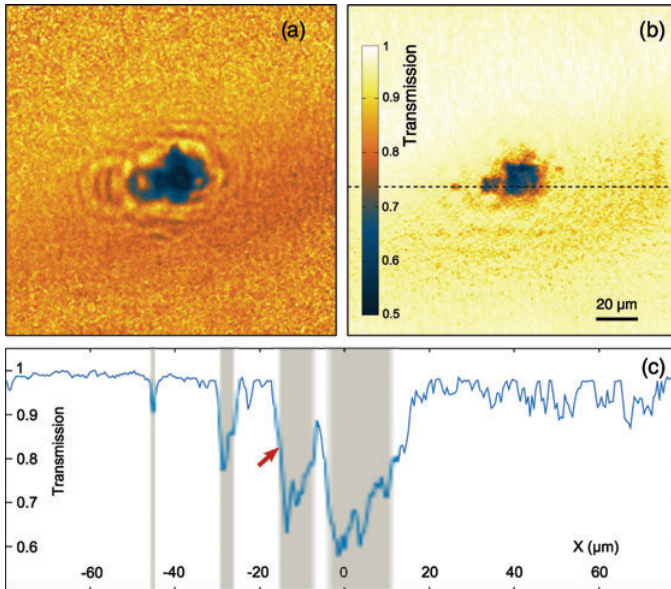


Fig. 5. Experimental hologram and reconstruction of a detail of the sample seen in Figure 2(a). (a) The recorded hologram. (b) The reconstructed transmission. (c) The data along the line in (b). The shaded areas show the position of the squares in (b). The edge marked with the arrow was used for determining the spatial resolution.

of the quality of the produced structures were not observed, yet a systematic study was not performed.

The sample shown in Figure 2(a) was used to determine the spatial resolution of the holography set-up. Figure 5 shows the results from the holography imaging. The first image, Figure 5(a) shows the recorded hologram, although Figure 5(b) shows the reconstructed transmission function. Figure 5(c) shows the data along the line in Figure 5(b). The spatial resolution was determined to be $1.5 \mu\text{m}$, measured at the edge indicated with the arrow. Here the resolution was defined as the lateral distance covered by 60% of the full height of the edge. The given number represents the highest achieved spatial resolution. A comparison of the measured edge with other edges shows, that not all edges are resolved equally well. The resolution varies throughout the image, mainly because of artefacts in the recorded holograms, but also because of a reduced signal-to-noise ratio at the edge of the beam. Note that the $2 \mu\text{m}$ sized square is visible in Figure 5(c).

Figure 6 shows the reconstructed object images for the phase sample. The large square seen in Figure 2(b) was imaged. Although Figure 6(a) shows the recorded hologram, Figure 6(b) shows the reconstructed phase shift and Figure 6(c) shows the data along the line in Figure 6(b). The calculated transmittance is 90%, and the estimated phase shift through

the aluminum is 0.51 rad, for 38 nm radiation. The measured transmittance is 87%, and the measured phase shift is 0.57 rad, calculated as the mean values of the complex modulus and phase angle in the area covered by the object in the reconstructed image. The measured transmission and phase shift agree well with the expected values. Figure 6(c) shows the data along the line in Figure 6(b) before applying the iterative algorithm (blue dashed line) and after 300 iterations (orange line). Further iterations do not improve the contrast, but increase the noise in the image and add artefacts. After applying the iterative algorithm, the contrast is significantly enhanced, and the phase shift is similar to the expected value. However, both the two-dimensional image and the line-out show a large amount of noise. The success of the iterative phase retrieval, and the quantitative reconstruction of the object properties, relies strongly on the stability of the source.

Summary and conclusions

We have demonstrated a method to produce arbitrary shapes and layer compositions on ultrathin silicon nitride membranes. The produced objects were used to demonstrate digital in-line holography with a HHG source. The reconstructed images match closely the sample specification.

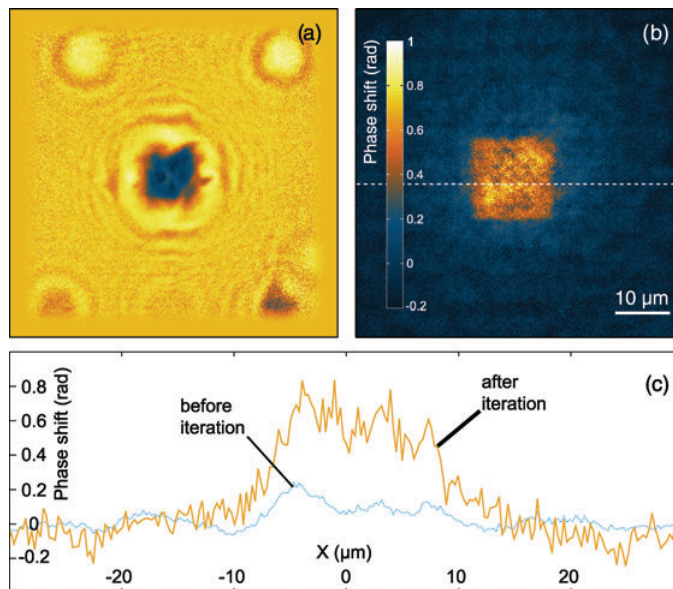
200 J. SCHWENKE *ET AL.*

Fig. 6. Experimental hologram and reconstruction of a detail of the sample seen in Figure 2(b). (a) The recorded hologram. (b) The reconstructed phase shift. (c) The data along the line in (b). The two lines show the reconstructed phase shift before (blue dashed) and after (orange) application of the iterative algorithm.

The spatial resolution is limited because of the numerical aperture of the XUV focusing optics. The iterative process increases the image quality by enhancing the contrast and removing contributions from the twin image. The remaining image distortions can be removed by better optics which less aberrations, and by improving the pointing stability of the laser and the mechanical stability of the experimental set-up.

Acknowledgements

This research was supported by the European Research Council (Advanced grant ALMA), the Marie Curie Early Stage Training Site (MAXLAS), the Marie Curie Initial Training Network ATTOFEL, the joint research activity ALADIN of Laserlab-Europe, the Knut and Alice Wallenberg Foundation and the Swedish Research Council. Partial support from the Nanometer Structure Consortium at Lund University (nmC@LU) is greatly appreciated. We would also like to thank Ulf Håkansson for helping with the AFM.

References

- Bartels, R.A., Paul, A., Green, H. *et al.* (2002) Generation of spatially coherent light at extreme ultraviolet wavelengths. *Science* **297**, 376–378.
- Bergh, M., Huldt, G.S., Tmneanu, N., Maia, F.R.N.C. & Hajdu, J. (2008) Feasibility of imaging living cells at subnanometer resolutions by ultrafast X-ray diffraction. *Q. Rev. Biophys.* **41**, 181–204.
- Broers, A., Hoole, A. & Ryan, J. (1996) Electron beam lithography—resolution limits. *Microelectron. Eng.* **32**, 131–142.
- Chapman, H.N. & Nugent, K.A. (2010) Coherent lensless X-ray imaging. *Nat. Photon.* **4**, 833–839.
- Chapman, H.N., Barty, A., Bogan, M.J. *et al.* (2006) Femtosecond diffractive imaging with a soft-X-ray free-electron laser. *Nat. Phys.* **2**, 839–843.
- Ferray, M., Huillier, A.L., Li, X.F., Lompre, L.A., Mainfray, G. & Manus, C. (1988) Multiple-harmonic conversion of 1064 nm radiation in rare gases. *J. Phys. B-At. Mol. Opt.* **21**, L31–L35.
- Fischbein, M.D. & Drndic, M. (2006) Nanogaps by direct lithography for high-resolution imaging and electronic characterization of nanostructures. *Appl. Phys. Lett.* **88**, 063116-1-063116-3.
- Gabor, D. (1948) A new microscopic principle. *Nature* **161**, 777–778.

- Genoud, G., Guilbaud, O., Mengotti, E., Pettersson, S.-G., Georgiadou, E., Pourtal, E., Wahlström, C.-G. & L'Huillier, A. (2007) XUV digital in-line holography using high-order harmonics. *App. Phys. B-Lasers O.* **90**, 533–538.
- He, X., Miranda, M., Schwenke, J. *et al.* (2009) Spatial and spectral properties of the high-order harmonic emission in argon for seeding applications. *Phys. Rev. A* **79**, 063829-1-063829-7.
- Howells, M.R., Beetz, T., Chapman, H.N. *et al.* (2009) An assessment of the resolution limitation due to radiation-damage in X-ray diffraction microscopy. *J. Electron Spectrosc.* **170**, 4–12.
- Krausz, F. & Ivanov, M. (2009) Attosecond physics. *Rev. Modern Phys.* **81**, 163–234.
- Latychevskaia, T. & Fink, H.-W. (2007) Solution to the twin image problem in holography. *Phys. Rev. Lett.* **98**, 233901-1-233901-4.
- McPherson, A., Gibson, G., Jara, H., Johann, U., Luk, T.S., McIntyre, I.A., Boyer, K. & Rhodes, C.K. (1987) Studies of multiphoton production of vacuum-ultraviolet radiation in the rare gases. *J. Opt. Soc. Am. B* **4**, 595–601.
- Morlens, A.-S., Gautier, J., Rey, G. *et al.* (2006) Submicrometer digital in-line holographic microscopy at 32 nm with high-order harmonics. *Opt. Lett.* **31**, 3095–3097.
- Neutze, R., Wouts, R., van der Spoel, D., Weckert, E. & Hajdu, J. (2000) Potential for biomolecular imaging with femtosecond X-ray pulses. *Nature* **406**, 752–757.
- Ravasio, A., Gauthier, D., Maia, F.R.N.C. *et al.* (2009) Single-shot diffractive imaging with a table-top femtosecond soft X-ray laser-harmonics source. *Phys. Rev. Lett.* **103**, 028104-1-028104-5.
- Schwenke, J., Mai, A., Miranda, M. *et al.* (2008) Single-shot holography using high-order harmonics. *J. Mod. Optic.* **55**, 2723–2730.
- Seibert, M.M., Ekeberg, T., Maia, F.R.N.C. *et al.* (2011) Single mimivirus particles intercepted and imaged with an X-ray laser. *Nature* **470**, 78–81.
- Vieu, C., Carcenac, F., Pépin, A. *et al.* (2000) Electron beam lithography: resolution limits and applications. *Appl. Surf. Sci.* **164**, 111–117.

PAPER XII

Macroscopic Phase Effects in Noncollinear High-Order Harmonic Generation

C. M. Heyl, P. Rudawski, F. Brizuela, J. Mauritsson and A. L'Huillier.
Physical Review Letters **112**, 143902 (2014).

Macroscopic Effects in Noncollinear High-Order Harmonic Generation

C. M. Heyl,* P. Rudawski, F. Brizuela, S. N. Bengtsson, J. Mauritsson, and A. L'Huillier

Department of Physics, Lund University, P.O. Box 118, SE-221 00 Lund, Sweden

(Received 12 September 2013; published 7 April 2014)

We study two-color high-order harmonic generation using an intense driving field and its weak second harmonic, crossed under a small angle in the focus. Employing sum- and difference-frequency generation processes, such a noncollinear scheme can be used to measure and control macroscopic phase matching effects by utilizing a geometrical phase mismatch component, which depends on the noncollinear angle. We further show how spatial phase effects in the generation volume are mapped out into the far field allowing a direct analogy with temporal carrier envelope effects in attosecond pulse generation.

DOI: 10.1103/PhysRevLett.112.143902

PACS numbers: 42.65.Ky, 42.65.Re

High-order harmonic generation (HHG) in gases using multicolor optical fields is becoming a common tool in attosecond science. Multicolor HHG has been implemented by mixing the fundamental field with waves at low harmonic [1–3] and at incommensurate [4,5] frequencies. Other schemes employ attosecond pulse trains mixed with the fundamental field [6] as well as synthesized light transients [7] for driving the HHG process. The control and flexibility brought about by using two or more driving fields is used, for example, to improve the efficiency of the generation process [3,8], to monitor the single atom response [9,10], and to implement gating techniques [11]. High-order wave mixing can further be beneficial for achieving phase matching [1,12–15].

Using multiple optical driving fields also allows for noncollinear geometries. This concept, used extensively in low-order frequency conversion processes such as optical parametric amplification, has barely been applied to attosecond science. In an early work, Birulin and co-workers [16] addressed theoretically the general concept of HHG in a noncollinear geometry. By mixing the fundamental and a weak second harmonic at an angle, Bertrand and co-workers [17] demonstrated the spatial separation of multiple extreme ultraviolet (XUV) beams corresponding to different sets of absorbed photon numbers from the two fields. A similar scheme was recently used [18] for reconstructing the spatiotemporal characteristics of the generated attosecond pulses. Other authors [19–21] concentrated on noncollinear sum-frequency generation (SFG) processes driven by two identical laser fields. Such a scheme allows for separation of the harmonics from the fundamental but suffers from phase matching problems.

In this Letter, we theoretically and experimentally examine the influence of noncollinear geometries in HHG, analyzing in detail the macroscopic aspects. We show for the first time, to our knowledge, how a weak noncollinear field can be used as a probe to monitor and control phase matching. We show that difference-frequency generation (DFG), where a photon (or several photons) is emitted in the conversion process, is in general more favorable than SFG [22], which becomes very inefficient with increasing noncollinear angle. This leads to the counterintuitive result that the XUV radiation is dominantly emitted outside the angle sector defined by the two driving

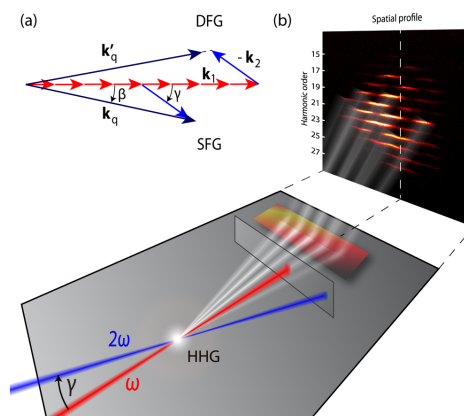


FIG. 1 (color online). (a) Wave vector representation of noncollinear wave mixing. (b) Schematic setup: a red (800 nm) and a blue (400 nm) laser beam are focused in a noncollinear geometry, resulting in the emission of spatially separated high-order harmonic beams. The depicted spectrum is a measured experimental microchannel plate image recorded at $\gamma \approx 2$ mrad and resampled for a linear energy scale. The noncollinear angle (γ) is exaggerated in this illustration.

Published by the American Physical Society under the terms of the Creative Commons Attribution 3.0 License. Further distribution of this work must maintain attribution to the author(s) and the published article's title, journal citation, and DOI.

fields. Our analysis is illustrated in an experiment where high-order harmonics are generated in argon using a high-energy 800 nm laser and its weak second harmonic, crossed under a noncollinear angle of a few mrad (Fig. 1). We identify two important regimes for noncollinear HHG: (i) the generation at noncollinear angles large enough to allow a direct spatial separation of all photon pathways leading to the same final energy [17] and (ii) the generation at smaller noncollinear angles leading to spatially resolved interferences between adjacent photon pathways. At large angles, our noncollinear generation scheme provides the functionality of an all-optical beam splitter, delivering multiple, angularly separated XUV beams. At small angles, the observed spatial interferences directly reflect the harmonic phase variation across the focal plane.

Noncollinear high-order harmonic generation illustrates beautifully the two fundamentally different but equivalent concepts of light, waves or photons. Both concepts are very useful for understanding the underlying principles and will therefore be used alternately in the discussion throughout this Letter. We begin by explaining the main features of noncollinear HHG resulting from the field distribution in the focal plane, followed by a more quantitative description including propagation effects.

In the photon picture, the combination of two laser fields with central frequencies ω_1 and ω_2 leads to radiation with frequency $\omega_q = m_1\omega_1 + m_2\omega_2$, where m_1 and m_2 are integers. Without loss of generality m_1 can be chosen to be positive and m_2 positive or negative, accounting for sum- and difference-frequency generation processes, respectively. The emission angle β of the generated radiation, measured from the propagation axis of the ω_1 field, can be deduced through k -vector addition and defined by the unit vector of the generated field [23] $\hat{\mathbf{k}}_q = (m_1\mathbf{k}_1 + m_2\mathbf{k}_2) / \|(m_1\mathbf{k}_1 + m_2\mathbf{k}_2)\|$ [Fig. 1(a)]. Throughout the Letter we use small angle approximations.

We consider the case of a fundamental beam and its second harmonic, i.e., $\omega_1 = \omega$ and $\omega_2 = 2\omega$. The generated frequencies are $\omega_q = q\omega$ with $q = m_1 + 2m_2$, where the net number of photons absorbed $m = m_1 + m_2$ has to be odd in order to satisfy parity conservation. Denoting by γ the angle between \mathbf{k}_1 and \mathbf{k}_2 , β can be approximated as

$$\beta(q, m_2) \approx \frac{2m_2}{q} \gamma, \quad m_2 = \begin{cases} \pm 1, 3, \dots & \text{if } q \text{ is even} \\ \pm 0, 2, \dots & \text{if } q \text{ is odd} \end{cases} \quad (1)$$

For sufficiently large γ , the number of ω_2 photons defines a unique emission angle so that all driving photon combinations that lead to the same final energy are spatially separated in the far field. A pattern of harmonic beams can then be detected for each harmonic order, as illustrated in Fig. 2(a). For small noncollinear angles such that $\Delta\beta_q = \beta(q, m_2 + 2) - \beta(q, m_2) < \Theta_q$, where Θ_q is the divergence angle of a single harmonic beam, the

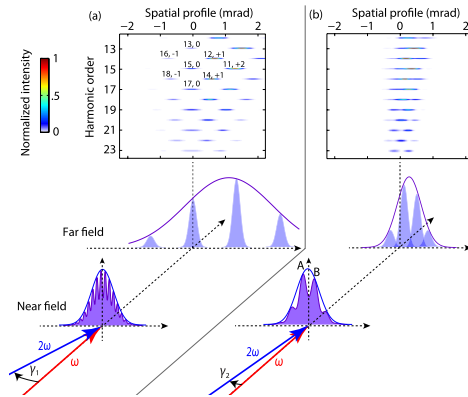


FIG. 2 (color online). Illustration of the interference concept: spatially resolved harmonic spectra as well as near- and far-field intensity distributions for a given harmonic order. (a) $\Delta\beta_q > \Theta_q$ and (b) $\Delta\beta_q < \Theta_q$. The spatial distribution of the high-order harmonic emission in the far field is defined by the interference grating in the focus representing multiple harmonic sources, determining intensity and phase of the emitted harmonics. The displayed far-field spectra were calculated using the strong field approximation, considering $\gamma = 5$ mrad (a) and $\gamma = 1.5$ mrad (b) with $I_{2\omega}/I_\omega = 0.05$ and $I_\omega = 2 \times 10^{14}$ W/cm², where I_ν denotes the focus intensity at central frequency ν .

harmonic beams with different m_2 orders can partly overlap spatially and interfere [Fig. 2(b)], as discussed in more detail later. The intensities of the two driving fields determine the probability for up-converting photons from one or the other driving field and define therefore the envelope position and width of the pattern in the far field. For the case of a weak ω_2 field, harmonic emission occurs at small angles around \mathbf{k}_1 and only low m_2 orders can be expected. For a given harmonic order q , an m_2 order will be separated from the ω beam if $\gamma \geq q/4f_\#m_2$, where $f_\# = f/D$ is the f number of the ω beam focused with a focal length f and with an initial beam diameter D .

From a wave perspective, the generated far-field pattern can be understood as the interference of multiple harmonic sources. These sources are created by the interference of the two driving fields, as illustrated in Fig. 2. The modulation of amplitude and phase of the ω - 2ω -driving field across the focal plane leads to an amplitude and phase modulation of the dipole oscillating at a given harmonic frequency. Note that the harmonic grating persists over the pulse duration while the intensity modulation at the fundamental frequencies is smeared out in time. All features of the far-field pattern mentioned above can be explained with this concept: the nonlinearity of the process determines the harmonic intensity

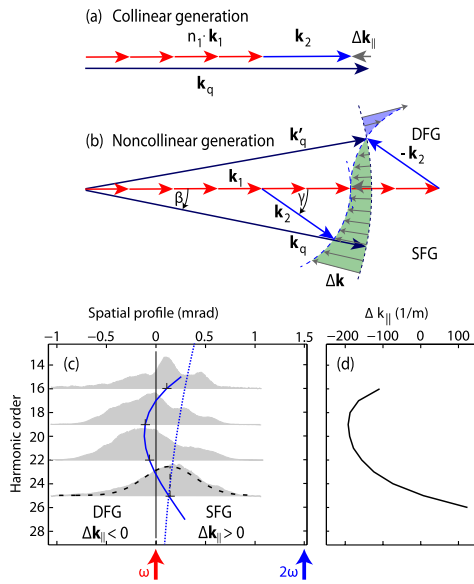


FIG. 3 (color online). (a),(b) Schematic phase matching scheme for noncollinear ω - 2ω HHG. In conditions where a phase mismatch is present for a collinear generation geometry (here illustrated for a negative $\Delta\mathbf{k}_{\parallel}$ on the optical axis), it is possible to find a corresponding noncollinear geometry at which the total phase mismatch is zero (e.g., considering DFG in the displayed scheme). The shaded areas indicate a negative (green) and positive (blue) $\Delta\mathbf{k}$. (c) Measured harmonic spatial profile averaged over the relative phase between the ω and 2ω fields for $\gamma \approx 1.5$ mrad: the solid blue line indicates the approximate center of the spatial profiles; the dotted blue line marks the calculated center of the harmonic beams in the absence of propagation effects. The two arrows mark the propagation directions of the ω and the 2ω beams. (d) Extracted wave vector mismatch $\Delta\mathbf{k}_{\parallel}$.

distribution in the focal plane and therefore the width of the envelope over the spatial distribution in the far field. The relative intensity of the two driving fields influences the phase of the source grid, which determines the position of the envelope in the far field.

Phase matching in HHG can be analyzed by adding the relevant wave vectors, as illustrated in Figs. 3(a) and 3(b). The total k -vector mismatch [24] for noncollinear HHG can be expressed as

$$\Delta\mathbf{k} = \Delta\mathbf{k}_{\parallel} + \Delta\mathbf{k}_{<},$$

$$\text{with } \Delta\mathbf{k}_{<} = m_2 \gamma^2 \underbrace{\left(\frac{2m_2}{q} - 1 \right)}_{<0} \frac{\omega}{c} \hat{\mathbf{k}}_q, \quad (2)$$

where $\Delta\mathbf{k}_{\parallel}$ is the k -vector mismatch corresponding to the collinear generation geometry [Fig. 3(a)] while $\Delta\mathbf{k}_{<}$ is the geometrical offset added by the noncollinear geometry. Considering a certain m_2 , phase matching ($\Delta\mathbf{k} = 0$) can be achieved by choosing the right angle γ . $\Delta\mathbf{k}_{<}$ is positive or negative depending on the sign of m_2 , i.e., on whether we consider DFG or SFG [Fig. 3(b)]. $\Delta\mathbf{k}_{\parallel}$ can be written as a sum of four components [25]: the wave vector mismatch due to the geometrical Gouy phase, two components that arise from dispersion in the partially ionized medium, and a contribution due to the intensity-dependent dipole phase. A limiting factor is ionization, which is intrinsically required for HHG but strongly reduces the efficiency due to the negative phase mismatch induced by plasma dispersion. Additionally, the Gouy phase can lead to a significant negative phase mismatch especially in the case of a tight focus or high harmonic orders. In both cases, the resulting negative $\Delta\mathbf{k}_{\parallel}$ can be compensated by a positive $\Delta\mathbf{k}_{<}$. In these conditions high harmonic emission driven by noncollinear DFG can dominate over noncollinear SFG. In the absence of propagation effects and for a weak perturbing 2ω field, the harmonic spatial profile is strongest at $\beta = 0$ ($m_2 = 0$) [17]. If the far-field pattern is predominantly emitted outside the angle sector defined by the two driving fields (as in Fig. 1), DFG dominates, indicating that $\Delta\mathbf{k}_{\parallel}$ is negative. If the emission maximum is located inside this angle sector, SFG dominates and $\Delta\mathbf{k}_{\parallel}$ is positive. Not only the sign, but also the magnitude of $\Delta\mathbf{k}_{\parallel}$ can be estimated as shown by the analysis of our experimental results presented below.

We performed experiments using a high-energy 40 fs Ti:sapphire laser system operating at a 10 Hz repetition rate [26]. The second harmonic field, with a pulse energy corresponding to 5% of the fundamental, was generated in one arm of a phase-stable Michelson-like interferometer and loosely focused together with the fundamental field into an argon gas cell ($f_{\#} \approx 200$). The interferometer allowed us to spatially displace the two beams so they could be focused with a small angle relative to each other. The generated harmonics were analyzed by an XUV spectrometer with an entrance slit and recorded by a microchannel plate detector. Our experimental conditions are chosen to strongly favor HHG emission from the short trajectory [26]. Due to the small angle, the beams corresponding to different m_2 orders interfere [case (b) in Fig. 2], and the spatial distribution in the far field depends on ϕ , the relative phase between the ω and the 2ω fields. Figure 4(a) shows a single shot harmonic spectrum recorded with $\gamma \approx 1.5$ mrad. Figure 3(c) presents the corresponding spatial intensity distributions for four harmonic orders, averaged over ϕ . The solid blue line in Fig. 3(c) shows that the center of the far-field distribution, obtained by fitting Gaussian envelopes to the experimental data, varies with harmonic order. In order to deduce the effect of phase matching from the spatial distribution, the ω -beam

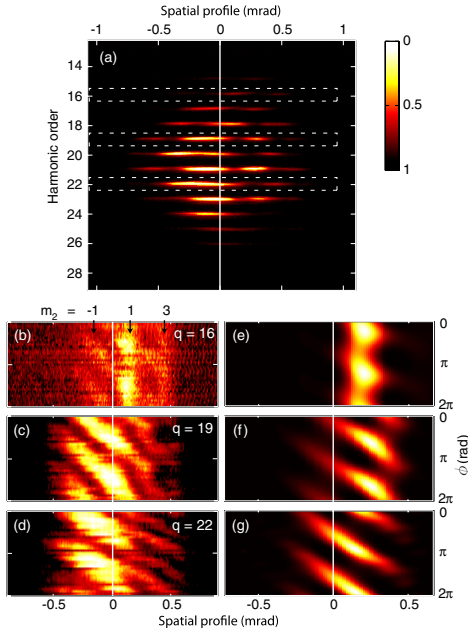


FIG. 4 (color online). (a) Single shot experimental harmonic spectrum generated in the same conditions as shown in Fig. 3(c). The dashed white lines indicate the region displayed spectrally integrated and normalized as a function of ϕ in (b)–(d). Corresponding SFA results are shown in (e)–(g). Note that the center of the spatial distribution is shifted compared to the experimentally measured patterns since propagation effects are not included in the simulations.

direction cannot be used as a reference, since the 2ω -field intensity is not negligible in our experimental conditions. Instead we calculate this reference [dotted blue line in Fig. 3(c)] using numerical simulations based on the strong field approximation (SFA), accounting for the noncollinear overlap of the two driving fields but neglecting propagation effects (see the Supplemental Material [27]). Experimentally, we clearly observe a dominant contribution on the left side from the reference direction, for most harmonic orders, which we relate to a dominant DFG contribution in our experimental conditions. The offset between the experimental beam centers and the SFA results allows us to deduce an approximate value for the effective $\Delta\mathbf{k}_{\parallel}$ as shown in Fig. 3(d) (see the Supplemental Material [27]).

Finally, we examine in more detail noncollinear HHG at small crossing angles and analyze the influence of interference effects on the harmonic spatial profile. Figures 4(b)–4(d) show the far-field profiles for harmonics 16, 19, and 22 as a function of ϕ . The position of the spatial

fringes varies periodically with ϕ and this variation becomes more pronounced as the harmonic order increases. This can be understood within the wave model: the harmonics generated at different source locations in the focal plane [e.g., A and B in Fig. 2(b)] interfere in the far field, and the interference pattern depends on their relative phase. The main contribution to this phase difference is due to the single atom response and can be expressed as $\Delta\varphi_s = \alpha_q(I_A - I_B)$, where $\alpha_q I$ denotes the harmonic dipole phase [28] at a corresponding driving field intensity I . When the phase ϕ is varied, the harmonic intensity grating in the focus moves across the focal plane and the difference between I_A and I_B changes. Consequently, the interference fringes in the far-field shift as clearly visible in Figs. 4(c) and 4(d). The slope reveals the dipole phase dependence on the intensity, which is small for low harmonic orders and increases with order, as expected for the short trajectory contribution [29]. Results from our SFA simulations, shown in Figs. 4(e)–4(g), reproduce fairly well the main features of the experimental interference patterns. The differences in width and shape of the spatial profiles (and consequently in the slope of the fringe pattern) can be explained by deviation from Gaussian optics including possible asymmetries of the fundamental beam shape in the focus as well as ionization effects leading to additional spatial broadening.

There is a clear analogy between the presented spatial phase effects and carrier envelope phase (CEP) dependent spectral fringes in HHG. Attosecond pulses are generated by a short fundamental pulse at a few instants in time, e.g., t_a and t_b at the corresponding driving field intensities I_a, I_b . The harmonic spectrum is a consequence of the interference between these pulses. Similarly to the spatial interference effect discussed above, the spectral interference pattern depends on the relative phase $\Delta\varphi_t = \alpha_q(I_a - I_b)$, which changes with CEP [30,31].

In summary, we have theoretically and experimentally investigated noncollinear HHG, focusing on the macroscopic aspects of the generation process. We have shown how a noncollinear second harmonic field can be used to probe phase matching by utilizing a geometrical phase mismatch component, introduced by the noncollinear geometry. Using difference-frequency generation processes, this component can be advantageous for phase-matched generation in a partly ionized medium. We further identify different noncollinear angle regimes leading either to well separated harmonic beams or to spatial interference structures in the far-field spectrum. These interferences are the spatial analog of temporal interference structures in attosecond pulse generation with few cycle pulses.

This research was supported by the Marie Curie program ATTOFEL (ITN), the European Research Council (ALMA), the Swedish Research Council, the Swedish Foundation for Strategic Research, and the Knut and Alice Wallenberg Foundation.

- *Corresponding author.
christoph.hey1@fysik.lth.se
- [1] H. Eichmann, S. Meyer, K. Riepl, C. Momma, and B. Wellegehausen, *Phys. Rev. A* **50**, R2834 (1994).
- [2] S. Watanabe, K. Kondo, Y. Nabekawa, A. Sagisaka, and Y. Kobayashi, *Phys. Rev. Lett.* **73**, 2692 (1994).
- [3] F. Brizuela, C. M. Heyl, P. Rudawski, D. Kroon, L. Rading, J. M. Dahlström, J. Mauritsson, P. Johnsson, C. L. Arnold, and A. L'Huillier, *Sci. Rep.* **3**, 1410 (2013).
- [4] M. B. Gaarde, P. Antoine, A. Persson, B. Carré, A. L'Huillier, and C.-G. Wahlström, *J. Phys. B* **29**, L163 (1996).
- [5] T. Pfeifer, L. Gallmann, M. J. Abel, P. M. Nagel, D. M. Neumark, and S. R. Leone, *Phys. Rev. Lett.* **97**, 163901 (2006).
- [6] A. Heinrich, W. Kornelis, M. P. Ancombe, C. P. Hauri, P. Schlup, J. Biegert, and U. Keller, *J. Phys. B* **39**, S275 (2006).
- [7] A. Wirth *et al.*, *Science* **334**, 195 (2011).
- [8] I. J. Kim, C. Kim, H. Kim, G. Lee, Y. Lee, J. Park, D. Cho, and C. Nam, *Phys. Rev. Lett.* **94**, 243901 (2005).
- [9] N. Dudovich, O. Smirnova, J. Levesque, Y. Mairesse, M. Yu. Ivanov, D. M. Villeneuve, and P. B. Corkum, *Nat. Phys.* **2**, 781 (2006).
- [10] D. Shafir, H. Soifer, B. D. Bruner, M. Dagan, Y. Mairesse, S. Patchkovskii, M. Yu. Ivanov, O. Smirnova, and N. Dudovich, *Nature (London)* **485**, 343 (2012).
- [11] J. Mauritsson, P. Johnsson, E. Gustafsson, A. L'Huillier, K. Schafer, and M. Gaarde, *Phys. Rev. Lett.* **97**, 013001 (2006).
- [12] R. Hilbig and R. Wallenstein, *Appl. Opt.* **21**, 913 (1982).
- [13] P. Shkolnikov, A. Kaplan, and A. Lago, *Opt. Lett.* **18**, 1700 (1993).
- [14] S. Meyer, H. Eichmann, T. Menzel, S. Nolte, B. Wellegehausen, B. Chichkov, and C. Momma, *Phys. Rev. Lett.* **76**, 3336 (1996).
- [15] O. Cohen, T. Popmintchev, D. Gaudiosi, M. Murnane, and H. Kapteyn, *Phys. Rev. Lett.* **98**, 043903 (2007).
- [16] A. V. Birulin, V. T. Platonenko, and V. V. Strelkov, *Quantum Electron.* **26**, 377 (1996).
- [17] J. Bertrand, H. J. Wörner, H.-C. Bandulet, É. Bisson, M. Spanner, J.-C. Kieffer, D. M. Villeneuve, and P. B. Corkum, *Phys. Rev. Lett.* **106**, 023001 (2011).
- [18] K. Kim, C. Zhang, A. D. Shiner, S. E. Kirkwood, E. Frumker, G. Gariepy, A. Naumov, D. M. Villeneuve, and P. B. Corkum, *Nat. Phys.* **9**, 159 (2013).
- [19] S. V. Fomichev, P. Breger, B. Carré, P. Agostini, and D. F. Zaretsky, *Laser Phys.* **12**, 383 (2002).
- [20] J. Wu and H. Zeng, *Opt. Lett.* **32**, 3315 (2007).
- [21] A. Ozawa, A. Vernaleken, W. Schneider, I. Gotlibovych, Th. Udem, and T. W. Hänsch, *Opt. Express* **16**, 6233 (2008).
- [22] We emphasize that a geometrical phase mismatch introduced by the noncollinear generation geometry leads to enhanced DFG emission, which is different from earlier results that show dominating DFG emission due to dispersion effects in collinear geometries [15].
- [23] Strictly speaking, this definition is an approximation, neglecting phase matching effects which can lead to a modified emission direction especially for large noncollinear angles and in the presence of radial field gradient vectors [32] caused e.g., by the intensity dependent dipole phase.
- [24] We define the k -vector mismatch as the difference in k vectors between fundamental and harmonic fields, e.g., $q\mathbf{k}_1 - \mathbf{k}_q$.
- [25] S. Kazamias, D. Douillet, F. Weihe, C. Valentin, A. Rousse, S. Sebban, G. Grillon, F. Augé, D. Hulin, and Ph. Balcou, *Phys. Rev. Lett.* **90**, 193901-1 (2003).
- [26] P. Rudawski *et al.*, *Rev. Sci. Instrum.* **84**, 073103 (2013).
- [27] See Supplemental Material at <http://link.aps.org/supplemental/10.1103/PhysRevLett.112.143902> for a description of the numerical SFA model as well as for details on the extraction of the effective k -vector mismatch.
- [28] M. Lewenstein, K. Kulander, K. Schafer, and P. Bucksbaum, *Phys. Rev. A* **51**, 1495 (1995).
- [29] K. Varjú *et al.*, *J. Mod. Opt.* **52**, 379 (2005).
- [30] E. Mansten *et al.*, *Phys. Rev. Lett.* **102**, 083002 (2009).
- [31] G. Sansone *et al.*, *Phys. Rev. A* **80**, 063837 (2009).
- [32] P. Balcou, P. Salières, A. L'Huillier, and M. Lewenstein, *Phys. Rev. A* **55**, 3204 (1997).

Supplementary information for "Macroscopic Effects in Noncollinear High-Order Harmonic Generation"

C. M. Heyl, P. Rudawski, F. Brizuela, S. N. Bengtsson, J. Mauritsson, and A. L'Huillier

This supplementary information contains:

- A. a description of the model used for the numerical simulations,
- B. a derivation of the method used to extract an effective wave vector mismatch.

A. Numerical simulations of the noncollinear HHG process

We perform two-dimensional calculations in order to simulate HHG using a noncollinear geometry. The single atom response was obtained by solving the time dependent Schrödinger Equation within the strong field approximation. The quasi-classical action for the electron motion in the continuum

$$S(\vec{p}, t, t_0) = \int_{t_0}^t dt' \left(\frac{[\vec{p} - e\vec{A}(t')]^2}{2m} + I_p \right) \quad (1)$$

is calculated for the vector potential \vec{A} of the combined fundamental and second harmonic field. I_p , m and e denote ionization potential, electron mass and charge, respectively. t_0 and t are tunneling and recombination times for an electron with canonical momentum \vec{p} . The laser induced dipole [1] was calculated by evaluating the integral:

$$\begin{aligned} x(t) = i \int_0^\infty d\tau \left(\frac{\pi}{\epsilon + i\tau/2} \right)^{3/2} & d_x^*(p_{st}(t, \tau) - A_x(t)) \\ & \times \exp[-iS_{st}(t, \tau)/\hbar] F(\tau) \\ & \times d_x(p_{st}(t, \tau) - A_x(t - \tau)) E(t - \tau) + c.c., \end{aligned} \quad (2)$$

considering a stationary phase approximation over momentum, with $p_{st}(t, \tau) = [E(t) - E(t - \tau)]/\tau$, where $\tau = t - t_0$ is the excursion time in the continuum. In accordance with our experimental conditions, the short trajectory contribution was selected via a filter function: $F(\tau) \approx 1$ for $\tau < 0.65T$ and $F(\tau) \approx 0$ for $\tau > 0.65T$, where $0.65T$ corresponds to the position of the cutoff. The integral in Eq. (2) is evaluated numerically on a finite temporal grid for all points along a one dimensional grid in the focal plane. The far-field emission is computed using Fourier methods. We have performed the calculations both in one dimension and in two dimensions and found that the far-field pattern did not change significantly when including the second dimension. Propagation effects are not taken into account.

B. Estimation of the global phase mismatch

As explained in the main Letter, the asymmetric distribution of the harmonic beams relative to the reference direction [dotted blue line in Fig. 3(c) of the main Letter] can be linked to macroscopic phase matching effects and allows an estimation of $\Delta k_{||}$.

The harmonic signal S_q can be calculated by integrating the dipole response along the propagation axis z over the medium length L , taking into account a global wave vector mismatch $\Delta k = \Delta k_{||} + \Delta k_{\perp}$ as well as re-absorption of the generated XUV emission in the generation gas, denoted by the absorption coefficient κ_q :

$$S_q \propto \left| \int_0^L d_q \exp [i(\Delta k + i\kappa_q)(L - z)] dz \right|^2 \quad (3)$$

Approximating the dipole amplitude d_q as well as Δk as constant over the medium length, Eq. (3) reduces to:

$$S_q \propto |d_q|^2 e^{-\kappa_q L} \cdot \frac{\cosh(\kappa_q L) - \cos(\Delta k L)}{\Delta k^2 + \kappa^2} \quad (4)$$

We now consider $S_q = S_q(m_2)$ for different emission directions, *i.e.* for different m_2 values, defined through Eq. (1) in the main Letter. $|d_q|^2$ has to be replaced by a function accounting for a reasonable scaling of the intensity of the

harmonic emission corresponding to different m_2 -orders. As an approximation and in agreement with our simulations, we replace $|d_q|^2$ in Eq. (4) by a Gaussian function of width Δm_2 , centered around m_2^0 :

$$S_q(m_2, \Delta k_{||}) \propto \exp \left[-4 \log(2) \frac{(m_2 - m_2^0)^2}{(\Delta m_2)^2} \right] \cdot \frac{e^{-\kappa_q L} \{ \cosh(\kappa_q L) - \cos [(\Delta k_{||} + \Delta k_{<}(m_2))L] \}}{[\Delta k_{||} + \Delta k_{<}(m_2)]^2 + \kappa^2} \quad (5)$$

$\Delta k_{<}$ is a function of m_2 , defined via Eq. (2) in the main Letter. m_2^0 has a dominant influence on the distribution $S_q(m_2, \Delta k_{||})$. In our analysis, we use the numerically extracted m_2^0 -values shown in Fig. 3 (c) in the main letter. Δm_2 influences $S_q(m_2, \Delta k_{||})$ only weakly and was set to $\Delta m_2 = 7$ in our analysis, reflecting an upper limit of the experimentally measured width. Considering further $L = 2$ cm and a generation pressure of $p = 2$ mbar in order to estimate κ_q , we can fit $S_q(m_2, \Delta k_{||})$ to the experimentally measured distribution by adjusting $\Delta k_{||}$ and thus extract $\Delta k_{||}$.

[1] M. Lewenstein *et al.*, Phys. Rev. A **51**, 1495 (1995).

PAPER XIII

Noncollinear Optical Gating

C. M. Heyl, S. Bengtsson, S. Carlström, J. Mauritsson, C. L. Arnold and A. L'Huillier.

New Journal of Physics, Fast Track Communications **16**, 052001 (2014).

In the version of this paper included in this thesis, Figure 4 was replaced by an updated version, published in a Corrigendum as: *New Journal of Physics* **16**, 109501 (2014).

New Journal of Physics

The open access journal at the forefront of physics

Deutsche Physikalische Gesellschaft  DPG | IOP Institute of Physics

Fast Track Communication

Noncollinear optical gating

C M Heyl, S N Bengtsson, S Carlström, J Mauritsson, C L Arnold and A L'Huillier

Department of Physics, Lund University, PO Box 118, SE-22100 Lund, Sweden
E-mail: christoph.hey1@fysik.lth.se

Received 25 April 2014

Accepted for publication 7 May 2014

Published 23 May 2014

New Journal of Physics **16** (2014) 052001

[doi:10.1088/1367-2630/16/5/052001](https://doi.org/10.1088/1367-2630/16/5/052001)

Abstract

We present a novel scheme for high-order harmonic generation, enabling the production of spatially separated isolated attosecond pulses. This can be achieved by driving the generation process with two identical, but temporally delayed laser pulses, which are noncollinearly overlapping in the generation medium. Our approach provides intense attosecond pulses directly separated from the fundamental field, which is left undistorted. The method is therefore ideally suited for pump-probe studies in the extreme ultraviolet regime and promises new advances for intra-cavity attosecond pulse generation. We present a theoretical description of noncollinear optical gating, with an analytical derivation and simulations using the strong field approximation.

Keywords: isolated attosecond pulses, high harmonic generation, attosecond physics, extreme nonlinear optics

1. Introduction

The generation of single attosecond pulses (SAPs) via high-order harmonic generation (HHG) has enabled a multitude of experiments providing insight into attosecond dynamics in atoms [1], molecules [2] and solids [3]. While the generation of trains of attosecond pulses, i.e. high-order harmonics, does not present any technical difficulty with present ultrafast laser



Content from this work may be used under the terms of the [Creative Commons Attribution 3.0 licence](https://creativecommons.org/licenses/by/3.0/).

Any further distribution of this work must maintain attribution to the author(s) and the title of the work, journal citation and DOI.

New Journal of Physics **16** (2014) 052001
1367-2630/14/052001+11\$33.00

© 2014 IOP Publishing Ltd and Deutsche Physikalische Gesellschaft

technology, the generation of SAPs remains challenging, requiring carrier-envelope-phase (CEP)-stable few-cycle driving laser pulses and/or advanced gating methods to confine the extreme ultraviolet (XUV) emission to a single half-cycle of the driving field. Commonly-used techniques are based on manipulating the polarization state of the driving field [4, 5], utilizing a high laser intensity to rapidly deplete the nonlinear medium [6] or altering the shape of the driving field via multi-color field synthesis [7]. Vincenti and co-workers recently introduced a conceptually different technique [8], named attosecond lighthouse, utilizing spatio-temporal couplings to angularly streak the generated attosecond pulses. The technique was experimentally implemented both in gases [9] and using plasma mirrors [10].

Most gating techniques imply extensive manipulation of the fundamental field and require spectral filtering of the harmonic radiation, limiting the efficiency and restricting any further use of the laser pulse. Using the fundamental field after generation is of interest for pump-probe experiments and essential for intra-cavity HHG [11, 12], a promising scheme that enables the generation of attosecond pulses at unprecedented power levels and repetition rates, with applications in ultrahigh precision frequency metrology. While the generation of high-order harmonics inside a cavity has been experimentally demonstrated [11, 12], that of isolated attosecond pulses remains an unsolved challenge, requiring broadband enhancement cavities [13] and suitable gating methods [14].

Here, we introduce an efficient gating technique, noncollinear optical gating (NOG), based on driving the HHG process in a noncollinear geometry. Noncollinear HHG has recently been employed for several applications [18, 19], including *in situ* diagnostics of the generation process [20], and proposed as out-coupling method for intra-cavity HHG [21, 22]. Here, we present a new implementation of noncollinear HHG, which is used to generate angularly streaked attosecond pulse trains, thus providing an efficient gate for SAP generation. Two identical but time-delayed, noncollinearly overlapping laser pulses form a driving field with rotating wave fronts. Consecutive attosecond pulses are emitted in different directions, as illustrated in figure 1. The two driving laser pulses are left unperturbed¹ after generation and are spatially separated from the XUV radiation emitted at the bisector of the two driving field propagation angles. Thus, our method opens new possibilities for attosecond pump-probe experiments [15–17] as well as for frequency-comb spectroscopy studies in the XUV regime.

The article is organized as follows: the method is described in sections 2 and 3. Numerical simulations are presented in section 4. In section 5, we discuss the influence of macroscopic propagation effects. Finally, in section 6, we compare our gating scheme with the attosecond lighthouse technique.

2. Principle of the gating method

We consider two identical laser pulses, which are overlapped in time and superimposed noncollinearly with an angle 2γ at the focus, thus forming a spatial intensity grating in the focal plane [19]. The far-field angular distribution of the harmonics generated in such a geometry is determined by the interference of multiple sources. In general, the harmonics are emitted in different directions [23], and consequently the corresponding attosecond pulses are angularly distorted. The angular emission characteristics simplify considerably at small noncollinear

¹ Perturbations intrinsic to the HHG process, e.g. due to plasma formation as well as possible perturbations induced when splitting an initial laser pulse into two pulses might of course occur.

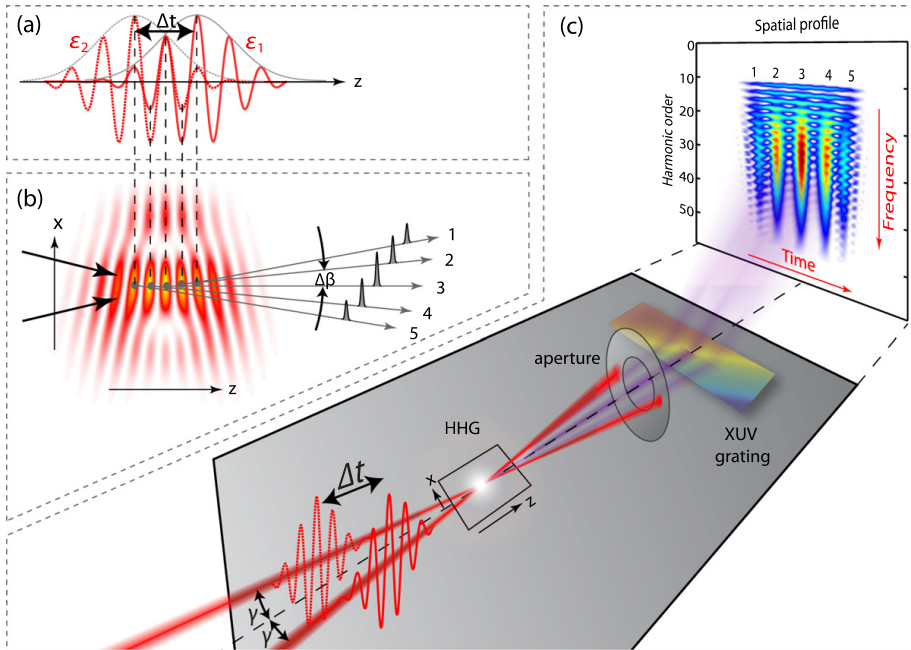


Figure 1. Principle of noncollinear optical gating. (a) A temporal delay between two few-cycle pulses leads to a rapidly changing amplitude ratio between subsequent half-cycles. (b) Overlapping these pulses noncollinearly causes a temporal rotation of the wavefronts (the figure displays $\Re(E)^2$ of the total field E). Attosecond pulses generated from subsequent half-cycles are therefore emitted in different directions. (c) Illustration of the experimental scheme: two noncollinearly overlapping driving pulses generate spatially separated isolated attosecond pulses in the angle sector between the fundamental propagation directions. The displayed spectrogram was calculated using a quasi-classical approach, considering a pulse duration and temporal delay of $2T$, where T is the field-cycle period. The observed continua, labelled 1–5, are characteristic of spatially separated attosecond pulses.

angle, when the intensity grating in the generation medium becomes a single maximum with weak satellites, as discussed in more detail below. In these conditions, the XUV emission follows the instantaneous direction of propagation of the total driving field (the z -axis in figure 1(c)), defined by the bisector of the two driving field propagation angles.

The wave front orientation in the focus of two noncollinearly overlapping laser fields with field envelope \mathcal{E}_1 and \mathcal{E}_2 , propagating along the wavevectors \mathbf{k}_1 and \mathbf{k}_2 respectively, can be defined through the composite wavevector at the point of intersection:

$$\mathbf{k}_{\text{tot}} = \frac{(\mathcal{E}_1 \mathbf{k}_1 + \mathcal{E}_2 \mathbf{k}_2)}{\sqrt{\mathcal{E}_1^2 + \mathcal{E}_2^2}}. \quad (1)$$

By taking the scalar product $\hat{\mathbf{x}} \cdot \mathbf{k}_{\text{tot}}/|\mathbf{k}_{\text{tot}}| = -\sin(\beta)$, in which $\hat{\mathbf{x}}$ is the unit vector in lateral direction (see figure 1(b), (c)) and β is the angle between \mathbf{k}_{tot} and the z -axis, we obtain for small γ :

$$\beta = \gamma \frac{1 - \xi}{1 + \xi}. \quad (2)$$

A variation of the amplitude ratio of the laser fields, $\xi = \mathcal{E}_2/\mathcal{E}_1$, results in a macroscopic tilt of the wave fronts and a change in the emission direction β . The introduction of a temporal delay Δt between two driving laser pulses leads to an amplitude ratio that changes rapidly from one half-cycle to the next (figure 1(a)), defining a unique orientation angle of the corresponding wave fronts as a function of time. The consequence is an ultrafast wave front rotation (WFR) in the focus (figure 1(b)), with attosecond pulses emitted in different directions [8]. The emission of XUV light is thus angularly streaked, mapping time into spatial position in the far-field [9]. A conventional imaging-XUV spectrometer displaying the spatially resolved spectral profile will therefore provide a spectrogram of the generated attosecond pulse train, i.e. frequency versus time, as illustrated in figure 1(c). The time-to-space mapping is defined through equation (2) where ξ varies with time depending on the envelope and separation of the driving fields.

Considering two Gaussian laser pulses with $\mathcal{E}_{1,2} = \exp[-2 \ln(2)(t \pm \Delta t/2)^2/\tau^2]$ and pulse duration τ (FWHM), we can deduce the emission angle as a function of time. The time-to-space mapping is approximately linear around $t = 0$, i.e. at the temporal center of the total driving field, where maximum WFR speed is achieved, with

$$\beta(t) = 2 \ln(2) \gamma \frac{\Delta t}{\tau^2} t. \quad (3)$$

In the temporal wings of the pulses, the WFR speed is reduced. The direction of the time axis itself is determined by the sign of the temporal delay, i.e. the order of the driving pulses. The WFR velocity increases linearly with Δt . Choosing $\Delta t \approx \tau$ ensures that the total field intensity does not exhibit a local minimum at $t = 0$.

3. Angular separation of the attosecond pulses

In order to isolate attosecond pulses emitted from subsequent half-cycles, the angle difference $\Delta\beta \approx \beta(T/2)$ has to be larger than the divergence angle of a SAP. We define this angle as $\Theta_q = W_q(z)/z$, with $W_q(z)$ denoting the beam radius in the far field at a distance z from the focus for a beam with central frequency $q\omega$. To estimate Θ_q , we consider the intensity grating of the fundamental field in the focal plane with a Gaussian envelope at the beam waist and radius W_0 . All spatial beam widths are defined at $1/e^2$ of the intensity profile. For small γ , the intensity distribution in the focal plane can be written as:

$$I(x, z = 0) \propto \cos^2[kx \sin(\gamma)] \exp\left(-\frac{2x^2}{W_0^2}\right). \quad (4)$$

In order to avoid interference effects due to multiple harmonic sources formed by the interference grating in the focus, we consider a degenerated grating with only one central maximum at $x = 0$ and weak satellites. Limiting the intensity of the first satellites to $1/e^2$ of the

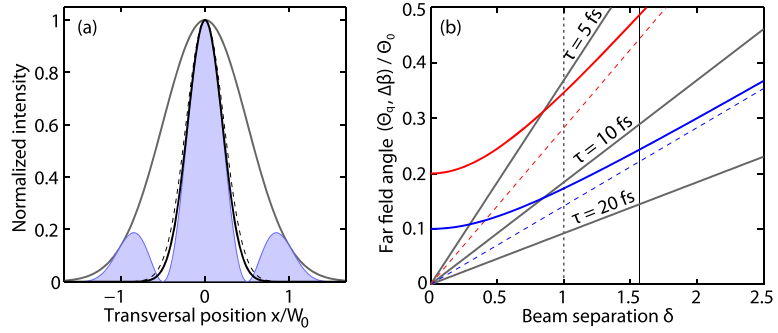


Figure 2. Intensity grating and gating condition. (a) Fundamental intensity distribution at $z = 0$ for $\gamma = \gamma_{\text{opt}}$ together with its Gaussian approximations considering (black solid line) and neglecting (black dashed line) the influence of the spatial envelope (gray solid line). (b) Θ_q , for $\eta = 5$ (solid red line) and $\eta = 10$ (solid blue line) together with their asymptotic approximations (dashed red and blue lines), plotted as a function of δ ; the solid gray lines indicate $\Delta\beta$ for different pulse lengths, considering a central wavelength of 800 nm. Both Θ_q and $\Delta\beta$ are normalized to the divergence Θ_0 . We also indicate the minimum δ which allows a direct separation of fundamental and SAP (dashed vertical line) and the maximum $\delta (= \pi/2)$ for which the satellite peaks can be neglected and for which gating can be achieved (solid vertical line).

central maximum implies that γ must be smaller than $\gamma_{\text{opt}} = \lambda/2W_0$ with λ denoting the carrier wavelength. Using Gaussian optics, we have $W_0 = f\lambda/(\pi W_f)$, where f is the focal length and W_f the beam radius before focusing. Defining $2x_0$ as the center-to-center separation of the two generation beams before focusing and $\delta = x_0/W_f$, the required intensity grating is obtained when $\delta \leq \pi/2$.

For small γ , the cosine²-intensity distribution caused by the beam interference can be approximated with a Gaussian function, $I(x, z = 0) \propto \exp(-2x^2/W_\gamma^2)$, with $W_\gamma^2 = 1/[k^2\gamma^2/2 + 1/W_0^2]$, as illustrated in figure 2(a). With the scaling relation $\Theta_q \propto 1/W_\gamma$, this leads to an expression for the divergence angle $\Theta_q = \Theta_q(\gamma)$ in units of $\Theta_q(0)$:

$$\frac{\Theta_q(\gamma)}{\Theta_q(0)} = \frac{W_0}{W_\gamma} = W_0 \sqrt{\frac{k^2\gamma^2}{2} + \frac{1}{W_0^2}}. \quad (5)$$

In order to determine whether the condition for SAP emission $\Delta\beta > \Theta_q$ is satisfied, we look at the scaling of $\Delta\beta$ and Θ_q with increasing noncollinear angle, or equivalently beam separation δ (figure 2(b)). $\Delta\beta$ is plotted as a function of γ for three different pulse lengths while Θ_q is shown for two different values of the ratio between the fundamental and the attosecond pulse divergence $\eta = \Theta_0/\Theta_q(0)$. While $\Delta\beta$ increases linearly with γ , Θ_q follows a nonlinear scaling relation. The conditions for SAP generation improve with increasing γ until Θ_q approaches an asymptotic linear dependence. Figure 2(b) shows that efficient gating requires short driving pulses and collimated harmonic beams. For $\eta = 10$ and $\lambda = 800$ nm, gating is achieved for

$\tau \leq 10$ fs and $\delta \geq 1$, while if $\eta = 5$, gating needs pulses of the order of 5 fs or less and similarly $\delta \geq 1$. The gating conditions improve until $\delta \simeq \pi/2$, which corresponds to the maximum allowed noncollinear angle $\gamma = \gamma_{\text{opt}}$. As an example, for $f=0.5$ m and $W_f=2$ mm we obtain $\gamma_{\text{opt}}=6.3$ mrad.

In summary, optimal conditions for SAP generation, which ensure minimized temporal satellite pulses as well as suppression of interference effects due to multiple sources in the focus, are obtained when the beam separation before focusing is approximately $\pi/2$ times the $1/e^2$ -diameter of the intensity profile. This condition is valid for loose and tight focal geometries, since the NOG scheme does not depend on focusing as long as η remains the same (see figure 2). With decreasing focal length, W_0 decreases and the SAP divergence increases. However, $\Delta\beta$ increases accordingly, and identical temporal SAP characteristics are obtained.

For $\gamma \simeq \gamma_{\text{opt}}$, the influence of the Gaussian envelope on the radial dimension of the harmonic source can be neglected, and the divergence can be approximated by its asymptotic value

$$\theta_q \approx \theta_q(0)W_0 \frac{k\gamma}{\sqrt{2}} = \frac{\lambda k}{\pi\sqrt{2}\eta}\gamma = \frac{\sqrt{2}\gamma}{\eta}. \tag{6}$$

Using equation (3) this leads to a simple condition for the maximum pulse duration allowing an angular separation of the generated attosecond pulses:

$$\tau \leq \frac{\ln(2)}{\sqrt{2}} \frac{\eta\lambda}{c}, \tag{7}$$

c denoting the speed of light. If the above condition is fulfilled, the emission direction between consecutive SAPs changes by at least the divergence angle of the same pulses. This is equivalent to limiting the on-axis intensity of pre- and post pulses to $1/e^2$ of the main pulse. For $\lambda = 800$ nm, and $\eta = 10$, we obtain $\tau \leq 13$ fs.

The factor $1/\eta$ can also be interpreted as a lower limit for the angular divergence of the harmonic emission at frequency $\eta\omega$, defined in units of the fundamental beam divergence. Thus, equation (7) leads to an approximate limit for the low-energy cutoff $E_{\text{low}} = \hbar\omega\eta$ of the generated spectral continua:

$$E_{\text{low}} \approx \frac{\hbar\omega^2\tau}{\pi\sqrt{2} \ln(2)}, \tag{8}$$

the high-energy limit being determined by the fundamental intensity. Using the above parameters and considering $\tau = 5$ fs at $\lambda = 800$ nm and a peak intensity of 2×10^{14} W cm⁻², we have $E_{\text{low}} = 5.9$ eV, leading to SAPs with up to 48 eV bandwidth if Ar is used for generation.

4. Simulations

We performed numerical calculations in order to simulate HHG in a noncollinear geometry. The single atom response was obtained by solving the time dependent Schrödinger equation within the strong field approximation [24], selecting the short trajectory contribution. The harmonic dipole response was calculated numerically on a finite temporal grid for all points

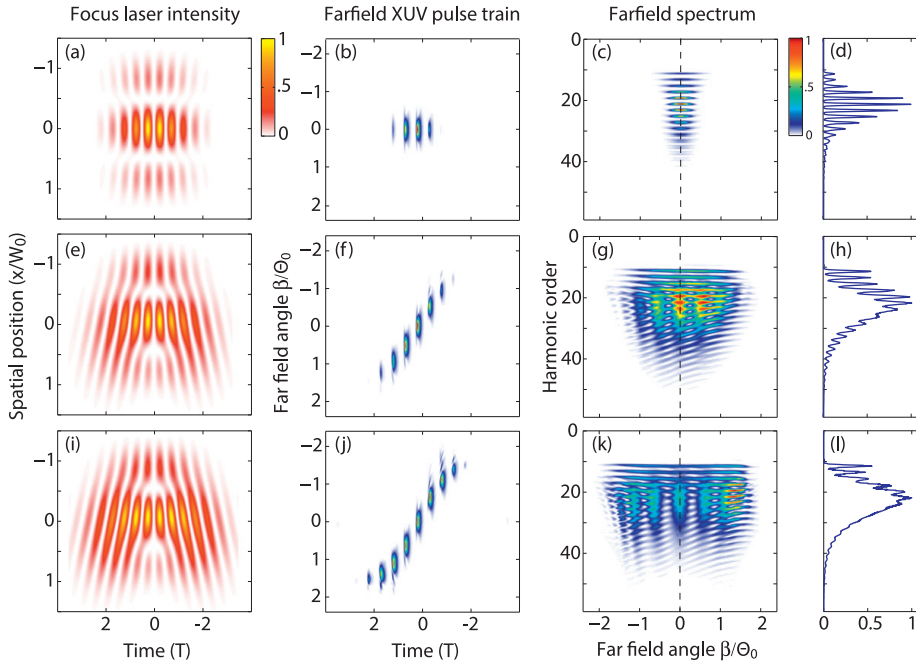


Figure 3. Simulations of noncollinear optical gating. Normalized spatio-temporal distribution $\Re(E)^2$ of the fundamental field interference pattern in the focus (first column), far-field intensity distribution of the attosecond pulse trains (second column), spatially-resolved spectrum (third column) and spectrum at $\beta = 0$ (fourth column) for three different cases: $\Delta t = 0$ (first row), $\Delta t = 2T = \tau$ (second row), and $\Delta t = 2.5T$ (third row).

along a one dimensional grid in the focal plane. The far-field emission was computed using Fraunhofer diffraction integrals. Propagation effects (see section 5) were not taken into account.

Figure 3 presents simulations of HHG in neon for two-cycle driving pulses ($\tau = 2T$), considering $\delta = \pi/2$. The first row (a) shows the focused laser $\Re(E)^2$, the attosecond pulse train in the far field (b), the far field spectrum (c) and a spectral line-out at $\beta = 0$ (d) when the two pulses are superposed with no time delay at the focus. The far-field intensity distribution is shown as a function of the propagation angle β , normalized to the divergence of the focused fundamental laser pulses. The generated attosecond pulse train includes approximately four pulses, which interfere in the far field, leading to a discrete HHG spectrum. The second and third rows present the same quantities for temporally-delayed driving pulses, with $\Delta t = 2T = \tau$ and $\Delta t = 2.5T$ respectively. The WFR ((e) and (i)) induced by the temporal separation streaks the attosecond pulses angularly as shown in (f) and (j). With increasing temporal delay, the discrete spectrum becomes a characteristic XUV spectrogram with discrete harmonic peaks at low energies and spectral continua towards the high-energy cut-off. The spatially overlapping contributions from consecutive attosecond pulses interfere, leading to a fringe pattern between

the spectral continua. The slope of the interference fringes, which increases with energy, reflects the harmonic dipole phase variation with driving field intensity [25].

A variation of the CEP ϕ_{CE} of the driving fields moves the wavefronts in time and leads to a spatial shift of the corresponding XUV spectrogram [9, 10], providing direct access to the CEP of the driving laser field. For the simulations presented in figure 3, ϕ_{CE} was chosen in order to emit a SAP at $\beta = 0$. Changing ϕ_{CE} by $\pi/2$ leads to the emission of two pulses at $\beta \approx \pm\Delta\beta/2$, thus providing two synchronized but spatially separated SAPs, of interest for attosecond-pump-attosecond-probe studies.

A variation of the relative phase between the two driving fields moves the fundamental intensity grating across the focal plane. A zero relative phase at the point of intersection ensures a central intensity maxima at $x = 0$, as shown in figure 3 (first column) while a phase shift of π leads to two intensity maxima in the focal plane and a phase singularity at $x = z = 0$ [26]. In the latter case, interference effects between the two harmonic sources in the focus lead to angularly distorted attosecond pulses, thus preventing efficient gating.

5. Propagation effects

Propagation effects in the nonlinear medium can be described in a similar way as for a collinear geometry. The noncollinear geometry adds a geometrical component to the total wavevector mismatch between fundamental beam and generated XUV field with central frequency $q\omega$ [19]. In the focus, the geometrical wave vector mismatch can be taken into account by replacing the component arising from the Gouy phase shift for one beam $\Delta k_c^q \approx -q/z_0$ (z_0 denotes the Rayleigh length) by:

$$\Delta k_{\text{nc}}^q = \Delta k_c^q \left(1 + \frac{\pi^2}{4} - \frac{\lambda\pi}{8z_0} \right). \tag{9}$$

The second term in equation (9) can be attributed to the noncollinear geometry considering plane waves (equivalent to the Gouy phase shift of a Gaussian beam with an initial beam radius of $W_f\pi/2$), the last term is caused by the off-axis components of the Gouy phase shift.

Δk_{nc}^q is equivalent to the wave vector mismatch for a collinear geometry with tighter focusing, which does not imply a lower conversion efficiency if the generation parameter are selected adequately [27]. As for collinear HHG, phase matching can be achieved by minimizing the total wave vector mismatch, i.e. adjusting gas pressure, medium length and laser intensity [28]. Our numerical simulations confirm the robustness of the NOG scheme even for a long medium, which is consistent with the findings presented in the supplementary information of [9] for the case of the lighthouse technique (see section 6).

6. Comparison with the attosecond lighthouse

Finally, we compare NOG with the attosecond lighthouse technique [8]. Both methods are based on WFR of the fundamental field, introducing an angular streaking effect. In the lighthouse configuration, WFR is achieved by focusing an angularly chirped laser pulse while an ultrafast amplitude modulation induces a rotating wave front in the NOG scheme. The lighthouse can also be seen as the continuous analog of NOG. The two techniques are compared

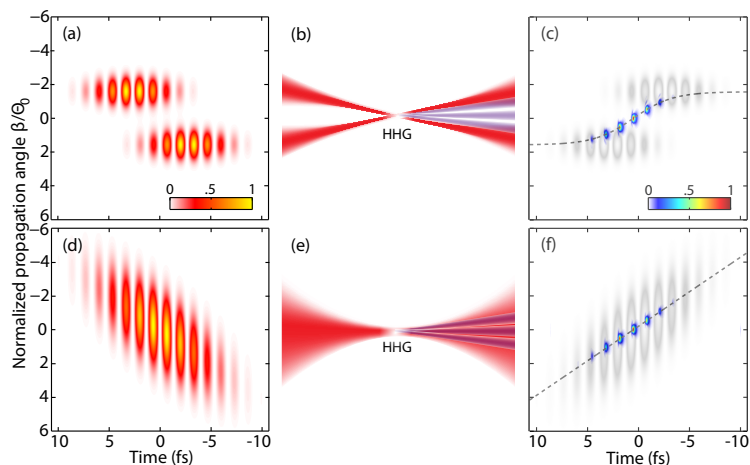


Figure 4. Comparison between NOG (a)–(c) and lighthouse (d)–(f). Normalized spatio-temporal field distribution $\Re(E)^2$ of the generation field before focusing (a), (d), focusing scheme (b), (e) and generated XUV intensity distribution (c), (f) at a focal length distance behind the focus. In order to achieve comparable spatio-temporal XUV pulse characteristics we consider $\Delta t = \tau$ for NOG, a beam radius before focusing that is factor of 3.7 larger for the lighthouse scheme than for NOG and laser pulses that have the same spectral bandwidth, corresponding to $\tau = 2T$. The dashed lines in (c), (f) indicate the time-to-space mapping.

in figure 4 for a two-cycle fundamental pulse and maximum WFR speed for the lighthouse scheme. Figures 4(a) and (d) show the spatio-temporal representation of the driving field distribution before focusing, while (c) and (f) present the angularly streaked attosecond pulse train in the far field together with the driving field after generation (in gray). Considering $\Delta t = \tau$ for the NOG scheme, both methods lead to angularly streaked attosecond pulse trains with very similar spatio-temporal characteristics and identical streaking efficiency at $t = 0$. Interestingly, the NOG scheme allows even faster WFR for $\Delta t > \tau$ (figure 2, third row) and thus a better spatial separation of the generated attosecond pulses while the WFR speed is limited in the lighthouse scheme [8]. Another important difference emerges for the fundamental field characteristics after generation. In the lighthouse scheme the fundamental field is chirped and distributed over the angle sector in which attosecond pulses are emitted. In the NOG scheme, two, nearly transform limited fundamental pulses (see footnote 1), leave the interaction process after generation and isolated attosecond pulses are emitted in the angle sector between the two driving fields.

7. Conclusion and outlook

In conclusion, we have introduced a new method for streaking attosecond pulse trains, which gives access to multiple, perfectly synchronized SAPs. NOG constitutes the first gating scheme that allows a direct spatial separation of fundamental driving field and generated attosecond pulses. It is therefore ideally suited for attosecond-pump-attosecond-probe studies, which

require high pulse energies. Finally, NOG can be applied to intracavity HHG, leading to the generation of isolated attosecond pulses at unprecedented average power levels and MHz repetition rates, promising advances in XUV-frequency-comb spectroscopy.

Acknowledgments

This research was supported by the Marie Curie program ATTOFEL (ITN), the European Research Council (ALMA, PALP), the Swedish Research Council, the Swedish Foundation for Strategic Research and the Knut and Alice Wallenberg Foundation.

References

- [1] Goulielmakis E *et al* 2010 Real-time observation of valence electron motion *Nature* **466** 739
- [2] Sansone G *et al* 2010 Electron localization following attosecond molecular photoionization *Nature* **465** 763
- [3] Cavalieri A *et al* 2007 Attosecond spectroscopy in condensed matter *Nature* **449** 1029
- [4] Sola I *et al* 2006 Controlling attosecond electron dynamics by phase-stabilized polarization gating *Nat. Phys.* **2** 319
- [5] Sansone G *et al* 2006 Isolated single-cycle attosecond pulses *Science* **314** 443
- [6] Ferrari F *et al* 2010 High-energy isolated attosecond pulses generated by above-saturation few-cycle fields *Nat. Photonics* **4** 875
- [7] Wirth A *et al* 2011 Synthesized light transients *Science* **334** 195
- [8] Vincenti H and Quéré F 2012 Attosecond lighthouses: how to use spatiotemporally coupled light fields to generate isolated attosecond pulses *Phys. Rev. Lett.* **108**
- [9] Kim K *et al* 2013 Photonic streaking of attosecond pulse trains *Nat. Photonics* **7** 651
- [10] Wheeler J *et al* 2012 Attosecond lighthouses from plasma mirrors *Nat. Photonics* **6** 829
- [11] Cingöz A *et al* 2012 Direct frequency comb spectroscopy in the extreme ultraviolet *Nature* **482** 68
- [12] Gohle C *et al* 2005 A frequency comb in the extreme ultraviolet *Nature* **436** 234
- [13] Pupeza I *et al* 2013 Compact high-repetition-rate source of coherent 100 eV radiation *Nat. Photonics* **7** 608
- [14] Pupeza I *et al* 2014 Cavity-enhanced high-harmonic generation with spatially tailored driving fields *Phys. Rev. Lett.* **112** 103902
- [15] Tzallas P *et al* 2011 Extreme-ultraviolet pump-probe studies of one-femtosecond-scale electron dynamics *Nat. Phys.* **7** 781
- [16] See reviews on attosecond photonics in *Nature Photonics*, March 2014
- [17] Nabekawa Y *et al* 2009 Interferometry of attosecond pulse trains in the extreme ultraviolet wavelength region *Phys. Rev. Lett.* **102** 213904
- [18] Daboussi S *et al* 2013 Double pulse quasi-collinear high harmonic generation scheme as a tool for x-ray laser plasma gain probing *Appl. Phys. B* **111** 7
- [19] Heyl C M *et al* 2014 Macroscopic effects in noncollinear high-order harmonic generation *Phys. Rev. Lett.* **112** 143902
- [20] Kim K *et al* 2013 Manipulation of quantum paths for space-time characterization of attosecond pulses *Nat. Phys.* **9** 159
- [21] Wu J and Zeng H 2007 Cavity-enhanced noncollinear high-harmonic generation for extreme ultraviolet frequency combs *Opt. Lett.* **32** 3315
- [22] Ozawa A *et al* 2008 Non-collinear high harmonic generation: a promising outcoupling method for cavity-assisted XUV generation *Opt. Express* **16** 6233

- [23] Bertrand J *et al* 2011 Ultrahigh-orderwave mixing in noncollinear high harmonic generation *Phys. Rev. Lett.* **106** 023001
- [24] Lewenstein M *et al* 1994 Theory of high-harmonic generation by low-frequency laser fields *Phys. Rev. A* **49** 2117
- [25] Varjú K *et al* 2005 Frequency chirp of harmonic and attosecond pulses *J. Mod. Opt.* **52** 379
- [26] Nye J and Berry M V 1974 Dislocations in wave trains *Proc. R. Soc. London* **336** 165
- [27] Heyl C M, Güdde J, L'Huillier A and Höfer U 2012 High-order harmonic generation with μJ laser pulses at high repetition rates *J. Phys. B: At. Mol. Opt. Phys.* **45** 074020
- [28] Gaarde M, Tate J and Schafer K 2008 Macroscopic aspects of attosecond pulse generation *J. Phys. B: At. Mol. Opt. Phys.* **41** 132001

PAPER XIV

Gating Attosecond Pulses in a Noncollinear Geometry

C. M. Heyl*, M. Louisy*, M. Miranda, D. Kroon, M. Kotur,
E. W. Larsen, S. N. Bengtsson, D. Guénot, L. Rading, F. Brizuela,
P. Rudawski, F. Campi, B. Kim, J. Mauritsson, P. Johnsson,
A. L'Huillier and C. L. Arnold; (* authors contributed equally).

In preparation.

Gating Attosecond Pulses in a Noncollinear Geometry

C. M. Heyl*, M. Louisy*, M. Miranda, E. W. Larsen, S. Bengtsson, D. Kroon, M. Kotur, D. Guénot, L. Rading, P. Rudawski, F. Brizuela, F. Campi, B. Kim, J. Mauritsson, P. Johnsson, A. L'Huillier, C.L. Arnold

* authors contributed equally

Department of Physics, Lund University,

P. O. Box 118, SE-221 00 Lund, Sweden

(Dated: November 4, 2014)

We provide first experimental evidence for angular gating of high-order harmonic emission, driven by two temporally delayed, intense, few-cycle laser pulses, overlapped noncollinearly in the generation medium. The noncollinear geometry has the benefit of spatially separating generated attosecond pulses from the driving infrared laser pulses, thus relaxing the need for filtering. We present first observations of multiple spectral continua, indicating the generation of isolated attosecond pulses emitted in different directions, which can be controlled by the carrier envelope phase of the driving laser pulses. This scheme is particularly suited for intra-cavity attosecond pulse generation as well as for the generation of energetic isolated attosecond pulses, essential for XUV-XUV pump-probe experiments.

PACS numbers: 42.65.Ky 42.65.Re

Table-top sources of coherent extreme ultraviolet (XUV) radiation are nowadays used in many laboratories, delivering coherent XUV pulses (isolated pulses or pulse trains) with attosecond duration. Such sources are commonly based on high-order harmonic generation (HHG) in gases, a process that requires intensities around 10^{14} W/cm², thus setting severe requirements on the laser pulses used for generation. Ultra-short laser pulses with rather high pulse energy are typically employed, implicitly limiting the repetition rate of attosecond sources due to average power restrictions. Many experiments, such as coincidence spectroscopy [1], photoelectron spectroscopy on surfaces [2] and time-resolved microscopy [3, 4] would, however, benefit greatly from higher repetition rates. A promising route towards multi-MHz attosecond sources relies on HHG inside passive enhancement cavities [5, 6]. In such a scheme, the low conversion efficiency of the HHG process is compensated by coherently superimposing many laser pulses inside the cavity, leading to a total power enhancement of two to three orders of magnitude [7]. Although successfully demonstrated for attosecond pulse trains [5, 6, 8–10], the generation of isolated attosecond pulses (IAPs) inside a cavity remains an unsolved challenge, limited mainly by dispersion management [11, 12] and out-coupling problems [13]. Traditional gating concepts for the generation of IAPs, such as polarization gating [14] or ionization gating [15] imply severe manipulations of the laser field and cannot easily be brought in line with enhancement cavity design consideration, due to an increased complexity of dispersion control. Recent attempts are however pointing towards the implementation of gating techniques and more efficient out-coupling [10, 16].

We recently proposed a new gating concept for IAP generation [17], noncollinear optical gating (NOG), which has the potential to facilitate intra-cavity IAP gating and efficient outcoupling for intra-cavity HHG. Similar to the recently introduced attosecond lighthouse [18], NOG em-

ploy a new degree of freedom for IAP gating: the spatial domain, accessible via spatio-temporal couplings [19]. NOG combines the recently introduced angular streaking concept [20] with noncollinear HHG, proposed [21] and tested [22] as outcoupling method for intra cavity HHG.

The generation of one or several angularly separated IAPs in a noncollinear geometry offers further new possibilities for attosecond-pump-attosecond-probe schemes [23–25]. As XUV-XUV pump-probe experiments are mainly limited by the low XUV photon flux of today's sources [26], better experimental schemes are needed. The noncollinear generation of more than one IAP includes the functionality of an all-optical broadband XUV beamsplitter, thus providing new possibilities for pump-probe measurements [27]. Moreover, noncollinear generation simplifies the separation from the fundamental field, as the IAPs leave the generation volume at a different angle than the fundamental driving field.

In this Letter, we experimentally test the NOG scheme, providing, for the first time, experimental evidence that attosecond angular streaking can be realized in a noncollinear generation geometry. We show the time-to-space mapping of attosecond pulse trains, resulting in multiple spectral continua in the spatially resolved XUV spectrum, indicating the generation of angularly displaced IAPs. We further investigate, how the time-to-space mapping process can be controlled with the time delay between the driving laser pulses and their carrier envelope phase (CEP), allowing us to select the number of XUV pulses.

Noncollinearly superimposing two identical and focused laser pulses at the position of the geometrical focus results in a transverse intensity grating with a periodicity $a = \lambda/2\gamma$ (small angle approximation) and a transverse envelope corresponding to the focal spot size of either pulse. Here λ is the carrier wavelength of the pulses and 2γ is the noncollinear angle between the two beams. For small noncollinear angles, such that $a \approx w_0$,

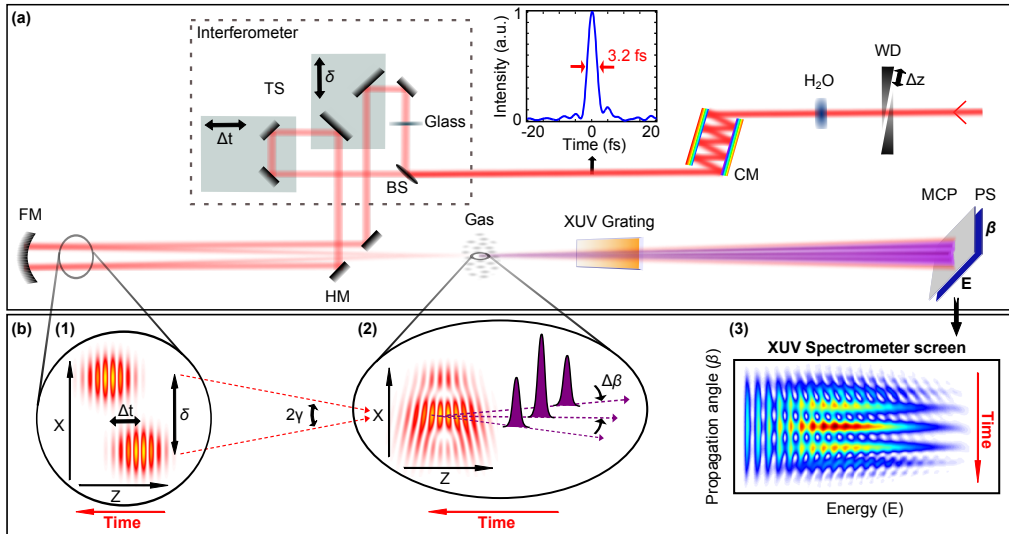


FIG. 1: (a) Schematic of the experimental setup. WD: motorized pair of wedges. H₂O: water cell. CM: chirped mirrors. BS: beam splitter. TS: translation stages. HM: holey mirror. FM: focusing mirror ($f=400$ mm). Gas: Argon. MCP: multi-channel plate. PS: phosphor screen. (b) Illustration of the IR laser pulses (1) in the far-field before focusing ($\Delta t > 0$), (2) at the position of the gas cell at gating conditions, and (3) of the angularly separated XUV half-cycle pulses (simulation).

where w_0 is the beam radius in the focus (all spatial beam dimensions are specified at $1/e^2$ of the intensity profile), the intensity grating collapses into a single maximum with weak satellites. In the far-field (before focusing) this corresponds to a separation of the two beams by approximately $\delta = \pi D/2$, where D is the diameter of either beam. The direction of XUV emission is imposed by the wave front orientation of the individual half-cycles of the driving field. For two identical pulses being focused noncollinearly with complete temporal overlap, the XUV emission is directed along the bisector of the two pulses, i.e. the optical axis. However, if a temporal separation (Δt) is introduced, the resulting amplitude variation between the two interfering pulses leads to an ultrafast wavefront rotation (WFR) between consecutive half-cycles of the driving field. If the WFR is fast enough, the XUV pulses originating from consecutive half-cycles are angularly separated from each other. This results in angularly streaked XUV emission, mapping time into spatial position in the far-field, similarly to attosecond lighthouse [18]. The wavefront rotation angle can be expressed as a function of the amplitude ratio $\xi(t, \Delta t) = \mathcal{E}_2/\mathcal{E}_1$ between the two driving field envelopes $\mathcal{E}_{1,2}$,

$$\beta(t, \Delta t) = \gamma \frac{1 - \xi(t, \Delta t)}{1 + \xi(t, \Delta t)}. \quad (1)$$

The principles underlying noncollinear optical gating are

described in detail in [17].

The experimental setup employed for NOG is illustrated in Fig. 1, together with the principle of the gating technique. We use a Ti:Sapphire based chirped pulse amplification laser, emitting pulses with a repetition rate of 1 kHz, centered around 800 nm, with 20 fs pulse duration (FWHM), and an energy of up to 5 mJ. Few-cycle pulses are obtained by post-compression using a hollow capillary [28] of 1 m length and 250 μm diameter, operated at 3 bars of He in differential pumping configuration [29]. Pulses with an energy of approximately 2.5 mJ are focused into the entrance of the capillary and 0.9 mJ are obtained at the output (transmission of 40%). The beam from the capillary is collimated with a $f=1.25$ m focal length spherical mirror and compressed with chirped mirrors in double-angle configuration (Ultrafast Innovations). A pair of motorized fused silica wedges [see Fig. 1(a)] is used for dispersion fine control, temporal characterisation as well as for scanning the carrier-envelope phase (CEP) of the pulses. A change of 28.9 μm thickness of fused silica corresponds to a CEP-slip of π . Consequently, we can easily scan multiple π of CEP-slip without significantly influencing the pulse duration. The CEP is stabilized with a commercial f-2f interferometer (Menlo Systems) at the output of the laser and a slow feedback loop to an acousto-optical programmable filter (DAZZLER), resulting in ≈ 150 mrad residual rms CEP instability for integration times of 30 ms. The pulses

are characterized with the d-scan technique consisting in recording frequency doubled spectra as a function of dispersion (glass insertion of the wedges) and retrieving iteratively the spectral phase from the measured fundamental and second harmonic generation spectra [30].

Initial d-scan characterizations showed sub-4 fs (FWHM) with residual third-order spectral phase and distinct satellites. If glass wedges and chirped mirrors are used for post-compression, third- and higher-order spectral phase contributions usually remain uncompensated. By introducing a water-filled cell of matched length (here 5 mm) into the beam path, an additional degree of freedom is obtained due to a different ratio between second- and third-order dispersion for water as compared to the typical glasses used for wedges [31]. With both second- and third-order phases compensated, a relatively clean pulse of 3.2 fs (Fourier limit 2.9 fs) at a carrier wavelength of 720 nm is obtained with only small satellites [see Fig. 1(a)]. The pulse energy after compression is ~ 0.5 mJ. After the post-compressor, the beam enters an interferometer setup consisting of a dispersion balanced beam splitter (Ventoon) and two translation stages to spatially (δ) and temporally (Δt) separate the pulses for noncollinear gating [Fig. 1(a)]. As alternative to the beam splitter, wave front division by means of a D-shaped mirror was used in some experiments.

The spatially and temporally displaced pulses enter vacuum through a thin (0.5 mm) AR-coated fused silica window and are focused noncollinearly with a $f=400$ mm spherical mirror into a pulsed Ar gas cell. Fig. 1b(2) illustrates the wave front rotation obtained at the focus in gating conditions. The XUV beams originating from consecutive half-cycles are spatially separated in the far-field and recorded with a flat-field XUV spectrometer, consisting of a curved grating, a multi-channel plate (MCP), and a phosphor screen.

Fig. 2(a) displays the XUV spatial far-field profile, integrated over photon energy, as a function of the temporal delay Δt in units of the cycle period T of the carrier. Three characteristic regimes can be identified. At delays much larger than the pulse duration τ (regime I), the two laser pulses do not interact, leading to angularly well separated XUV emissions at $\beta = \gamma$ for $t \gg 0$ ($\xi \approx 0$) and $\beta = -\gamma$ for $t \ll 0$ ($\xi \approx \infty$) [Eq. (1)]. The intensity modulations with delay, visible in this region, may be explained by the influence of weak temporal satellite pulses. For delays around $\pm T$ (regime II), the detected XUV radiation covers a large angle sector, approximately centered at the optical axis. In this regime where both pulses overlap partially, the emission angle $\beta(t)$ varies rapidly with time, leading to an ultrafast WFR. The attosecond pulse train is streaked across the angle sector from $-\gamma$ to γ , leading to a wide angular spread of the emitted XUV radiation. Finally, at complete temporal overlap (regime III), the spatial emission profile is confined to a small angle sector around the optical axis. In this case, the amplitude ratio of the two fundamental fields does not change in time ($\beta = 0$) and the attosec-

ond pulse train is emitted on axis.

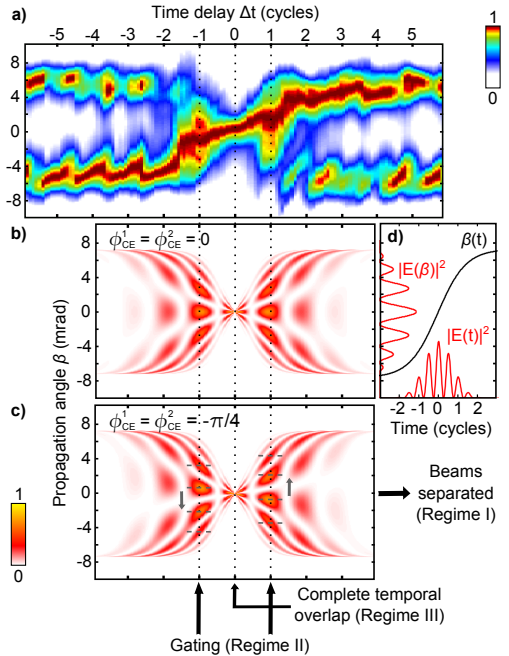


FIG. 2: (a) Experimentally measured spectrally integrated (25 – 50 eV) XUV far-field profile vs. time delay Δt . (b) and (c): Wavefront orientation map displaying $\Re[E(\Delta t, \beta)]^2$, indicating the orientation of individual half-cycles as a function of the time delay for $\phi_{CE}^{1,2} = 0$ (b) and $\phi_{CE}^{1,2} = -\pi/4$ (c). (d) Illustration of the time-to-angle mapping: $\Re[E(\beta)]^2$ and the corresponding $\Re[E(t)]^2$ for $\Delta t = -T$ together with the time-to-angle mapping function $\beta(t)$. The vertical curve $\Re[E(\beta)]^2$ corresponds to a line-out taken from (b) at $\Delta t = -T$. The arrows in (c) indicate the pattern movement with decreasing CEP.

The far-field XUV intensity distribution shows a distinct asymmetry relative to the optical axis [Fig. 2(a)], which is inverted when the delay changes sign. For negative (positive) delays, the fundamental pulse generating the XUV beam on the lower part of the figure ($\beta \leq 0$) comes first (second) [see also Fig. 1b(1)]. The observed asymmetry can be explained by the influence of ionization. Depletion as well as phase mismatch due to plasma dispersion lead to less efficient XUV generation for positive angles at negative delays as well as for negative angles at positive delays.

The delay-dependent XUV emission characteristics can be better understood with the help of a *wave front orientation map* where the square of the real part of the fundamental field on axis, $E = E_1 + E_2$ with

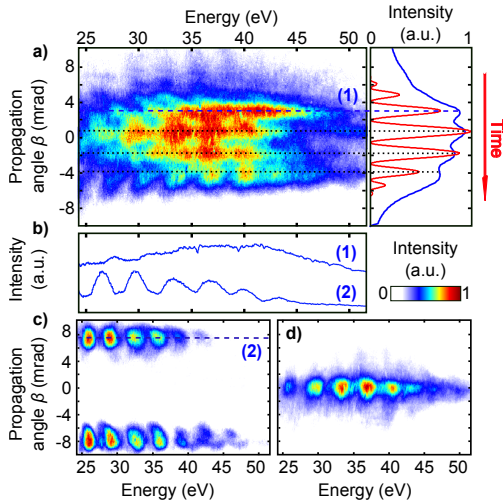


FIG. 3: Angularly resolved far-field XUV spectra for three different time delays: (a) Regime II: $\Delta t \approx T$, (c) Regime I: $|\Delta t| \gg 0$, (d) Regime III: $\Delta t = 0$. (b) Line-outs of the XUV emission spectra indicated by a blue dashed line in (a) and (c). The right side panel in (a) shows the spectrally integrated spatial profile (blue line) together with a line-out of the calculated wavefront orientation map for $\Delta t = T$ and $\phi_{\text{CE}}^{1,2} = \pi/4$ [see Fig. 2(c)].

$E_{1,2} = \mathcal{E}_{1,2} \exp[i(\omega t \pm \Delta t/2) + \phi_{\text{CE}}^{1,2}]$ is plotted as a function of Δt and β . $\phi_{\text{CE}}^{1,2}$ denote the CEPs for the two laser pulses. We consider a Gaussian carrier envelope $\mathcal{E}_{1,2} = \exp[-2 \ln(2)(t \pm \Delta t/2)^2/\tau^2]$. Fig. 2(b) and (c) show examples of such wavefront orientation maps for the experimental conditions and for two different CEPs, identical for the two pulses, equal to 0 and $-\pi/4$. Each vertical line-out in these figures represents the angular electrical field distribution $\Re[E(\beta)]^2$, i.e. its temporal distribution $\Re[E(t)]^2$ mapped onto the emission angle. The time-to-angle mapping is defined in Eq. (1) and represented in Fig. 2(d) for $\Delta t = -T$. For $\phi_{\text{CE}}^2 = \phi_{\text{CE}}^1$, emission angles close to the optical axis are only defined for integer numbers of cycle delays. This corresponds to a total relative phase between the two fields at focus equal to zero, such that the intensity grating has a maximum on the optical axis [see Fig. 1 b(2)]. For $|\Delta t| \approx T$, most interesting for gating, several distinct maxima are visible along β , indicating the orientations of consecutive half-cycles. For larger delays $|\Delta t| \approx nT$, where n is an integer, the angular separation between consecutive wavefronts is increased even further, but at the same time the field intensity is reduced significantly, leading to only weak XUV emission. For delays such that $\Delta t = (n + 1/2)T$, partially overlapped pulses interfere destructively on the optical axis, resulting in two weaker off-axis maxima and

strongly reduced XUV, suppressing efficient gating [17]. Gating is possible even with a difference in CEP for the two pulses. In this case, it will not occur for delays equal to a multiple of T and the symmetry between positive and negative delays will be lost.

Fig. 3 shows angularly-resolved XUV spectra for the three delay regimes presented above. In (c) the XUV radiation is emitted at $\beta = \pm\gamma$ and the spectra are modulated corresponding to pulse trains in the temporal domain. In (d), a pulse train is emitted on axis. Finally in (a) the radiation is emitted in different directions and the spectra are almost continuous, indicating the emission of several IAPs. The modulated and continuous emissions are compared in (b). The right side panel in (a) presents the spectrally integrated spatial profiles which compares well with the predictions from the wavefront orientation maps. These results show that the NOG technique allows a clear spatial separation of consecutive IAPs.

In Fig. 2(b,c), the maxima in the wavefront orientation map shift with CEP and consequently the XUV emission angle rotates. This shift occurs in different directions for positive and negative delays. When the CEP of both driving pulses is decreased, the XUV emission angle rotates upwards for $\Delta t = T$ and downwards for $\Delta t = -T$. This leads to a spatially asymmetric XUV intensity distribution for $\Delta t = \pm T$. The asymmetry observed in our experiment [Fig. 2(a)] is most likely due to a negative CEP.

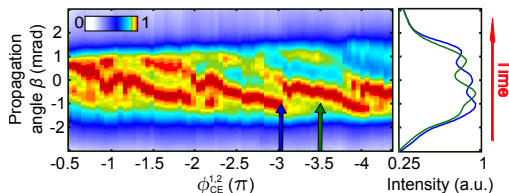


FIG. 4: Spectrally integrated (20 – 50 eV) spatial XUV far-field profile as a function of CEP for $\Delta t \approx -T$. In the right panel, two lineouts with a CEP offset of $\pi/2$ are shown. The lineout location is marked with arrows in the main panel.

In Fig. 4 we plot the spatially resolved XUV signal integrated over photon energy as a function of the CEP. The fringes show the downward shift (towards negative β) of the XUV emission in the far-field as the CEP decreases. For the experimental scan shown here, a D-shaped mirror was used for wave front division in the interferometer. This allowed us to avoid residual differences in dispersion for both pulses but led to a reduced beam size. A smaller noncollinear angle was used, resulting in less divergent far-field profiles. Furthermore, fewer attosecond pulses were observed, most likely due to an even better compressed laser pulse. The angular rotation of the XUV emission pattern with CEP demonstrates that the CEP is a sensitive parameter for controlling the emission di-

rection of the generated attosecond pulses. If an aperture is placed on the optical axis, an IAP can be selected. Alternatively, two attosecond pulses can be selected off-axis if the CEP is changed by $\pi/2$. The selection of multiple angularly separated IAPs is of interest for attosecond pump-probe experiments [27].

Since the CEP strongly affects the gating process, the emission direction of the emitted XUV beams becomes a sensitive probe for shot-to-shot CEP fluctuations on-target, when single-shot spectra are recorded. In our measurements, the XUV signal was integrated over a few shots. The fluctuations visible in Fig. 4 correspond to a stability of ≈ 500 mrad, most likely reduced by pointing instabilities dynamically changing the coupling into the hollow capillary as well as by pulse to pulse energy fluctuations inside the capillary [32, 33]. When multi-shot spectra are recorded, the shot-to-shot CEP fluctuations result in a loss of contrast in the recorded spatio-spectral patterns and thus, the emission from individual IAPs appears angularly less separated than predicted by simulations [17]. Another reason for the reduced contrast in Fig. 3(a) as well as for the low visibility of the gating in Fig. 2(a), despite the short duration of the driving laser pulses, is most likely a residual higher order chirp, clearly visible by the satellite pulse distribution in the pulse profile [see Fig. 1(a)]. Numerical simulations show that a residual chirp can prevent efficient gating. The CEP stability on-target can in the future be strongly improved by implementing a fast pointing stabilization for the coupling into the capillary as well as by measuring and stabilizing the CEP behind the capillary in single-

shot [34].

In conclusion, we provided evidence that noncollinear optical gating can be achieved experimentally, potentially giving access to multiple, perfectly synchronised IAPs. The NOG is the first gating technique that allows a direct spatial separation of fundamental driving field and generated attosecond pulses. We have shown that the CEP dependence of the time-to-space mapping can be used to control the direction and number of emitted IAPs. This makes the NOG technique ideally suited for experiments that require high XUV peak energy, such as attosecond-pump-attosecond-probe schemes. Finally, noncollinear gating is a promising candidate to obtain IAPs from enhancement cavities. In this case, the noncollinear geometry has to be achieved by either synchronizing two independent enhancement cavities [35], which share one generation medium or by designing an enhancement cavity with two circulating pulses, which meet noncollinearly in the generation medium [21]. For such approaches, elaborate cavity design including dispersion management to support few-cycle pulses needs to be addressed, however with the prospects of obtaining IAPs at unprecedented repetition rate and power as well as a continuous XUV frequency-comb.

Acknowledgements

This research was supported by the Marie Curie program ATTOFEL (ITN), the European Research Council (ALMA, PALP), the Swedish Research Council, the Swedish Foundation for Strategic Research and the Knut and Alice Wallenberg Foundation.

-
- [1] J. Ullrich *et al.*, Reports on Progress in Physics **66**, 1463 (2003).
 - [2] T. Haerlammert and H. Zacharias, Current Opinion in Solid State and Materials Science **13**, 13 (2009).
 - [3] M. I. Stockman *et al.*, Nature Photonics **1**, 539 (2007).
 - [4] E. Mårzell *et al.*, Annalen der Physik **525**, 162 (2013).
 - [5] R. Jones *et al.*, Physical Review Letters **94**, 193201 (2005).
 - [6] C. Gohle *et al.*, Nature **436**, 234 (2005).
 - [7] A. Mills *et al.*, Journal of Physics B: Atomic, Molecular and Optical Physics **45**, 142001 (2012).
 - [8] A. Ozawa *et al.*, Physical Review Letters **100**, (2008).
 - [9] A. Cingöz *et al.*, Nature **482**, 68 (2012).
 - [10] I. Pupeza *et al.*, Nature Photonics (2013).
 - [11] A. Schliesser *et al.*, Optics Express **14**, 147 (2006).
 - [12] T. Hammond, A. Mills, and D. Jones, Optics Express **17**, 8998 (2009).
 - [13] I. Pupeza, E. Fill, and F. Krausz, Optics Express **19**, 12108 (2011).
 - [14] I. J. Sola *et al.*, Nature Phys. **2**, 319 (2006).
 - [15] F. Ferrari *et al.*, Nature Photonics **4**, 875 (2010).
 - [16] I. Pupeza *et al.*, Physical Review Letters **112**, (2014).
 - [17] C. Heyl *et al.*, New Journal of Physics **16**, 052001 (2014).
 - [18] H. Vincenti and F. Quéré, Physical Review Letters **108**, 113904 (2012).
 - [19] S. Akturk *et al.*, Journal of Optics **12**, 093001 (2010).
 - [20] K. Kim *et al.*, Nature Photonics **7**, (2013).
 - [21] K. Moll, R. Jones, and J. Ye, Optics Express **14**, 8189 (2006).
 - [22] A. Ozawa *et al.*, Optics Express **16**, 6233 (2008).
 - [23] Y. Nabekawa *et al.*, Physical Review Letters **102**, 213904 (2009).
 - [24] P. Tzallas *et al.*, Nature Physics **7**, 781 (2011).
 - [25] E. Takahashi *et al.*, Nature Communications **4**, 2691 (2013).
 - [26] S. Leone *et al.*, Nature Photonics **8**, 162 (2014).
 - [27] F. Quéré *et al.*, Journal of Physics B: Atomic, Molecular and Optical Physics **47**, 124004 (2014).
 - [28] M. Nisoli *et al.*, Opt. Lett. **22**, 522 (1997).
 - [29] A. Suda *et al.*, Appl. Phys. Lett. **86**, 111116 (2005).
 - [30] M. Miranda *et al.*, Opt. Express **20**, 688 (2012).
 - [31] F. Silva *et al.*, Opt. Express **22**, 10181 (2014).
 - [32] H. Wang *et al.*, Opt. Express **17**, 12082 (2009).
 - [33] F. Lücking *et al.*, Opt. Lett. **39**, 2302 (2014).
 - [34] T. Fordell *et al.*, Opt. Express **19**, 23652 (2011).
 - [35] C. Benko *et al.*, Nature Photonics **8**, 530 (2014).